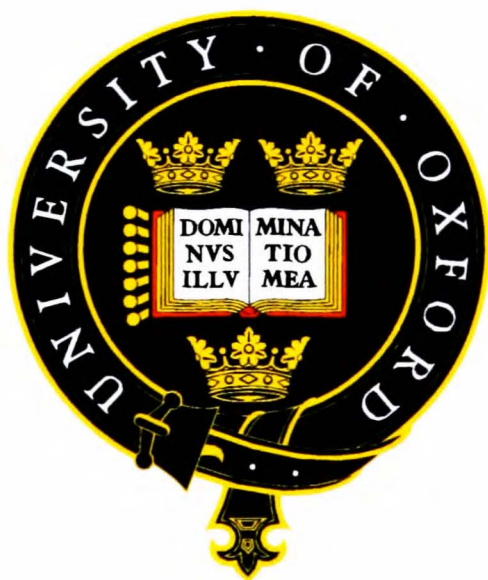


Vacuum Deposited Coatings on Polyester Films

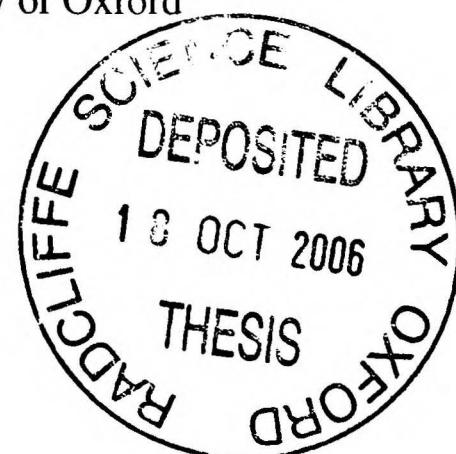
David Howells

Department of Materials and Wolfson College



A thesis submitted for the degree of Doctor of Philosophy at the University of Oxford

Hilary Term 2006



Vacuum Deposited Coatings on Polyester Films

David Howells
Doctor of Philosophy

Wolfson College
Hilary Term 2006

ABSTRACT

The work contained in this thesis examines how the properties of polyester film substrates affect the structure and performance of thin coatings vacuum-deposited upon them, particularly with regards to their function as gas barriers for use in packaging.

By modifying the surface of a PET film prior to deposition, with either oxygen or argon plasma, an increase in adhesion between the polymer and coating by 50% occurs for both aluminium and SiO_x layers. A reduction in the density of pinhole defects is also observed after such treatment.

A set of silicon oxide (SiO_x) coatings, deposited using a novel PECVD method, that display excellent barrier to water vapour permeation, impressive mechanical properties and good adhesion to the base film, is studied. Water vapour transmission rates as low as $2 \times 10^{-4} \text{ g m}^{-2} \text{ day}^{-1}$ are reported for these thin films as a result of their thickness and structure, where the deposition of the coating in several layers prevents defects extending throughout the coating. A high level of carbon incorporated in these films makes them flexible with relatively high strain to failure and low stress.

The properties of the SiO_x coatings vary significantly depending on the substrate on which they are deposited. By tailoring the polyester film properties during manufacture, a wide range of substrates with differing properties is produced. The most relevant appear to be the surface thermal and mechanical properties. SiO_x layers on heat stabilised PET (with or without an additional primer layer) and PEN outperform an equivalent coating on standard PET film by two orders of magnitude, in terms of gas barrier, and also possess superior mechanical properties. This is due to the enhanced thermal stability of the surfaces of these films as they undergo heating during deposition, as thermally induced motion of the chains at the surface of a plain PET film is thought to create defects. Substrate roughness is found to affect the morphology of deposited coatings but not the permeation of gas through them. The importance of substrate selection is illustrated by substituting PET with PEN, for example, where improvement in barrier is comparable to that achieved by coating a polymer film in the first place.

PREFACE

The work presented in this thesis was carried out by the author in the Department of Materials, University of Oxford between October 2002 and February 2006 under the supervision of Dr Hazel Assender and Dr Bernard Henry. The work was supported by the EPSRC and DuPont-Teijin Films as a CASE Award.

No part of this thesis has been previously submitted for a degree at this University or elsewhere. The research described is original; where the work of others is cited in the text this is acknowledged and referenced. A list of references is given at the end of the thesis.

Some of the work in this thesis has been, or is soon to be, published as follows:

D.G. Howells, B.M. Henry, J. Madocks, H.E. Assender, "High Quality PECVD Silicon Oxide Gas Barrier Coatings on Polyester Films", submitted to *Thin Solid Films*.

D.G. Howells, B.M. Henry, J. Madocks, Y. Leterrier, J.-A.E. Manson, H.E. Assender, "Mechanical Properties of SiO_x Gas Barrier Coatings on Polyester Films", in preparation.

D.G. Howells, B.M. Henry, L. Medico, Y. Leterrier, J.-A.E. Manson, H.E. Assender. "The Influence of the Polyester Substrate on the Structure and Performance of Vacuum Deposited Coatings", *48th Annual Technical Conference Proceedings of the Society of Vacuum Coaters*. 2005, p. 638

D.G. Howells, B.M. Henry, H. E. Assender, C.R.M. Grovenor, L. Médico, Y. Leterrier and J.-A. E. Manson. "Microstructural and Mechanical Properties of PECVD Films on Polyester Films" *Proceedings of the AIMCAL Fall Technical Conference, 18th International Vacuum Web Coating Conference, 2004*

Acknowledgements

I would first like to thank Dr Hazel Assender for offering me the opportunity to study for a DPhil and for her helpful supervision throughout the project. The useful insights and discussions she has provided during my research, plus the encouragement to attend conferences has made my time here so much more productive and enjoyable. I must also thank Dr Bernard Henry for his supervision and expertise in the area of barrier coatings and permeation testing, helping me to prepare for my conference talk and for using his extensive contact list to arrange for me the collaboration with General Plasma.

During this thesis I have worked with a number of external parties and first and foremost I should thank Dr's Julian Robinson, Chris Borman and Mark Hodgson from DuPont Teijin Films (my CASE sponsor) for supervising the work I have done, providing me with polymer films and always being willing to answer any queries I might have. I should also thank DTF and the EPSRC for providing the funding for me to conduct my research. I am also appreciative of the samples sent to me by Dr's John Madocks and Casey Finstad at General Plasma and their subsequent advice and ideas. Dr Yves Leterrier of the EPFL in Lausanne deserves special mention for allowing me to visit his laboratory on three separate occasions to perform mechanical testing of my samples and for explaining to me the fundamentals of the fragmentation test. Gregory Tornare and Leo Medico should also be mentioned for their friendly assistance during my visits to the EPFL.

In the Department of Materials at Oxford there are almost too many people to acknowledge for their assistance over the past 3 years. Dr Alison Crossley for performing XPS experiments and her advice on surface characterisation and careers, Richard Turner for his assistance on the sputter kit, gas permeation kit and the web coater, Dr Ahmet Gün Erlat for teaching me the dark art of sputtering, Dr John Topping for running the web coater and allowing me to use his home-made sputter kit, Dr Kyriakos Porfyrakis for teaching me how to use the AFM, Tony Brown and Mel Mead for their assistance in the Begbroke cleanroom when using the PECVD and plasma treater and Kei Shinotsuka for showing me how to measure glass transition temperatures using AFM and for his useful discussion about polymers and AFM in particular. Thanks to Dr Robert Jacobs from the Chemistry department for allowing me to use their AFM and contact angle facilities.

Outside of work I would like to mention friends from Wolfson College, particularly Shaun, Martin and Ben – the 354 Cowley Road boys – for providing first-class amusement, discussion and friendship over the three years, and the numerous members of the football team who have helped me fill my Saturdays.

I must finally thank my family for all the love and support they have given to me over the years and I would particularly like to thank Becs for her patience in listening to my ideas, moans and rants and for giving me good advice on any number of occasions. Despite completing a thesis herself she has always been extremely supportive, full of thoughts and ideas and great company over the last 3 years.

Glossary of Terms

ACF	Autocorrelation function	A	Exposed film area
AFM	Atomic force microscopy	D	Diffusion coefficient
aPET	Amorphous PET	E	Young's modulus
BD	Biaxially drawn	E_A	Activation energy
BE	Binding energy	h	Thickness
BIF	Barrier improvement factor	H	Hurst exponent
CA	Contact angle	J	Flux
CD	Crack density	l_c	Critical stress transfer length
cdf	Cumulative distribution function	M_w	Molecular weight
COS	Crack onset strain	P	Permeability
CVD	Chemical vapour deposition	P_f	Failure probability
DEG	Diethylene glycol	R	Universal gas constant
DSC	Differential scanning calorimetry	R_q	rms roughness
DTF	Dupont-Teijin Films	R_x	Radius of curvature
EA	Ethyl acrylate	S	Solubility
F-PET	Filled poly(ethylene terephthalate)	T	Temperature
FTIR	Fourier transform infra red (spectroscopy)	T_c	Critical thickness
FWHM	Full width half maximum	T_g	Glass transition temperature
HMDSO	Hexamethyldisiloxane	T_m	Melting temperature
HS PET	Heat stabilised PET		
IFSS	Interfacial shear stress		
ILT	Ideal laminate theory	α	Weibull shape parameter
KE	Kinetic energy	β	Weibull scale parameter
LCTE	Linear coefficient of thermal expansion	Γ	Gamma function
LFM	Lateral force microscopy	γ	Surface tension
MA	Methyl acrylamide	ε	Tensile strain
MD	Machine direction	θ	Contact angle
MMA	Methyl methacrylate	Π	Transmission rate
OLED	Organic light emitting device	σ_i	Internal stress
OTR	Oxygen transmission rate	σ_{max}	Cohesive strength
PC	Poly(carbonate)	σ_T	True stress
PDPS	Penning discharge plasma source	τ	Interfacial shear stress
PE	Poly(ethylene)	ν	Poisson's ratio
PECVD	Plasma enhanced chemical vapour deposition		
PEN	Poly(ethylene naphthalate)		
PES	Poly(ether sulphone)		
PET	Poly(ethylene terephthalate)		
PP	Poly(propylene)		
PS	Poly(styrene)		
PT	Plasma treated		
PVD	Physical vapour deposition		
R2R	Roll to roll		
rf	Radio frequency		
RH	Relative humidity		
RIE	Reactive ion etching		
rms	Root-mean-square		
sccm	Standard cubic centimetres per minute		
SD	Standard deviation		
SEM	Scanning electron microscopy		
TD	Transverse direction		
TEM	Transmission electron microscopy		
UHV	Ultra high vacuum		
UV	Ultraviolet		
WAXD	Wide angle X-ray diffraction		
WVTR	Water vapour transmission rate		
XPS	X-ray photoelectron spectroscopy		
XRF	X-ray fluorescence		

Table of Contents

Chapter 1. Introduction	1
1.1 Overview.....	1
1.2 Introduction to Polyester Film	3
1.2.1 Synthesis of PET	4
1.2.2 Structure of PET	5
1.3 Polyethylene Naphthalate (PEN).....	8
1.4 The Manufacture of Polyester Films	10
1.5 Evolution of Polyester Film Structure During Manufacture	12
1.5.1 Structural development during uniaxial drawing	12
1.5.2 Biaxially drawing the film.....	16
1.5.3 Heat setting	18
1.6 Modifications to Polymer Films During Manufacture.....	20
Chapter 2. Vacuum Deposited Coatings for Gas Barrier Applications.	22
2.1 Permeation of Gases Through Solids.....	22
2.1.1 Permeation of gas and water vapour through polymers	25
2.1.2 Why should gas barrier be improved by a thin metal or ceramic coating?	27
2.2 Methods of Coating Deposition	30
2.2.1 Chemical Vapour Deposition	30
2.2.1.1 <i>Plasma Enhanced Chemical Vapour Deposition</i>	30
2.2.2 Physical Vapour Deposition	33
2.2.2.1 <i>Sputtering</i>	33
2.2.2.2 <i>Evaporation</i>	35
2.2.3 Nucleation and growth of the vacuum deposited coating.....	36
2.2.4 How thick does a barrier coating need to be?.....	38
2.3 Why Does Gas Still Travel Through Coated Films?	40
2.3.1 Defect controlled oxygen permeation.....	40
2.3.2 Defect controlled water vapour permeation	43
2.4 Current Barrier Technologies	46
2.4.1 Multilayer coatings.....	47
2.5 Mechanical Properties and Adhesion	50
2.5.1 Internal stresses.....	50
2.5.2 Adhesion.....	54
2.6 Substrate Effects	59
2.6.1 Plasma surface modification.....	60
2.6.2 Effects of plasma treatment on vacuum deposited coatings.....	64
2.7 Conclusion	65
Chapter 3. Experimental Methods	67
3.1 Atomic Force Microscopy	67
3.1.1 Contact Mode AFM.....	67
3.1.2 Tapping Mode.....	69
3.1.3 Force-distance curves	70

3.1.4 Details of AFM imaging.....	71
3.1.5 Glass transition temperature measurement.....	72
3.2 Scanning Electron Microscopy (SEM)	72
3.3 X-ray Photoelectron Spectroscopy (XPS).....	73
3.4 Contact Angles	76
3.5 Water Vapour Permeation Measurement.....	77
3.6 Internal Stresses.....	79
3.7 Mechanical Properties.....	80
3.7.1 Fragmentation testing	80
3.7.2 Cohesive strength	82
3.7.3 Adhesive strength	84
Chapter 4. The Properties of Polyester Substrates.....	87
4.1 Introduction	87
4.2 Surface Topography	88
4.3 Surface Chemistry	95
4.4 Surface Glass Transition Temperature (T_g)	98
4.5 Mechanical Properties.....	100
4.6 The Importance of Substrate Selection	103
4.6.1 Deposition process.....	103
4.6.2 Microstructural studies	104
4.7 Summary	106
Chapter 5. Vacuum Deposited Coatings on Plasma Treated PET Film	
.....	109
5.1 Plasma Treatment of PET	110
5.1.1 Experimental set-up.....	110
5.1.2 Oxygen Plasma Treatment.....	112
5.1.2.1 Wettability.....	112
5.1.2.2 Surface chemistry	113
5.1.2.3 Surface topography.....	117
5.1.3 Argon plasma treatment.....	120
5.1.4 Ar-O ₂ gas mixtures	124
5.2 Sputtered Aluminium Coatings.....	124
5.2.1 Experimental.....	124
5.2.2 Water vapour permeation	125
5.2.3 Microstructure	126
5.2.4 Interfacial bonding.....	128
5.2.5 Adhesion.....	131
5.3 Batch PECVD SiO_x Coatings.....	134
5.3.1 Film fabrication	134
5.3.2 Microstructure	135
5.3.3 Interfacial bonding.....	138
5.3.4 Adhesion.....	140
5.4 Summary	141

Chapter 6. Silicon Oxide Gas Barrier Coatings on Polyester Films:	
Effect of the Substrate	146
6.1 Deposition Method.....	148
6.2 Physical Properties of the Coating.....	152
6.2.1 Batch 1	152
6.2.2 Batch 2.....	153
6.3 Water Permeation Through the Coated Films	155
6.3.1 Batch 1	155
<i>6.3.1.1 Microstructure.....</i>	<i>156</i>
6.3.2 Gas barrier properties of Batch 2 coatings	159
<i>6.3.2.1 Microstructure of Batch 2 coatings</i>	<i>167</i>
6.4 Internal Stresses.....	170
6.4.1 Batch 1	170
6.4.2 Batch 2.....	172
6.5 Fragmentation Testing	175
6.5.1 Batch 1	175
<i>6.5.1.1 A note concerning the error bounds for fragmentation test data.....</i>	<i>178</i>
6.5.2 Fragmentation testing of Batch 2 samples.....	179
6.5.3 Adhesive strength of the composites.....	184
<i>6.5.3.1 The case of the acrylate primer layer</i>	<i>188</i>
6.6 Summary	191
Chapter 7. Conclusions and Suggestions for Further Work.....	195
7.1 Conclusions.....	195
7.2 Suggestions for Further Work.....	199
Chapter 8. Bibliography.....	201

Chapter 1. Introduction

1.1 Overview

Many food and beverage [1-3], pharmaceutical [4], medical [5] and opto-electronic [6, 7] goods are encapsulated in packaging so that the product does not come into physical contact with the surrounding environment. As well as physically containing the product the benefits of packaging include hygiene, maintaining the appearance and function of the product, branding, improved appearance and ease of transport. Additionally, the packaging is often required to protect a product from exposure to atmospheric oxygen and water vapour that could chemically degrade it. It is also frequently required to prevent loss of aroma, from food for example, or gas (such as CO₂ in the case of carbonated beverages) from a product. Either aspect of gas transport reduces the life-time of many goods and must be limited. Glass is traditionally used as a packaging material, in bottles and screens for example, as it is almost impermeable to gas transport, is transparent and can easily be shaped, although its weight and brittleness mean that it is not an ideal material in many cases.

In the last few decades the advances in polymer science have seen polymeric materials usurp glass in many packaging applications [2, 3], due to their light-weight, non brittle, flexible character and reduced costs of manufacture and transportation. The most popular thin film packaging materials are polyethylene (PE), polypropylene (PP) and polyester – particularly polyethylene terephthalate (PET). Polymer film is not particularly effective in preventing the transport of gas, however, and a thin secondary ceramic or metallic

layer is usually deposited upon it to improve its barrier performance by up to 3 orders of magnitude, so that it is suitable for packaging use. Such coatings, as well as being effective barriers to gas transport must possess a host of other important properties to be successful, such as high mechanical strength and adhesion to the base film (so that the composite maintains its structural integrity through its lifecycle), chemical inertness, low toxicity and in many cases transparency [8]. The coatings must be deposited on an industrial scale to meet demand and be affordable. It should also be noted that the polymer-coating bilayer structure that is employed as a gas barrier forms only part of a typical polymeric packaging composite material. Figure 1.1(a) displays the complexity of the structure of a typical food package [9], with multiple polymer layers that are coextruded, heat sealed or laminated. Also shown (Figure 1.1(b)) is a schematic of a proposed F-OLED (flexible organic light emitting device) structure, which is a major driver to improvements in gas barrier technology today [7].

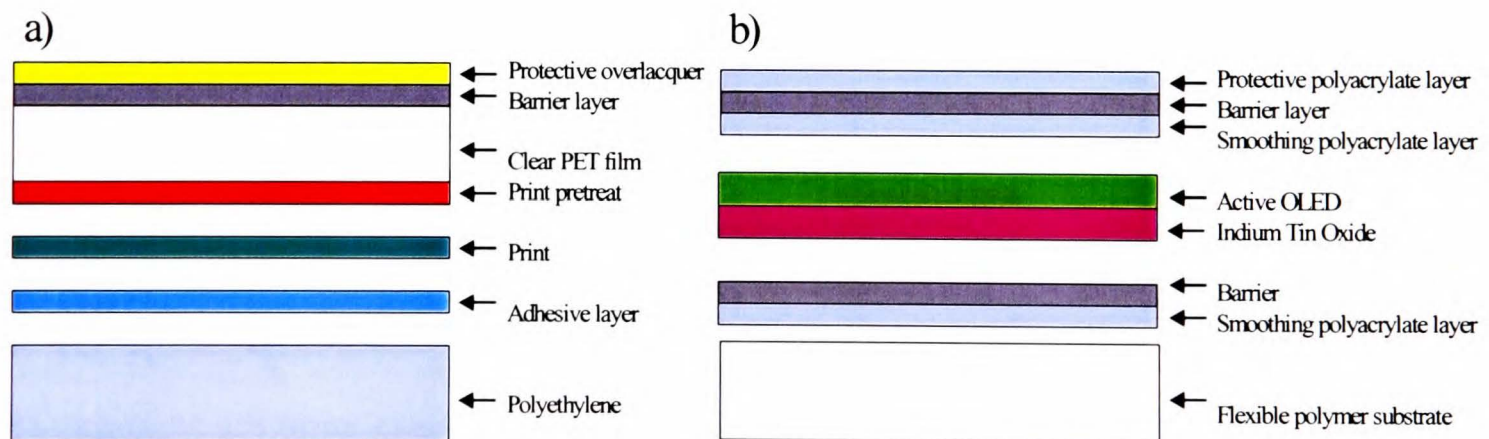


Figure 1.1 Schematic multilayer structure of (a) packaging for food, (b) an OLED device.

In this thesis I shall report how modifying the characteristics of polyester film in the bilayer barrier composite affects the structure and properties of the subsequently

deposited barrier coating. I will also describe a promising silicon oxide coating that outperforms all previously reported single-layer barrier coatings in the literature, deposited using a novel method. Polyester, particularly PET, is chosen as the base substrate in this study as it is commonly used in packaging, due to its favourable properties and relatively low cost, and has shown promise in high barrier applications, such as flexible displays.

1.2 Introduction to Polyester Film

The most commonly used polyester is PET [poly(ethylene terephthalate)] which was first discovered in the 19th century, although it was only identified as being useful as a fibre forming material in 1941 by J. R. Whinfield and J. T. Dickson at ICI, when a replacement for silk was sought [10]. Companies such as ICI and E. I. duPont de Nemours & Co. led the way in PET technology and in the 1950's the process of stretching and uniaxially orienting polyester fibres and films was developed. A decade later the process of biaxially drawing polyester film was developed (with either simultaneous or subsequent orientation orthogonal to the roll direction). The resultant films were found to be superior materials with enhanced mechanical properties and a lower gas permeability. In addition, PET products are pure, chemically inert, clear and their light weight means that they are more economical than, say, glass equivalents.

The relative low cost and ease of manufacture and processing of PET has led to a boom in its global production over the last 30 years – from below 500 tonnes in 1970 to over 1.2 million tonnes in 1990, a significant portion of this increase solely attributable to the

development of PET beverage bottles [11]. In the years between 1995 and 2000 the total world consumption of PET was more than doubled to over 7 million tonnes per year and from 2000 to 2005 the increase in consumption was expected to be 10% per annum. With such widespread use it is encouraging that PET is easily recyclable, a case in point being the recycling of PET bottle resin into fibres for anoraks and duvets. Recycled PET is also often re-used in containers where it is sandwiched between layers of virgin PET. Figure 1.2 summarises the growth in global consumption of PET over the past 25 years [10].

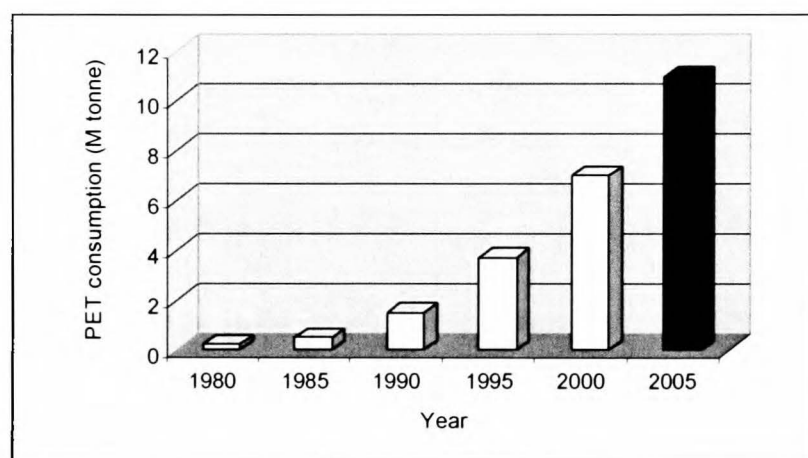


Figure 1.2 Worldwide consumption of PET (2005 column is a forecast; Reproduced from [10]).

1.2.1 Synthesis of PET

PET is a condensation polymer typically produced via the transesterification of terephthalic acid (TA) and ethylene glycol, with the following chemical structure (Figure 1.3). More recently dimethyl terephthalate (DMT) has replaced TA as a precursor as it is easier to purify and is more soluble, thereby increasing the rate of esterification. Once the monomer is synthesised it undergoes a polycondensation reaction at 270-285°C, a pressure of less than 0.13 kPa and in the presence of a catalyst, often antimony trioxide [11].



Figure 1.3 Chemical structure of PET.

The repeat unit has an atomic mass of 192 and the typical molecular weight (M_w) of the polymer used in commercial applications is between 20 000 and 80 000, such that the chain length is between 100 and 400 repeat units. Care must be taken when producing high M_w polymer as thermal decomposition of the end groups competes with polymerisation due to the high temperatures used in the synthesis. For oriented films and fibres a M_w of 35 000-40 000 is preferred. When considering PET structure it should be noted that there is a small amount (ca 1%) of diethylene glycol (DEG) present as copolymerised units in the chains [12]. There are also cyclic trimer products which can migrate to the surface of melt extruded fibres and films, causing difficulties in some applications. Both of these structural imperfections are unavoidable side products of the PET synthesis.

1.2.2 Structure of PET

PET has a relatively slow crystallisation rate and can be easily quenched from the molten state to produce a totally amorphous glass. Depending on the nature of the amorphous phase the glass transition temperature, T_g , ranges from 60-120°C [11]. At similar temperatures, crystallisation of the PET is known to occur, with a greater rate of

crystallisation at higher temperatures up to about 160°C [11, 13]. The unit cell of a PET crystal is shown in Figure 1.4. It is triclinic [14] with dimensions $a = 0.448 \pm 0.004$ nm; $b = 0.589 \pm 0.004$ nm; $c = 1.071 \pm 0.004$ nm and angles $\alpha = 99.80 \pm 0.30^\circ$; $\beta = 117.60 \pm 0.70^\circ$ and $\gamma = 111.50 \pm 0.30^\circ$. There is one chain with one monomer in the unit cell, the density of which has been measured to be between 1.455 g m^{-3} and 1.515 g m^{-3} [11]. Meanwhile the totally amorphous region is less dense with values ranging from 1.328 g m^{-3} and 1.341 g m^{-3} . The variation in density for both phases is mainly thought to be due to variation in the DEG content, although in the amorphous region the extent of orientation can also play a part [15]. What constitutes amorphous material in polymers is a matter of debate as some non-crystalline phases exhibit orientation and order, more so than for a completely random network of chains. This type of region in polymers is often termed the mesophase.

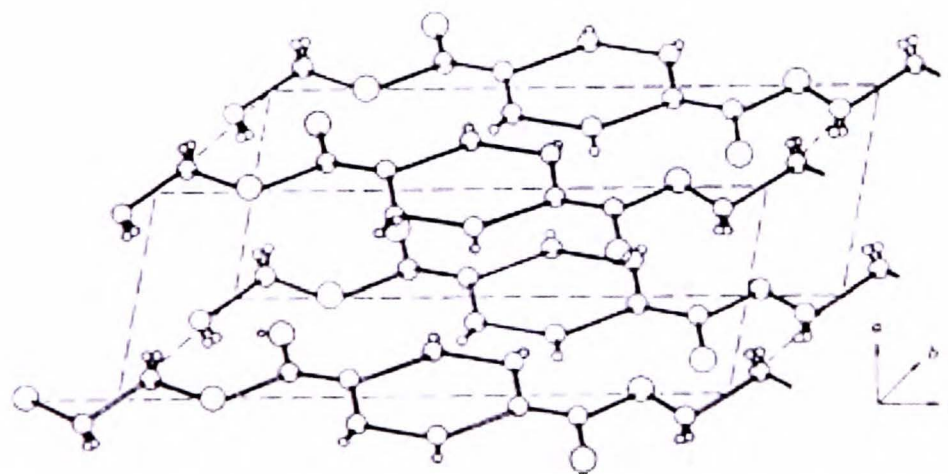


Figure 1.4 Unit cell of crystalline PET (Reproduced from [16]).

PET crystal morphology has generally been found to adhere to the lamellar model, particularly for crystals grown under quiescent conditions from dilute solutions or melts. Individual lamellae are the basic structural unit of polymer crystals and are 3-D platelet-like structures with a thickness of around 10 nm and lateral dimensions of the order of a

micron [17]. The thickness of lamellae is considerably less than the length of an individual molecular chain and it is widely accepted that the lamellae consist of folded chains, their direction being perpendicular to their basal plane [18], as shown in Figure 1.5(a), and (b). This schematic illustrates two of the models of lamellar structure, which vary in the degree and uniformity of chain refolding. Often these lamellae combine to form large polycrystalline structures called spherulites which consist of individual lamellae radiating outwards from a nucleus [19]. A schematic of such a feature is shown in Figure 1.5(c). The interlamellar spaces are thought to be filled with amorphous or “mesophase” material.

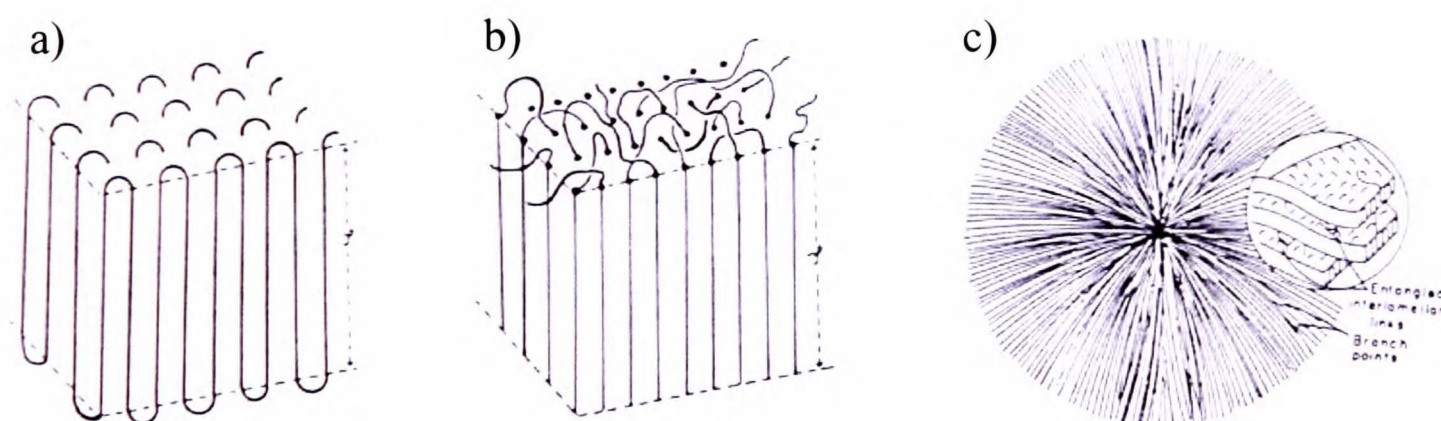


Figure 1.5 Lamellar structure of PET (a) adjacent re-entry model, (b) switchboard model, (c) spherulites (reproduced from [17]).

When crystallisation is accompanied and/or promoted by an applied stress, oriented fibrillar crystals are formed by alignment of polymer chains and the partial crystallisation of several polymer molecules [20, 21]. This is an important feature of drawn films and fibres, which exhibit a 1-D fibrillar crystal structure at high orientation.

A crucial factor in PET crystal growth is the conformation of the $-O-CH_2-CH_2-O-$ sections of the polymer chain which can exist in either a *trans* or *gauche* conformation as shown in Figure 1.6. It is well established that only PET chains with a *trans* conformation are present in crystallites [14, 22], that is during crystallisation some *gauche* conformers are converted to *trans* as only this conformation enables the close packing of chains required for crystal growth [20]. Such a conformational change is estimated to require 5.3 kJ mol^{-1} of energy [23]. The amorphous phase is home to both *gauche* and a lesser amount of *trans* segments which are thought to exist in a more ordered mesophase [24].

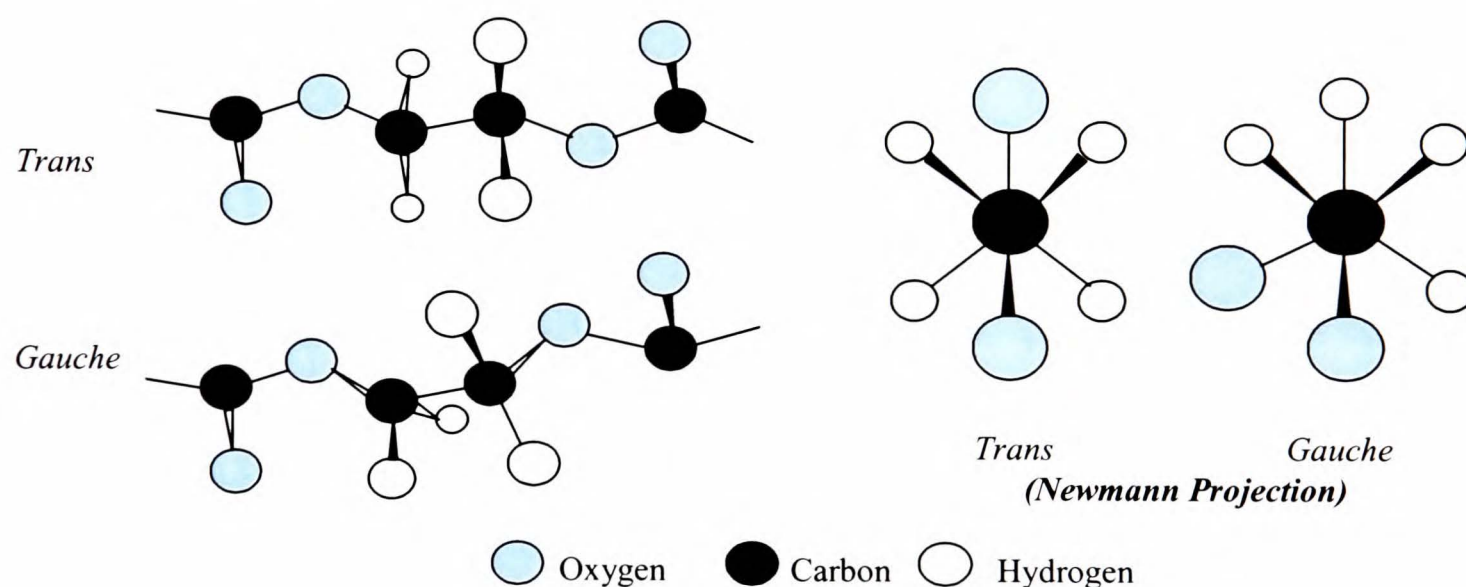


Figure 1.6 Conformers of PET.

1.3 Polyethylene Naphthalate (PEN)

PEN is a high barrier polyester that was developed in the 1980s and has the potential to replace glass in some market segments [25]. It is an ideal material for high performance packaging [10] as it has a gas barrier (O_2 , CO_2) five times better than PET, a water vapour barrier four times as good, greater stiffness and temperature stability and a higher

T_g at 120°C compared to ~75°C for PET. It is produced by condensation polymerisation of 2,6-naphthalenedicarboxylic acid and ethylene glycol but the limited availability of dicarboxylic acid monomer means that the introduction of PEN into high volume commercial packaging applications has been restricted.

Structurally PEN differs from PET in that it contains a naphthalene ring instead of benzene in its repeat unit, which improves its mechanical properties as well as its barrier to gas permeation. It has been reported that PEN has two crystal forms, that are both triclinic and that are dependent on the temperature of crystallization [26]. The α form is yielded at 180°C with unit cell parameters $a = 0.657$ nm; $b = 0.575$ nm; $c = 1.32$ nm; $\alpha = 81.2^\circ$; $\beta = 144^\circ$ and $\gamma = 100^\circ$ and is the form found in drawn PEN film, with one chain per unit cell [26]. At a crystallisation temperature of 240°C the β form is given. The presence of a mesophase in drawn PEN that is neither fully crystalline nor amorphous, yet exhibits spatial order, has been reported [27].

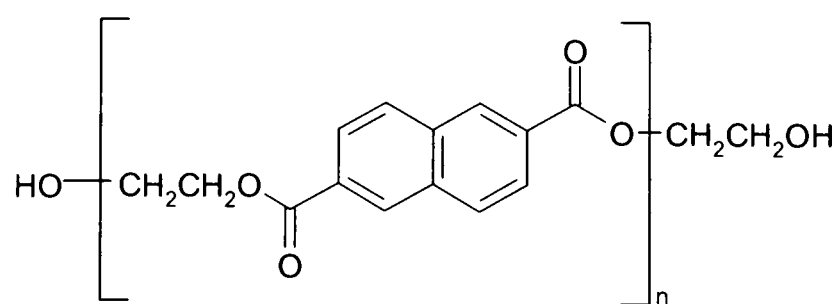


Figure 1.7 Chemical structure of PEN.

1.4 The Manufacture of Polyester Films

After synthesis of the polymer is complete, the resultant chips are thoroughly dried to minimise hydrolytic degradation and the production of flat film may begin [11, 28]. Figure 1.8 shows a schematic of the process. First, the dried chips are fed into an extruder with operating temperatures of 270-300°C and pressures of 6 – 20 MPa in an inert atmosphere. The melt is extruded through slot dies and cast onto a drum which is chilled, so that rapid cooling of the melt is achieved. Such a precaution is required to prevent the growth of large crystallites that cause haze and hinder the drawing process.

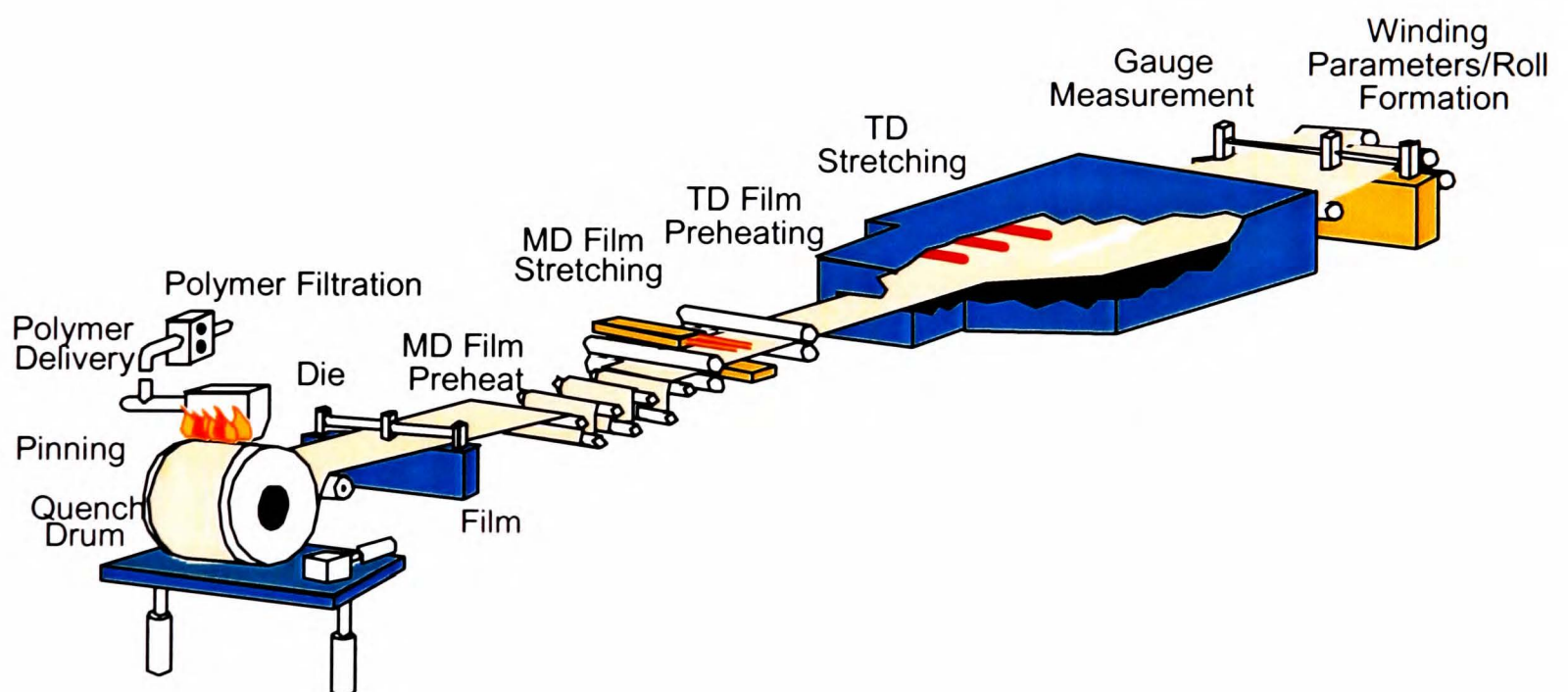


Figure 1.8 Schematic of polyester thin film manufacture.

The amorphous film is then drawn in the machine direction (MD) in the gaps between the heated parallel rolls to a draw ratio that will depend on the desired properties of the finished film. The stretched film then passes over cooling rolls to stabilise its structure. If

no other process is performed on the film, it is known as uniaxially drawn film and will have a significant orientation of molecules in the amorphous phase in the draw direction (the MD) and strain-induced crystallisation will have occurred, resulting in a semicrystalline film with a degree of crystallinity of around 15%.

Biaxially drawn film is achieved when the uniaxially stretched film is first preheated to around 100°C and then reaches the stenter, where it is stretched in the transverse direction (TD), as it is led along diverging rails, by a factor of 3 or 4. This film now has a crystallinity of about 30% and the polymer chains and crystallites are now fairly evenly oriented in both the MD and TD if the draw ratio is comparable to that in the machine direction. This method is sequential stretching: it is also possible to perform simultaneous stretching in the MD and TD which is a more complex technique, but one that often produces superior films in terms of dimensional stability and flatness [29].

Finally, a common step utilised by polyester film manufacturers is the “heat set” or thermal stabilisation of the film to prevent shrinkage of the film after tension is removed [28, 30, 31]. Additionally, when subjected to temperatures above 60°C it is known that drawn PET can suffer significant shrinkage, often called thermal relaxation, due to contraction of the relatively oriented amorphous phase to a more random, disordered state [29, 32]. To overcome this problem, the film’s dimensional stability can be increased by a heat treatment in the range 150-220°C. This process encourages crystalline growth as well as the melting and recrystallisation of metastable crystals, and oriented amorphous regions may exhibit significant molecular relaxation. In addition ester exchange reactions

may occur. The end product is a film with increased dimensional stability, due to a crystallinity of around 50% accompanied by relaxed amorphous regions.

1.5 Evolution of Polyester Film Structure During Manufacture

An understanding of the evolution and final structure of the PET film during and after the drawing process is necessary to explain its properties as a stand-alone film and for any subsequent modifications, such as the vacuum deposition of a coating for gas barrier applications. After extrusion the film cast onto the cooling drum should be totally amorphous, although insufficient cooling, or a slow cooling rate can lead to some orientation and increased *trans* content. Once the drawing process begins rapid structural change ensues, to which a myriad of research papers have been devoted [22, 30, 31, 33-42] and which are summarized here. However, it is worth noting that most of the experiments reported are performed on the laboratory scale and are not a true representation of the industrial scale manufacturing processes used to make the films. In the following sections notes are made where the process for PEN differs significantly to that of PET.

1.5.1 Structural development during uniaxial drawing

The most common methods of examining the structural development are IR and Raman spectroscopies, X-ray diffraction and birefringence and density measurements on thin films. It is now established that deformation of PET above T_g leads to:

- Rubber-like behaviour of the amorphous phase due to physical entanglements [43, 44]

- A decrease in the proportion of glycol groups exhibiting a *gauche* conformation, due to chain extension [22]
- The aromatic rings in the chains progressively orienting themselves so that they are parallel to the plane of deformation [22, 45]
- The development of a highly oriented amorphous phase, consisting of chains in their *trans* conformation [22, 35, 36]
- Confinement of *gauche* conformers in the less oriented amorphous phase
- The appearance of small and oriented crystals, involving only chains having a *trans* configuration [22]

The degree of crystallinity has been found to vary with draw ratio as an S-shaped curve where it is almost negligible up to draw ratio of 2-2.5 and then increases to above 30% for draw ratios up to 5 [31, 39]. The stress-induced crystalline phase has been repeatedly found to consist of oriented microfibrils embedded in an oriented amorphous phase [39, 46, 47], although it is not totally clear whether this structure is entirely independent of the quenching step that is required between deformation and measurement.

Until a few years ago, the conventional wisdom on strain-induced crystallisation was that based on work by Salem [42] who divided the process into two stages: (1) initial stage where stress increases rapidly due to fast crystallisation and (2) a second stage where dramatic increase in stress (strain hardening) is observed with only a moderate increase in crystallinity. Also examining uniaxial deformation of amorphous PET above T_g , Gorlier *et al.* [39] propose a 3 step model: First, molecular orientation occurs due to strong molecular interactions then nuclei appear as a result of this orientation, forming a

network structure responsible for strain hardening. Crystallisation then follows through the growth process.

Real time measurements of structural formation in PET films and fibres have been achieved by the use of an intense synchrotron X-ray source, first by Welsh *et al.* [48]. Subsequently, Blundell and co workers [41, 49] investigated the structural development of PET films during fast drawing and found that crystallisation did not occur under fast drawing, rather a mesomorphic structure (smectic A) appeared upon extension. They proposed that the smectic structure was a precursor of crystals, based on the simultaneous appearance of a triclinic crystal peak and the disappearance of the smectic peak. This work has been followed up by Kawakami *et al.* [40] who detail the formation of an oriented mesophase up to 180% strain and that it provides the nucleation sites for crystallisation (Zone 1). Zone 2, from 180% strain to 380%, sees the onset of crystallisation, albeit the crystals are poorly oriented and defective at first and through this zone 3-dimensional crystal growth, crystal perfection and increased crystal orientation are observed by synchrotron WAXD. Finally, Zone 3, from 380% to breakage of the PET was found to have increased crystallinity (continued growth) and orientation and is characterised by a stable crystal morphology.

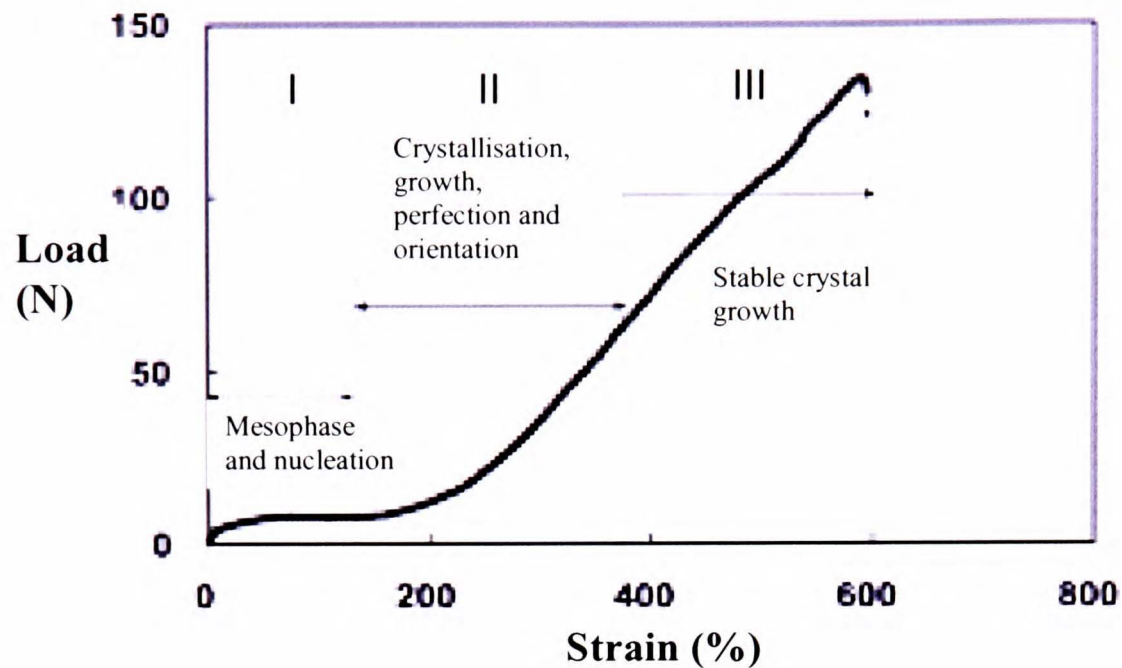


Figure 1.9 Structural evolution of PET during drawing (reproduced from [40]).

There are additional difficulties in drawing PEN into films compared to PET, including a higher drawing temperature to reach the glass transition and necking of the film being apparent for PEN even above the T_g [26, 50, 51]. Necking during uniaxial drawing is thought to be the result of the randomly oriented amorphous chains aligning themselves with their rings parallel to the film surface with one dimensional order in the thickness direction (Figure 1.10) and occurs up to 30°C above the T_g [50]. At temperatures much higher than this strain induced crystallisation, which is required for film stability and uniformity, is eliminated and thermal crystallization, which is detrimental to film appearance, is observed instead. PEN films therefore have a much narrower processing temperature window than PET but high draw ratios can yield uniform film if the draw temperature is about 150°C.

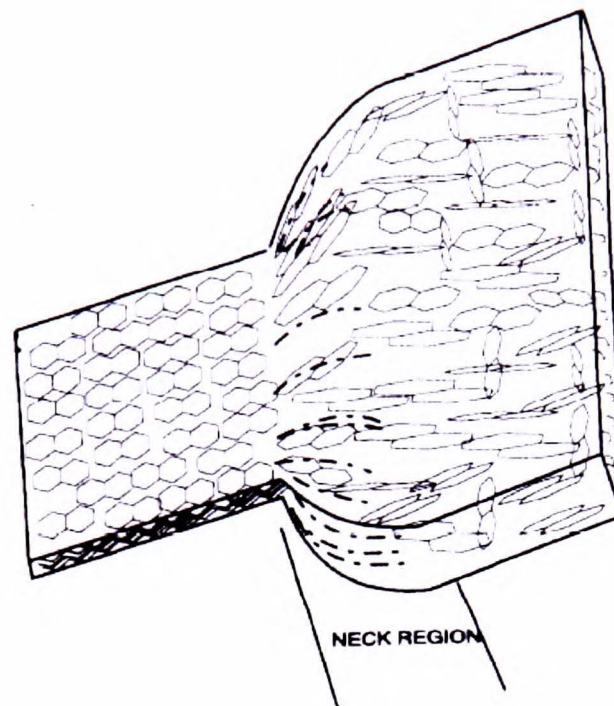


Figure 1.10 Proposed molecular basis of necking in drawn PEN film [50].

1.5.2 Biaxially drawing the film

In the processing of biaxially drawn films, the first MD stretch is to a draw ratio of about 4, meaning that the polymer is within zone 3 of the model proposed by Kawakami [40] and that there is a well oriented, stable crystal structure within an oriented amorphous phase in the direction of the draw. The subsequent effects of the second transverse draw are less well studied, due to the increased complexity of the film's processing history and the fact that at the start of the process the material is semicrystalline and not a rubber-like amorphous network.

Recent work on this issue has been conducted in a series of papers by Faisant de Champchesnel and various co-workers [45, 52, 53]. At a temperature of 120°C and by using WAXD they observe a reduction in crystalline orientation in the MD with increased c-axis orientation in the TD [52]. This is attributed to the progressive breaking and rotating of crystals originally in the MD towards the TD and then the subsequent

crystal growth caused by the small reoriented crystals acting as nuclei. A subsequent publication considers the effect of the size of the crystals in the TD direction after a uniaxial deformation [45]. They find that short crystals (in the c-axis direction) break and rotate more easily than longer ones (due to more molecular mobility associated with lower crystallinity) and act as nuclei for further crystal formation and growth. Therefore a film containing smaller crystals is easier to stretch into biaxially drawn film. In the same paper a temperature for TD of 120°C is found to be optimum to allow sufficient rotation of the smaller crystalline units while being low enough to avoid rapid crystallisation in the MD. Tassin *et al.* [54] also note the rotation of crystals from MD oriented to TD oriented using WAXD, with a significant number oriented in intermediate directions.

Work on the effect of TD stretching on the amorphous regions is relatively scarce. Gohil and Salem [55] conclude that a sequential transverse draw causes rotation of the non-crystalline oriented chains from the MD to TD and that a balanced biaxial orientation distribution occurs before the TD draw ratio equals the MD one. Equal draw ratios lead to the non-crystalline chains being predominantly ordered in the TD. Furthermore a WAXD and IR dichroism investigation of the amorphous phase suggests that larger crystals hinder the realignment of non-crystalline chains and that the phenyl rings do not lie in the plane of the draw as they would in the crystalline phase [52].

Studies of simultaneous biaxial stretching, by Buckley and various coworkers [43, 56, 57], have shown that just above T_g uncrosslinked amorphous PET behaves like a rubber with entanglements acting as physical network junctions, supporting earlier work by

Ward and others [44, 58] who observed this for uniaxial and biaxial drawing of PET at 85°C. As temperature increases above 100°C “entanglement slippage” occurs and the PET becomes less crosslinked and less rubbery as a result [57]. The slippage was observed to be arrested at a critical degree of orientation, due to topological constraint resulting from increased order and alignment of the chains, but not strictly crystallisation as this only occurs after drawing ceases at the fast strain rates used. They also present a “glass/rubber” constitutive model that accurately describes the behaviour of amorphous polymers near the glass transition during biaxial drawing and calculate that there are 17 monomer units in a chain between entanglements [43]. Subsequent evolution of the model is able to predict PET drawing behaviour at a greater range of temperatures and encompasses crystallization and strain stiffening effects [57].

1.5.3 Heat setting

The final process to induce structural change in the PET film is the heat-set stage, aimed at making the film more dimensionally stable at high temperatures, particularly above T_g . It is associated with a large increase in crystallinity and prevents shrinkage of the film post-drawing. Varma *et al.* [59] observed a steep increase in crystallinity of biaxially drawn film after heating at 150°C in unconstrained conditions and suggested a structure consisting of a matrix of perpendicularly oriented crystals. A mechanism for heat treating in oriented films was elaborated by Gohil in 1993 [29]. By using a three regime model the following conclusions were made:

- In the temperature range $T_g - T_{max}$ (Regime II, and T_{max} is the temperature of maximum rate of crystallisation), relaxation is minimal compared to the increase

in crystallinity, due to increased crystal growth and the fusing together of adjacent micellar crystals.

- This results in more physical tie points for the free amorphous chains, leading to a constrained amorphous phase with reduced molecular mobility.
- Regime III ($T_{max} - T_m$, where T_m is the melting temperature) heat treatment causes a lamellar crystal structure to form due to melting and recrystallisation and the degree of crystallinity increases. The number of taut interconnecting tie molecules decreases and the amorphous phase becomes more relaxed as a result.

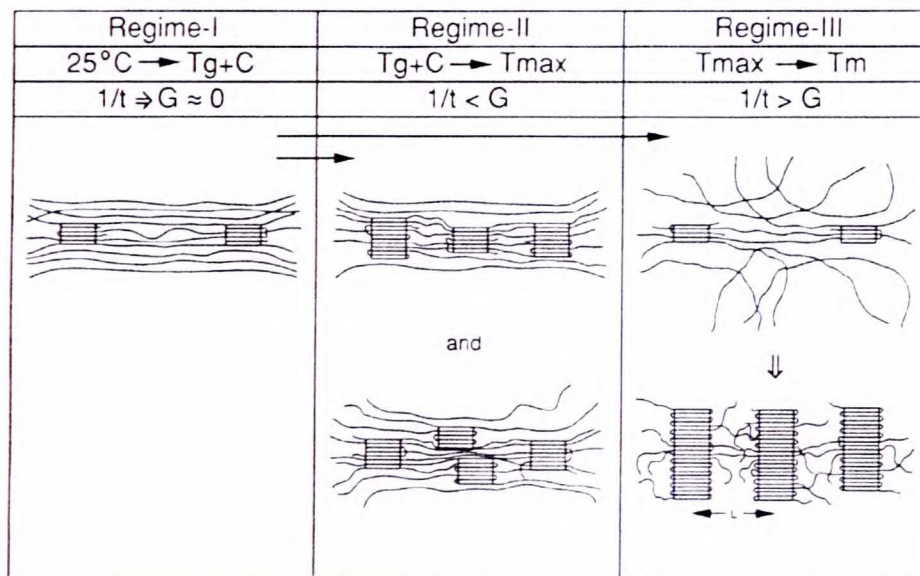


Figure 1.11 Gohil model of heat setting regimes on structure of PET (Reproduced from [29]). $1/t$ is rate of relaxation of the molecules and G is the rate of crystallisation.

Later, Greener *et al.* [60] suggest that under constrained conditions the chain folded lamellar crystal growth occurs perpendicularly to the stretching direction, nucleating from the fibrillar structures formed during stretching. The lamellar size is found to be dependent on the heat-set temperature and the end result is an interlocking paracrystalline network that enhances the dimensional stability of the film. During film manufacture, for

the heat setting of biaxially drawn film, temperatures typically up to 230°C are used on a time scale of seconds before tension is withdrawn from the film.

The effects of a heat setting stage are similar for PEN [61, 62] and can completely eliminate shrinkage of the film at subsequent temperatures at or below the heat set temperature. Hardy *et al.* report that increased crystallinity is observed and a more disordered, unoriented amorphous phase results from a heat treatment at 260°C [63].

1.6 Modifications to Polymer Films During Manufacture

For many commercial applications, additives are incorporated into the polymeric films before the drawing process to impart a particular property to the film. The main application of these filler particles is to reduce “blocking” (the adhesion of adjacent surfaces) in the roll, thus making the film much easier to handle [64]. This is achieved as the particles protrude from the film surface by a distance up to a few hundred nm and reduce the surface contact between layers. Typically, fine silica and clays are used with diameters of the order of a micron for antiblock purposes, whilst carbon black is used to make the insulating polyester film more conductive. High volume % quantities of BaSO₄ or polypropylene can be added to cause the film to become opaque, by introducing voiding in the film which causes scattering between polymer and the void [28]. Filler particles also, as a general rule, increase the dimensional stability and the stiffness of the film. Despite the fact that the filler particles protrude from the surface of the film they are covered by a thin film of PET so that the surface chemistry is in effect unchanged [65].

Coextruded films are gaining prominence recently as they are showing promise in high gas barrier applications, where they allow control of the surface characteristics of the film. Two or three discrete layer composites can be fabricated by the use of a large extruder for the core of the film and smaller ones for 1 or both of the surface layers, together with a multi manifold die. An example is the 12 μm Hostaphan film [66] which has a plain PET core, with a filled PET layer on one side to ease processability (antiblock) and a PEN layer on the reverse to act as a model surface for vacuum deposition of a barrier coating.

Chapter 2. Vacuum Deposited Coatings for Gas Barrier Applications

The aims of this chapter are three-fold. First, the theory of gas transport through solids will be briefly outlined to explain why metal and ceramic coatings are used to reduce the permeation of gas and vapour through polymer film, secondly the techniques used to deposit coatings under vacuum will be described. Finally, the bulk of the chapter will review the literature concerning gas barriers, with a focus on the mechanisms of permeation, current requirements and measurement techniques and the various issues that must be addressed to ensure maximum barrier is achieved throughout the lifecycle of the composite. The role of the substrate shall be carefully considered.

2.1 Permeation of Gases Through Solids

Ideally, from a packaging point of view, encapsulating a product with a solid material would completely protect it from gases present in the atmosphere and/or prevent loss of gas or aroma from the product. However, the phenomenon of diffusion – the movement of matter through a medium driven by the kinetic motion of atoms and molecules – makes complete separation impossible. The role of a gas barrier is to prevent directional diffusion, the flux of matter from the ambient exterior to the interior of a package or vice versa, that is caused by the concentration gradient of the permeating species and the inclination of the system to reach equilibrium. A schematic of diffusion through a section of material is shown in Figure 2.1.

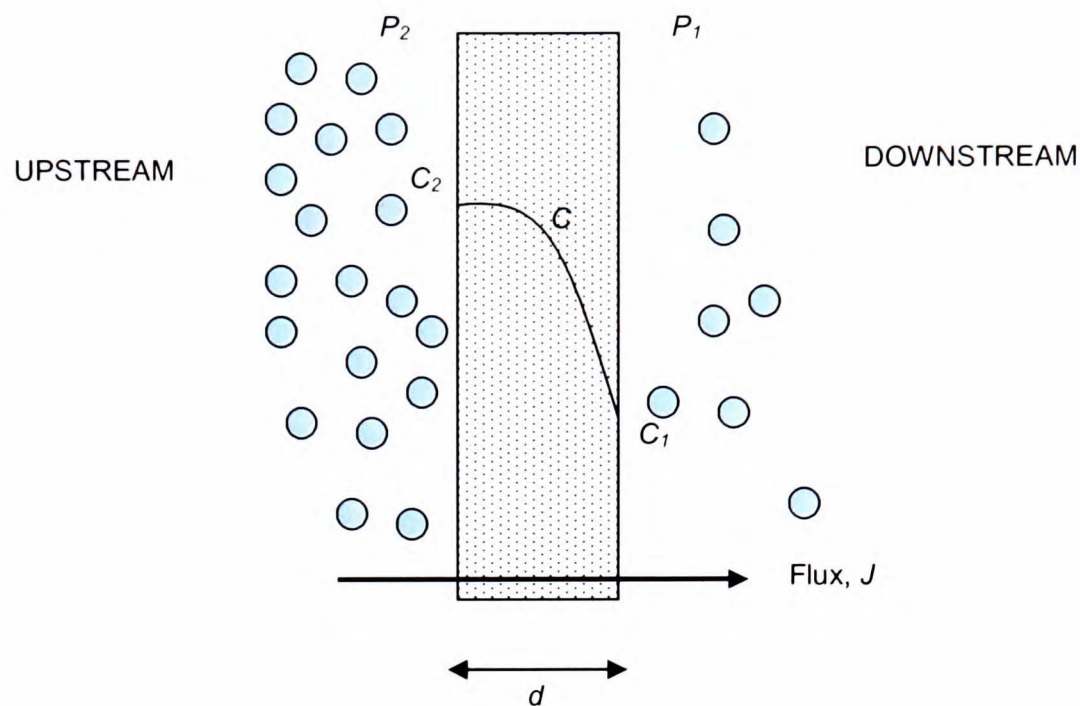


Figure 2.1 Schematic of the diffusion of a species through a solid substance.

At steady state, where the concentration is independent of time, the diffusion process can be described by Fick's 1st law, which states [67-69]:

$$J_i = D_{ij} \frac{\partial c_i}{\partial x} \quad (2.1)$$

where J_i is the permeant flux in the direction of flow as a function of the concentration gradient ($\partial c_i / \partial x$) and D_{ij} is the diffusion coefficient of the gas i in medium j . For a measure of how much gas penetrates the barrier the value of permeation is required.

Assuming steady state flow, the integration of (2.1) gives:

$$J_i = D_{ij} \frac{(c_2 - c_1)}{d} \quad (2.2)$$

where c_1 and c_2 are the permeant concentrations at the low and high concentration sides of the film respectively. By assuming Henry's Law, which describes the solubility, S , of a gas in a solid with no dissociation of the gas at the surface:

$$c_x = Sp_x \quad (2.3)$$

where c_x and p_x are the concentration and pressure respectively, and substituting into (2.2) to give:

$$J_i = \frac{D_{ij}S(p_2 - p_1)}{d} = \frac{P_m}{d} \cdot \Delta p \quad (2.4)$$

where $P_m = DS$ is the molar permeability of the film normalised to a unit thickness. It may also be given by:

$$P_m = \frac{Md}{At\Delta p} \quad (2.5)$$

where M is the amount (volume or mass) of the gas permeating, d is the film thickness, A is the exposed film area, t is time and Δp is the difference in pressure of the permeant either side of the film. The quantity P_m is often divided by the thickness to give the permeance or permeation of the gas through the film. Often in the literature, the performance of a barrier coating is quantified as a gas transmission rate, Π , given by:

$$\Pi = \frac{P_m \Delta p}{d} = \frac{M}{At} \quad (2.6)$$

and is generally reported in units of $\text{cm}^3 \text{ m}^{-2} \text{ day}^{-1}$ for O_2 and noble gases and $\text{g m}^{-2} \text{ day}^{-1}$ for water vapour. Quite often the barrier improvement factor (BIF) is reported, which is simply the ratio of the transmission rates of the uncoated (Π_s) and coated (Π_c) substrate respectively:

$$BIF = \frac{\Pi_s}{\Pi_c} \quad (2.7)$$

2.1.1 Permeation of gas and water vapour through polymers

Permeation through polymers is generally assumed to follow three stages; first, sorption of the gas into the polymer; second, diffusion of the gas through the bulk polymer; and third, desorption from the opposite face of the film. For most polymers, including PET, the process has been shown to be Fickian in nature [70] and obeys Henry's Law. After the gas has dissolved in the polymer, transport of penetrant gas molecules through semicrystalline polymer films takes place exclusively through the amorphous regions with crystallites acting as impediments and increasing the tortuosity of the diffusion path [71]. The diffusion step can be thought of as a series of jumps for the permeant from one space to the next, in the direction of the concentration gradient. The rate at which this occurs is dependent on many factors. The larger the permeant molecule, the slower the permeation rate [69] as more energy is required to create a hole in the structure for the molecule to occupy. In polymers the holes will either be created by continuous chain motion or frozen-in voids and cracks in the glassy regions. The gas molecule is thought to

be adsorbed to the walls of the space it occupies, held by van der Waals forces which must be overcome before the next “jump”. Several authors have reported reduced permeability in polymers after drawing, caused by creation of impermeable regions of *trans* conformers and a relatively tightly packed structure [72, 73]. McGonigle *et al.* [74] propose that the orientation and distribution of crystallites in the amorphous matrix controls the permeation of noble gases and O₂ through PET and PEN films.

The transport of water vapour through polymer films is potentially more complicated, due to its polar nature which can result in hydrogen bonding to the polymer matrix or to other water molecules, leading to non-ideal behaviour. For hydrophilic polymers, poly(vinyl alcohol) for example, the water uptake is considerable and can lead to plasticisation which effects the free volume present in the polymer [75]. Several authors make a case for ideal behaviour for water transport through polymers, with Orchard *et al.* [73] concluding that O₂ and H₂O permeation through PET follow the same mechanism. Yasuda and Stannett [76] report that no clustering of water molecules takes place in “hydrophobic” polymers such as PE, PP or PET and that the diffusion is Fickian, similarly Shigetomi *et al.* [77] observe Fickian sorption-rate curves in PET which may be due to the very low water vapour sorption characteristic of the polymer. An FTIR investigation of water sorption in PET by Fukuda *et al.* [78] concludes that water molecules sorbed in PET interact much less with each other, that is a lower degree of H-bonding is observed, than for water in the liquid state. The degree of H-bonding is less than one but not so small that it is in the vapour state. They also conclude that sorbed water is randomly dissolved without any strong interaction with the polymer chains.

Similar to O₂ transport Lasoki and Hobbs [79] conclude that the water permeability of semicrystalline polymers is dominated by diffusion through amorphous regions and is proportional to the square of the amorphous volume fraction, with drawing increasing the barrier to permeation.

Typical diffusivities and transmission rates for oxygen and water vapour transport through PET films are 10^{-9} and 10^{-13} cm² s⁻¹ [67] and 1-100 cm³ m⁻² day⁻¹ and 1-30 g m⁻² day⁻¹ [6] respectively, depending on the thickness, and PEN offers a four or five-fold improvement on these figures. For packaging purposes an improvement in the transmission rates by at least an order of magnitude is required for these films to be commercially useful.

2.1.2 Why should gas barrier be improved by a thin metal or ceramic coating?

Bulk metal and ceramic materials are superior gas barriers to polymers by several orders of magnitude in many cases. Taking amorphous silicon oxide glass as an example, in the bulk form it is practically impermeable to O₂ and H₂O due to the constricted interstitial spaces of the Si-O lattice. Diffusivities as low as 10^{-18} - 10^{-19} cm² s⁻¹ for water vapour permeation and 10^{-13} cm² s⁻¹ for oxygen have been reported for defect-free silicon oxide glasses [67], much lower than for a typical polymer [80]. Therefore it seems plausible that by placing a continuous layer of glass or metal onto a polymer film an extremely good flexible barrier will result.

This is further demonstrated by considering the energetics of the permeation process. The permeation of gases through a film or membrane is temperature dependent and in glasses

and polymers (below the T_g) can be described using the well known Arrhenius relation [80]:

$$\Pi = \Pi_o \exp\left(\frac{-E_A}{RT}\right) \quad (2.8)$$

where E_A is the apparent activation energy of permeation (kJ mol^{-1}), R is the gas constant ($\text{J mol}^{-1} \text{K}^{-1}$) and T is the absolute temperature (K). Π_o is a constant specific to the gas and barrier material studied. The value of E_A can give useful information about the mechanism of permeation through a bilayer film, if the ideal laminate theory (ILT) is applied to the system [80, 81]. ILT states that for a bilaminate structure the permeability of the composite to a gas can be given by:

$$\frac{1}{\Pi_T} = \frac{d_T}{P_T} = \frac{d_s}{P_s} + \frac{d_c}{P_c} \quad (2.9)$$

where Π is the transmission rate through the structure, P is the permeability, d is thickness and the subscripts T , S and C represent the total composite, the substrate and the coating respectively. It predicts that barrier improves with increasing thickness of the coating (which is true, but only for a narrow range of thickness). By substituting in the Arrhenius activated equation we can express the transmission rate through the composite as:

$$\Pi_T = \left(\frac{1}{\Pi_s} \cdot \exp\left(\frac{E_{A(s)}}{RT}\right) + \frac{1}{\Pi_c} \cdot \exp\left(\frac{E_{A(c)}}{RT}\right) \right)^{-1} \quad (2.10)$$

where each component is continuous and free of defects. The importance of a barrier coating such as SiO_x becomes obvious when the E_A values of the bulk constituents are considered. For polymers, E_A with values up to 60 kJ mol^{-1} are typical for water and oxygen permeation ($10\text{-}60^\circ\text{C}$), while for bulk amorphous silicon oxide glass the values are about 84 kJ mol^{-1} for water [82] and $84\text{-}300 \text{ kJ mol}^{-1}$ for oxygen permeation [83]. The higher values for the SiO_x show that much more energy is required to activate the permeant and to distort the barrier matrix so that it may move to the next vacancy, therefore it is a much more effective barrier. A significantly improved barrier should then be achieved by depositing glass onto a polymer and ideally the composite will combine the flexibility of a polymer film with the low permeability of the glass, so that in effect we have “flexible glass” [7].

Unfortunately, things aren't quite that simple, and after a description of the deposition techniques commonly used to deposit barrier coatings we shall see why our coated films aren't quite as good as we would expect.

2.2 Methods of Coating Deposition

Vacuum-deposition techniques can fall under two general categories – chemical vapour deposition (CVD) and physical vapour deposition (PVD). The latter is typically used on the industrial manufacturing scale, particularly for metallised polymer film and paper.

2.2.1 Chemical Vapour Deposition

CVD [84] processes involve the activation of reactant species in the vicinity of a substrate, where they condense and react to form a thin film. This is often done thermally, although the temperatures required are too high if polymer films are the substrates. In many cases the reactants are excited by an electric field into a plasma before reacting at the surface, resulting in lower temperature deposition and increased ion bombardment of the film that can be altered to tailor the thin film properties. This process is known as Plasma Enhanced Chemical Vapour Deposition (PECVD) and is used to deposit gas barrier coatings such as silicon oxide and nitride. It is also widely used in the semiconductor industry.

2.2.1.1 Plasma Enhanced Chemical Vapour Deposition

PECVD [84, 85] is typically performed under vacuum, with base pressures of $\sim 10^{-5}$ Torr and operating pressure of 10-1000 mTorr depending on the process. When the plasma initiates, energy from the (usually r.f.) electric field is coupled into the reactant gases via the kinetic energy of a few free electrons. These electrons gain energy rapidly through the electric field and lose energy slowly through elastic collisions. The high-energy electrons

are capable of inelastic collisions that cause the reactant gas molecules to dissociate and ionize, producing secondary electrons by various electron-impact reactions. In a steady-state discharge, the electrons generated by electron-impact reactions equal those electrons that are lost to the electrode, walls, and reactive species by attachment and recombination reactions. Next, transport of the reactive species, created by gas molecules collided with electrons, occurs from the plasma to the substrate surface concurrently with the occurrence of many elastic and inelastic collisions in both the plasma and sheath regions, with the generation of more radicals and ions. At the substrate surface adsorption and/or reaction of reactive species (radical adsorption and ion incorporation) occurs and the coating nucleates. Finally, the reactive species and/or reaction products incorporate into the growing film or re-emit from the surface back to the gas phase. A schematic of a typical PECVD reactor, and the processes occurring during deposition is shown in Figure 2.2.

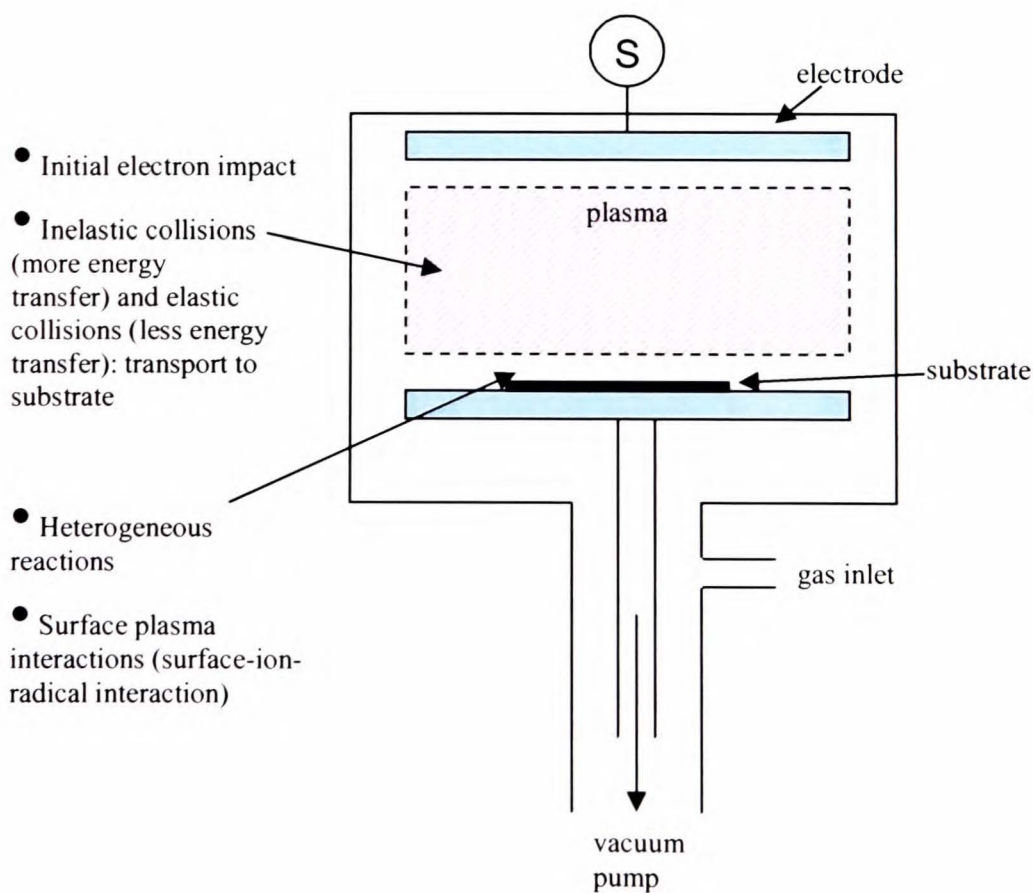


Figure 2.2 Schematic of a typical parallel plate PECVD reactor.

To deposit silicon oxide coatings by this method silane (SiH_4) and nitrous oxide (N_2O) are traditionally used in the semiconductor industry, although silane is difficult to handle and high operating temperatures are preferred which are unsuitable for polymer substrates. Carbon-containing precursors, such as hexamethyldisiloxane (HMDSO) or tetramethoxysilane (TMOS) with oxygen gas, are often used instead [86-88]. Films deposited from such gases usually contain residual carbon, caused by incomplete dissociation of the silicon precursor and the incorporation of hydrocarbon radicals from the plasma. This can impart colour to the film, a characteristic that may be undesirable. Such impurities can be eliminated from the film if appropriate care is taken, either by depositing when the substrate temperature is greater than that of the chamber walls or by increasing the oxygen flow rate so that the oxidation rate is sufficiently fast and little carbon is incorporated [89, 90]. On occasions it is preferable for the silica to contain an amount of carbon as it often makes the coating less prone to brittle failure [91].

Despite the impressive properties that PECVD films often possess, the deposition technique is not widely used in large area substrate markets such as packaging barrier film. Generally PECVD deposition rates cannot match those of evaporation metallising, the equipment is more complex and expensive and coating uniformity has been difficult to achieve for large area substrates. Handling the precursor gases and dealing with the by-products of the process are other difficulties associated with PECVD. In recent times, efforts have been made to improve PECVD deposition of SiO_x on roll-to-roll (R2R) machines that enable a high output of coated material [87, 92].

2.2.2 Physical Vapour Deposition

The two most common methods of PVD are sputtering and evaporation. These techniques are briefly described as follows:

2.2.2.1 Sputtering

The sputtering process involves the physical vaporisation of atoms from a surface by momentum transfer from bombarding energetic atomic-sized particles [93, 94]. Typically, the bombarding species are atoms of a noble gas, usually argon, that are accelerated in an electric field. The material being sputtered (either a metal or a compound) is known as the sputtering target and is held at a negative potential so that it acts as a cathode and attracts positive ions from the plasma. To increase the sputtering rate and make the process more efficient a magnetic field is applied to the target so that secondary electrons ejected from the target during sputtering are confined to the target surface and continually circle it [95, 96]. The high flux of electrons then creates a high density plasma from which cations are accelerated to bombard the target material. The erosion of the target after continuous sputtering is then characterised by a closed circle and is known as a “racetrack”. The technique is known as magnetron sputtering and a schematic of the planar magnetron arrangement is shown in Figure 2.3.

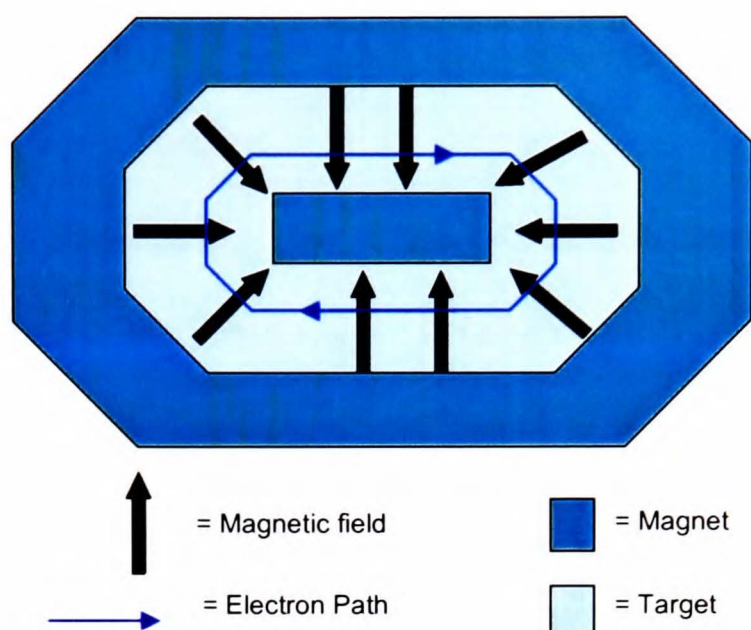


Figure 2.3 Magnetron sputtering with race-track electron path.

For transparent barrier coatings in packaging, a metal oxide/nitride such as AlO_x or SiO_x/SiN , is usually used. To produce such ceramic coatings, two methods can be employed. The first is to sputter the desired ceramic compound such as AlO_x directly from a target. This approach is not ideal however, as heat dissipation is relatively low in such a target and the build-up of heat from the sputtering process can lead to damage to the target. The rate of sputtering for a ceramic target is also much slower than from a metallic one, due to the covalent bonding inherent in its structure [97, 98]. The preferred method to deposit ceramic coatings is by reactive sputtering [93, 98], where a reactive gas (oxygen if a metal-oxide is required) is admitted to the sputtering chamber and chemically reacts with the sputtered material at the substrate surface. By altering the reactive gas partial pressure, the stoichiometry of the oxide can be altered. Argon is still used to sputter the target as the reactive gas atoms are too light and have insufficient momentum. The reactive process is difficult to control as the gas also reacts with the target surface resulting in poisoning – if this becomes severe then an abrupt increase in the chamber pressure is observed as less metal is sputtered and fewer reactions with the

reactive gas take place, accompanied by a reduced sputtering rate and a gas-rich coating. A number of methods have been used to combat this phenomenon, the most popular being feedback loops developed in the 1980s where the flow of gas is regulated depending on the voltage at the target (target voltage control) or the relative amount of metal species present in the plasma (plasma emission monitoring). Details of these techniques are beyond the scope of this summary and the reader is directed to the review of Safi [98] for further information, together with the work of Thornton [99-101] on sputtered coating structure and Jacquet and various coworkers for studies of AlO_x and TiO_x layers on PET [102-107].

2.2.2.2 Evaporation

Deposition by evaporation [94] of a metallic material is achieved by heating it in some way, most often by electric current or by an electron beam gun which offers greater evaporation rates [108]. By heating the target material, the constituent atoms gain more kinetic energy and as the temperature increases a greater number can overcome the separation energy and evaporate. The species evaporated are usually atoms, molecules and clusters of various character. Similar to the sputtering process, a reactive gas can be admitted so that compound layers may be deposited although a high gas pressure is a requirement to achieve the required stoichiometry, which then has negative effects on the density and crystallinity of the deposited film. Typically, evaporation is used to metallise polymer film and paper with thin layers of aluminium and is favoured due to its relative simplicity and high deposition rates.

2.2.3 Nucleation and growth of the vacuum deposited coating

For both CVD and PVD methods there are three basic models for thin film growth [84, 108], as pictured in Figure 2.5:

- 1) 3-dimensional island growth (Volmer-Weber): Small clusters nucleate on the substrate surface. Further growth takes place as the film atoms are more strongly bound to each other than the substrate. Eventually, the islands coalesce to form a continuous film
- 2) Layer by layer (Franck-van der Merwe) growth – the atoms are more strongly bonded to the substrate surface than each other and form a continuous layer structure
- 3) Stranski-Krastanov (SK) growth: A combination of 1) and 2) - after a few monolayers are deposited, layer by layer growth becomes unfavourable and islands form on top of the initial layers. The reasons for this are poorly understood.

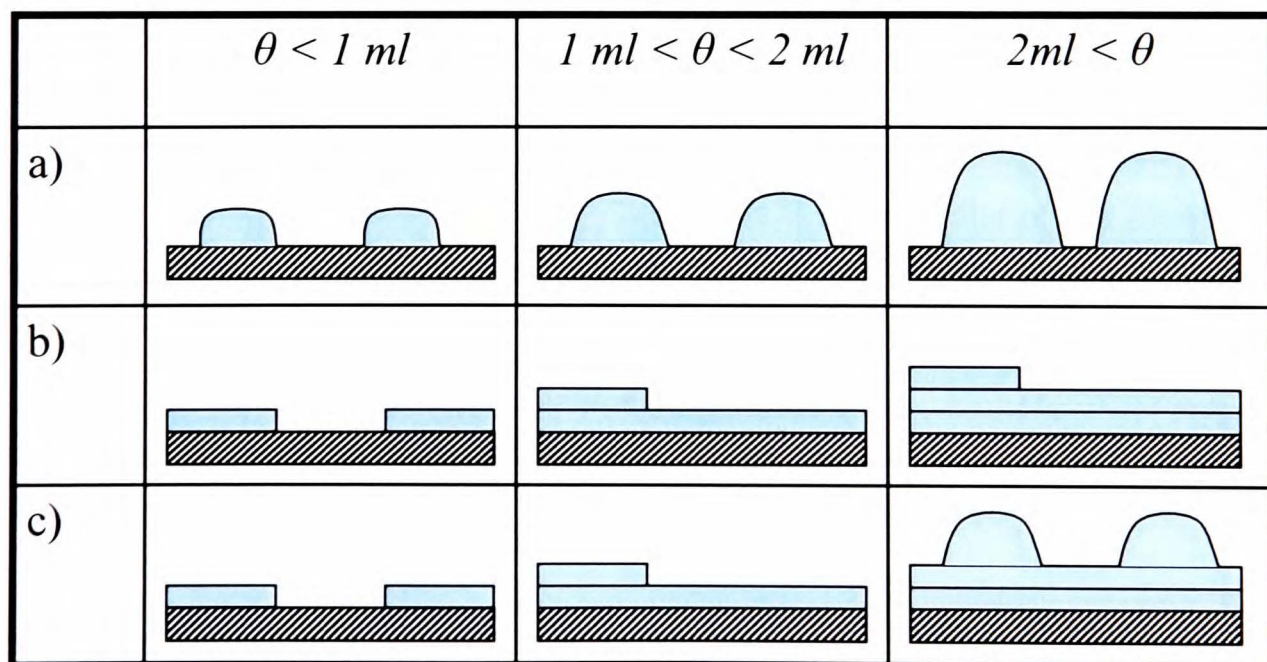


Figure 2.5 Growth modes for coatings, θ is the coverage and ml is the number of monolayers. a) 3D island growth, b) layer by layer, Franck-van der Merwe growth, c) Stranski-Krastanov growth.

The growth mechanism depends on both process and substrate factors. Most commonly, for metal and ceramic coatings on polymer film, island growth is observed, although the nucleation density and island size can be altered by modifying the substrate or the deposition parameters. An example of the substrate effect is shown by Deng *et al.* [109], who investigate the deposition of AlO_x on PET and PP. They find that for 1 nm thick films island nucleation is apparent on both substrates and incomplete coverage results, with a gas permeation no less than the bare substrate. 10 nm thick films show reduced water and oxygen permeation on both substrates but the effect is much more marked for the PET composite. Furthermore, AFM imaging shows that the coating on PP is much rougher than the bare substrate, whereas on PET there is little difference. The observed effects are explained by the presence of carbonyl groups in PET that create more nucleation sites so that coalescence occurs at a lower thickness. Henry *et al.* [110] report much finer spacing between sputtered AlO_x nucleation sites than for Al in the early stages of growth, speculating that the oxygen present in the plasma for AlO_x deposition may functionalise the surface in some way, creating more nucleation sites. In the case of PECVD coatings it appears that the growth mechanism follows that of the Franck-van der Meuve case. Dennler *et al.* [111] demonstrate that SiO_2 layers on PET, PP and PI (polyimide) grow by the layer-by-layer mechanism, and that complete coverage of the substrate (albeit with a copious number of pinhole defects) occurs at thicknesses as low as 2 nm, using XPS, Rutherford backscattering and SEM/reactive ion etching defect analysis. Their work is in agreement with other (cited) authors for PECVD SiO_x and they subsequently reach similar conclusions with Si_3N_4 films on Kapton PI film although, in

contrast, Felts [112] explains the poor barrier of ultrathin PECVD films using the island growth argument.

2.2.4 How thick does a barrier coating need to be?

By plotting oxygen or water transmission rates against the thickness of a barrier coating, many authors have observed a “U” shaped curve. For a typical effective barrier the transmission rate decreases gradually for very small thicknesses due to nucleation and then rapidly by about 2 orders of magnitude at about ~15-70 nm, depending on the process and material used, to a minimum value [113]. The thickness at which this occurs is known as the critical thickness, T_c , which is often a lower value for PECVD and sputtered coatings than for evaporated layers of the same material (for example SiO_x) [113]. It is thought that the critical thickness indicates complete coverage of the substrate by the coating and as such is dependent on the growth mode, nucleation density and the roughness of the substrate. It is usually between 15 and 100 nm but occasionally, a much greater value of T_c for SiO_x coatings is reported, such as that by Klemberg *et al.* [114] who found that at a thickness of 500 nm the T_c is still not reached for PECVD coatings where HMDSO is the precursor. Similarly, again with HMDSO and O_2 as the precursor gases, Bieder *et al.* [115] find that the T_c for WVTR is about 700 nm and for OTR no limiting barrier is reached up to 2000 nm thickness. Whatever the value of T_c , a golden rule for barrier materials is that the deposited film must be thicker than it for it to be fully effective.

As the thickness continually increases a point is reached where the transmission rate begins to increase again quite rapidly and a degradation of the barrier is observed. The reason for this is thought to be the build up of compressive stress in the deposited layer that at a certain thickness results in cracking of the coating and a corresponding increase in permeation [112, 116]. The thickness at which this occurs is dependent on the materials and deposition process used. For large area commercial applications such as packaging, the coating thickness must be a minimum so that barrier is achieved (T_c) and the cost of fabrication is minimised, through reduced use of materials and increased throughput. Figure 2.6 shows a schematic of the thickness effect for gas barrier films accompanied by experimental data from [117].

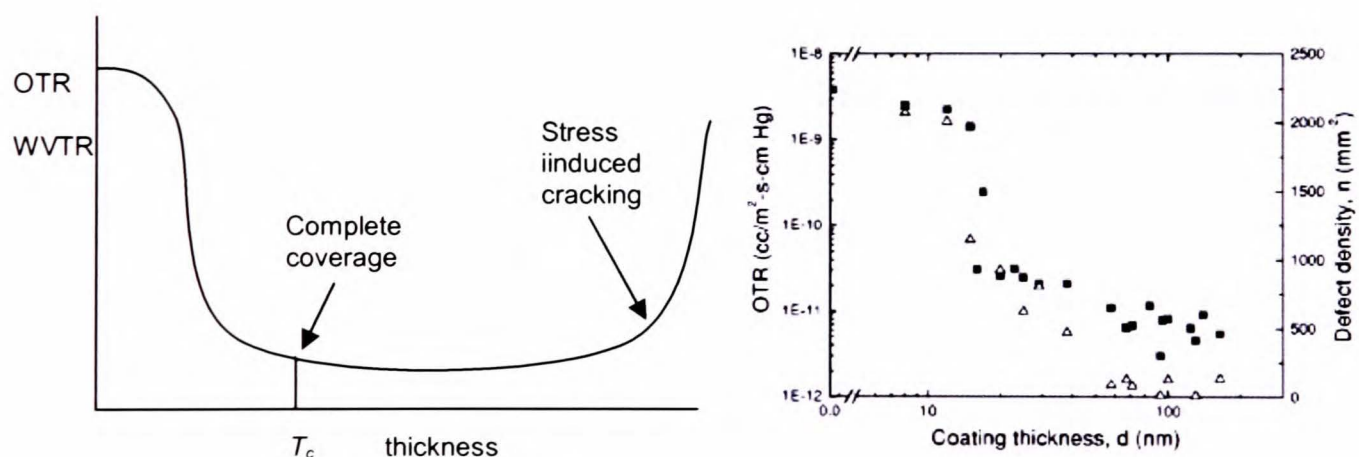


Figure 2.6 Effect of thickness on barrier performance for a vacuum deposited coating and experimental data from [117] showing a T_c of 15-20 nm for SiO_x on PET (■ = OTR, Δ = defects).

For almost all single-layer barrier coatings the improvement in barrier is less than three orders of magnitude, which is much less than would be expected for the bulk ceramic and metal materials. The reason for this is the presence of defects in the coating, that are responsible for permeation through the coatings and which are described next, with an

emphasis on O₂ and H₂O vapour, as these are the most relevant and most commonly studied gases in the literature.

2.3 Why Does Gas Still Travel Through Coated Films?

2.3.1 Defect controlled oxygen permeation

Oxygen transport through vacuum deposited coatings primarily takes place through pinhole defects. These are roughly cylindrical pores in the coating that extend through the structure providing a direct path from the atmosphere to the polymer, with a radius of 0.5-50 μm . The first work to characterise the permeation through defect-containing films was done by Prins and Hermans [118] in 1959 on metallised polymer, who constructed a model which predicted that the flux of gas through the coated film increased linearly with the diffusion coefficient of the substrate polymer, the concentration gradient across the coated polymer and the area fraction exposed by the pinholes. The flux was also expected to be independent of the coating thickness, a fact confirmed by Jamieson and Windle [119] in their study of Al-metallised PET. They also report a linear correlation between the O₂ permeability and the pinhole density and similar size distributions for both pinholes and dust particles on the PET film prior to deposition, with dust particles being held responsible for the formation of the pinholes. “Scuffing” of these particles was found to lead to lines of pinholes during handling of the metallised films. Even though the surface area fraction of defects is small, lateral diffusion causes the total permeation rate through many small pinholes to be much higher than if the same pinhole area was composed of fewer, larger defects according to the models of Rossi and Nulman [120]

and Hanika *et al.* [121]. As such the concentration gradient across the film is greatest where the polymer film is exposed by pinholes and improving the barrier performance of the polymer in these regions should increase the overall performance of the composite.

da Silva Sobrinho and various co-workers [117, 122] find that OTR is proportional to pinhole density for SiO_x on PET films, similar to the findings made for Al films by Jamieson and Windle [119] and detail a new method for measuring defect densities for thin transparent films, a task that is traditionally difficult to perform. The basis of the technique is reactive ion etching of the coated film, which has little effect on the SiO_x layer but which etches away the underlying polymer (“undercutting”). The cavity of polymer formed not only deepens with exposure time but also spreads laterally under the silica film so that eventually the defects are visible by optical microscopy. By measuring the radius of the holes as a function of etching time the original defect size can be extrapolated. For PECVD SiO_x films a Gaussian size distribution of pinholes is observed with a mean radius of $0.6 \mu\text{m}$.

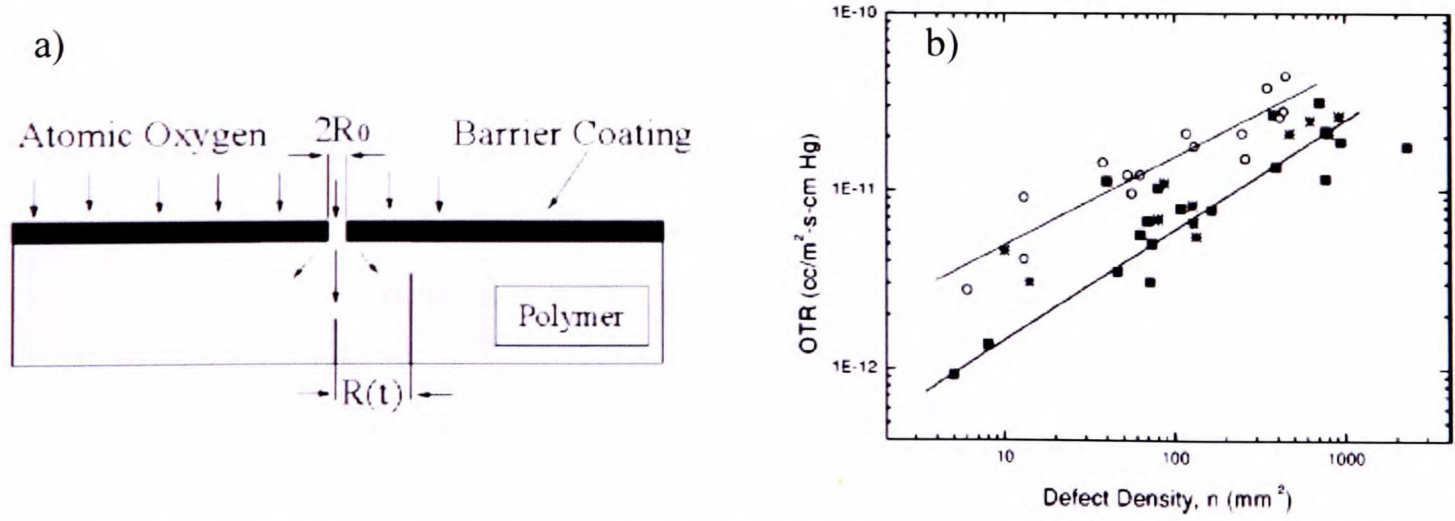


Figure 2.7 (a) RIE undercutting of the polymer to image defects [122]; (b) Correlation of OTR with pinhole density [117]: (■) SiN/PET, (*) SiO₂/PET, (○) Al/PET from reference [119].

Further evidence for the defect controlled O₂ permeation through coated PET films is obtained in the analysis of the activation energy of permeation. Several authors find that although a SiO_x [80, 117, 123] or Al/AlO_x [110] coating improves the barrier performance, the activation energy of permeation is the same for both coated and uncoated films indicating that the rate determining step in the permeation mechanism is the same in both cases – diffusion through the polymer.

In coatings with very few pinhole defects, the permeation of gas is still not as low as expected and must be transported through the coating by different pathways [124]. These are thought to exist in the morphology of the coating, as it has been shown that growth of deposited films is often columnar and there is a wealth of evidence based on AFM imaging that nanometre sized pores exist between the “grains” that make up the coating [123, 125-127]. Several authors have made a link between O₂ permeation rate and the surface roughness, with a rougher coating being more permeable, possibly due to larger intergranular pores. Using transmission electron microscopy, Erlat *et al.* [123] have shown SiO_x films to have intergranular defects of the order 4-6 nm in diameter, covering as much as 30% of the surface area, although they fabricated superior films with no defects larger than 1 nm observed. In ultrathin SiO_x films (2-10 nm) Dennler *et al.* [111] characterise a number of defects, which they believe are less than 50 nm in diameter with a coverage of <1%, using the etching method described earlier, and to which they attribute the negligible barrier performance. Once again, activation energy analysis shows that the O₂ permeation is limited by the polymer and not the coating for these cases. Tropsha and Harvey [80] propose a simple model for O₂ diffusion through SiO_x coated

films (Figure 2.8) and interestingly find that after coating both sides of the film, the transmission rate decreases and the activation energy increases by 54 kJ mol^{-1} , indicative of a permeation process controlled by diffusion through the coating, probably because the defects in the two silica layers are decoupled.

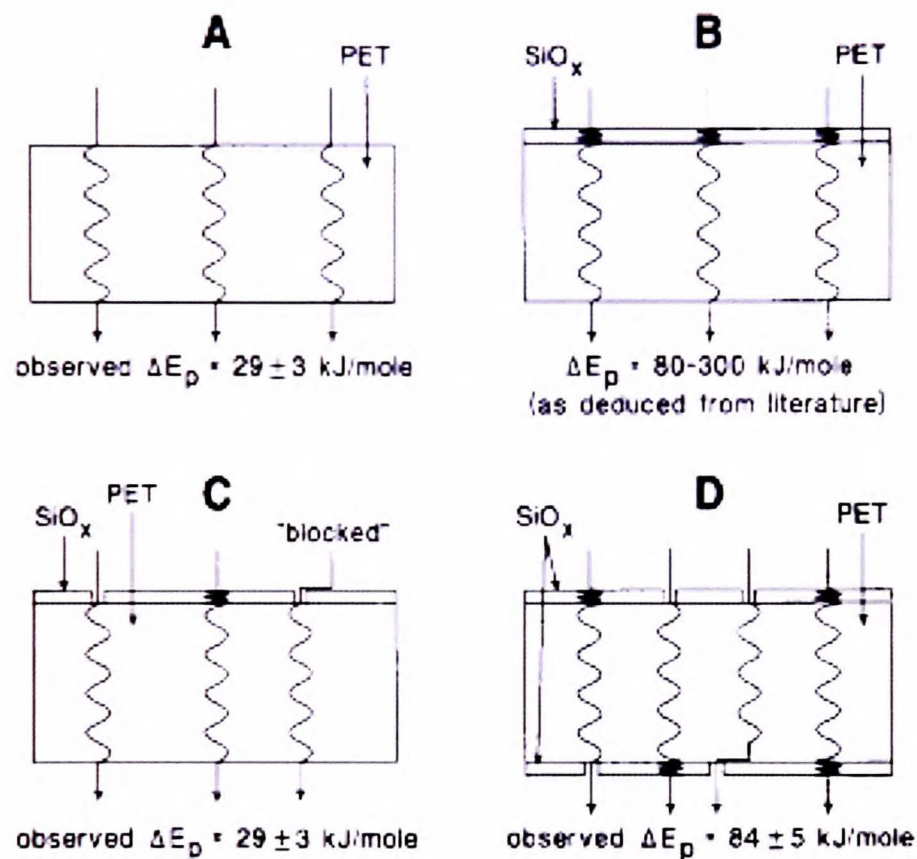


Figure 2.8 Empirical model of oxygen transport through (a) uncoated PET, (b) PET film coated on one side with a hypothetically defect-free, continuous layer of “glass”, (c) PET film coated on one side with an imperfect, noncontinuous layer of SiO_x , and (d) PET film coated on two sides with imperfect, noncontinuous layers of SiO_x [80].

2.3.2 Defect controlled water vapour permeation

For water vapour transport through barrier films, less literature is devoted to the mechanism of permeation, probably due to the added complexity of the interactions between the vapour and the coating. Garcia-Ayuso *et al.* [125] were among the first to show that water vapour permeation may be independent of pinhole density, and

concluded that on a 0.5 μm scale a smoother coating presented a better barrier than a rough one. This was seen to indicate that the growth mode of the silicon oxide films examined could affect the permeation mechanism and that the pathways were relatively small in diameter. Subsequently, the same authors [128] examined whether surface diffusivity is an important factor but failed to give a conclusive answer based on AFM and fractal analysis.

Using a small group of substrates (PET, PP, polycarbonate and polystyrene) Tropsha and Harvey [80] found that the activation energy of permeation for water vapour through 100 nm SiO_x coatings is 54 kJ mol^{-1} , irrespective of the substrate, concluding that the water interacts with the coating, possibly chemically. Subsequently, it was reported by the same group that for SiO_x coatings with compact microstructure and few large-scale defects, the increase in E_A by 20 kJ mol^{-1} was due to both physically constrained H_2O molecules and chemically interacting H_2O molecules (via H-bonding) in defects measuring on the same scale as the water molecules [123]. Transport through the oxide is the rate limiting step.

Interaction of water vapour with a coating has been proposed for other inorganic layers, such as Al, AlO_x and AlO_xN_y [110, 126, 127, 129], with transport through nanoscale tortuous pathways leading to an increased E_A of permeation over the bare substrate. In 2004 Erlat *et al.* [127] investigated the water permeation through AlO_xN_y layers, identifying that water vapour permeates predominantly (~80% of the flux) through the tortuous nanoscale pathways in the coating structure and chemically interacts with the pore walls (N-rich sites in this case). Using SIMS and isotopic labelling, they postulated

that after adsorption and dissociation into OH and H adsorbed species, oxygen atoms are trapped and H₂ permeates essentially unhindered before reacting with oxygen (present at 100% RH and also diffusing) so that the water is reformed at the other side of the film. The mechanism and reactions are shown below and it must be mentioned that the proposed mechanism of chemical reaction was provided as a possibility, rather than a statement of fact.

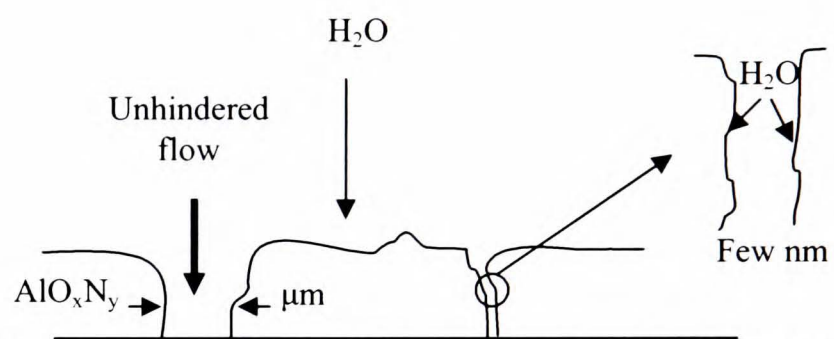
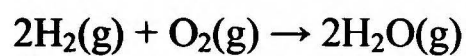
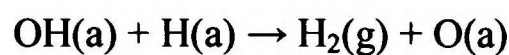


Fig 2.9 Mechanism of H₂O permeation in AlO_xN_y coatings [127].

A subsequent paper by Koo *et al.* [130], investigates evaporated SiO_x and SnO_x on polycarbonate films. A much denser coating is achieved by ion bombardment during the evaporation process and the SnO_x is found to provide a more effective barrier than SiO_x, with a much larger E_A of permeation for water vapour. This is explained by the greater polarity of the tin oxide and the increased chemical interaction this material has with water, leading to a more complete coverage of the pore walls with adsorbed OH groups. They propose that the OH groups then interact strongly with permeating water molecules and a higher activation energy is required for the H₂O to dissociate and travel through the coating. This is quite a different mechanism to that of Erlat *et al.* [127] and there is some doubt in the literature as to the exact nature of the chemical behaviour of water as it permeates through the nanoscale pores. As a useful generalisation, the pores in the

coatings may be thought to act like chromatography columns, with a more polar material causing the water molecules to travel through the coating more slowly.

2.4 Current Barrier Technologies

As has been shown countless times, a single layer coating improves the barrier of a polymer film by up to three orders of magnitude. A selective summary of barriers on PET and other relevant films reported in the literature, including critical thickness, OTR and WVTR (and barrier improvement factor, BIF) of the coating at T_c and the deposition process, is given in Table 2.1.

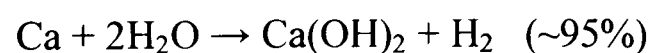
Table 2.1 Summary of flexible gas barrier technologies.

Material	Process	T_c (nm)	OTR $\text{cm}^3 \text{m}^{-2} \text{day}^{-1}$ (BIF)	WVTR $\text{g m}^{-2} \text{day}^{-1}$ (BIF)	Source
SiO _x /PEN	PECVD	≥1000	-	<0.01 (>100)	[91]
SiO _x /PET	PECVD	700	-	0.13 (>150)	[115]
SiO _x /PET	PECVD	-	0.44 (182)	-	[123]
SiO _x /PET	PECVD	15-20	0.05 (~200)	-	[117]
SiO _x /PET	PECVD	40	0.1 (~100)	-	[113]
SiO _x /PES/SiO _x	PECVD	100	-	0.1 (~500)	[131]
Al/PET	Evaporation	40	0.5 (~300)	0.3 (~120)	[132]
Al/PET	Evaporation	50	0.02 (>200)	0.05 (~900)	[133]
Al/PET	Evaporation	<15	0.1 (~100)		[119]
AlO _x /PET	sputtering	17	1.45 (100)	0.44 (100)	[126]
AlO _x N _y /PET	sputtering	60	1 (~80)	0.1 (40)	[127]
SnO ₂ /PC	Ion beam assisted evaporation	80	-	<0.01 (>300)	[130]
ITO/PET	sputtering	37	0.78 (~200)	0.1 (~440)	[126]

The current driving force in the development of gas barrier coatings is to achieve flexible material that can encapsulate OLED displays and protect the organic and cathode

materials from water vapour and oxygen. The widely quoted estimated barrier requirements are an OTR of $10^{-5} \text{ cm}^3 \text{ m}^{-2} \text{ day}^{-1}$ and a WVTR of $10^{-6} \text{ g m}^{-2} \text{ day}^{-1}$ for an OLED lifetime of $>10\,000 \text{ h}$ and a recent review of OLEDs and the barrier requirements is given by Lewis and Weaver [134].

To measure the low permeation rates required for OLEDs, new methodology has been recently developed because commercially available instruments, such as the industry standard (ASTM 1249) Permatran from Mocon, Inc [135, 136] (see Chapter 3.5) can only measure to $5 \times 10^{-3} \text{ g m}^{-2} \text{ day}^{-1}$. In the so-called calcium test [137] the degradation of a layer of calcium is monitored and as water vapour permeation takes place it becomes more transparent and less conductive, as it reacts to form the hydroxide. The permeation rate can then be calculated from the optical density [138] or electrical resistance [139] of the Ca film. This technique can differentiate between defect controlled and bulk permeation by the patterns of degradation on the Ca film [134], although about 5% of the degradation is thought to be due to O_2 permeation. The chemical reactions taking place are shown below [138]:



2.4.1 Multilayer coatings

The current favourites to achieve suitable barrier for OLEDs are multilayer coatings. These materials consist of alternating layers of deposited polymer and metal oxide that

form a stack of material. The polymer is usually evaporated from solution and cured on the polymer surface by UV radiation or electrons and is an acrylate species, first reported by Shaw in the early 1990's [140, 141]. Affinito [142, 143] was one of the first to report that even though the deposited polymer layer (often called PML – polymer multilayer) adds little barrier improvement to the substrate, once AlO_x was sputtered onto it an order of magnitude improvement in O_2 transmission rate over an equivalent single layer of AlO_x was observed. Furthermore, deposition of a second polyacrylate layer on the PML/oxide bilayer yielded another order of magnitude improvement in barrier performance. It turns out that the acrylate layers achieve the following [7, 142]:

- 1) The interlayer levels out the surface (planarisation) so that debris is covered by liquid oligomer that is then cured. The smooth surface is beneficial for dense coating growth with few defects.
- 2) The top coat acts to protect the oxide from damage in the various rolling processes and other handling damage.
- 3) By building a stack of alternating polymer and oxide layers, defects in the oxide layers are “decoupled” and do not cross the thickness of the stack. There are no direct paths from surface to polymer film resulting in a very high barrier.

An example multilayer is reported by Weaver *et al.* [144] on PET with 5 alternating polyacrylate/ Al_2O_3 layers. Acrylic monomer is flash evaporated onto the substrate to form an extremely smooth layer and then a 10-30 nm thick Al_2O_3 coating is sputtered on

top. The process is repeated 5 times and a WVTR of $2 \times 10^{-6} \text{ g m}^{-2} \text{ day}^{-1}$ is reported for the resultant composite, which is pictured in Figure 2.10(a).

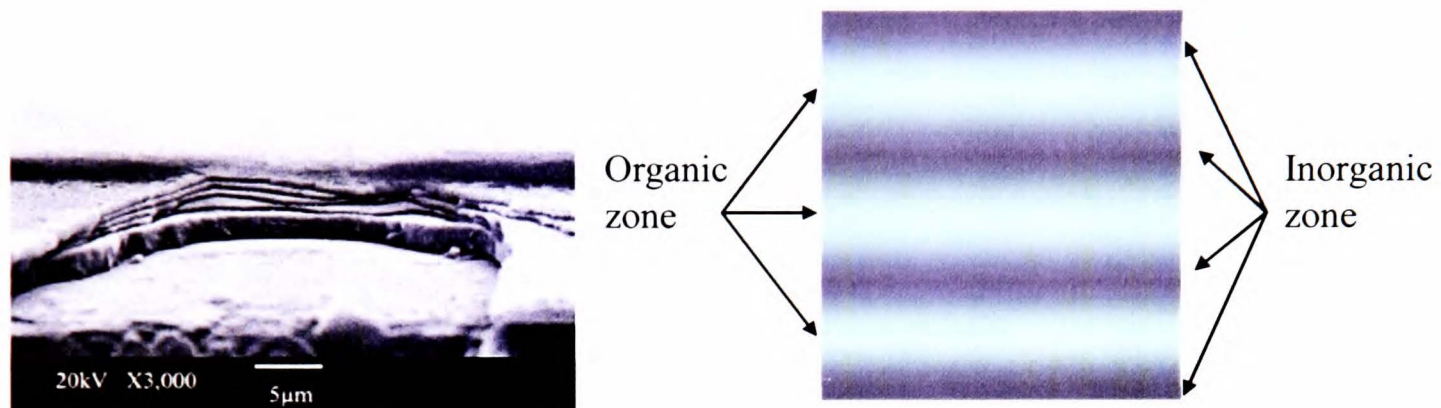


Fig 2.10 Left - SEM cross section of a PML/Al₂O₃ multilayer stack from Weaver *et al.* [144]; Right - schematic of the graduated single layer coating of Kim *et al.* [138].

A recently reported development in single layer coatings by workers at General Electric [138, 145] has seen WVTR's of less than $1 \times 10^{-5} \text{ g m}^{-2} \text{ day}^{-1}$ on polycarbonate substrates achieved for PECVD Si based coatings, although their film could also be described as a multilayer. It works on a similar principle to multilayer stacks with a graded single hybrid layer made up of inorganic (SiO_xN_y) and organic materials (SiC_xH_y) achieved by varying the gas composition of the PECVD process (Figure 2.10(b)). The organic regions decouple the defects in the inorganic regions and a smooth transition between the two phases is achieved by careful control of the processing. The layer is found to have improved mechanical properties to those of multilayer stacks.

An important point to make about permeation measurements generally, and for multilayers in particular, is the need to allow time for the system to equilibrate and reach steady state before measurement (lag time, shown in Figure 2.11). Graff *et al.* [146] believe that the low rates of H₂O permeation through ultrahigh barriers reported in the

literature are due to long lag times, rather than equilibrium diffusion effects and that the permeation rates are underestimated, which may have serious consequences for device lifetimes.

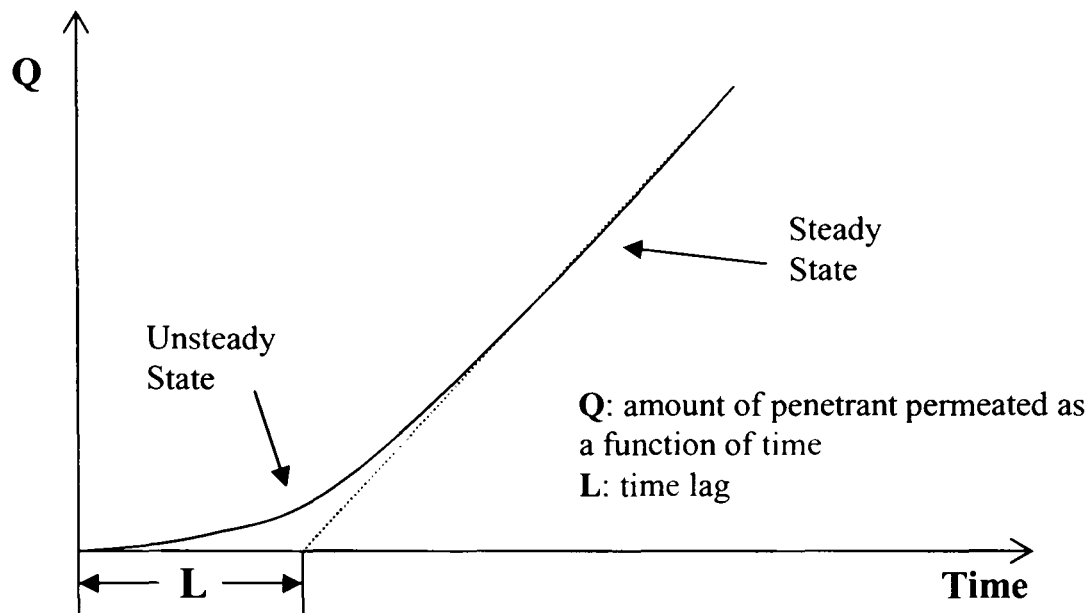


Figure 2.11 Typical permeation against time curve showing the time lag phenomenon and equilibrium.

2.5 Mechanical Properties and Adhesion

2.5.1 Internal stresses

In composite structures where dissimilar materials with different thermo-mechanical properties are processed together, internal stresses will often be present. Such stresses must be controlled in the case of metal or oxide films on polymer substrates as aspects of the coating performance, such as adhesion [8, 147], can be strongly affected by them. Tensile stresses greater than the cohesive strength of the coating lead to cracking and excessive levels of compressive strength result in buckling and debonding. If internal stress, often known as residual stress, is present in the coating then curling of the

composite film will be observed, with a radius of curvature R . Stresses are compressive in the coating if they are on the convex of the curl and are denoted as being negative. This is usually the case for deposited oxide films and any change in the internal stress state will manifest itself as a change in the radius of curvature. The stress is given by the Stoney formula [148]:

$$\sigma_i = -\frac{E_s h_s^2}{6R h_c} \quad (2.11)$$

where E_s is the Young's modulus of the substrate and h_c and h_s are the thickness of the coating and substrate respectively. This expression is for uniaxial in-plane stress and Poisson's ratio effects are neglected. Often, the biaxial in-plane stress is calculated which requires an extra factor of $(1-\nu_s)$ in the denominator, where ν_s is substrate Poisson's ratio. The Stoney formula is generally acceptable if the coating-to-substrate thickness ratio is less than 10^{-3} (e.g. a 100 nm thick coating on 100 μm thick PET) and according to Klein [149] a ratio of 0.1 is acceptable, particularly if correction factors are included. Reviews of various modifications to the Stoney formula to accommodate for factors such as thickness can be found in [8].

Internal stresses in vacuum deposited coatings are caused by two main factors during deposition – (i) the intrinsic stress, σ_f , associated with the growth process of the film and (ii) the thermal stress, σ_{th} , due to the difference of thermal expansion coefficients of the substrate and deposited material. Additional internal stress, σ_e , can result after the deposition process from the elastic recovery of the substrate upon unloading after coating

deposition, subsequent thermal and mechanical processing and ageing [150, 151]. The total internal stress, σ_i , is therefore given by:

$$\sigma_i = \sigma_f + \sigma_{th} + \sigma_e \quad (2.12)$$

The origins and reasons for the existence of intrinsic stresses in vacuum deposited coatings are not well elaborated in the literature. PVD and CVD techniques are both non-equilibrium thermodynamic processes, which lead to a quenched disorder state in the coating associated with nanovoids of 2-4 Angstroms [8]. The accumulation of atomic forces generated throughout the coating by particles impinging its surface during growth is cited as an explanation, as well as structural reordering and filling of the voids during ion or atomic bombardment [107]. No general model exists to predict the stress state in deposited coatings, if one existed it would be limited to specific materials and deposition method [152].

Thermal stresses arise due to rapid substrate heating during deposition and as a result of the large differences in coefficients of thermal expansion between the oxide and the polymer. Assuming thermoelastic behaviour the in-plane thermal stress is given by [8, 107]:

$$\sigma_{th} = \frac{E_c}{(1-\nu_c)} \int_{T_1}^{T_2} [\alpha_s - \alpha_c] \cdot dT \quad (2.13)$$

where the prefactor of the integral represents the coating biaxial modulus, E_c and ν_c are the Young's modulus and Poisson's ratio respectively and α_c and α_s are the linear coefficients of thermal expansion (LCTE) of the substrate and coating. Using Equation 2.13, Leterrier [8] calculates a thermal stress and strain of -378 MPa and -0.5% respectively for SiO_x on a polymer film, which is comparable to the total residual strains reported by Yanaka *et al.* [153, 154], for evaporated SiO_x layers on PET films, indicating that thermal stresses dominate the total stresses for this type of coating. In the same literature it was found that the compressive stress decreased for higher thicknesses with stress relaxation, in the form of nanoscopic cracks, being apparent. The work of Ben Amor *et al.* [102], investigating titania films on PET, contrasts with these findings on two counts. First, thermal stress only contributes about 10% to the total residual stress of the films and secondly the compressive stress increases with thickness, which is accounted for by the accumulation of defects and impurities (although the range of thicknesses examined is not divulged). Interestingly, the stress can be controlled by altering the gas pressure during deposition with an increase in power density of the sputtering target and a decrease in plasma pressure leading to higher compressive stresses (Figure 2.12). For thin PECVD SiO_x layers on PET, the internal stress is generally found to be less than -200 MPa and does not seriously affect the mechanical properties of the composite [8, 91, 155].

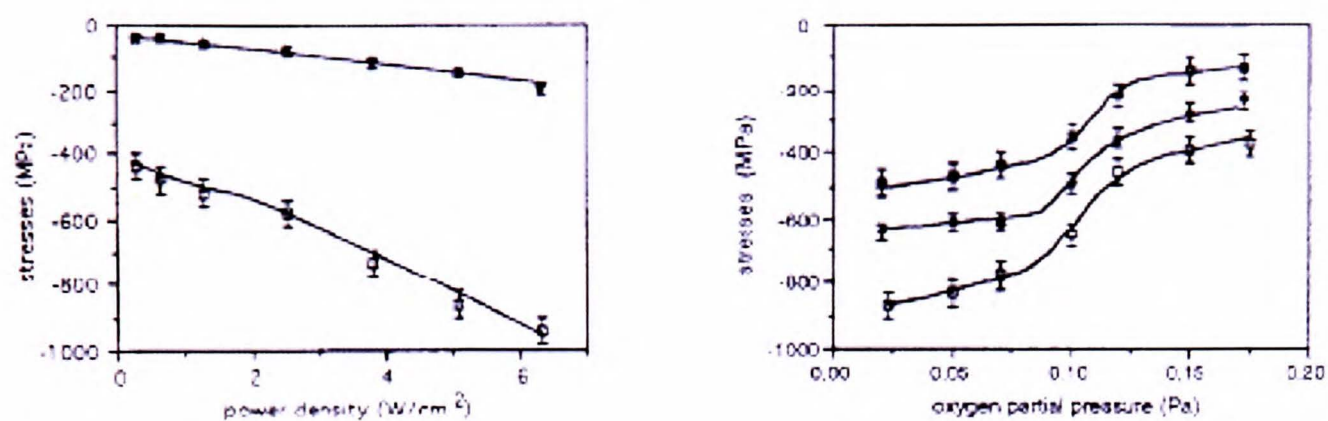


Figure 2.12 Compressive stress in reactively sputtered TiO_x films. Left; the effects of target power density on thermal (\blacklozenge) and total (\square) stress. Right; effect of oxygen partial pressure on the compressive stress for 50 nm (\blacksquare), 100 nm (\blacklozenge) and 200 nm (\square) films. Reproduced from [102].

Rochat *et al.* [155] have shown that control of the internal stress state after deposition by heat treatments can improve the performance of thin SiO_x films on PET immensely. After annealing for 10 minutes at 150°C the substrate shrinks by 1.8%, leading to an order of magnitude increase in the internal stress of the coating. This is then responsible for improved crack onset strain and apparent cohesive and adhesive strength properties by up to 40%. The gas barrier properties of the film are unaffected by the treatment showing that the defect population and microstructure are unchanged.

2.5.2 Adhesion

The adhesion of a coating to the substrate is an important property, as any failure of the interface will degrade the properties of a gas barrier [8, 156]. It is controlled by the interactions between the metal/oxide and the polymer and the levels of process induced stress. It is a difficult property to measure quantitatively and there are three main methods that are used for oxide films on polymer substrates.

The most commonly used is the peel test [107, 157] where the thin coating is peeled from the substrate of well defined width at a specific angle, usually 90° or 180° , using a backing material such as ethylene acrylic acid (EAA). The force applied to the backing material so that the coating begins to peel off the substrate is known as the peel strength and is a qualitative guide to the adhesion, useful for comparative purposes. The drawbacks are that often the peel strength of oxide coatings exceeds the measurement limit [158, 159] and the introduction of a third body – the adhesive, complicates the determination of the absolute value of adhesion. The second method incorporates various scratching and indentation techniques [147, 160]. In the scratch test a stylus is drawn across the coating under increasing vertical load and the critical load of failure is often taken as a semi-quantitative measure of adhesion. The disadvantage of the technique is the introduction of a third body, the stylus or indenter, which yields a complex triaxial stress field in the polymer substrate and an absolute value of adhesion cannot be obtained [8], although again it is useful as a comparative tool.

The fragmentation test has been used in the last 10-15 years to measure the adhesion of thin oxide films to polymer substrates [8]. In this technique the evolution of cracking patterns in the brittle coating is monitored as a function of the tensile strain applied to the substrate by *in-situ* optical or scanning electron microscopy. The adhesion is represented by the interfacial shear strength and is related to the number of cracks at saturation (when no more cracks appear as the applied strain increases). It is usual to apply uniaxial tension to the film, although biaxial tension may be applied to elucidate information about the coating failure mechanism. The cracking of SiO_x films under uniaxial strain on PET is

widely reported and shown in Figure 2.13 as a function of strain. It can be seen that there are three main stages [8, 161]. First is the rupture of parallel strips, perpendicular to the strain direction (A). These strips are then ruptured again to form smaller rectangular fragments, along with cracks parallel to the load direction (transverse cracking) (B). This results from compressive stresses due to the contraction of the film perpendicular to the direction of the load, in accordance with Poisson's ratio. The third effect is the delamination of the strips from the substrate and the fragmentation virtually stops (C).

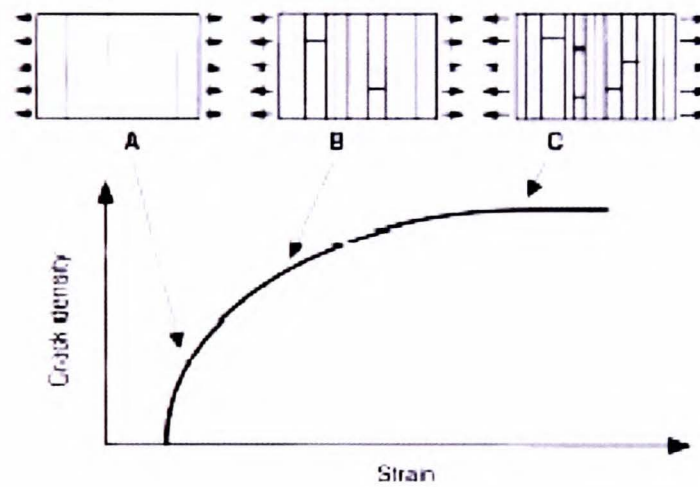


Figure 2.13 Evolution of cracking in a brittle coating on a ductile substrate with applied uniaxial strain [8].

The interfacial shear strength is most commonly reported using the shear-lag analysis of Kelly and Tyson [161, 162] which assumes a perfectly plastic interface, that was originally developed for fibre reinforced composites, and is given as:

$$\tau = 2 h_c \sigma_{max}(l_c) / l_c \quad (2.14)$$

where h_c is the coating thickness, σ_{max} is the size dependent cohesive strength of the coating and l_c is the critical stress transfer length (the minimum length of coating that can

undergo fragmentation). It cannot be measured directly and is related to the average fragment length, l_{sat} , by $l_{sat} = 0.67 l_c$.

The tensile strength, σ_{max} , of brittle materials, including ceramic coatings, is controlled by defects and is size dependent, described by the Weibull weakest link model [161, 163-165]. Only volume defects are considered, leading to the two parameter distribution:

$$\sigma_{max}(l) = \beta(l/l_0)^{-1/\alpha} \cdot \Gamma(1 + 1/\alpha) \quad (2.15)$$

where l_0 is a normalisation factor equal to 1 μm , Γ is the gamma function and α and β are the Weibull shape and scale factors, respectively, derived from a linear extrapolation of the initial region of a plot of crack density (mm^{-1}) against applied strain in logarithmic coordinates. It should be noted that both τ and σ_{max} are effective, practical values and that internal stress must be considered before the intrinsic properties are calculated [8]. The analysis of the fragmentation test is described in more detail in Chapter 3.7.

From the wealth of literature published by Leterrier and various co-workers [8, 161, 166-171] concerning the fragmentation of silica films on PET and other polymers, the following general points can be made for SiO_x thicknesses ranging from 7 nm to 150 nm:

- Thick coatings crack earlier than thinner ones and have a lower crack density at saturation.

- The cohesive strength of thick coatings is less than thinner ones, due to the presence of larger defects (signified by the shape parameter α)
- The interfacial shear strength is independent of the thickness of the coating
- The adhesion of SiO_x to PET is good, due to Si-O-C bonding at the interface, with the IFSS always equal to or greater than the substrate yield stress. The interface is found to be stronger under shear than the polymer which yields first.
- A balance between barrier and mechanical strength must be made so that maximum barrier is achieved and a high crack onset strain and cohesive strength are observed for the deposited film. This is thought to be at a thickness of about 50 nm for SiO_x as a barrier to O_2 permeation (Figure 2.14).

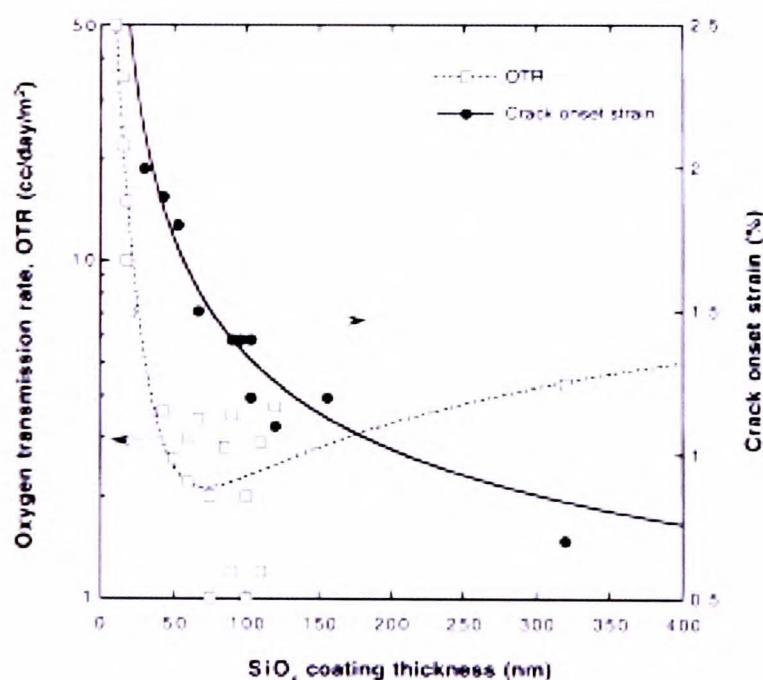


Figure 2.14 The effect of SiO_x film thickness on OTR and crack onset strain [8].

The shear lag approach to the fragmentation test on SiO_x -PET composites has also been examined by McGuigan *et al.* [172] who detail a model that predicts the average crack density and crack opening as a function of applied strain and Yanaka *et al.* [173] who

find that increasing temperature from 26 to 150°C has no effect on the crack onset strain and fracture stress, but increases the number of cracks observed after the COS.

2.6 Substrate Effects

The effect that the substrate properties have on the deposited coating is a factor that is generally overlooked in the literature, with the focus being on the deposition technique and processing conditions. Of primary concern is the cleanliness of the surface, as it is known that debris is responsible for the creation of pinhole defects [119]. Filler particles in the film, which protrude by up to 100 nm, are also thought to be responsible for defects. To smoothen the surface polyacrylate layers, thicker than those in multilayer stacks, are deposited before the barrier to reduce the roughness to less than 1 nm. Such a step can reduce the permeation of gas through coated films by an order of magnitude due to the reduction in the defect density [142, 143]. A smooth substrate surface is also thought to lead to a less columnar morphology so that fewer intergranular defects exist to facilitate gas transport in the absence of pinholes. Although polymer film surfaces are well characterised on the nanoscale [174-176], little work has been published on the link between the substrate morphology at this scale and coating structure/performance for gas barrier films, even with the knowledge that the coating structure on this scale can control permeation mechanisms in the absence of large scale defects. Additionally, scratches on the substrate, caused by winding and handling, should be considered [129] for their influence on the coating as Rochat *et al.* [169] note that SiO_x coatings preferentially buckle under compression at the sites of such features. The same authors also find that filler particles reduce the crack onset strain and increase the width of the defect size

distribution, and for polyamide film preferential delamination of the coating at spherulite boundaries is observed [177].

Other film substrates are being considered as alternatives to PET and PEN for high barrier applications. Such polymers include polycarbonate [145] and polyethersulphone [131], films with inherently inferior barrier to PET but with a higher T_g and good thermal stability which means that higher deposition temperatures are possible and a denser, less defect prone coating may be produced. Often these substrates will be heat stabilised to increase their stability for demanding applications [6]. Whatever the substrate, it will need to be functionalised and cleaned prior to deposition to ensure good adhesion and microstructure. To this end, plasma treatments of the film surface prior to deposition are performed.

2.6.1 Plasma surface modification

Plasma treatments are often used to modify the surface of the polymer so that it forms a superior interface with the coating. Abundant literature [178-189] reports the influence of plasma treatments using various gases (O_2 , Ar, CO_2 , O_2 -He mixtures) on the surface chemistry and morphology of polymers and PET in particular. In the case of polyesters, the bonds about the ester group have been identified as weak points for chain scission although aromatic groups are thought to stabilise them – PET has been found to be much more stable to degradation than poly(methyl methacrylate) [190].

The plasma gas most commonly used for the treatment of polymers is argon as it can be controlled to give mild treatments and a r.f. plasma at 13.56 MHz is typically used. An investigation by Beake *et al.* [180] into the evolution of topography of biaxially drawn films with Ar plasma treatment time found that the rms roughness remained unchanged at any time scale but that ridged structures began to appear that were always perpendicular to the final, transverse draw direction (Figure 2.15). Using a silica filled PET film they were able to calculate that the PET was being etched at 4 nm min^{-1} at a pressure of 0.1mbar. A similar etching study with helium found the rate to be comparable at $4.5 - 6 \text{ nm min}^{-1}$ with a lower pressure and greater plasma power [178]. A further study by Beake *et al.* [179] shows that contact AFM damages the modified surface clearly and that tapping-mode is more appropriate. Gupta *et al.* [181], using an argon plasma at a much greater power, observed a linear increase in roughness over 100 s of treatment and observed that the wavelength of the features remained constant – consistent with preferential etching of the surface.

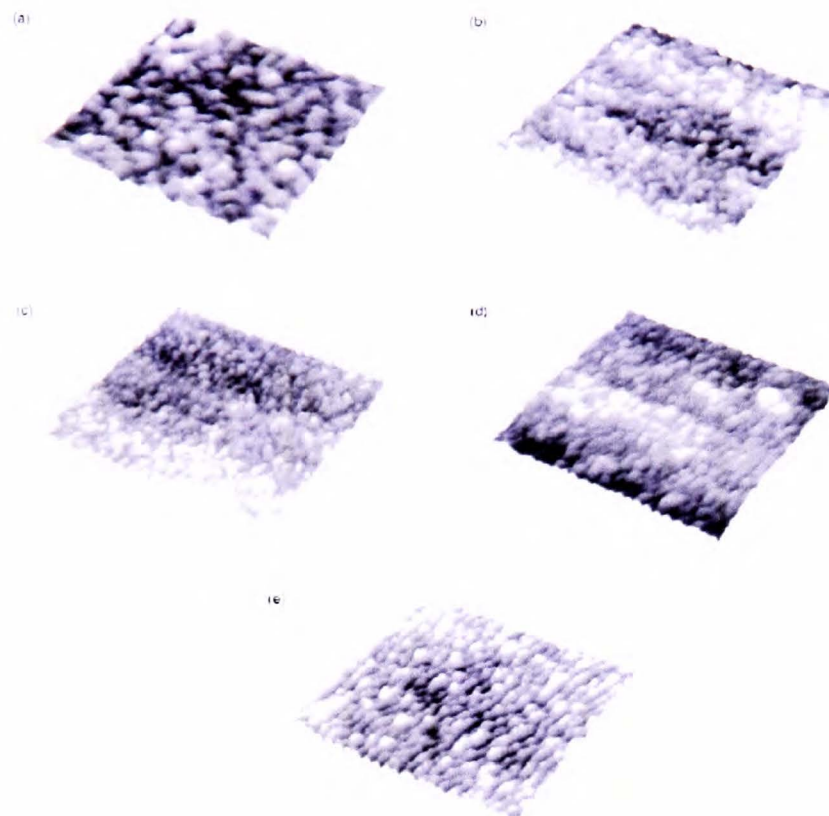


Figure 2.15 Non-contact mode SFM image of plasma treated Melinex 'O'. 0.1 mbar argon pressure; (a) 1 min, (b) 10 min, (c) 20 min, (d) 60 min, (e) 90 min treatment. Image size: 1.6 μm x 1.6 μm . Reproduced from [180].

Much more attention has been paid to the chemical effects of plasma treatment at the polymer surface by the use of wettability (contact angle) and XPS measurements. In general, the surface chemistry and wettability are altered much more rapidly than the topography. An argon plasma is found to decrease the contact angle of water on PET from 78° to anywhere between 25° and 35° in seconds, depending on the process conditions [179-181] and using a pulsed argon plasma, Inagaki [191] found that the contact angle reached a threshold at about 40 degrees after ten seconds. An increase in plasma power has been found to lower the contact angle, as has a decrease in chamber pressure [179, 180]. The contact angle is thought to reach a stable threshold (as opposed to becoming completely wettable with an angle of 0°) due to the competition between etching of the surface and chemical functionalisation. The observed increase in

hydrophilicity suggests the creation of reactive oxygen-containing functional groups at the PET surface.

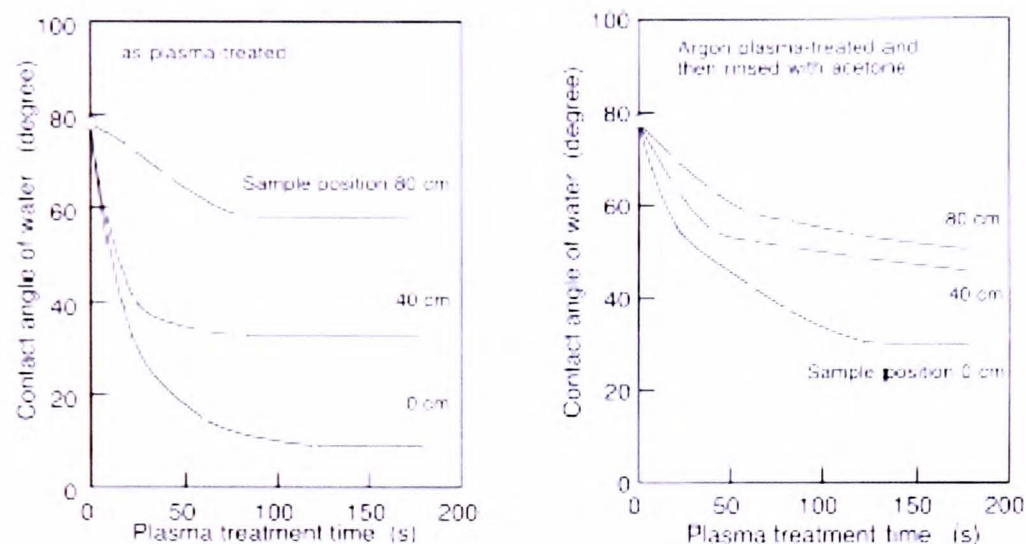


Figure 2.16 Decrease in water contact angle on Ar plasma treated PET (75W) as a function of time. Effects of washing and the sample-to-plasma distance on the contact angle are observed.

By using the van Oss [192] approach for quantifying surface tension, Beake *et al.* [179] showed that the basic component of surface tension increased with plasma treatment but the acidic component increased only slightly from its original negligible value. This supported their XPS analysis that only carbonyl groups were formed by a mild Ar treatment. Cueff *et al.* make similar conclusions from XPS data that carbonyl groups are the only oxygen functionality to increase in composition [193]. An increase in acidic and basic components was observed when treating polyethylene with oxygen plasma – attributed to phenol, carboxylic acid and carbonyl groups [194].

Gupta *et al.* [181] proposed that as well as carbonyl groups, phenol and hydroperoxy (-OOH) groups were formed by a high power Ar plasma (Figure 2.17) and oxygen plasma has been found to introduce carboxylic acid functionality to the PET surface [185, 195]

with an increase in the O:C ratio. XPS and wettability measurements have been used to show that the ageing of plasma treated films [186, 196, 197] occurs as the polar groups either react at the surface or migrate to the bulk over time.

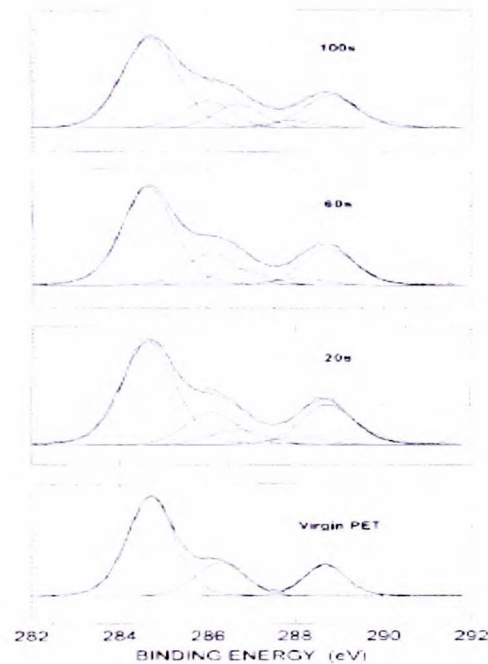


Figure 2.17 Evolution of PET surface chemistry with time under an Ar plasma with introduction of phenols (286.7 eV) and carbonyls (288.1 eV) [181].

2.6.2 Effects of plasma treatment on vacuum deposited coatings

For metal coatings on polymers, an increase in the degree of interfacial bonding is observed by XPS and manifests itself in a higher adhesion value for silver and aluminium layers, after the substrate is pretreated. A 15 fold improvement in Al adhesion to PET is reported by d'Agostino *et al.* [198] for a NH_3 plasma treatment lasting less than a second. Moosheimer [199] and co-workers find that for Al layers on polypropylene the oxygen barrier improves dramatically (improved adhesion is also observed) when a gentle O_2 plasma pretreatment is applied. This is attributed to the cleaning effect of the plasma which results in a smoother surface that encourages fewer defects. For Ag layers

deposited on O₂ plasma treated PET, Gerenser [195] finds that plasma induced acid groups are the main reaction sites for interfacial covalent bonding, using XPS, so that the interface is characterised by silver carboxylate species. An estimated 4-fold increase in chemical bonding is estimated after plasma treatment which is consistent with observed increases in adhesion. Similarly, the adhesion of titanium layers on PET is enhanced by Ar and N₂O plasma treatments [200]. The adhesion of metal films is also improved by heating the PET substrate to above 100°C according to Silvain *et al.* [157, 201] who credit this to the tendency of the benzene rings of the film to orient parallel to the surface during heating and presenting the carbonyl groups to the surface so that they are available for bonding.

For SiO_x coatings the influence of plasma treatments is not well examined. On PE it is shown that plasma treatment with N₂ improves the adhesion of the coating to the film through enhanced chemical bonding [202]. The interface between SiO_x films and PET was found to be about 50 nm for PECVD films and a only few nm for PVD films which explains the enhanced adhesion of the PECVD films on PET, as reported by da Silva Sobrinho *et al.* [203].

2.7 Conclusion

The fabrication and evaluation of flexible packaging with high gas barrier presents considerable challenges and many factors must be considered to produce effective material - the deposition technique, substrate, coating material and processing parameters all play a part in determining the final properties of the composite. PECVD SiO_x films

appear to be the most promising (and well studied) single layer barrier films as they are transparent, offer a low critical thickness, good barrier, impressive mechanical properties and adhere well to the substrate. However, large-scale deposition is still economically unviable by this method and aluminium metallisation prevails in most large scale packaging where transparency is not a requirement. The importance of the substrate mainly lies in the formation of defects in the coating by surface debris on the film and plasma treatment is required to ensure the surface is clean and functionalised for good adhesion. Much more work is required to understand the influence (if any) of the nanoscale surface features of the substrate on the coating, particularly its microstructure and any subsequent effect on barrier.

Furthermore, it is evident from this overview of gas barrier coatings on polymer films that although great effort has been made to improve the materials and to explain the mechanisms of gas and water permeation through deposited films, more knowledge is required to transfer the properties of the bulk materials to the thin coating form. There seems to be a limit at which single layer films can block water and O₂ permeation, which is adequate for some food and pharmaceuticals packaging, but which is insufficient for applications such as beer bottles, flexible displays and electronic paper. The main reason for this is defects, and it seems the prevailing wisdom is that the best method to overcome these is to use multiple, alternating organic and inorganic layers that decouple the defects in the oxide layers. Whether the observed improvement in barrier is down to reduced steady state flux or extended lag-times is open to debate. The mechanical properties of these films also need further scrutiny if they are to be commercially viable.

Chapter 3. Experimental Methods

In this section a description of the characterisation techniques used for this thesis is presented. The methods used to deposit coatings and determine their thickness are described in the relevant chapters.

3.1 Atomic Force Microscopy

AFM has been used to study the surface topography of the polymer substrates as well as the vacuum deposited coatings. First reported in 1986 by Binnig *et al.* [204], it has found wide application in the physical and biological sciences. The principles behind the operation of a typical AFM in its basic contact mode are as follows [205].

3.1.1 Contact Mode AFM

An AFM probe consists of an extremely fine tip, typically Si_3N_4 (radius of curvature ~ 10 nm), attached to the bottom side of a reflective cantilever. A laser is positioned onto the top, gold coated cantilever surface so that it reflects into a photodetector, with two side-by-side photodiodes. The difference between the two photodiode signals indicates the position of the laser on the detector and thus the angular deflection of the cantilever. The tip is brought into contact with the specimen, which is placed on a piezoelectric crystal holder so that voltages applied to the holder allow lateral movement of the sample relative to the tip. By raster scanning of the tip an image is built up. The force between the sample and tip can be measured with great precision as it is proportional to the cantilever deflection, with the constant of proportionality being the spring constant of the

cantilever. Most AFMs work by maintaining a constant tip-specimen attractive force, and as the tip moves over undulations in the topography the cantilever will bend as the distance between tip and sample changes. The deviation of the cantilever is measured and the piezoelectric element receives a voltage so that it moves the specimen vertically to achieve the original cantilever deflection (and therefore tip-sample force). This voltage is a measure of the vertical features on the surface and has an effective resolution of less than 1 Angstrom.

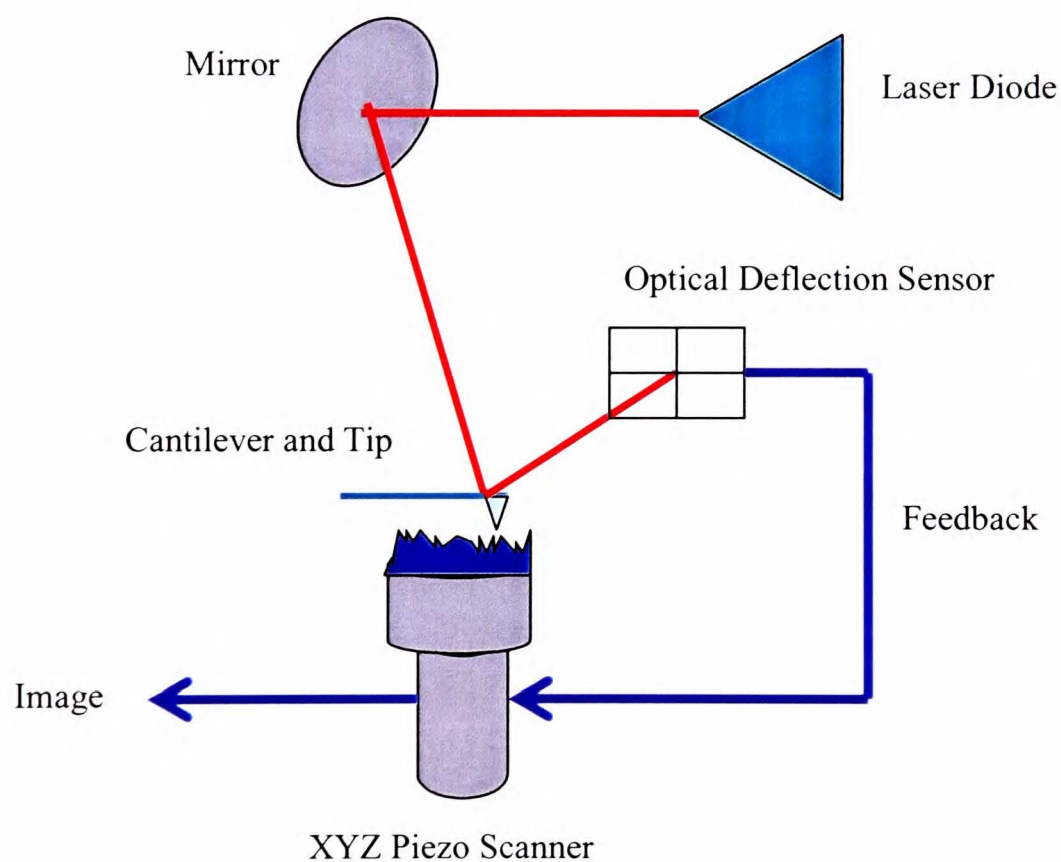


Figure 3.1 Schematic of the operation of an AFM.

In ambient conditions sample surfaces are covered by adsorbed gases (water vapour, hydrocarbons and N_2), that can produce a meniscus when the probe is in contact [205]. Consequently, surface tension pulls the tip towards the sample, which can then damage it. Imaging with the sample and probe immersed in liquid can eliminate the meniscus and

damage to the sample by attractive forces but may adversely affect sensitive samples chemically.

Although lateral shearing and mechanical ploughing forces can damage soft samples, the response of the substrate to them can be determined by measuring the twisting motion of the cantilever as it drags along the surface, which is known as lateral force microscopy (LFM) [206, 207]. Areas of high friction cause a higher degree of twisting of the cantilever so that areas of differing frictional coefficient (and possibly surface chemistry) can be distinguished using this mode, which runs concurrently with the contact AFM. The principle drawback of LFM is that topographical features can also cause the cantilever to twist so that great care is required to separate artefacts created by height and areas of differing frictional behaviour. Recently, chemically modified tips [208, 209] have been used to accentuate the frictional forces at the surface due to adhesion and to provide higher contrast between areas of differing chemistry in heterogeneous materials.

3.1.2 Tapping Mode

Tapping Mode AFM is a more recent development that allows imaging of delicate samples as the tip does not contact the sample for any great length of time [210, 211]. It also eliminates difficulties associated with friction and adhesion as the tip does not move laterally when in contact with the specimen. The cantilever is oscillated at or near its resonant frequency by a piezoelectric crystal with an amplitude typically greater than 20 nm. As the tip approaches the surface it begins to lightly touch the surface and lift off at a frequency of 50-500 kHz. During scanning the cantilever oscillation amplitude is kept

constant by a feedback loop at a level to cause a minimum applied normal force to the specimen. When the tip passes over a peak in the surface the amplitude of the cantilever oscillation decreases as it has less room to oscillate and conversely the amplitude of oscillation increases as the tip passes over a trough. The amplitude of oscillation is monitored using the laser-photodiode system and the feedback loop adjusts the tip-sample separation to maintain a constant amplitude and force on the sample. As a result, topography can be mapped accurately without subjecting it to damaging shearing forces by the cantilever. The radius of curvature of TM-AFM tips is between 5-10 nm enabling high resolution imaging.

Associated with TM-AFM is phase imaging which can give useful information about variation in surface mechanical properties in addition to clearer images of morphology. Operating concurrently with Tapping Mode, in this function the phase lag between the driving oscillation applied to the cantilever and the response of the cantilever is measured so that a higher phase lag corresponds to a higher rate of energy dissipation upon surface contact [175, 210]. Stiff material would exhibit a lower energy dissipation and phase lag than a softer, more viscous material. Therefore it is possible to distinguish areas of varying elastic properties on a material's surface.

3.1.3 Force-distance curves

Another method to gauge a specimen's surface elastic properties is to approach the surface with the tip until contact is made and then to retract the tip from the sample. Due to surface tension between the sample and tip the tip dissociates from the sample at a

displacement, x , from the undistorted surface [210]. By plotting a graph of force against distance the value of x , often known as the snap-off displacement, can be extracted. A larger value of x corresponds to a more viscous material and this technique is well suited to polymeric samples. As shown in Chapter 4 it is a technique useful in approximating the surface glass transition temperature, T_g , of a polymer as the viscosity of polymers changes dramatically in this region of temperature [212].

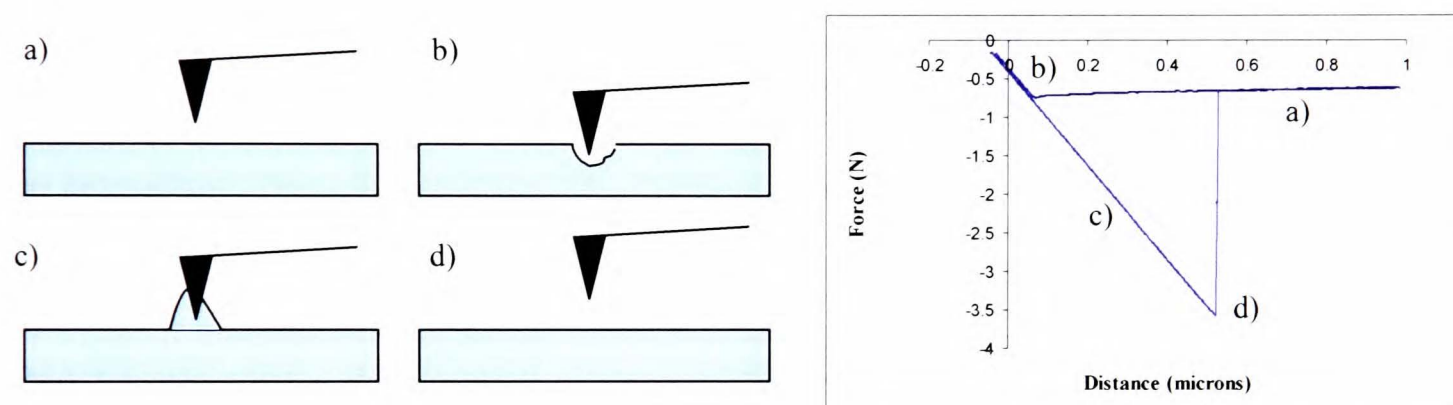


Figure 3.2 Force-distance curves by AFM: a) approaching the surface, b) contact and slight embedding into surface, c) retraction and hysteresis, d) snap-off.

3.1.4 Details of AFM imaging

Contact mode AFM and force-distance measurements were performed using a Model CP, Park Scientific Instruments (Sunnyvale, USA) instrument using gold coated Si Ultralevers with tips of radius ~ 10 nm and a spring constant of 0.4 N m^{-1} . For contact mode a low normal force of 1 nN was applied to limit damage of the substrate and the scanning rate was kept to a maximum of 0.7 Hz to prevent the tip from “jumping”.

Tapping Mode images were taken using a Digital Instruments Nanoscope Multimode AFM. The probe consisted of an etched single crystal of silicon with a nominal tip radius

of between 5 and 10 nm. The spring constant of the cantilevers ranged from 20 to 100 N/m. Typical scan rates used were 1-1.5 Hz.

3.1.5 Glass transition temperature measurement

To measure the surface T_g of the polymer the tip was held just in contact with the surface and then moved 1 nm towards it, before being retracted by a sufficient distance to dissociate from the sample (0.5-1.5 μm). For each curve three sweeps were made at a rate of 0.7 Hz and averaged to give a force-distance curve. A blunt tip was used to maximise the tip-sample interaction that produces the hysteresis effect. Eight force distance curves were taken at each temperature in increments of 5°C starting from 30°C. The sample was heated *in-situ* using an electrical contact situated beneath it, with a current supplied by a Metrix AX 322 power supply. A change in the gradient of a plot of snap-off displacement against temperature is an indication of the T_g . The heater was calibrated for experimental conditions by heating Wood's Metal (50% Bi, 25% Pb, 12.5% Sn, 12.5% Cd) and monitoring the temperature of this alloy with a thermocouple as the voltage from the power unit increased (an initial calibration of the heating stage had been performed earlier, by heating indium to yield a voltage vs temperature plot, by Mr Kei Shinotsuka).

3.2 Scanning Electron Microscopy (SEM)

SEM was used to examine the presence of defects in the coating of the order of 1 μm in size and to examine how the coating conformed over features such as filler particles in the base film. Samples were prepared by sticking a 0.5 x 0.5 cm piece of coated film to a

SEM stub using conductive silver paint. The corners of the film were coated with the paint so that they enabled a good electrical contact with the stub (to prevent charge building up on the surface). Aluminium coatings were found to be conductive and did not require a top layer such as gold to prevent charging. Silicon oxide coatings, on the other hand, did charge up unless a top layer was first deposited. Gold was found to cause artefacts when examining the specimen at high magnification (>20 000x) so as an alternative, 3 nm thick layers of platinum were deposited using a Cressington sputtering chamber.

To examine the coatings at low magnification (<10 000x) a JEOL 840F microscope was used at operating voltages 3-5 keV. For studies up to 100 000x magnification a JEOL 6500F was used with operating voltages 1-5 keV.

3.3 X-ray Photoelectron Spectroscopy (XPS)

XPS is a powerful tool for analysing elemental composition at the surface of a material, with characterisation involving the irradiation of a specimen with X-rays in an ultra high vacuum chamber. The most common X-ray sources are MgK α (1253.6 eV) or AlK α (1486.6 eV) X-rays. When X-ray photons strike the surface they can either pass through it, be scattered by an atomic orbital electron or transfer their total energy to the electron, leading to the emission of the electron (termed a photoelectron) with a kinetic energy KE that can be expressed by [65, 213]:

$$KE = h\nu - BE + W \tag{3.1}$$

Where $h\nu$ is the energy of the exciting X-ray radiation, BE is the binding energy of the photoelectron and W is the spectrometer work function. For the energy of X-ray photons used in this technique it is the core electrons (1s, 2s) that are emitted for the lighter elements (C, O, N) and 2p shell electrons for Si and Al. As the elements get heavier, the electrons are excited from orbitals further from the nucleus. The photoelectrons are detected by a spectrometer, separated according to their energies and counted by an analyzer. The measured kinetic energies and X-ray energy are then used to calculate the binding energies of the photoelectrons, which are plotted against the number of electrons counted (intensity) to give an XPS spectrum. Each atom has a specific binding energy for electrons emitted from a given atomic orbital, allowing a wealth of chemical information to be obtained. Additionally when photoelectron emission occurs, electrons in higher atomic orbitals drop down to occupy the core level, leading to the emission of X-rays and valence electrons (Auger electrons) depending on the energy level from which the electron has transferred from [65]. The latter can give useful additional information about a material.

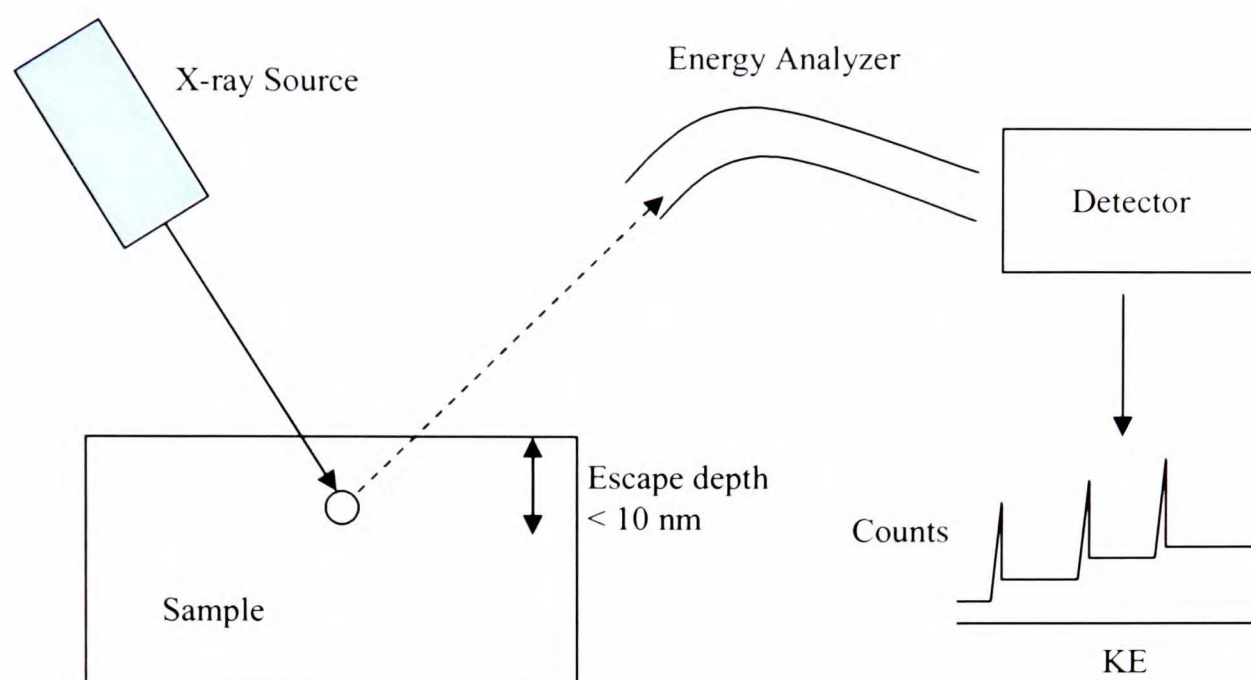


Figure 3.3 Schematic of the operation of an XPS.

The sampling depth of the technique is a maximum of 10 nm, for although the X-rays penetrate deeper than this the emitted electrons can only escape with no energy loss very close to the surface. XPS is capable of identifying all elements bar H and He at concentrations of higher than 0.1%, allowing determination of the elemental composition at the surface as well as any lateral variation for a given sample. Importantly, subtle changes in BE of the core electrons for an atom when bonded to more electropositive or electronegative atoms allows information to be obtained about oxidation states and the bonding environment of a given atom.

The analysis was performed in a VG ESCALAB MkII, with a base pressure of 5×10^{-10} mbar in the analysis chamber. The pressure during analysis was 1×10^{-9} mbar. 200 Watt MgK α X-rays (1253.6 eV) were used to excite photoelectrons. Detailed scans were recorded with a pass energy of 20 eV. A 5 mm aperture was used as the entrance slit to

the spectrometer enabling electrons to be collected from a 5 mm diameter area of the sample. The C 1s peak was used as a reference at 284.7 eV and sensitivity factors of 0.25, 0.66, 0.27 and 0.185 were used to calculate the area of C 1s, O 1s, Si 2p and Al 2p peaks respectively, after Briggs and Seah [65]. XPSpeak software was used to plot the spectra, eliminate background effects (using the Shirley method) and calculate the areas of the BE peaks. The binding energies of the elements and chemical groups examined in this study were taken from the literature, the online surface science/ESCA forum, www.uksaf.org, and in-house knowledge from ICI and DTF [214].

3.4 Contact Angles

The contact angle (CA) of water on a surface can give information about the chemistry of the material in contact with the droplet. The method was used to quickly assess how plasma treatments affected the surface chemistry – a more functionalised surface would be expected to reduce the contact angle as the water spreads over the surface.

The sessile drop method [215, 216], where one droplet is deposited on the surface by a syringe (it is “laid down” rather than dropped) and a measurement of the angle θ is taken, was used. Figure 3.4 shows a droplet in equilibrium on a surface.

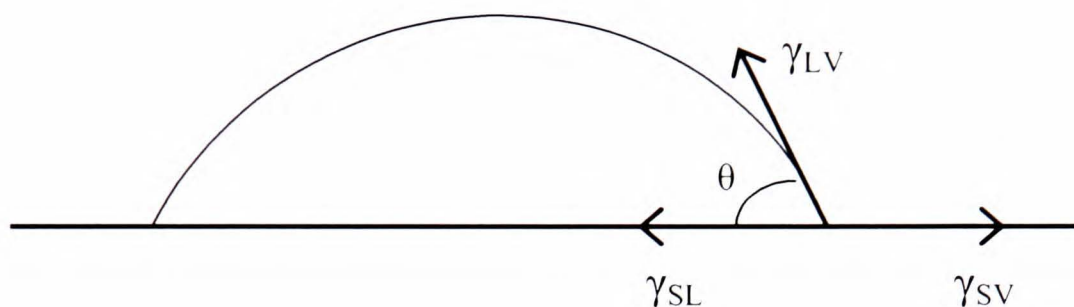


Figure 3.4 Contact angle of a liquid in equilibrium on a smooth surface.

The equilibrium can be mathematically expressed using the Young Equation:

$$\gamma_{LV} \cos \theta = \gamma_{SV} - \gamma_{SL} \quad (3.2)$$

where θ is the contact angle and γ_{ij} are the appropriate interfacial tensions between the “S” solid, “L” liquid and “V” vapour. The contact angle can decrease as the water evaporates [217] so measurements were taken as soon as the droplet had settled. To measure the CA of water an IT Concepts Tracker Drop Shape Analyser was used and the CA on both sides of the droplet was measured using the software. Typical volume of the droplet was a few microlitres.

3.5 Water Vapour Permeation Measurement

Water vapour transmission rates (WVTR) through gas barrier films were measured using a Permatran W 3/31 permeation measurement system (MOCON, Inc., MN). An exposure area of 50 cm^2 was used and mounted into the test cell, with the coated side facing the permeant. The edges of the test cell were tightly sealed by an O-ring to prevent air

leakage into the cell. Water vapour was delivered to the barrier film by a moist sponge in the outer chamber so that the relative humidity was 100%. Any water that permeates through the barrier is carried away by zero grade N₂ gas (99.999%, H₂O < 2 ppm), through an exhaust line to a pressure modulated infrared detection system [136]. The units of WVTR are g m⁻² day⁻¹ with conditioning times set to at least 24 h and often longer for high barriers as indicated in this thesis where relevant. Such time is required to allow sufficient water to pass through the barrier so that equilibrium is achieved. WVTR values were obtained at temperatures ranging from 30-50°C.

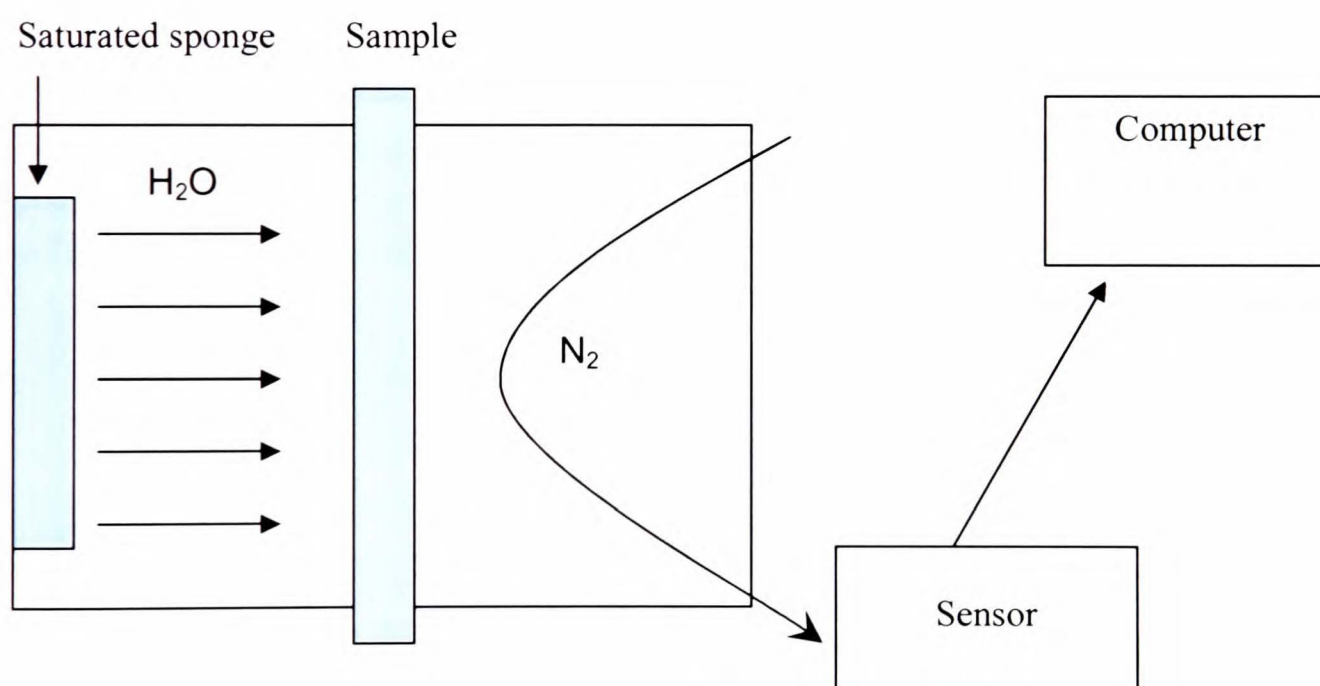


Figure 3.5 Method of measuring water vapour permeation – schematic of operation of the Permatran W 3/31.

3.6 Internal Stresses

In-plane deposition-induced internal stresses, σ_i , were calculated using the radius of curvature of the films before, R_1 , and after, R_2 , deposition [218]:

$$\sigma_i = \frac{E_s h_s^2}{6(1-\nu_s)h_c} \left(1 + \frac{h_c}{h_s} \left(4 \frac{E_c}{E_s} - 1 \right) \right) \cdot \left(\frac{1}{R_2} - \frac{1}{R_1} \right) \quad (3.3)$$

E_s and E_c are the Young's moduli of substrate and coating respectively, ν_s is the substrate Poisson's ratio and h_s and h_c are the respective thicknesses. Compressive stresses are denoted as being negative and the coating is on the convex side of the curled film. The radii R_1 and R_2 of the samples supported freely on two vertical aluminium plates were measured with an Olympus SZH binocular lens. The Young's modulus of SiO_x was assumed to be 80 GPa, following literature reports [161], the Young's modulus of the substrates were determined from tensile testing, and their Poisson's ratio was assumed to be 0.3 (manufacturer's data [219]).

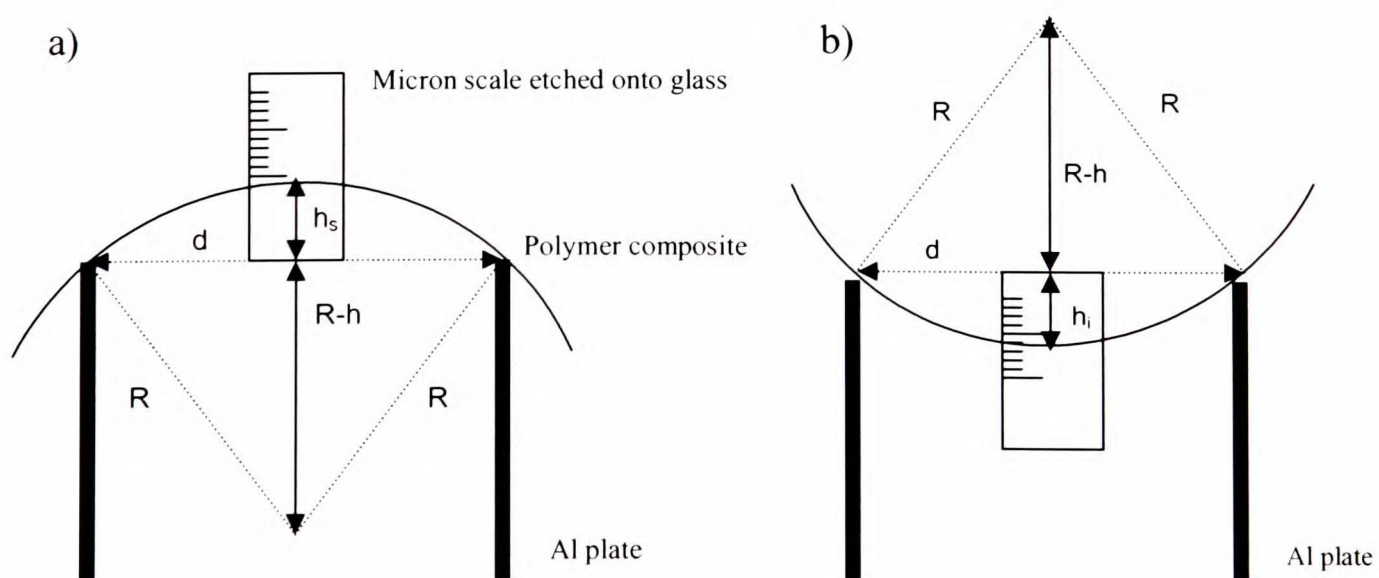


Figure 3.6 Radius of curvature measurements.

From the experiment shown in Figure 3.6, the radius of curvature, R , is calculated knowing the spacing between the plates, d , and the deflection due to stress, h , by:

$$R = \frac{d^2}{8h} + \frac{h}{2} \quad (3.4)$$

The value of h is affected by the weight of the sample which must be accounted for. The true value is obtained by simply measuring the deflections h_s and h_i , caused by stress and gravity and shown in Figure 3.6 a) and b) respectively, and then:

$$h = h_s + \frac{h_i - h_s}{2} \quad (3.5)$$

where the 2^{nd} term accounts for the weight of the specimen.

3.7 Mechanical Properties

3.7.1 Fragmentation testing

The mechanical and adhesive properties of the coating were examined using a fragmentation test, in which the onset and development of cracking of the brittle coating was monitored as a function of the applied uniaxial tensile load, *in-situ* under an optical microscope. Rectangular film specimens (approx 40x10 mm) underwent tensile loading in a computer controlled Minimat unit (Rheometric Systems) by means of a stepper

motor (load 1000 N). This unit provides measurement of displacement within 1 μm accuracy. Accurate measurement of specimen strain was achieved by a non-contact video extensometry technique, in which the relative displacement between the centres of gravity of ink markers deposited onto the surface of the specimen was monitored by means of image processing tools during application of the load [166]. This overcame problems such as possible slippage of the specimen in the clamps. Sandpaper was glued to the ends of the specimen in the clamps to minimise damage to the coating and slippage.

The tensile unit was placed under an optical microscope (Olympus BX60) for analysis. Cracking of the coating was analyzed at increasing strain levels in terms of crack density (CD), defined as the inverse of the average fragment length (l) and calculated from the average number of cracks, N_i , counted on k (typically 5-10) micrographs of width W , at strain ε , as:

$$CD = (1 + \varepsilon) \sum_{i=1}^k N_i / kW \quad (3.6)$$

The factor $(1 + \varepsilon)$ corrects for crack opening to the first approximation .

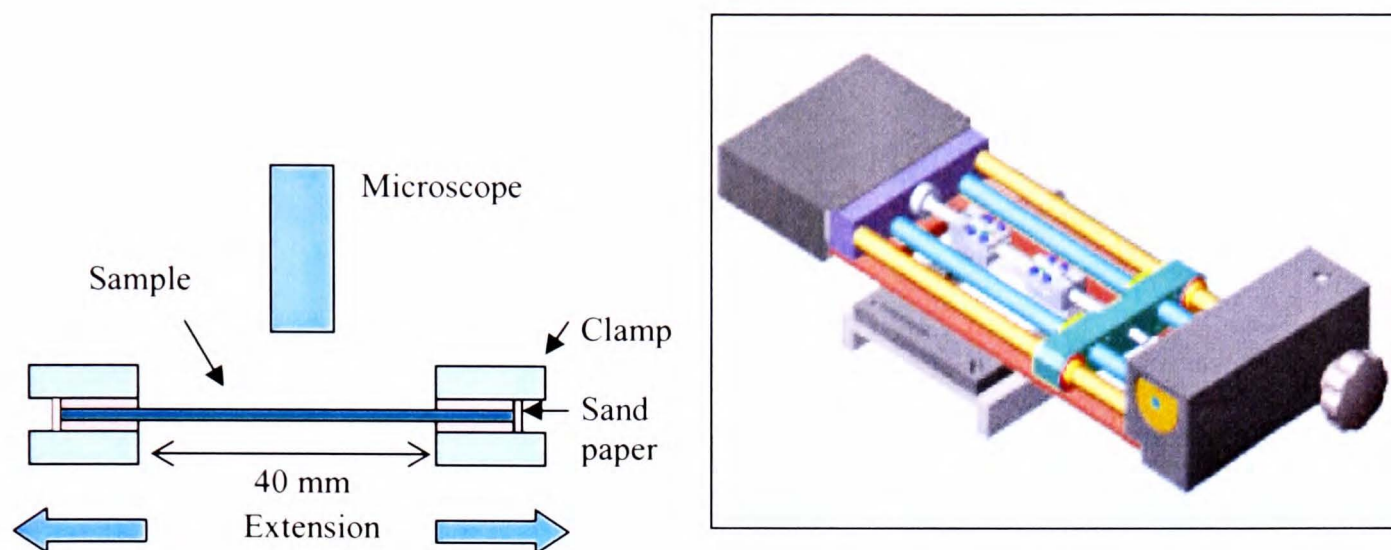


Figure 3.7 The fragmentation test. Left, side view schematic of the experimental set-up; Right, the Minimat testing stage.

3.7.2 Cohesive strength

The tensile strength of the coating, σ_t , can simply be calculated from the crack onset strain (COS) and the Young's Modulus of the coating, E_c :

$$\sigma_t = E_c \cdot \text{COS} \quad (3.7)$$

and gives the stress required for the coating to undergo brittle failure.

Another useful measure of coating strength is the maximum cohesive strength of the SiO_x fragments at saturation, σ_{max} , as this value is required to measure the adhesive strength of the coating/polymer interface. However, at saturation the fragment length is too small to measure its strength directly. Nevertheless it can be modelled using the Weibull [165] distribution for the probability of failure of ceramics which assumes the weakest link argument, based on the idea that failure at any flaw leads to total failure of the material

[164]. The strength of coating fragments depends on the probability of having a critical size defect, which for a uniform defect distribution is related to the volume (i.e. length) of coating under stress. The probability of failure of a specimen can be expressed by [161, 164]:

$$P_f = 1 - \exp\left[-\frac{l}{l_0}\left(\frac{\sigma}{\beta}\right)^\alpha\right] \quad (3.8)$$

Following from this, in the initial stages of fragmentation, the average fragment length, $\langle l \rangle$, (in μm) at small strains can be expressed as:

$$\langle l \rangle = l_0(\sigma/\beta)^{-\alpha} \quad (3.9)$$

l_0 is a normalizing factor chosen to be 1 μm , σ is the axial stress in the coating and α and β are the Weibull shape and scale factors respectively [161]. α and β can then be extrapolated from a plot of $\ln \langle l \rangle$ against $\ln \sigma$ where α is $-\text{gradient}$ and $\beta = \exp(\text{intercept} / \alpha)$. α is known as the scale parameter or Weibull modulus and is an indication of the distribution of failure stresses – a higher value represents a narrow distribution and a higher reliability. β is a normalising factor, often termed the scale parameter, and has no physical significance [163].

With these parameters the coating strength at critical length is given by:

$$\sigma_{max}(l_c) = \beta(l_c/l_0)^{-1/\alpha} \cdot \Gamma(1 + 1/\alpha) \quad (3.10)$$

Where Γ is the gamma function. The critical length is the smallest fragment that can undergo failure and is related to the average fragment length at saturation ($\langle l_{sat} \rangle = 1/CD_{sat}$) by $l_c = 1.5\langle l_{sat} \rangle$.

The crack onset strain (COS) and coating strength determined by this method are an observed, apparent measure of the coating properties. To correct for compressive strain, the intrinsic value of each is given as follows:

$$COS^* = COS + \varepsilon_i \quad (3.11)$$

$$\sigma_{max}^*(l_c) = \sigma_{max}(l_c) + 0.67\sigma_i \quad (3.12)$$

where COS^* is the intrinsic crack onset strain, $\sigma_{max}^*(l_c)$ is the intrinsic cohesive strength and ε_i and σ_i are the internal strain and stress respectively (negative for compression) [8].

The factor 0.67 results from the relaxation of the stress at the fragment edges. Throughout this work the * superscript refers to the intrinsic property, after internal stresses have been accounted for.

3.7.3 Adhesive strength

The adhesion between the coating and polymer, defined as the interfacial shear strength, τ , is derived from the CD at saturation (and therefore l_c) following an adapted version of

the Kelly-Tyson model [161, 162], which assumes a perfectly plastic interface, and therefore a constant IFSS, and was originally developed for fibre-reinforced materials (the fibre is analogous to the coating and the matrix is analogous to the polymer substrate). Important aspects of this model are that the applied load is transferred from the polymer to the coating by means of shear forces at the interface, thereby stretching the coating and that these are limited by the shear yield stress of the polymer or by the shear strength of the interface (whichever is lower). Plastic flow of the substrate and the flow stress are greatest beneath the cracks and the fragment edges and a higher crack count (low fragment length) signifies a larger interfacial shear strength.

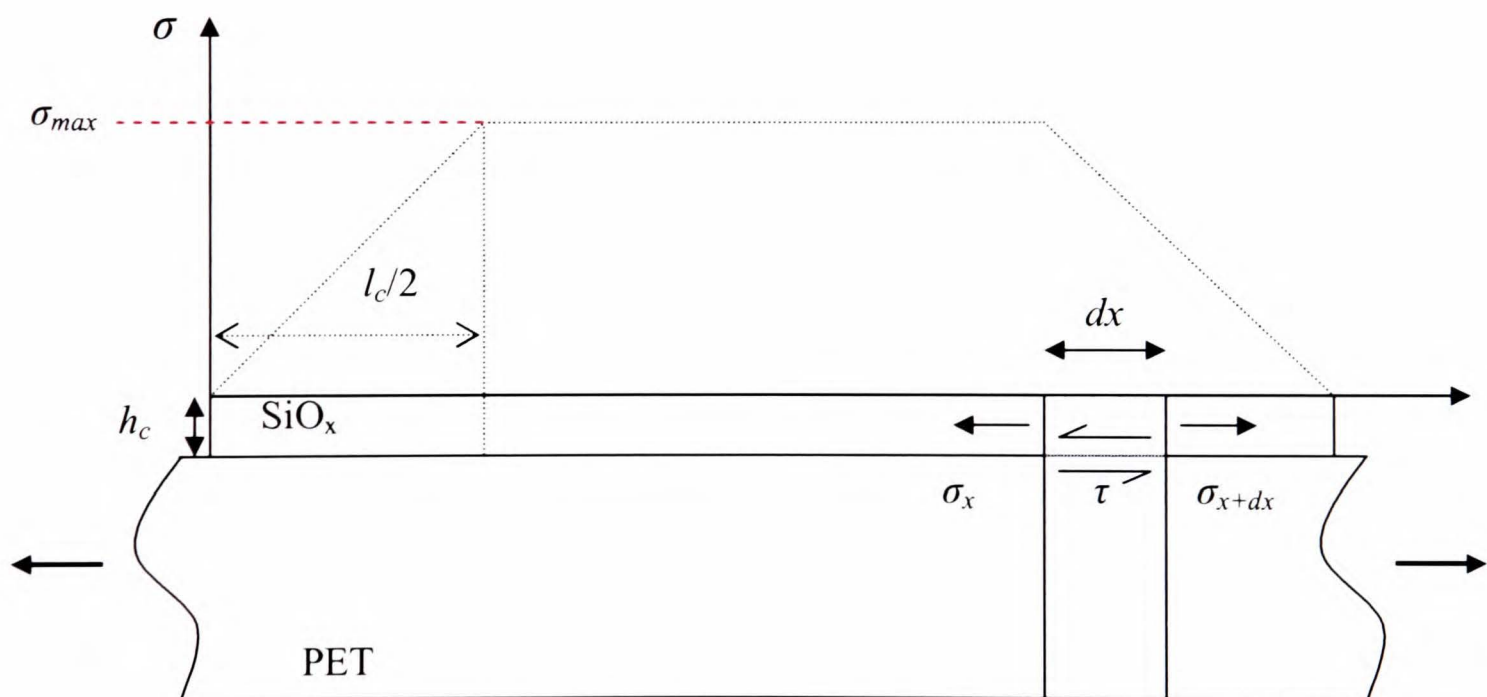


Figure 3.8 Schematic representation of the stress transfer between PET and a SiO_x coating when the composite is under tensile load.

The force balance for a thin brittle coating on a ductile polymer surface is shown in Figure 3.8. Analysis of the force balance over x gives:

$$[(\sigma_x + d\sigma_x).h_c.W] - [\sigma_x.h_c.W] = \tau.dx.W \quad (3.13)$$

where σ_x is the tensile stress acting on the coating, h_c is the coating thickness and W is the coating width. Consequently, the force acting over an infinitesimally small length of coating, dx , can be expressed as [170]:

$$\frac{d\sigma_x}{dx} = \frac{\tau}{h_c} \quad (3.14)$$

The integration of this equilibrium, with limits of 0 and $l_c/2$ because this is the minimum fragment length that can exist at saturation, leads to:

$$\tau = 2 h_c \sigma_{max}(l_c) / l_c \quad (3.15)$$

where h_c is the coating thickness. The intrinsic interfacial shear strength, τ^* , is then simply given by:

$$\tau^* = 2 h_c \sigma_{max}^*(l_c) / l_c \quad (3.16)$$

Chapter 4. The Properties of Polyester Substrates

4.1 Introduction

Polyester film can be modified in a myriad of different ways during manufacture to achieve various properties, depending on the application for which it is required. The major polyester manufacturers supply hundreds of different types of film, with variation in chemistry, thickness, draw ratios, heat set regimes, filler particles and multilayers [10]. This chapter describes the relevant properties of a small range of biaxially drawn (BD) polyester films that were studied throughout this thesis. The six films, all supplied by DuPont-Teijin Films (DTF), are as follows;

Table 4.1 Polyester substrates.

Substrate	Thickness (μm)	Notes
PET	125	Standard grade biaxially drawn PET
Heat Stabilised (HS) PET*	175	Subjected to an additional heat stabilisation stage after film is manufactured, in a separate heating process in a temperature controlled oven with negligible tension applied
HS PET_P*	175	An additional acrylate “primer” coating is applied on one side of the PET before transverse drawing to improve adhesion between the film and any deposited ink or coating. The coating is then crosslinked during the heat set process. It is approximately 40 nm thick and is a terpolymer of methyl methacrylate (MMA), ethyl acrylate (EA) and methylacrylamide, with crosslinking agents and surfactants also present. The film then undergoes the heat stabilisation step as above.
Filled PET (F-PET)	75	The film is loaded with 0.21 weight % of china clay particles which act as antiblocking agents
Amorphous PET (aPET)	30	A coextruded film with one layer of regular PET and another layer of amorphous PET (contains 18% isophthalic acid)
PEN	125	Standard grade biaxially drawn PEN

* A note should be made that all the films (bar the aPET) underwent heat setting after the final draw (see Chapter 1.5) and that the additional heat stabilisation step for HS PET takes place after winding when the film is subsequently unwound and fed through a second heating process in a temperature controlled oven (~190°C for about 30 seconds) with negligible tension applied. The aim of the additional step is to reduce thermal shrinkage later on in the film's life.

4.2 Surface Topography

AFM was used to study the surface of the polymers, and each of the six films has a unique topography, created by the different manufacturing processes. All of the surfaces are randomly structured which means quantitatively describing them is difficult and statistical methods are required [220, 221]. The most commonly used measure is the root-mean-square (rms) roughness, R_q , which measures the rms of the deviation (Z_i) about an average height, Z , following:

$$R_q = \sqrt{\frac{1}{n} \sum_{i=1}^n (Z_i - \bar{Z})^2} \quad (4.1)$$

1 x 1 μm AFM images of the surfaces of the six films are shown in Figure 4.1. Tapping mode AFM has been found to give better quality images of the polymer films than contact mode and is the technique used to capture the images shown here.

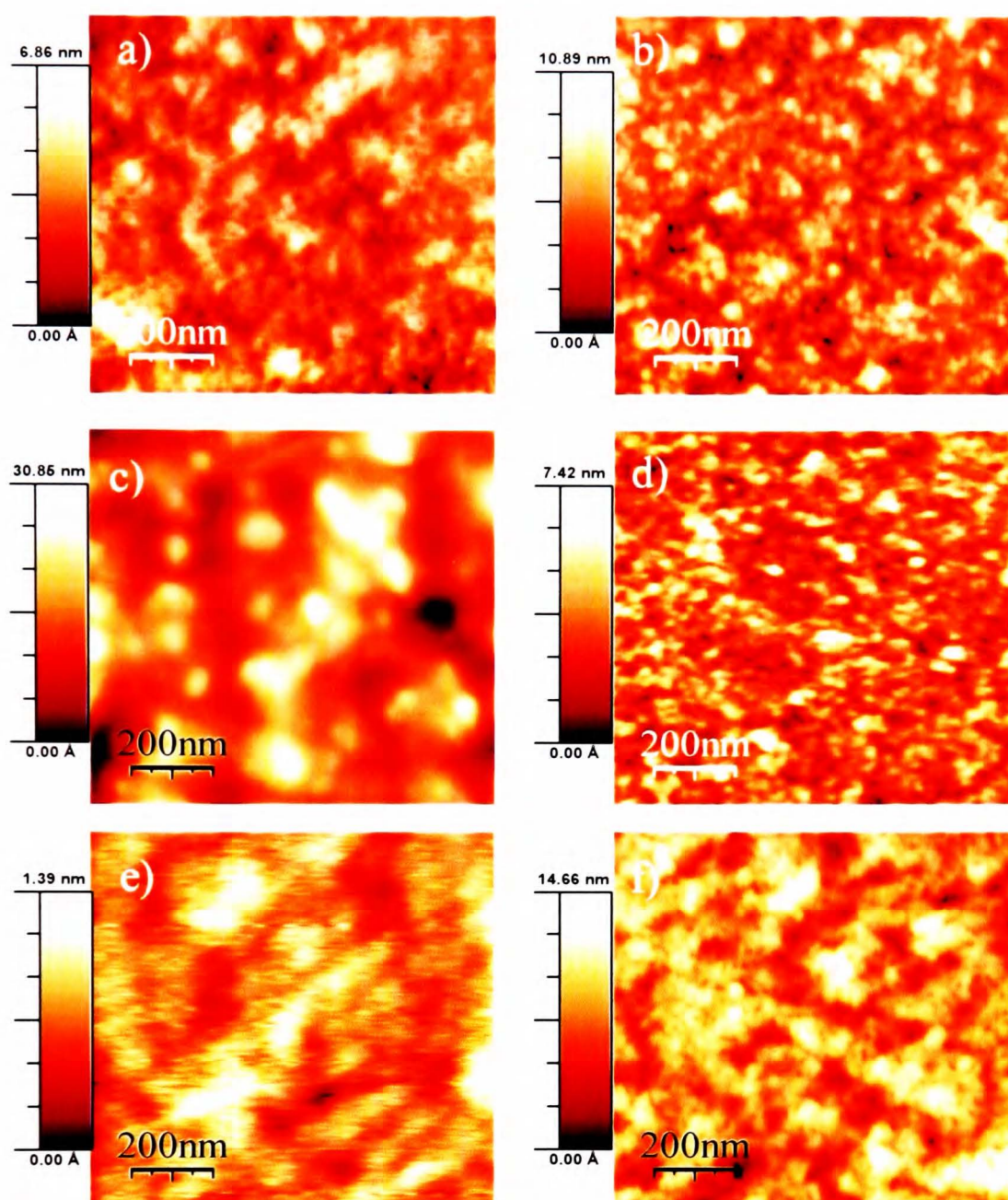


Figure 4.1 1 μm x 1 μm AFM images of a) PET, b) HS PET, c) HS PET_P, d) F-PET, e) amorphous PET and f) PEN.

Table 4.2 Surface roughness values for polyester substrates.

Substrate	R_q (nm) (1 μm x 1 μm scan)
PET	0.9 ± 0.1
HS PET	1.5 ± 0.1
HS PET_P	6.2 ± 1.0
F-PET*	1.0 ± 0.1
aPET	0.2 ± 0.05
PEN	1.9 ± 0.2

*In regions with no filler particles

Table 4.2 shows differences in the surface roughness for the various films. The amorphous PET surface is the smoothest with an R_q of only 0.2 nm. The biaxially drawn

PET is rougher due to its semicrystalline nature and the visible “hills” are probably due to crystallites as previously suggested in the literature [174] – this structure is also evident between filler particles on the filled PET film. The heat stabilisation process is found to roughen the surface by 50% which is probably due to increased crystallisation at the surface and which is characterised by a greater number of discrete features in the 30-50 nm size range. The accompanying phase images show more clearly the presence of the crystalline features on the heat stabilised film (Figure 4.2).

The addition of a primer layer to the HS PET significantly roughens the surface to 6.2 nm. The coating thickness is of the order of 40 nm thick and such a roughness value would suggest uneven coverage of the acrylate on the film. The primer is deposited as an emulsion of polymer particles in aqueous solution (latex), leading to a lumpy, rough coating with what appears to be particles embedded in some sort of matrix. Phase imaging suggests that the coverage of the film is complete.

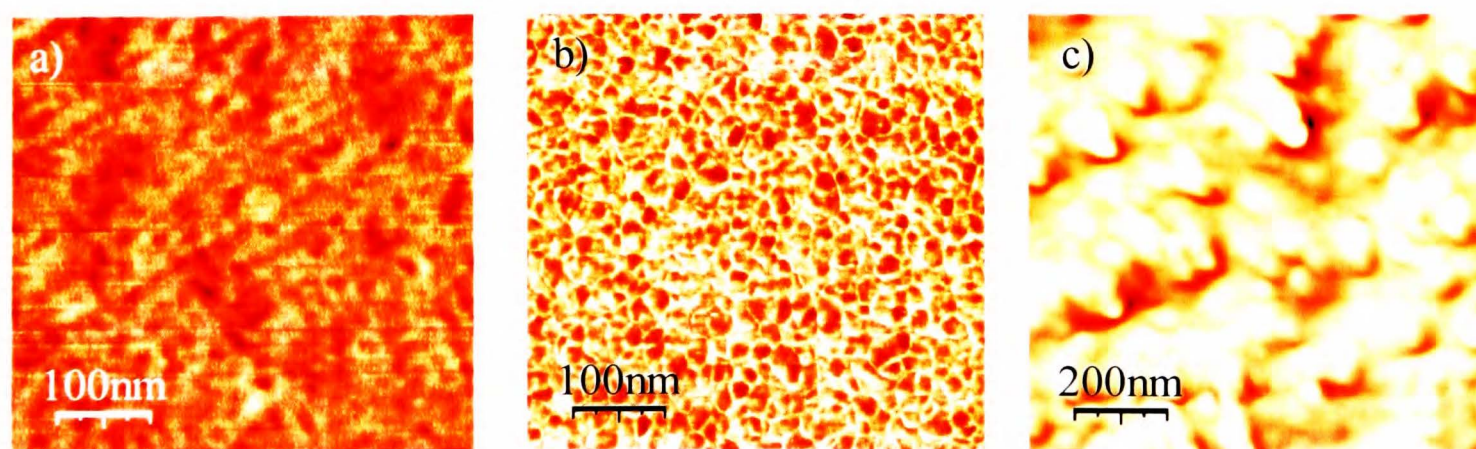


Figure 4.2 Phase images of a) PET, b) HS PET and c) HS PET_P. Z scale is 5° for images a) and b) and 40° for image c). The whiter the feature the greater the phase lag.

Although the rms-roughness is a useful measure of the surface topography, care must be taken when quoting a value so that the scale at which the measurement is taken is also given. The reason for this is two fold – first, in the case of the filled film it is easy to “miss” large features, such as particles, with small scans but when the sampling area is increased more large scale features are observed and the roughness increases. The second is that surfaces often have the property of self affine scaling [222, 223] – that is when the scale of viewing is increased in one or two axes, the 3rd axis (or a statistical measure of it) increases by a different degree. This is expressed mathematically as [224]:

$$\langle |h(X_1) - h(X_2)| \rangle \sim x^H \quad x = X_1 - X_2 \quad (4.2)$$

where the left hand term represents the roughness of the surface, x is the length scale over which the measurement is taken and H is the Hurst exponent, sometimes known as the roughness exponent in the literature. The value of H ranges from 0-1 and is a measure of how the roughness scales with changes in the scale of measurement [225]. According to Lapique *et al.* [226] it can also give an indication of the lateral scale of the topography but not of the scale of the roughness. It is calculated by plotting a graph of roughness against scale (in the case of AFM the scan width) on a double logarithmic scale and is simply the gradient.

An example of the effect of scale on the roughness measurements can be taken from the filled and unfilled PET surfaces. Table 4.3 shows that increasing the scale of measurement for a filled PET surface has a much larger effect on the roughness value

than for the plain PET, due to the detection of more filler particles as the scale increases. The accompanying Hurst exponent is larger for filled PET than for PET or the other substrates which all have relatively low values of H, showing that the roughness value is more affected by scale (in the range sampled) and that the dominant surface features responsible for the roughness are spaced further apart on the filled film.

Table 4.3 Effect of scale on roughness.

Scan width (μm)	PET R_q (nm)	F-PET R_q (nm)
50	2.0	39.0
20	1.5	19.6
10	1.3	5.8
5	1.1	4.0
2	0.9	1.7
1	0.9	1.0
	H = 0.22	H = 0.96

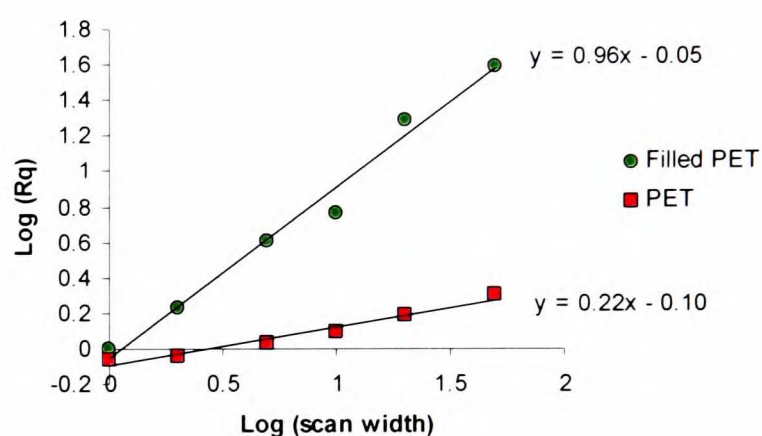


Figure 4.3 Hurst Plot for two polyester surfaces.

At higher scan sizes the R_q values for filled PET are so much higher due to the presence of the filler particles protruding from the surface and depressions in the polymer film surrounding them, similar to observations made by Beake *et al.* [175]. Figure 4.4 shows an AFM image of the filler particles on the surface as well as dark areas corresponding to troughs in the film. Also shown is the size distribution of the filler particles, determined by counting and measuring the diameter of the particles from a number of AFM images at different scan sizes so that the total area sampled is $20\,000\ \mu\text{m}^2$. The mean particle diameter is found to be between 1.4 and $1.7\ \mu\text{m}$ and the particle density $4000\ \text{mm}^{-2}$. The high roughness of this film is beneficial in terms of antiblock functionality, but may pose

problems for vacuum coating deposition unless the coating is particularly conformal to the substrate.

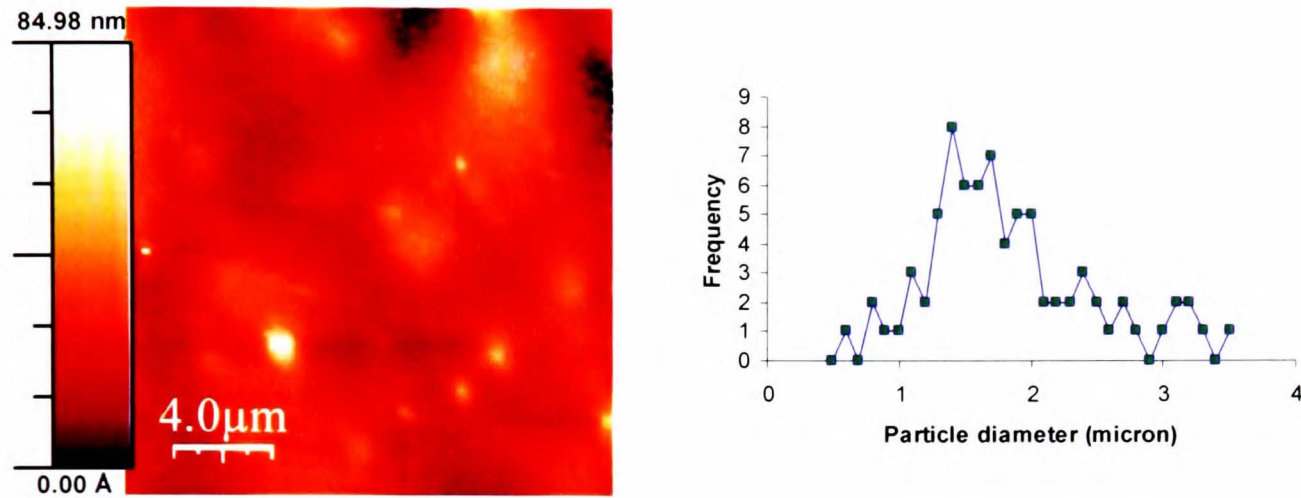


Figure 4.4 20 x 20 μm AFM image of filled PET film and the size distribution of the china clay particles at the surface of this film.

To measure the lateral scale of the surface roughness the use of an autocorrelation function (ACF) was attempted, as this has found utility in characterising the topography of amorphous systems such as polymers [224, 227, 228]. For a random rough surface, ACF is given by:

$$ACF(\tau) = \lim_{L \rightarrow \infty} \frac{1}{L} \int_{-L/2}^{L/2} z(x)z(x + \tau)dx \quad (4.3)$$

Where $z(x)$ is the height distribution of a surface with length $2L$ and τ is a distance between two random height measurements [229]. For a purely random surface ACF will decrease monotonically from its maximum value $ACF(0)=1$ to $ACF(\infty)=0$. If on the other hand the surface is a periodic one with period λ , then $ACF(m\lambda)=1$ for any integer m . Hence a random surface that contains a weak non-random periodic component will result in ACF having local maxima, as is schematically illustrated below.

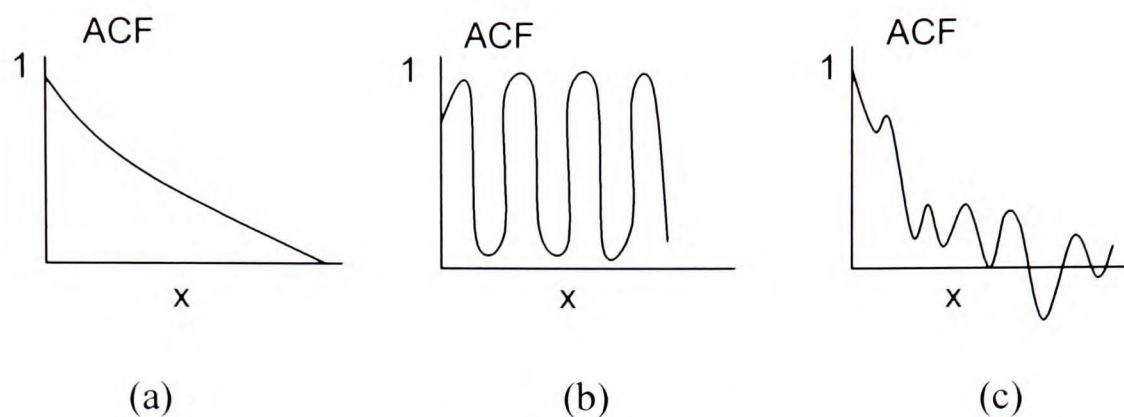


Figure 4.5 ACF of (a) a purely random surface, (b) a periodic surface, (c) a random surface with a periodic component.

It is usual for the ACF to be simulated by an exponential function given by [224, 227]:

$$\text{ACF}(\tau) = \exp(-\tau/T) \quad (4.4)$$

Where T is the characteristic lateral correlation length and is defined as the distance in which ACF drops to a value e^{-1} , when correlation in arrangement of the surface features is lost. So far the ACF has been found useful in detecting and characterising regular distribution patterns in surface features, such as rubber particles in polymer sheets [229].

In the case of the polyester film surfaces examined in this work, the autocorrelation function was calculated using a MAPLE-based algorithm described elsewhere [224]. Unfortunately it failed to find any correlation in height and the function takes a form similar to the monotonic decay in Figure 4.5(a). This is a clear indication of the random nature of the surfaces examined and also demonstrates the difficulty in quantitatively describing the polymer surface.

4.3 Surface Chemistry

The chemistry at the surface of the films can be probed by XPS to give a picture of the elemental composition and chemical bonding in this region. The carbon 1s spectrum is usually examined in the case of polymer films as this gives the most information on chemical bonding, due to easily detectable shifts in binding energies caused by bonding to electronegative atoms, such as oxygen. The spectra for both PET and PEN are shown in Figure 4.6. Also shown is the C 1s spectrum for the primer acrylate layer.

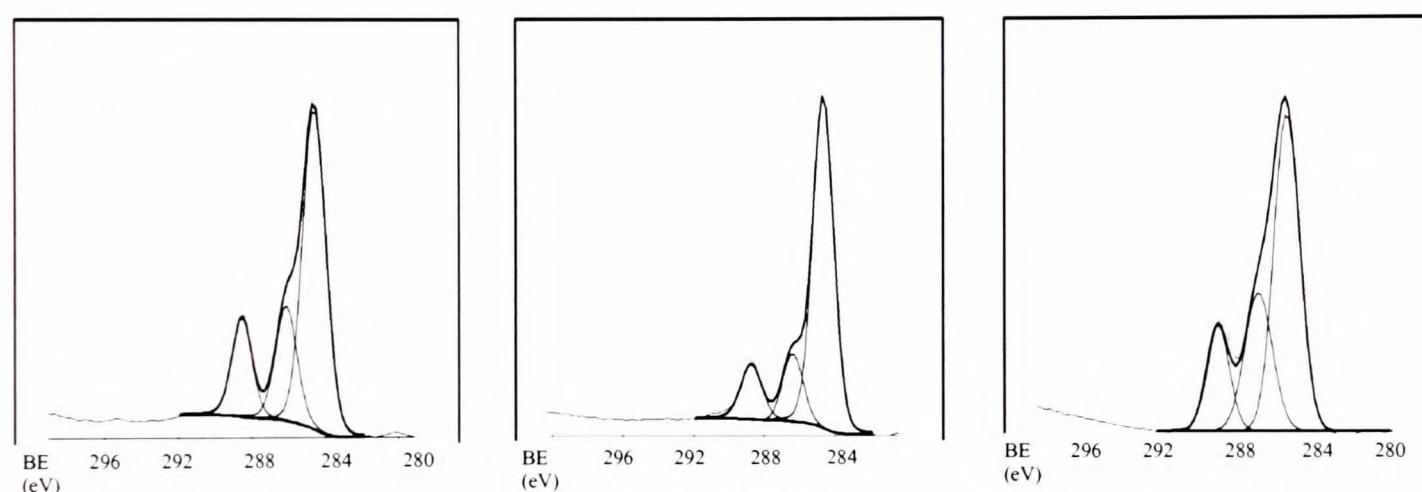


Figure 4.6 XPS C 1s spectra for (l-r) PET, PEN, acrylate primer.

For all the substrates there are three bonding environments for carbon: C-C, C-O and O=C-O [65, 230, 231]. Their binding energies and abundance at the surface are displayed in Table 4.4, and the atoms in the chemical structure of the polyester corresponding to each BE are labelled in Figure 4.7. When peak fitting to the convoluted C 1s spectrum, parameters were kept as consistent as possible, to allow meaningful comparison between samples. A maximum peak FWHM (full width at half maximum) value of 1.8 was allowed, the peaks were Gaussian with 10 % Lorentzian character and

peak positions were fixed, with the C-C peak acting as a reference at 284.7 eV. It is worth noting that the filler particles have no effect on the surface chemistry – despite protruding from the film they are covered by a thin “skin” of polymer and the XPS spectra show no difference to those of plain PET. It is common in the literature for a “shake-up” peak at ~ 292 eV to be observed due to π - π^* transitions in the aromatic system [65]. The relatively low resolution of the spectrometer used in this study meant that this feature went undetected.

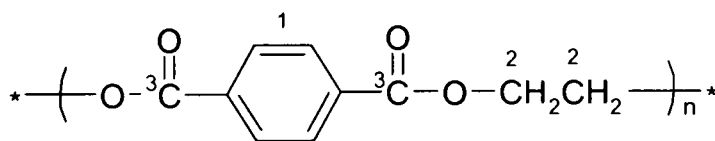
Table 4.4 Composition of polyester film surfaces (theoretical composition in brackets).

Substrate surface	1. C-C [%] (284.7 eV)	2. C-O [%] (286.3 eV)	3. O=C-O [%] (288.5 eV)	Water contact angle
PET	65 (60)	19 (20)	15 (20)	78°
PEN	73 (72)	14 (14)	13 (14)	83°
Acrylate	57 (60)	26 (20)	17 (20)	67°

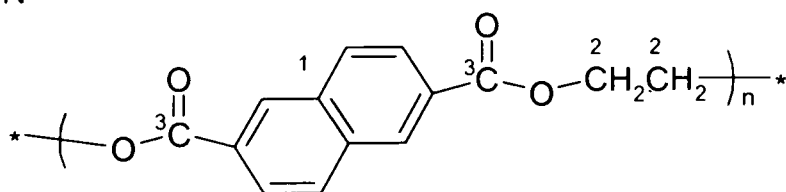
PEN is found to have the correct ratio of bonding groups as expected from its chemical structure, with more carbon and less oxygen than PET. This is reflected in the contact angle of water measurements on the surface of these substrates, with water droplets forming an angle of 78° to the horizontal on PET and an angle of 83° on PEN, and is due to the slightly more hydrophilic nature (higher density of oxygen-containing functional groups) on PET than PEN. PET has slightly more carbon on the surface than expected and less of the ester group, which could partly be due to carbon contamination on the film surface. The roughness of the substrate was found to have no significance on the contact angle of water on the PET surfaces as the aPET, BD PET and filled PET had contact angles within error of each other.

The acrylate primer layer is a terpolymer of mainly methyl methacrylate (MMA) and ethyl acrylate (EA) with a small amount of methylacrylamide (MA). The methylacrylamide contains nitrogen and this is detected at 2% in the elemental composition, the expected composition of this film does not take into account this monomer due to its low quantity and the lack of previous characterisation in the literature. There is more oxygen contained in this surface than PET and the contact angle of water on it is accordingly lower at 67°. There seems to be a marked imbalance in the quantity of C-O compared to a lower than expected degree of C=O bonding for this surface, which may be explained by the presence of surfactants and crosslinking agents in the acrylate layer.

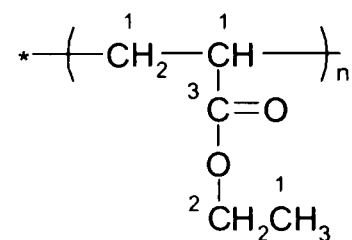
a) PET



b) PEN



c.1) Acrylate - ethyl acrylate



c.2) Acrylate - methyl methacrylate

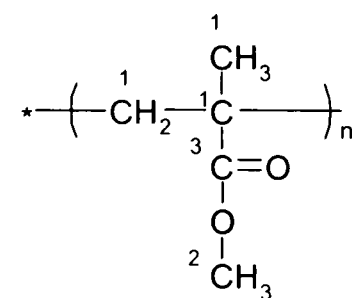


Figure 4.7 Chemical structure and assignment of binding energies (see Table 4.4) for polyester film surfaces.

4.4 Surface Glass Transition Temperature (T_g)

The glass transition temperature is the temperature at which the glassy state of the amorphous polymeric material adopts a liquid-like character and is manifested in an abrupt change in material properties, such as Young's modulus and density at that given temperature. The value or range of temperature is dependent on many factors, including the orientation of the amorphous phase, processing history, presence of crystallites or impurities in the amorphous matrix, the rate of temperature increase and the measurement technique. Therefore reported values of the T_g of PET vary significantly from 60-120°C [232]. The vacuum deposition of a coating inevitably leads to high energy species bombarding the substrate with a subsequent heating effect, which is particularly relevant for PET films as the T_g is in the typical range of deposition temperatures [233, 234]. The heating is caused by condensation of the deposited species on the substrate, bombardment by electrons, photons and ions and radiant heat from the target/boat for sputtering/evaporation. In web coaters the deposition drum is usually chilled to $\sim -20^\circ\text{C}$ to cool the substrate, although this only has limited success due to poor thermal conductance of the polymer and a gap of air between polymer and drum [235].

The T_g at the surface of polymeric films has been found to be less than that of the bulk by a number of authors [236, 237] and although the polyester films are semicrystalline it is expected that the amorphous regions present at the surface will undergo thermally induced modification during deposition. It is therefore useful to know the surface T_g of the given films so that the thermal effects of the deposition may be considered.

To measure the T_g at the surface a method based on AFM was used [212], described in Chapter 3. By repeating force-distance plots at increasing temperature and plotting snap-off displacement as a function of temperature, the T_g is determined at the point at which the gradient of the plot changes. This is shown for PET below in Figure 4.8(a) where a value of 80°C is measured. This is greater than reported values of surface T_g and is most likely due to increased orientation and the constraining effect of crystallites in the BD film, which act as tie points and physical obstacles to the motion of the amorphous regions [238, 239]. At temperatures greater than 90°C crystallisation of the surface was apparent as the snap-off displacement suddenly decreased. Attempts to measure the T_g of the amorphous regions at the surface of the HS PET film were thwarted by the fact that the tip repeatedly struck crystallites (characterised by a much lower snap-off displacement) and there were very few amorphous regions to sample. This is further evidence of greater surface crystallinity for the HS PET film.

PEN was found to have a surface T_g of 118°C, almost 40°C greater than PET and will be much less affected by the thermal conditions during deposition. For both PET and PEN the surface and bulk T_g (as measured by DTF) are very similar. On the other hand the primer has a low surface T_g of only 50°C (Figure 4.8(b)). As mentioned earlier it is a terpolymer made up primarily of ethyl acrylate and methyl methacrylate, whose homopolymers have T_g of -8°C and 105°C respectively [232], so a measured value somewhere between these two bounds seems reasonable and suggests a roughly similar proportion of each monomer in the film.

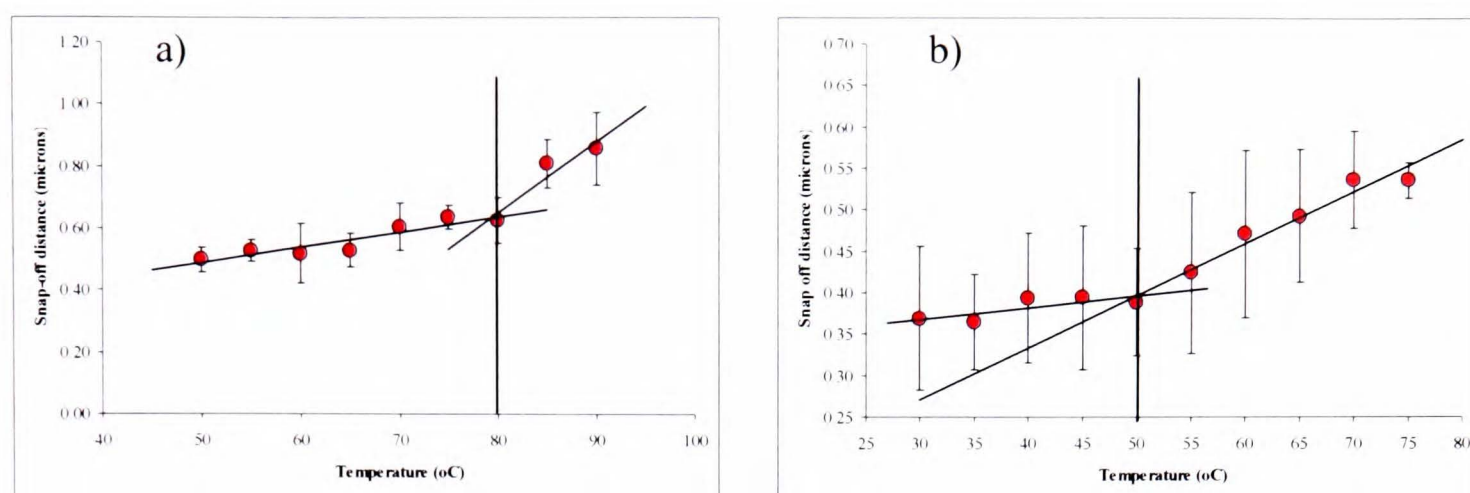


Figure 4.8 Surface T_g determination for a) PET and b) acrylate primer.

4.5 Mechanical Properties

The mechanical properties of the polyester films were examined using tensile testing of the films in the transverse direction. Stress-strain curves were produced for four substrates - PET, PEN, HS PET and the filled PET film at a constant extension rate of 0.4 mm min^{-1} . The true stress, σ_T , is plotted as a function of strain to account for the change in cross sectional area during extension. The true stress is valid in cases where the volume of the specimen remains constant and is given by the expression:

$$\sigma_T = \sigma_N(1 + \varepsilon) \quad (4.5)$$

Where the nominal stress, $\sigma_N = F/A$, F is the applied force, A is the cross sectional area and ε is the tensile strain.

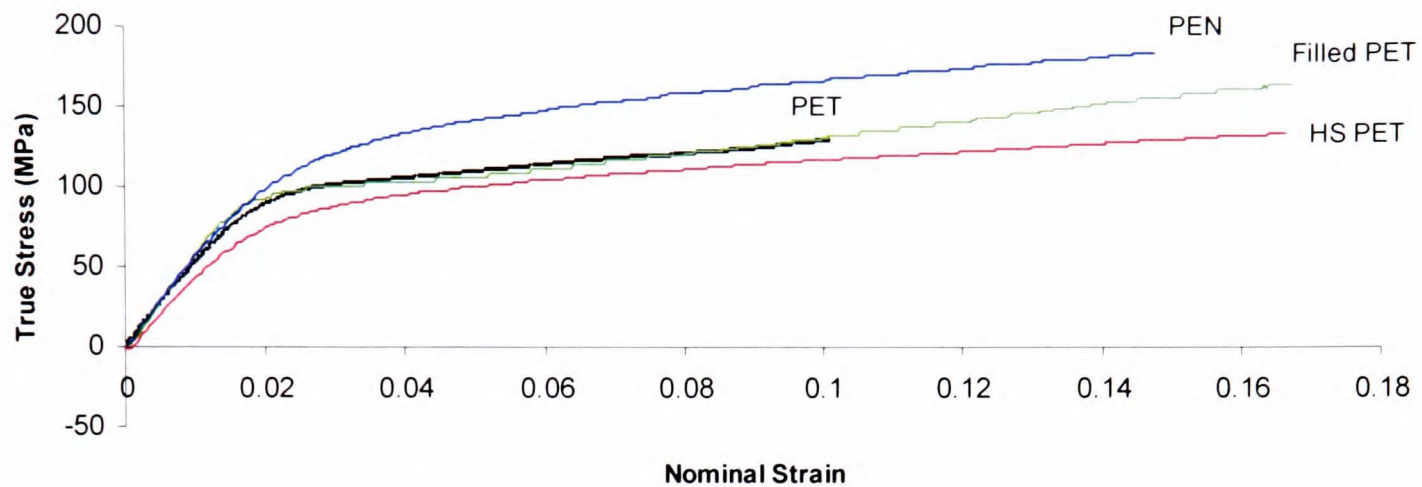


Figure 4.9 Stress-strain curves for polyester films.

The stress-strain curves in Figure 4.9 present several interesting points. First of all it appears that the plain PET and filled PET have very similar properties, with yield at about 100 MPa and 2.5% strain. Instead of completely plastically yielding these films show a small degree of strain hardening almost immediately after the yield point, due to their high crystallinity and similar observations have been made in the literature [29, 34, 161].

The HS PET film is found to have inferior mechanical properties to the plain PET. It has a lower Young's modulus, a lower yield stress and appears to strain harden less in the strain regime examined here. The heat stabilisation process involves unwinding and re-heating the film (held at virtually zero line tension, to enable it to shrink) at temperatures in Regime III described by Gohil [29] (in the region of 200°C) which is expected to have two main effects on the structure of the film. The first is that metastable crystals melt and larger crystals form as a result of crystal growth and recrystallisation, leading to a small increase in crystallinity. The second is that the amorphous phase completely relaxes and the film is "pre-shrunk" so that minimal shrinkage occurs during subsequent heating.

This relaxed amorphous phase is then responsible for the lower modulus and yield stress as it must be reoriented under tension. The reduced stiffness of the HS film may also suggest that the increased crystallinity observed at the surface by AFM and force-distance measurements may not be present throughout the bulk of the film, probably due to the fact that the T_g is lower at the surface leading to a higher degree of crystallisation there than in the bulk. Crystallisation at the surface has been found to occur more quickly and at lower temperatures than in the bulk for PET by a number of authors [240, 241] albeit for amorphous spin coated films at temperatures of around 100°C. The film is 175 μm thick meaning that the average temperature experienced in the bulk may be less than that at the surface by some margin, due to low thermal conductance, leading to a tiered structure with increased crystallinity at the surface created by thermal gradients. However, there is no direct experimental evidence for differential crystallinity through the thickness of the film.

Finally, as expected from the literature [10, 25, 63], PEN exhibits a greater modulus and yield stress than PET. The improved properties are mainly due to the increased bulk of the naphthalene ring in the PEN structure. The mechanical properties of all the films are summarised in Table 4.5. Also included are shrinkage data supplied by DTF, obtained in conditions relevant for vacuum deposition of coatings and which demonstrate the reduced shrinkage for filled PET, PEN and particularly the HS PET over the standard PET grade. It is a useful property to know as substrate shrinkage during deposition is responsible for contributing to stresses in the coating [155].

Table 4.5 Mechanical properties of selected polyester films.

Substrate	Modulus (GPa)	Yield strain (%)	Yield Stress (MPa)	Shrinkage (%) after 5 min at 190°C
PET	4.8	2.5	100	TD 3, MD 3
Filled PET	5.3	2.5	100	TD 1, MD 3
HS PET	4.5	3.0	90	TD 0.03, MD 0.1
PEN	6.1	3.5	130	TD 0.8, MD 0.8

4.6 The Importance of Substrate Selection

The general theme of this thesis is to demonstrate that modifying a polyester substrate can improve the properties of the coating deposited upon it. However, in this short section I will demonstrate how the wrong choice of substrate could lead to a deterioration in the properties of the deposited layer. Thin TiO_x coatings deposited on BD PET, aPET and BaSO_4 filled-PET by reactive magnetron sputtering [93] were examined. The latter substrate was loaded with 18 weight % BaSO_4 particles and as a consequence was white and opaque with a high surface roughness (due to voiding surrounding the particles). Ultimately, the investigation into TiO_x as a gas barrier material was frustrated by technical difficulties surrounding the deposition process and consequently the finer details of the deposition technique itself are ignored here. A few pertinent observations were made regarding the substrates however, which will be described as follows.

4.6.1 Deposition process

The substrate was held 11 cm from the Ti target in a vacuum chamber of base pressure $\sim 10^{-2}$ mTorr. A flow rate of Ar of 70 sccm was used to strike a plasma at 850 W

(Advanced Energy PE2500 medium frequency (40 kHz) AC power source) and the flow of oxygen was controlled using Plasma Emission Monitoring (PEM), described by Safi [98], and varied between 15 and 25 sccm. The deposition pressure was 2.6 mTorr. By conducting depositions with these conditions for different times the deposition rate could be extrapolated from a thickness v deposition time plot, where the thickness of the films over 50 nm were obtained using a Rudolph Auto EL-II Ellipsometer (wavelength 632.8 nm, 70° incidence angle). For this analysis reflective substrates are required and so silicon wafers were coated concurrently with the polymer film.

The deposition rate was found to be 0.1 nm s^{-1} and the refractive index of the films was 2.1, suggesting that the TiO_x is amorphous. Thicknesses of 10 nm and 50 nm were chosen for analysis as these are often the quoted lower and upper limits for the critical thickness, T_c , of gas barrier coatings.

4.6.2 Microstructural studies

AFM images taken of 10 nm thick TiO_x show that the coating on the aPET displays a smoother morphology made up of finer grains than for the BD PET (Figure 4.10). This is probably a result of the smoother surface of the underlying substrate, and is a desirable property as it is generally believed that a smoother coating has good barrier properties. However, the micrographs for 50 nm thick TiO_x exhibit an extremely rough surface on the aPET substrate with a folded morphology of ridges and troughs. This is a clear indication that the substrate was undergoing heating during deposition and that the temperature was in the vicinity of the T_g (exacerbated by no substrate cooling and the

short distance from target to substrate). As the amorphous layer relaxed significantly it led to shrinkage of the film which was observed by eye after the samples were removed from the deposition chamber. The extra time required to deposit the thicker film obviously results in harsher thermal conditions which alter the structure of the amorphous film significantly. On BD PET the 50 nm thick coating has the same morphology as that of the 10 nm one and little shrinkage is observed, due to the relatively high degree of crystallinity of the film introduced in the drawing process.

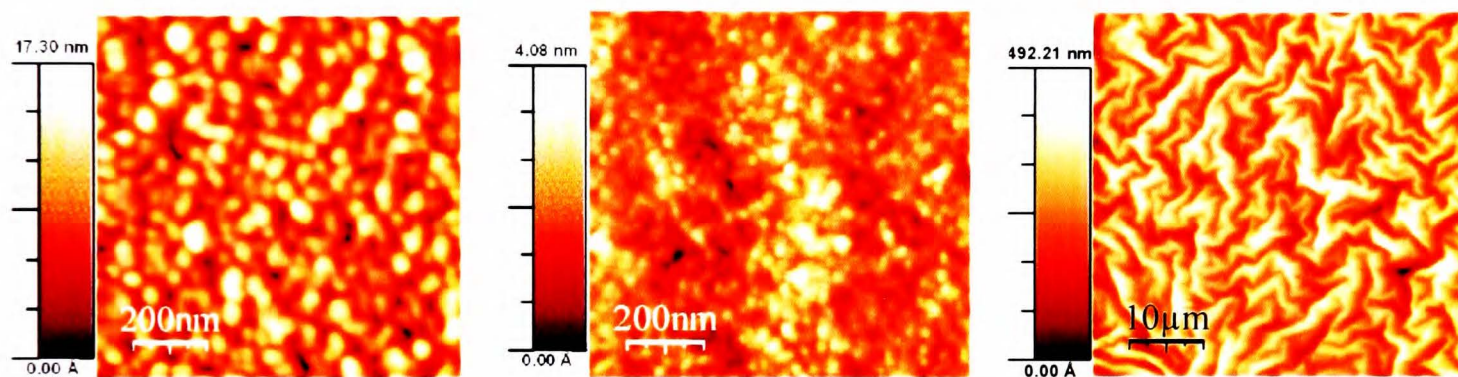


Figure 4.10 AFM images of the microstructure of (l-r) 10 nm TiO_x on BD PET; 10 nm TiO_x on aPET and 50 nm TiO_x on aPET (50 μm x 50 μm image).

AFM and SEM images of a 50 nm thick TiO_x coating on the BaSO_4 filled PET film clearly show a number of holes in the coating surrounding the filler particles. These result from atomic shadowing [101] – the height of the particles prevents uniform coverage of the substrate by the TiO_x as they interfere with the flux of approaching sputtered particles. Such defects are expected to lead to a poor barrier capability and could be reduced in number by rotating or tilting the sample during deposition, or by increasing the number of sputtering targets.

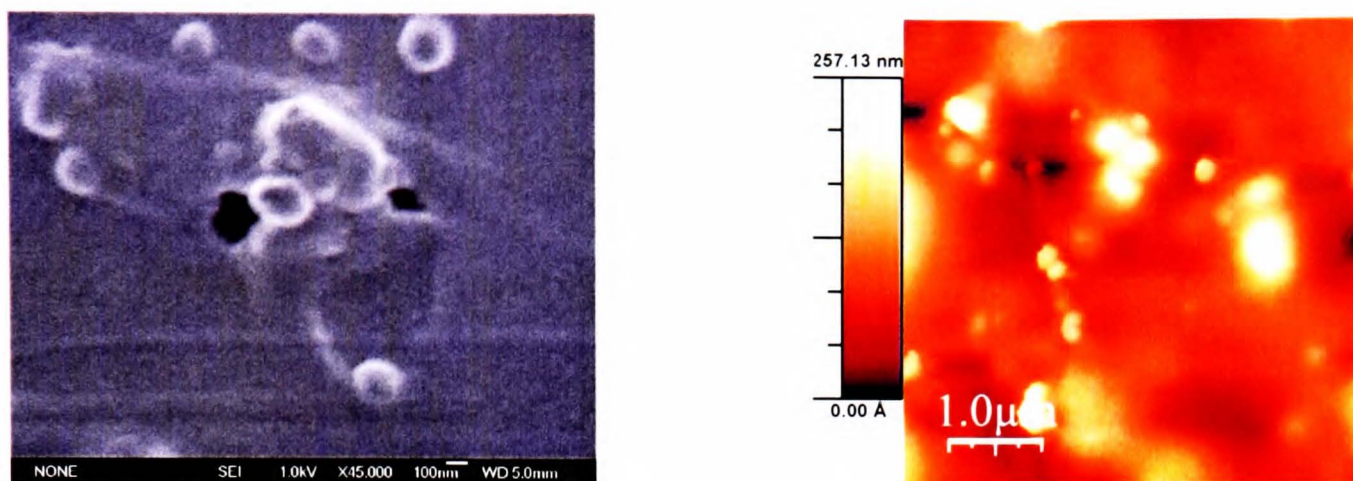


Figure 4.11 Left, SEM micrograph of 50 nm TiO_x on BaSO_4 filled PET and right, a $50\ \mu\text{m} \times 50\ \mu\text{m}$ AFM image both showing defects in the coating.

4.7 Summary

The properties of polyester films can be dramatically altered during manufacturing and a survey of several different films has shown this to be the case. The films studied were chosen, with guidance from DuPont-Teijin Films, so that they may display superior performance in composites than a standard BD PET film. The main points concerning the substrates can be summarised as follows:

- An additional heat stabilisation stage causes the HS PET to roughen at the surface due to increased crystallisation. The relaxed amorphous phase that the heat treatment produces results in a lower modulus and yield stress, but importantly the film undergoes very little shrinkage upon heating.
- A thin acrylate primer layer deposited on the HS PET causes the surface to roughen dramatically, probably due to an uneven coverage. The surface has more

oxygen present and a lower contact angle of water, suggesting that it contains a higher density of functional groups than PET.

- Filler particles significantly increase the roughness of the film and are covered by a thin film of polymer. Preliminary studies of sputtered TiO_x coatings on a BaSO_4 filled substrate suggest that the protruding filler particles promote the formation of defects by atomic shadowing, a feature not associated with good barriers.
- An amorphous layer coextruded onto a PET film has the smoothest surface. A 10 nm thick TiO_x layer on this substrate shows a promising microstructure for a gas barrier but as the coating thickness increases to 50 nm (with an associated increase in substrate heating) the aPET significantly relaxes, causing a rough, ridged morphology to form and significant shrinkage of the film is observed.
- PEN, an alternative high performance polyester, has superior mechanical properties to PET including a higher tensile modulus and yield stress. Its surface chemistry has a lower density of oxygen-containing functional groups than PET and is found to be slightly more hydrophobic. Both films have similar surface morphology, although the PEN is twice as rough.
- The surface glass transition temperatures of the acrylate and the PET surface (50°C and 80°C respectively) were measured and are in the range of typical deposition temperatures. Therefore, temperature will be an important factor when

considering how the substrate affects the properties of the coating, as demonstrated by the shrinkage of the aPET during sputtering. The surface T_g of PEN was found to be 118°C and is expected to be high enough so that thermal conditions do not significantly affect the surface structure.

In Chapter 6, the effect that these substrates have on a roll-to-roll PECVD SiO_x coating is closely examined and many of the observations made in this chapter are important in explaining the properties of the polymer-SiO_x composites.

Chapter 5. Vacuum Deposited Coatings on Plasma Treated PET Film

Polymer films have favourable properties for applications such as packaging due to their high strength to weight ratio, flexibility, transparency, chemical resistance and low cost. A disadvantage however is their low surface energy (chemically, most of the polymer is hydrocarbon) and the presence of surface contamination (release agents, oils and low molecular weight oligomers) which often result in poor adhesion to a second material, such as a coating. Poor adhesion is unacceptable in barrier systems as any failure of the composite will result in increased exposure to air of the packaged goods. To improve the surface properties of a polymer film several approaches have been employed including chemical processes, exposure to flames, laser irradiation [242] and ion beam bombardment [243]. The most commonly used method of surface modification at present is a plasma treatment, usually under vacuum prior to deposition, although treatments have been recently carried out at atmospheric pressure [189, 244]. The treatments often add chemically functional groups to the surface that enable covalent bonding between the two components of the composite. This is particularly important for polyolefins, for example polypropylene, which are purely hydrocarbon. Although PET is relatively well functionalised at the surface due to the ester groups, plasma treatments are still employed to add further functional groups or to convert the esters to more reactive acid and hydroxyl groups. The main role however, is to etch away contaminants and debris from the surface of the film with the aim of minimising the creation of pinhole defects and

ensuring a good contact between polymer and coating. By altering the identity of the plasma gas, a range of surface specific modifications can be achieved.

Although the plasma treatment of PET, particularly with argon, is well studied in the literature [181-183, 245], less is known about the effect of an oxygen plasma and gas mixtures on the surface properties. Relatively little published work has concentrated on observing the effect of the plasma treatment on the interface and the structure of a deposited film, although some work concerning adhesion and interfacial bonding is reported for metal coatings [133, 156, 199, 246]. In this Chapter I describe how oxygen and argon treatments affect biaxially drawn PET and improve the quality of sputtered aluminium and PECVD silicon oxide films deposited in “batch” coaters (as opposed to roll-to-roll).

5.1 Plasma Treatment of PET

5.1.1 Experimental set-up

All plasma treatments were conducted using an Oxford Instruments PlasmaLab 80+ RIE system, a schematic of which is shown in Figure 5.1. A plasma is generated when a gas is subjected to an electric field, in this case radiofrequency (13.56 MHz) is applied to the cathode, under vacuum. First, natural radiation ionises a small fraction of the gas species and the free electrons are accelerated by the field before undergoing ionising collisions with neutral gas species. This in turn creates further free electrons, leading to an avalanche of collisions that produces a large and equal number of electrons and ions. The

ions are then accelerated across the cathode dark space from the plasma towards the cathode upon which the sample is placed. The ions sputter away surface material, implant themselves in the sample and initiate reaction mechanisms that functionalise the surface.

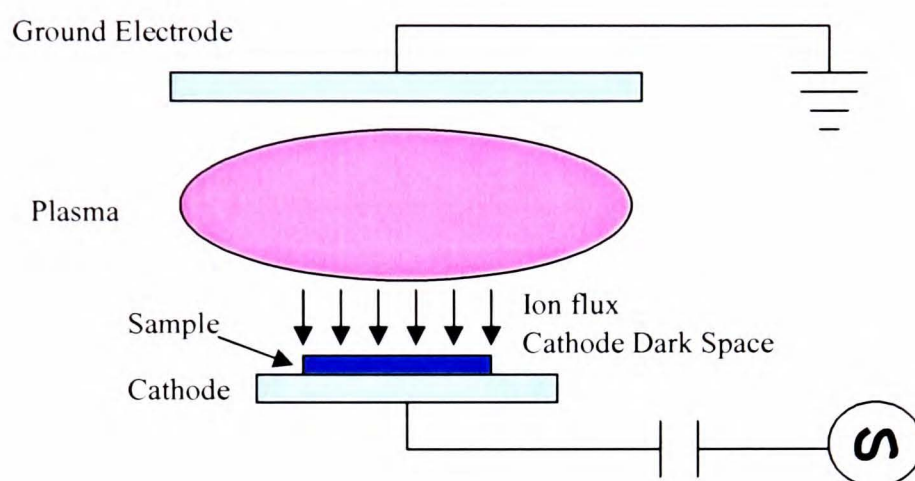


Figure 5.1 Schematic of the plasma treatment apparatus.

Biaxially drawn PET film was exposed to plasma treatment using the gases:

- 1) Oxygen
- 2) Argon
- 3) Oxygen-argon mixture

The operating conditions were a pressure of 100 mTorr and a flow rate of gas of 20 sccm. The power applied to the cathode ranged from 10-200 W and treatment times lasted from 10 s to 160 s. The effects of varying the treatment time and power on the substrate properties are described as follows, using atomic force microscopy, water contact angle analysis and X-ray photoelectron spectroscopy.

5.1.2 Oxygen Plasma Treatment

5.1.2.1 Wettability

Contact angles of water on the treated surface were measured to estimate the hydrophilicity and functionalisation of the surface (no more than five hours after treatment). The sessile drop method is quick and easy to perform, with a more hydrophilic surface having a lower contact angle as the water prefers to spread out on it rather than interacting with itself. The wetting behaviour for three substrates - untreated PET and PET treated with a 20 W and 200 W oxygen plasma respectively, for 80 seconds - are shown in Figure 5.2.

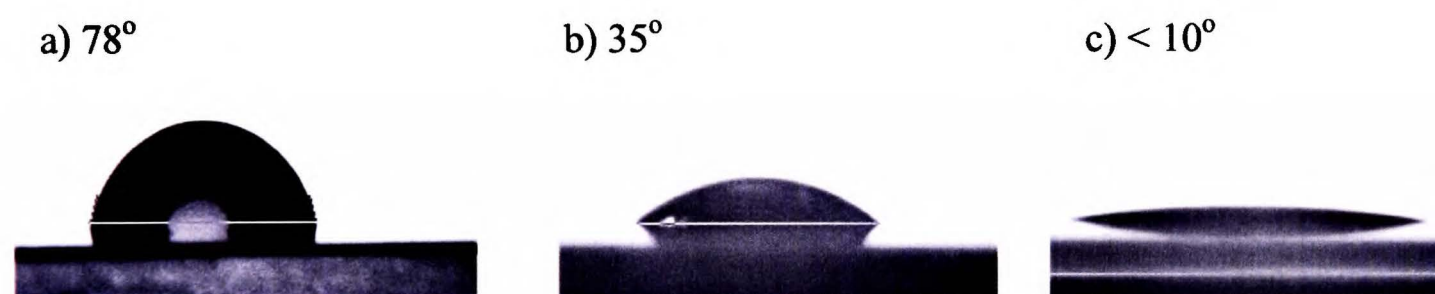


Figure 5.2 Contact angle of water on a) PET, b) PET exposed to a 20 W oxygen plasma for 80 seconds, c) PET exposed to 200 W O₂ plasma for 80 seconds.

It is clear from Figure 5.2 that the 20 W plasma treatment has an effect on the water contact angle, reducing it from 78° to 35°, which is a result of increased functionalisation at the surface. Increasing the power to 200 W over the same time period leads to almost complete wetting of the polymer surface. Next we observe the evolution of the contact angle as a function of treatment time, from 10 – 160 s for two plasma powers.

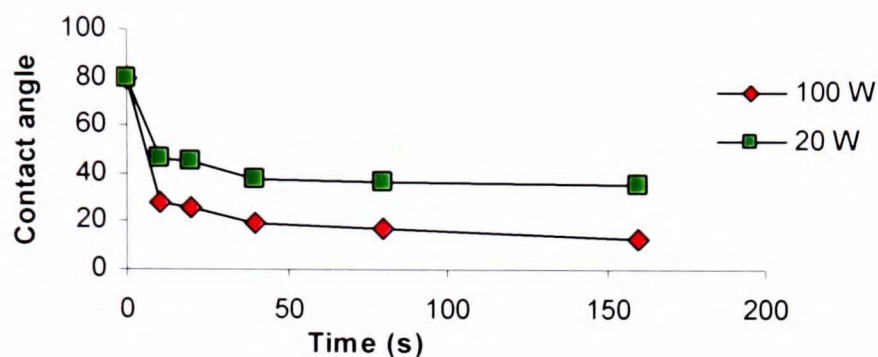


Figure 5.3 Plot of water contact angle as a function of plasma treatment time for an oxygen plasma at different powers.

After just 10 seconds, the plasma has already had a large effect on the contact angle, reducing it by more than 30 degrees. The angle slowly decreases with more time until it levels out at a further 10 degrees lower. It appears that the initial 10 second treatment does a significant job of altering the surface, with further time only modifying it marginally. An increase in the power of the treatment leads to a smaller contact angle, typically 20 degrees less for a power of 100 W compared to a 20 W plasma. This is due to an increase in the energy of the reactive ions in the plasma that are more likely to sputter surface debris (such as hydrocarbon) and to react with the PET surface, creating more functional groups, with both serving to make the surface more hydrophilic.

5.1.2.2 Surface chemistry

XPS is used to probe the chemistry at the polymer surface due to its high resolution and its low sampling depth, typically 10 nm, which allows a good determination of the elemental composition at the surface. In addition, XPS can give information regarding

the carbon bonding environments so we can tell whether functional groups have been added to the surface.

a) Elemental composition

The O:C ratio is considered in this case. As the plasma treatment is conducted it is expected that more oxygen will be bonded at the surface and that the ratio will therefore increase. Figure 5.4 shows that the O:C ratio increases quickly at 10 seconds and then slowly increases to a value of 0.5, from an initial value of 0.38. This initial steep rise and subsequent slower change with time mirrors the contact angle behaviour where a sharp decline in the water contact angle was first observed before a levelling off after 10 seconds.

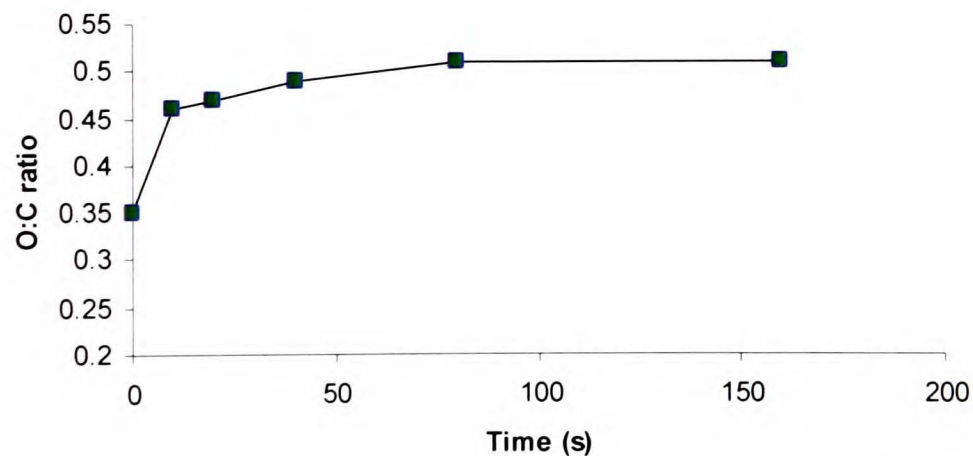


Figure 5.4 Evolution of oxygen to carbon ratio of a PET surface with oxygen plasma treatment time.

b) Carbon bonding environments

The bonding of the carbon atoms at the surface can be examined by looking at the C 1s spectrum of an XPS scan. A carbon peak is typically found at a binding energy (BE) of 285 eV and more precisely a C-C/C-H peak is invariably found at 284.7 eV. When the

carbon is bonded to a more electronegative atom (O, F, N) its bonding peak is shifted to a higher BE, in the case of oxygen by approximately 1.5 eV. Conversely, bonding to a more electropositive atom (Al, Si) shifts the BE lower. The exact position of various functional groups in the C 1s spectrum have been determined over the years and can be found in Briggs and Seah [65]. This allows us to determine to a large extent how the functionality of the surface is modified by a plasma treatment.

Typically, the C 1s spectrum is a convolution of peaks, especially when acquired on a relatively low resolution system as for this work. Using literature values it is possible to deconvolute the spectrum using peak-fitting software. The BE's for various functional groups are shown below:

Table 5.1 Binding energies of carbon species in C 1s XPS spectrum.

Bonding	C-C	C-O-C, C-O(O)H	C=O	O-C=O, HO-C=O
BE (eV)	284.7	286.3	287.5	288.7

These four peaks were thought to be sufficient to fit the spectra for the treated films. Other groups have differentiated between phenols and ether groups [181, 185] (a spacing of ~0.3 eV) but such resolution is impossible in this case. The fitted peaks were always 90:10 Gaussian:Lorentzian as often used in the literature and the peak widths limited to no more than 1.8 eV at FWHM.

Figure 5.5 shows the C 1s spectra for virgin PET and PET exposed to an O₂ plasma for 80 seconds at 20 W.

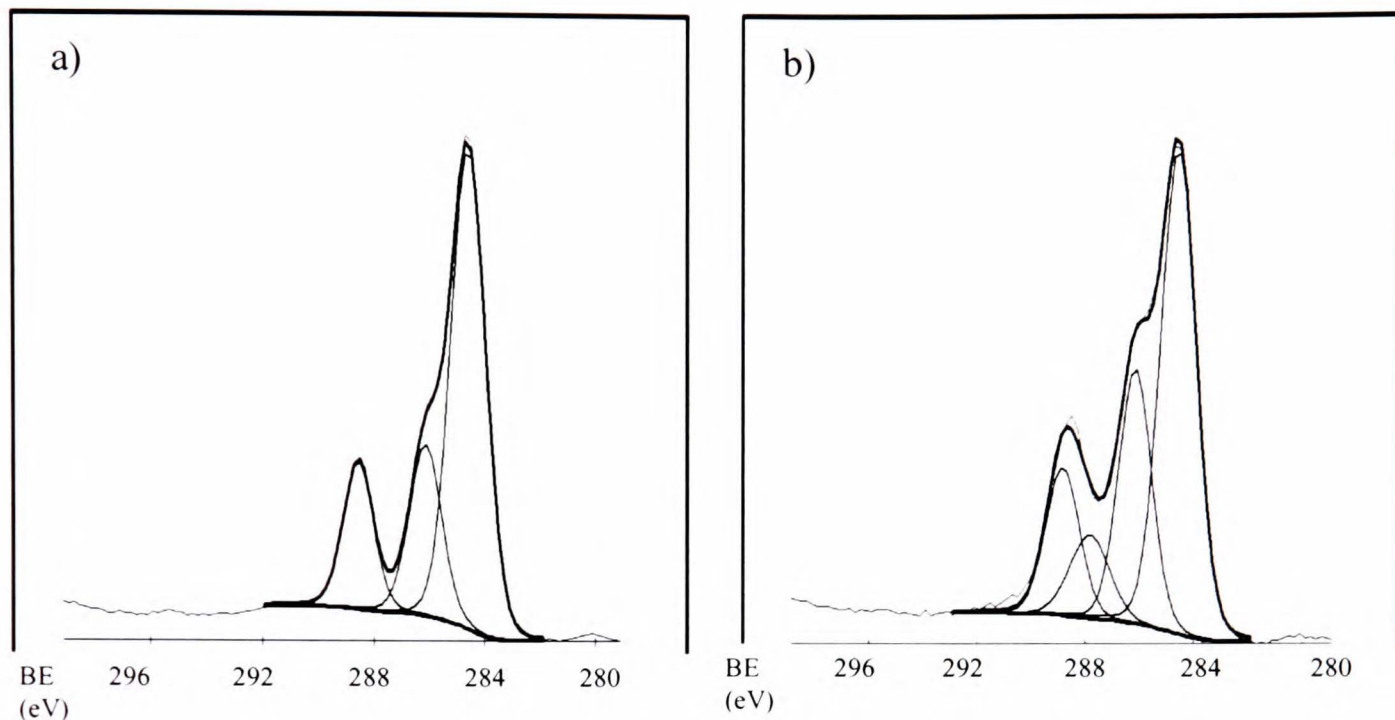


Figure 5.5 C 1s spectra of a) PET, b) oxygen PT PET (20 W, 80 s).

By comparing the two spectra it is immediately evident that the oxygen plasma has introduced an extra functional group, in the form of a carbonyl C=O. Secondly, the peaks for the ether and the ester carbon increase in intensity and broaden, showing the incorporation of hydroxylic and carboxylic acid functions at the treated surface. Such observations explain the increase in the O:C ratio and the increased hydrophilicity of the surface, as demonstrated by water contact angle measurements. If the spectrometer were sensitive enough it would have been interesting to know if the aromatic signal disappeared, which would indicate whether the benzene ring engaged in bonding with oxygen. Previous reports suggest that the “shake-up” peak is unchanged after oxygen [185] and helium treatments [196] so that no functionalisation of the aromatic ring takes place

The evolution of the functional group composition of the surface with time for a 20 W plasma is shown in Table 5.2. It is noticeable that after 10 seconds the C-C signal decreases but the only significant increase is in the carbonyl group concentration. After 20 seconds treatment the other functional groups increase in their composition and reach a plateau at which further treatment results in negligible change of the surface chemistry. This is most likely due to the simultaneous etching and functionalisation of the surface where some kind of equilibrium is reached.

Table 5.2 Chemical composition of PET surface after oxygen plasma treatment (20 W).

Treatment time (s)	C-C (%)	C-O, C-OH (%)	C=O (%)	O-C=O, HO-C=O (%)
0	65	19	0	15
10	60	18	6	16
20	53	22	6	19
80	52	23	6	20
160	54	23	5	18

5.1.2.3 Surface topography

It appears that over a prolonged period, an oxygen plasma can serve to roughen the PET surface, most likely by etching away the softer amorphous regions between the surface crystals. The AFM images below show a PET surface before and after treatment with a 20 W plasma for a 10 and 160 s treatment respectively. A low contact force (0.5 nN) was used to image plasma treated films as it is known that contact mode can drag low molecular weight material, created by the treatment, across the surface leading to poor quality, streaky images [180].

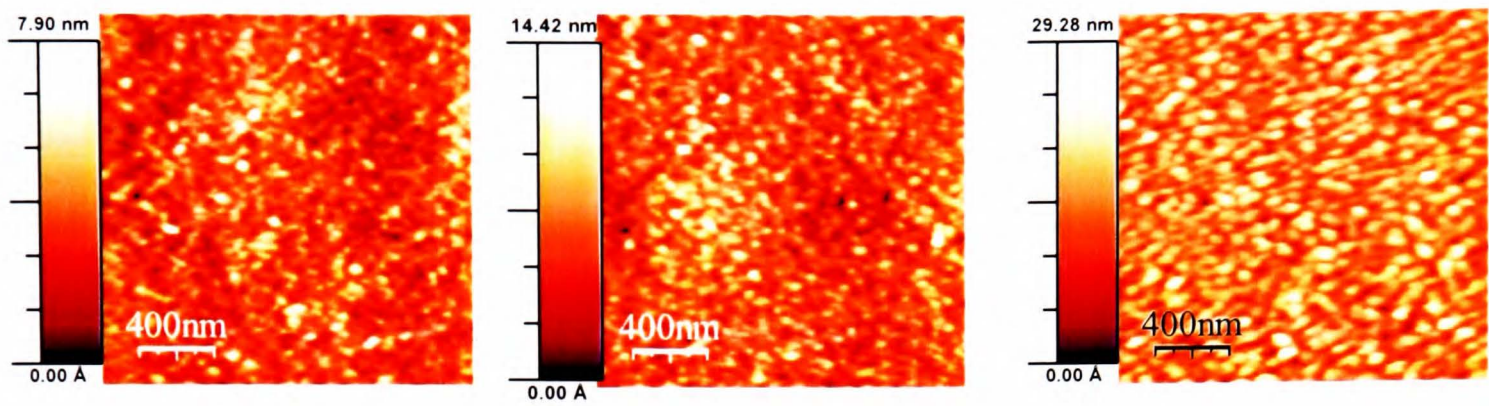


Figure 5.6 2 x 2 μm AFM images of a) PET, b) O₂ PT PET (10 s treat), c) O₂ PT PET (160 s treat).

After 10 seconds of treatment there is little difference between the treated and untreated samples, however after 160 seconds we see a much rougher surface ($R_q = 3.2$ nm) with larger features emerging. Figure 5.7 shows the evolution of roughness with time for the 20 W O₂ plasma treatment.

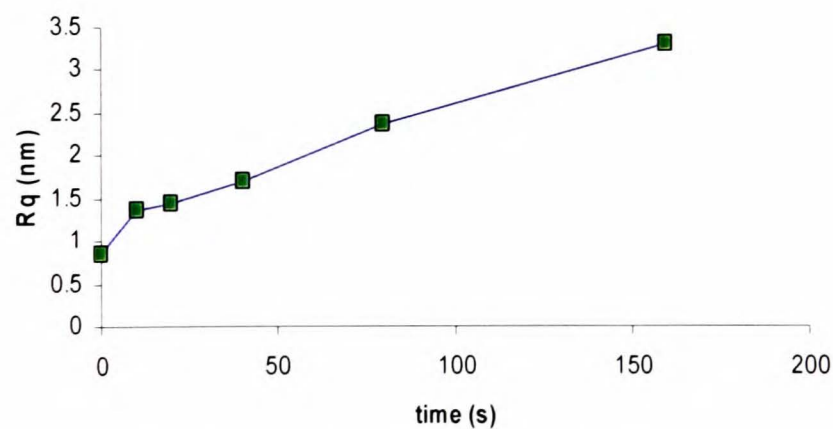


Figure 5.7 Evolution of surface roughness as a function of O₂ plasma treatment time.

It is important to bear in mind that the effects of a plasma treatment do gradually deteriorate with time [181, 196]. Many web coaters have in-line plasma treaters so that the deposition occurs immediately after pretreatment and minimum ageing occurs. Figure 5.8(a) shows that even after a day, the CA of water on the surface begins to increase, the reason being that the oxidised chains at the surface are free to move and rotate and some

of them will migrate into the bulk of the film or react with each other to leave a less polar surface. The surface will also play host to increasing numbers of ambient contaminants over time and it is observed that after a week the CA increases by almost 10 degrees. With this in mind, all deposition onto plasma treated film was conducted on the same day as the treatment to minimise this ageing effect.

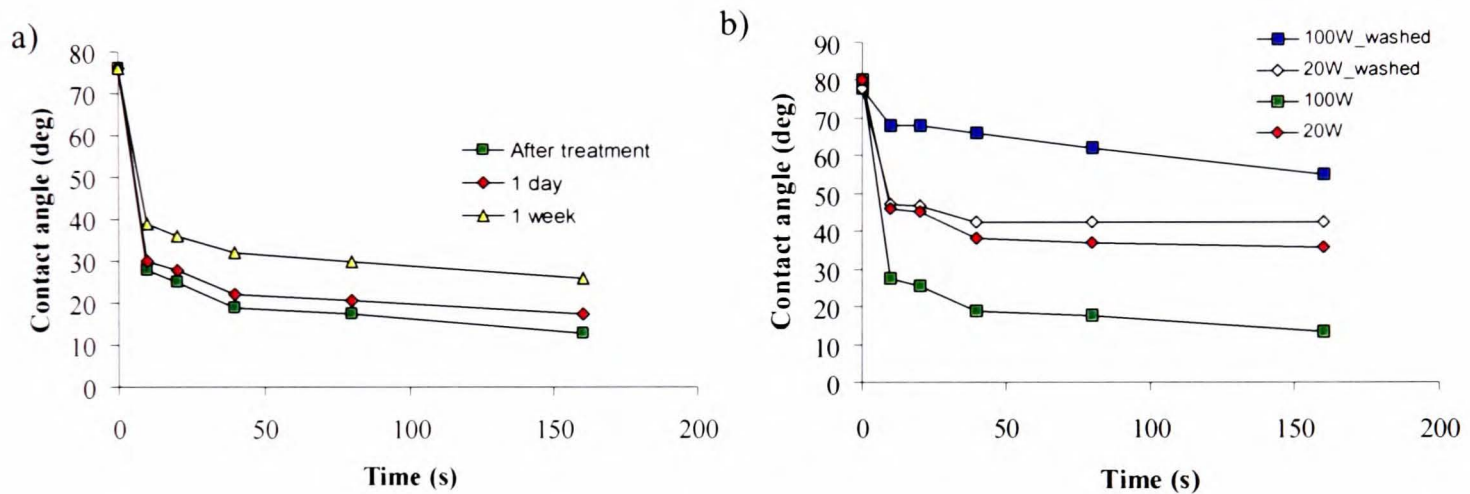


Figure 5.8 (a) ageing of oxygen plasma treated PET film surfaces; (b) washing experiments.

Another factor to consider when plasma treating a surface is the fact that a high power plasma can degrade the surface, resulting in loosely bonded low molecular weight species at the surface [182]. A simple washing experiment, where treated films at powers of 20 W and 100 W were placed into a beaker of acetone and sonically agitated for one minute before drying and testing, was performed with the results shown in Figure 5.8(b). Prior to washing, the 100 W treated surface has a CA of water 20° below that of the surface exposed to the 20 W treatment. After washing the CA is 10° higher than for the surface treated at the lower power and it is clear to see that using a high powered plasma creates more loosely bonded material at the surface – in a sense we are “over-cooking” the

material. At the 20 W level we observe little difference between the washed and unwashed specimens and this power level was chosen for our pretreatments.

5.1.3 Argon plasma treatment

Argon plasma is widely used to clean substrate surfaces before deposition and has the advantage of being safer to handle and manage than oxygen. The intended effect is not to add functionality to a surface but to clean it and cause chemical rearrangements at the surface, thereby increasing the density of chemical groups available for bonding with a deposited species. By first examining the contact angle of water on the treated surfaces a similar pattern emerges to that of the oxygen plasma as an initial decrease in angle is observed and then a plateau is reached after 20 s treatment time. The plateau angle of 50° is greater than that for oxygen by 10 degrees or so for the same power, showing that less functionality is created at the surface, in agreement with Inagaki *et al.* [184].

The differences in surface treatment between Ar and O₂ plasma can be shown using the approach of Owens and Wendt [185, 247] for the surface energies of solids. The main assumption is that the surface energy is the sum of a polar interaction component, γ^p , and a dispersive interaction component, γ^d . Their approach leads to this modified version of the Young Equation [248]:

$$\gamma_L(1 + \cos \theta) = 2(\gamma_L^d \gamma_S^d)^{1/2} + 2(\gamma_L^p \gamma_S^p)^{1/2} \quad (5.1)$$

where θ = contact angle, γ_L is the surface tension of test liquid (mN m^{-1}), γ_L^P is the polar contribution and γ_L^d is the dispersive contribution to the surface tension of the test liquid. γ_S^P and γ_S^d are the respective polar and dispersive components of the surface free energy, γ_S , which is the sum of the two. The components for the liquids are known from the literature but to determine those of the surface, γ_S^P and γ_S^d , two test liquids are required (one polar, one apolar) and so water and diiodomethane were chosen. The polar and dispersive components of the surface energy of the solid were then found by solving the simultaneous equations, yielded by using the two liquids, with the Solver function of Microsoft Excel. The total surface energy is then simply the sum of the two.

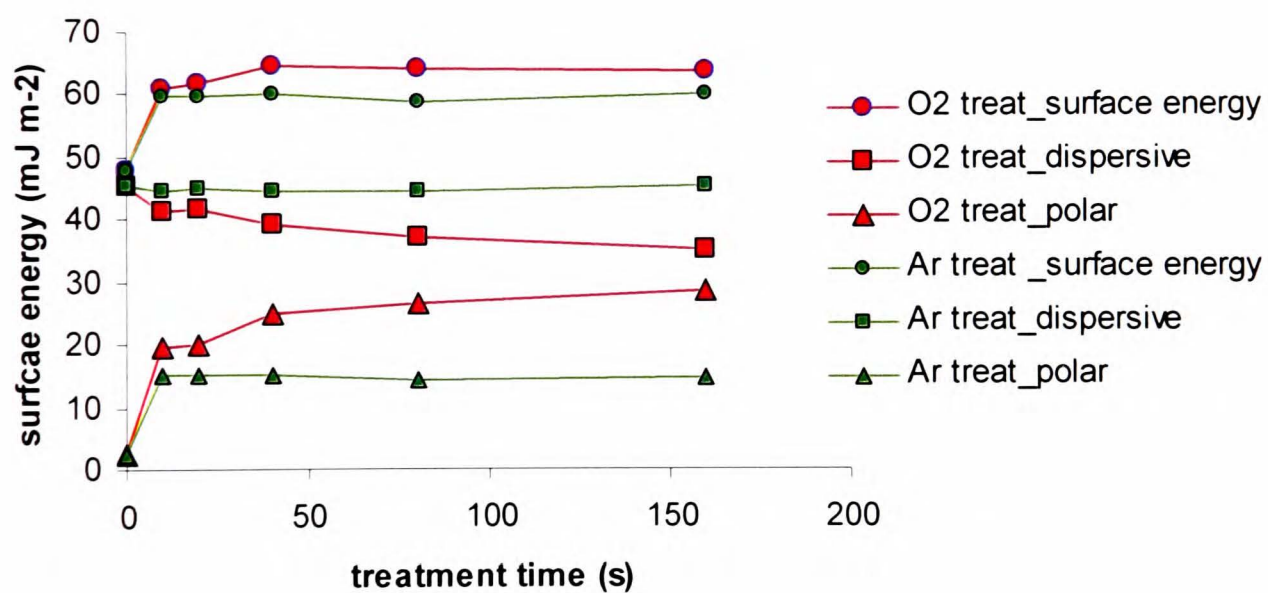


Figure 5.9 Surface energy as a function of plasma treatment time for O₂ and Ar gases.

The surface energy values of PET after 20 W Ar and O₂ plasma treatments of varying duration are shown in Figure 5.9. The total surface energy of the PET surface is similar after either treatment, increasing from 47 to 60 mJ m^{-2} after 10 seconds and not increasing much after that. After 10 seconds the polar component has increased from 2 to 15 mJ m^{-2} for both treatments and whereas this level remains constant for the Ar

treatment, the polar component for the O₂ treatment slowly increases with time so that it is almost 30 mJ m⁻² after 160 s. This is an indication of the increasing functionalisation of the surface by O₂ plasma as the treatment proceeds and is accompanied by a decrease in the dispersive component of the surface energy as polar groups dominate over apolar groups at the surface. The dispersive component for Ar treated surfaces remains constant over the treatment process, a sign that no oxygen is added to the surface. It appears that the increase in surface energy due to argon treatment is down to the removal of hydrophobic surface contamination, such as hydrocarbons, and surface rearrangements of existing polar groups. The dispersive contribution to the surface energy of the Ar treated film is much greater than for the O₂ treated film at longer treatment times, balancing out the difference in polar energy and resulting in similar total surface energies for both treated films.

XPS investigations of the Ar treated samples show no increase in the O:C ratio for the argon treated PET, irrespective of treatment time. Examining the C 1s spectra for the Ar plasma treated samples it is evident that the bonding at the surface undergoes change, most notably an additional peak is detected at 287.5 eV corresponding to carbonyl groups, presumably created by scission of the ester groups of the polymer (Figure 5.10). The creation of carbonyl groups by argon plasma treatments has been noticed by several authors [105, 179, 193]. As well as carbonyl group formation we see that broadening of the C-O-C peak also occurs, indicating phenol/hydroxyl/peroxyl formation [181] – unfortunately the resolution of the XPS does not allow us to make more detailed and

quantitative conclusions as to the exact nature of the bonding at the surface but it is clear to see that the surface is less modified by an Ar treatment than an O₂ one.

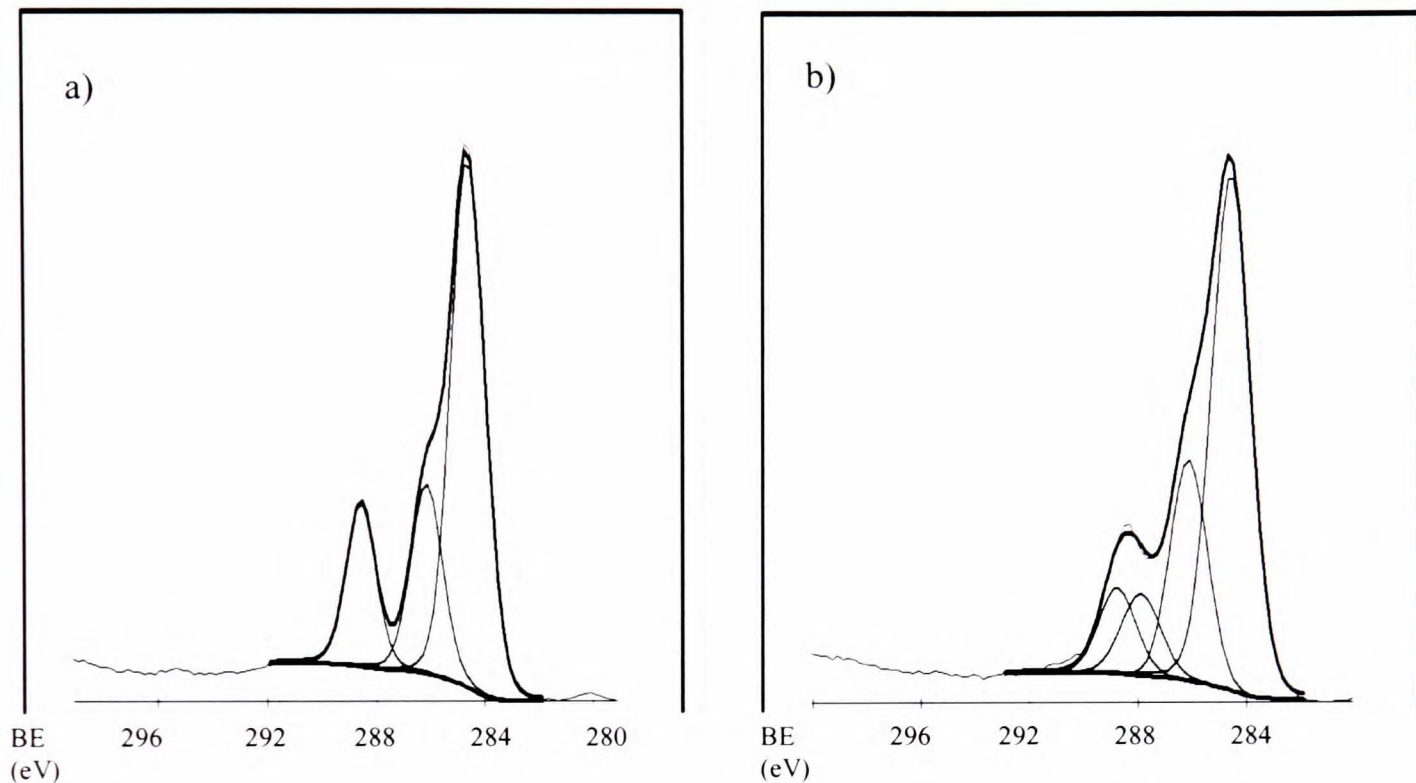


Figure 5.10 XPS C 1s spectra of a) PET, b) Ar treated PET.

The surface topography of an Ar plasma treated PET sample is very similar to that of the untreated surface. After 10 s treatment slight roughening is observed but further treatment leads to no overall change in the surface morphology and no further roughening. Surface etching by Ar plasma has been observed by other authors [180], but over a longer time span, indicating that the O₂ plasma is more effective at etching the polymer over shorter timescales [184].

5.1.4 Ar-O₂ gas mixtures

Recent reports have suggested that a mixture of oxygen and a noble gas, particularly helium, as the plasma species is especially effective in respect to surface modification due to the production of high energy atomic oxygen/radical species that react with the PET very favourably and can cause crosslinking of surface chains, limiting the ageing process [197]. With this in mind mixtures of argon and oxygen gas were used to treat the surface to gauge whether any improvement over pure oxygen plasma was possible. However, water contact angle and XPS measurements indicated that the Ar/O₂ mixture performed equally as well as the pure oxygen plasma and no appreciable improvement was observed. This was true regardless of the relative proportions of the gases and could be a sign that Ar is less effective than He in producing reactive oxygen species in the plasma. Also, the system I used was a reactive ion etcher, in which ions are the dominant species bombarding the polyester surface. The effect of creating more reactive oxygen radicals would therefore be less relevant, as these are only partially responsible for surface modification in the system used here.

5.2 Sputtered Aluminium Coatings

5.2.1 Experimental

To deposit aluminium coatings an Accentus d.c. sputterer was used in a cleanroom environment. The substrates (typically 100 x 100 mm) were placed on rotatable plates which themselves rotated round the chamber and under the Al target, to reduce heating of the substrate and to ensure complete coverage by the aluminium, by minimising atomic

shadowing effects. The target voltage was 350 V and the current was approximately 1.69 A to give a power of 590 W. The pressure was 5 mTorr and the deposition rate calculated to be 6.6 nm min^{-1} . The thickness of several samples run for different times was measured using profilometry to get a thickness v time plot. Samples of 80 nm and approximately 4 nm thickness were chosen for analysis, the latter for study of the interface - fabricated by rotating the samples once under the target. Whether the 4 nm thick coating uniformly coats the PET or is in the nucleation stage is unclear.

For plasma treated polyester, the treatment conditions were 100% O₂ gas at a flow rate of 20 sccm, a power of 20 W and a pressure of 100 mTorr. The length of treatment was 80 s.

5.2.2 Water vapour permeation

The WVTR through the 80 nm thick Al-coated films was measured at 40°C and the deposited layers were found to be very poor barriers, with the coatings on untreated film adding no improvement in barrier and in the case of PEN actually increasing water vapour permeation (Table 5.3). This may have been down to process induced damage of the film from arcing. The plasma treatment increases the barrier properties of the composite slightly but it is apparent that the quality of the coating is poor and that any substrate effects are being masked by the poor quality of the aluminium film. Previously, Al coatings of a similar thickness on PET have been reported to give WVTR values between 1 and $0.05 \text{ g m}^{-2} \text{ day}^{-1}$ depending on the deposition conditions [132, 133].

Table 5.3 Water vapour permeation through 80 nm thick Al-coated polyester film.

Substrate	WVTR $\text{g m}^{-2} \text{ day}^{-1}$	SD (n=12)
PET	4.13	0.22
PET_Al	3.65	1.34
PT PET_Al	1.46	0.79
PEN	1.5	0.3
PEN_Al	3.91	1.42
PT PEN_Al	0.8	0.57

5.2.3 Microstructure

The density of pinholes and other large-scale defects must be minimised in a coating as these are responsible for significant gas transport [113, 124]. They are typically caused by debris on the surface and by flaws in the deposition process, such as arcing. Plasma treatment can be useful in etching away debris from the surface, in Table 5.4 we see that a plasma treatment significantly reduces the number of pinholes in the Al films by more than an order of magnitude. The density of pinholes (per mm) was estimated by taking 25 SEM micrographs at a magnification of 3000x, counting the visible defects and scaling accordingly. Defects in the size range 0.5 – 3 μm were included in the count.

Table 5.4 Large scale defects in 80 nm thick Al coatings on polyester.

Substrate	Pinholes mm ⁻¹
PET	9400
PEN	4600
PET_P	3200
PT PET	280

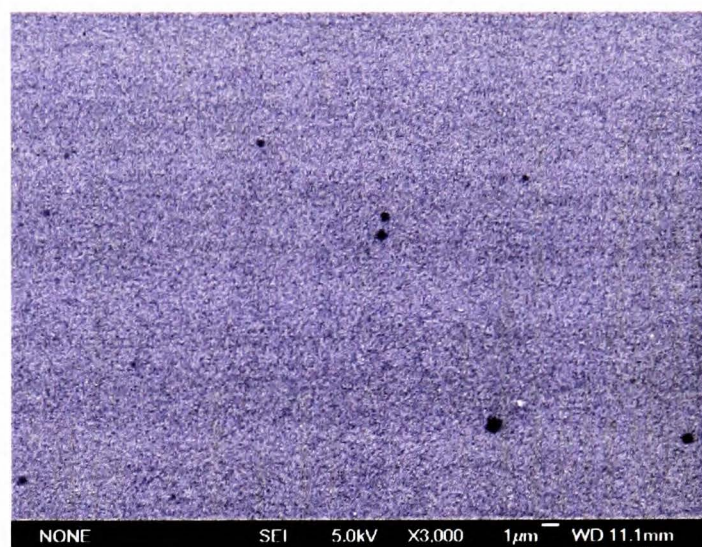


Figure 5.11 SEM micrograph of pinhole defects in an Al coating on PET.

As well as the significant reduction in pinhole density for Al deposited on a plasma treated PET surface, we see some improvement for the PEN and acrylate samples. This is mainly due to the superior finish of these films as they are sold to higher “end value” markets. The high numbers of pinholes observed by SEM would explain the generally poor quality of the Al barriers to water vapour permeation.

The fine scale structure of the coatings was examined using tapping mode AFM, after contact mode was found to give images with artefacts present – possibly due to the tip picking up debris from the surface. For all coated substrates the coating is characterised by small “grains” of approximately 25-30 nm in diameter, tightly packed against each other. It is probable that between these grains are small defects that could be responsible for gas transport. Generally these are too small to be imaged by the AFM tip although some possible defects are apparent as shown in Figure 5.12. It is clear that the plasma

treatment does not affect the small scale structure – it was hypothesised that the treatment would lead to a greater density of nucleation sites and consequently smaller individual “columns” of sputtered material. The similarity of microstructure in each case may well be due to the size of the sputtered Al particles which are likely to be small agglomerates of atoms, of the order of a few nanometres in diameter, so that the grain size is determined by the deposition process, rather than the substrate. The increased roughness of the plasma treated substrates also seems to have little influence over the final morphology of the Al film.

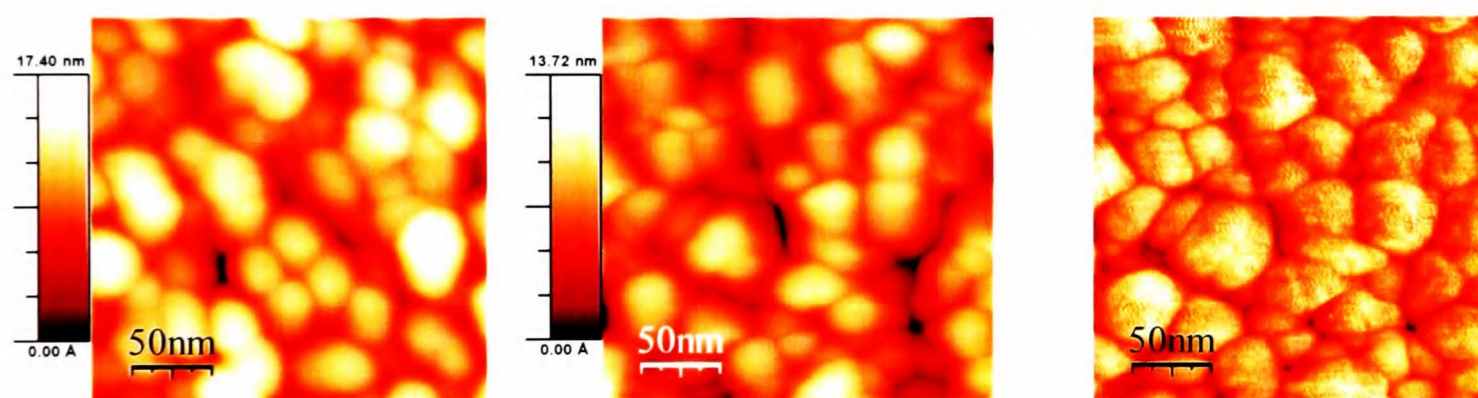


Figure 5.12 0.25 x 0.25 μm Tapping Mode AFM images of 80 nm thick Al on a) PET, b) O_2 PT PET, c) phase image accompanying (b).

5.2.4 Interfacial bonding

The bonding at the interface was probed using XPS. This technique samples to a depth of about 10 nm, consequently by examining a 4 nm thick coating with this technique we can get information about carbon bonding environments at the interface. By comparing the bonding for coated treated and untreated substrates we can determine whether extra interfacial bonding is induced by the plasma treatment.

The area of an XPS spectrum with the most pertinent information is the C 1s region, and Figure 5.13 shows spectra from coated untreated and treated substrates, as well as uncoated PET.

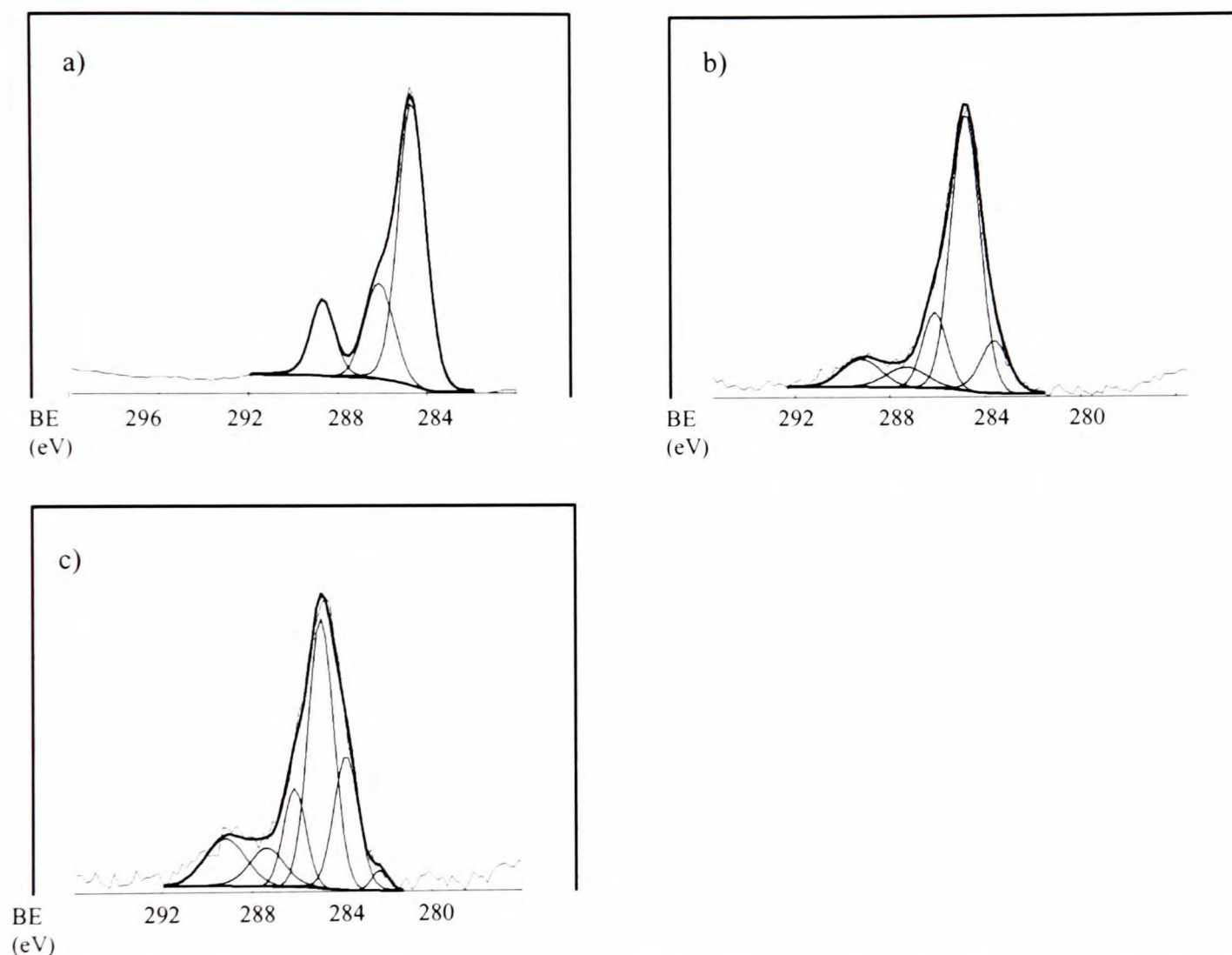


Figure 5.13 C 1s spectra of Al-PET interface, a) PET, b) Al-coated PET, c) Al-coated O₂ PT PET.

Comparing the interface of the Al-coated PET to the plain surface it is clear there are a few differences in the carbon bonding environments. Importantly there is a new peak at 283.6 eV, which is attributable to C-O-Al bonding, probably between ester/carbonyl groups and the deposited species [105, 249, 250]. An accompanying reduction in the intensity in the ester peak at 289.2 eV adds credence to this suggestion.

Another bonding peak is observed at 287.3 eV due to bonding of the form O-C-O-Al, which at first glance looks very similar to the bonding represented at 283.6 eV so why the large difference in binding energy? The reason lies in the nature of the bonding – for the peak at 283.6 eV it is clear that the carbon is bonded to a more electropositive atom (in this case aluminium) as well as oxygen and a reasonable conclusion to draw is that there is a cyclic complex formed by the C-O-Al as shown in Figure 5.14. This is supported by work from Sandrin and Sacher [250]. Secondly, the peak at 287.3 eV is consistent with a carbon bonded to two oxygen atoms, as each bond to oxygen shifts the BE by approximately 1.5 eV (from 284.7 eV), and is indicative of “linear” bonding.

Other authors [249, 251] have noticed that a third peak at approximately 282.3 eV sometimes appears at the interface, which is caused by C-Al carbide bonding. This is not present at the interface for the untreated PET and we can only conclude that no carbide bonding is present between the two layers. To check this conclusion it would have been useful to observe any changes in the aromatic π - π^* transition peak at 292 eV as this would disappear if there was any carbide bonding with the benzene rings in the polymer [250]. However, the resolution of the spectrometer is relatively low and unable to detect this peak even for the uncoated PET.

Turning our attention next to spectrum 5.13(c) showing the interface between PT PET and the aluminium we see an increase in intensity of the cyclic bonding peak at 283.6 eV. Table 5.5 shows the relative intensities of the various peaks for each of the coated substrates.

Table 5.5 Summary of bonding at the interface for PET-Al composites.

Substrate	C-O-Al (cyclic) 283.6 eV	C-C 284.7 eV	C-O 286.1 eV	C=O, O-C-O-Al 287.5 eV	O-C=O 289.2 eV
PET	0.12	0.59	0.14	0.08	0.07
PT PET	0.16	0.49	0.14	0.12	0.09

By introducing more oxygen-containing functional groups at the polymer surface, the consequence is to increase the interfacial bonding, as witnessed for the two types of bond represented by increased intensities at 283.6 eV and 287.5 eV. Such an increase in these types of bonding is expected to increase the adhesion between the two layers [133].

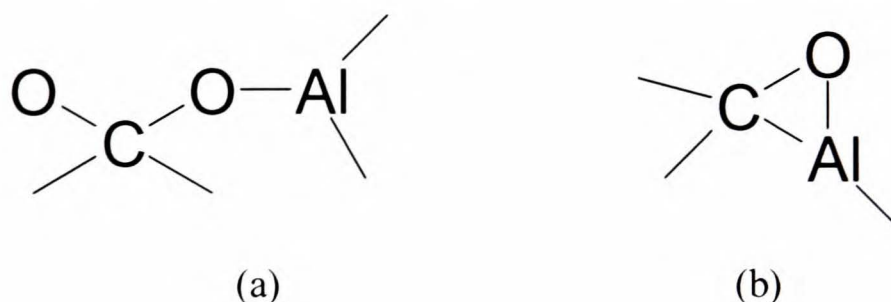


Figure 5.14 Bonding schemes at the interface, (a) linear bonding, (b) cyclic bonding.

5.2.5 Adhesion

The adhesion of the aluminium to the polyester samples was measured using the uniaxial fragmentation test where the evolution of cracking with applied strain was monitored using *in-situ* optical microscopy, as described in Chapter 3.7. Figure 5.15 shows how the cracking patterns observed evolve with applied strain.

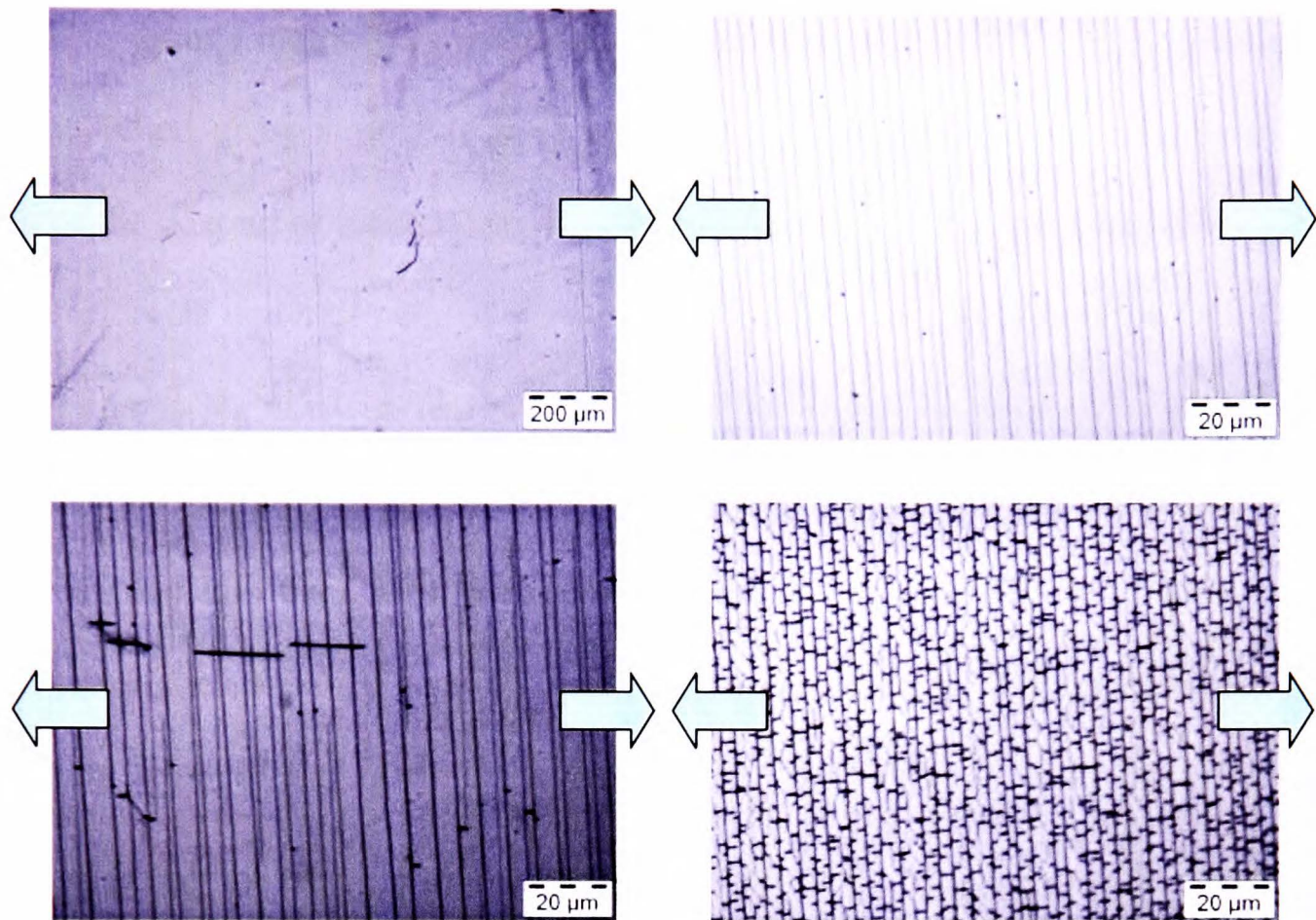


Figure 5.15 Reflection optical microscopy images of the cracking of an 80 nm thick Al coating on PET at different tensile strains (direction of applied tensile stress indicated by arrows). a) Crack onset from pinholes (1.2% strain), b) further cracking (4.3% strain), c) transverse cracking (5% strain), d) saturation (10 % strain).

The interfacial shear strength of the composite was calculated using the Kelly-Tyson model of a perfectly plastic interface. This model relates the IFSS to the coating thickness, h_c , the coating strength of fragments of a critical length l_c , $\sigma_{max}(l_c)$, and the crack density at saturation, CD_{sat} , [161]:

$$\tau = 1.337 h_c \sigma_{max}(l_c) CD_{sat} \quad (5.2)$$

It is the norm to calculate the value of $\sigma_{max}(l_c)$ using Weibull statistics applied to the early fragmentation process, just after crack onset. However, for these samples there was insufficient data taken in this region to justify using this method. Instead the strength was

calculated by simply multiplying the crack onset strain by the modulus of the aluminium coating, assumed to be similar to bulk aluminium at 70 GPa. This is effectively the strength of the coating of infinite length, rather than at the critical stress transfer length, and is therefore an underestimate of the cohesive strength and consequently of the IFSS. As we are comparing like with like however, this detail should be of small consequence. In Table 5.6 the plasma treatment is seen to increase the adhesion of the aluminium to the substrate by just less than 50%, manifested by the much larger CD at saturation. We attribute this to the additional bonding observed at the interface by XPS and conclude that this bonding is important for the adhesive strength. The values of adhesion though are still relatively low, much less than the shear yield stress of the polymer (55 MPa), indicating that the interface is relatively weak and that more interfacial bonding is required to achieve better adhesion. Similar improvements in adhesion for oxygen plasma treated polymer are reported by Bichler *et al.* [159] using peel testing for Al deposited on plasma treated polypropylene and by Ardelean *et al.* [251] who investigated O₂/He plasma treatments and saw a significant increase in adhesion due to enhanced covalent bonding (Al-O-C and Al-C) at the interface.

Table 5.6 Mechanical properties of Al coated PET films.

Substrate	COS %	CD mm ⁻¹	IFSS MPa
PET	1.18	219	19 ± 2
PT PET	1.25	293	27 ± 3

5.3 Batch PECVD SiO_x Coatings

5.3.1 Film fabrication

Thin SiO_x films were deposited using an Oxford Instruments Plasmalab 80+ PECVD coater in a clean room environment. The polyester film (50 x 50 mm) was placed on a platten at a temperature of 80°C and the vacuum chamber evacuated to a base pressure of 10⁻² mTorr. The precursor gases, NO₂ and SiH₄/N₂, were delivered at flow rates of 700 sccm and 210 sccm respectively and an r.f. power of 20 W was used to strike the plasma. The deposition pressure was 1000 mTorr. The deposition time was 60 s, in which time coatings of thickness 110 nm were deposited, as measured by ellipsometry and AFM “step” measurements on an equivalent coating deposited on a silicon wafer. Extremely thin coatings, approximately 2-5 nm thick were deposited by coating for just 4 seconds. The uncertainty in the thickness is due to a short delay for the plasma to strike up after the run starts and no method of accurately measuring it.

SiO_x was also deposited on plasma treated polyester, the pre-treatment conditions were 100% O₂ gas at a flow rate of 20 sccm, a power of 20 W and a pressure of 100 mTorr. The time of treatment was 80 s. Some PET film was also pre-treated using an Ar plasma with exactly the same process conditions.

The silica films were found to be amorphous by X-ray diffraction measurement, with a refractive index of 1.46, as expected for SiO₂ [252, 253], and no absorbance in the UV-visible region of the electromagnetic spectrum (300-700 nm). XPS showed there to be a stoichiometry of SiO_x where $x = 2.0 \pm 0.2$. Permeation data are not presented for these

materials due to problems with the Permatran apparatus at the time of testing and insufficient material remaining after other tests had been performed.

5.3.2 Microstructure

The microstructure of these coatings was difficult to characterise using contact-mode AFM. Rhombus shaped features of the size 300-500 nm were imaged, and their orientation remained unchanged despite rotating the sample. The features are no doubt artefacts caused by either tip damage, or the tip dragging debris along the surface. They were repeatably observed after exchanging tips and it appears that the sample damaged the tip in some way.

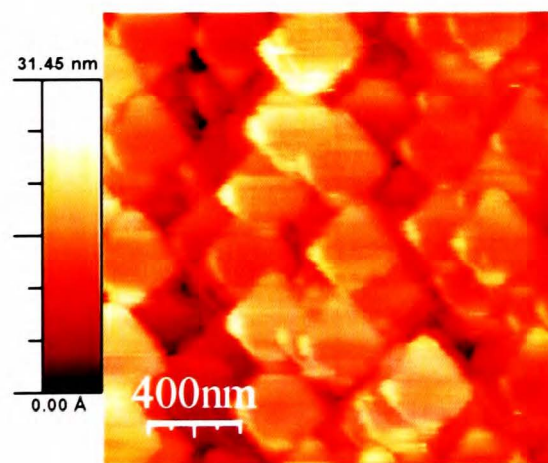


Figure 5.16 Artefacts observed when imaging SiO_x coatings with contact mode AFM.

Tapping mode AFM was found to give much better images, in Figure 5.17 we observe surface features of the order of 100 nm or less forming the structure of the 110 nm thick SiO_x coating. Similar to the findings for the aluminium layers, there is little variance in microstructure between coatings deposited on plain PET and those on the treated film.

The particle size and the roughness are comparable for all three coated substrates and it appears the plasma treatments have little influence over this aspect of the composite's character.

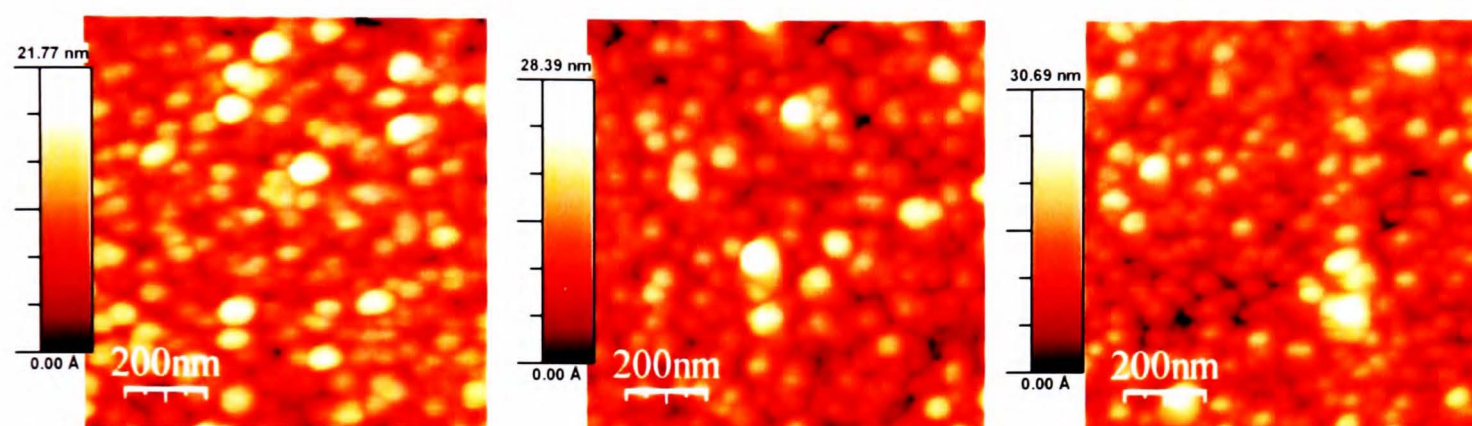


Figure 5.17 1 x 1 μm AFM scans of 110 nm thick SiO_x film on a) PET, b) argon plasma treated PET, c) oxygen plasma treated PET.

The extremely thin 2-5 nm coatings produced on the substrates were also examined to find any evidence of plasma treatment influencing the nucleation of the silica on the PET. Such thin coatings are traditionally difficult to image as the thickness is the same or less than the roughness of the substrate, making it impossible to distinguish between polymer “artefacts” and deposited silica. One method is to apply a large force to the AFM tip in contact mode so that it damages the soft polymer but not the silica, thereby creating areas of contrast [110] – this is only applicable if the exposed polymer areas are relatively large and poor nucleation is apparent. In this case the method failed to give conclusive images.

Using tapping mode and accompanying phase imaging it is possible to get an impression of the coating microstructure even at such low thicknesses (Figure 5.18). The topography of the surface changes slightly when the thin film is deposited, it roughens and small particles less than 50 nm in diameter are observed. This is confirmed by the phase images

beneath the topography showing a network of small features similar in size to those in the topography images and with what appears to be complete coverage of the surface, whether or not the film has been pre-treated. The white marks on the phase images are most likely “powder” which has formed due to reactions in the gas phase and fallen, like snow, onto the surface of the film. The silica deposited on the O₂ plasma treated surface appears to be rougher than that on untreated PET (1.85 nm compared to 1.13 nm) and this would be a consequence of the roughening of the substrate during plasma treatment as observed earlier. Otherwise no difference in terms of nucleation density or particle size is apparent and it appears that plasma treatment has no effect on the microstructure of the deposited film either at the nucleation stage or in more advanced stages of growth.

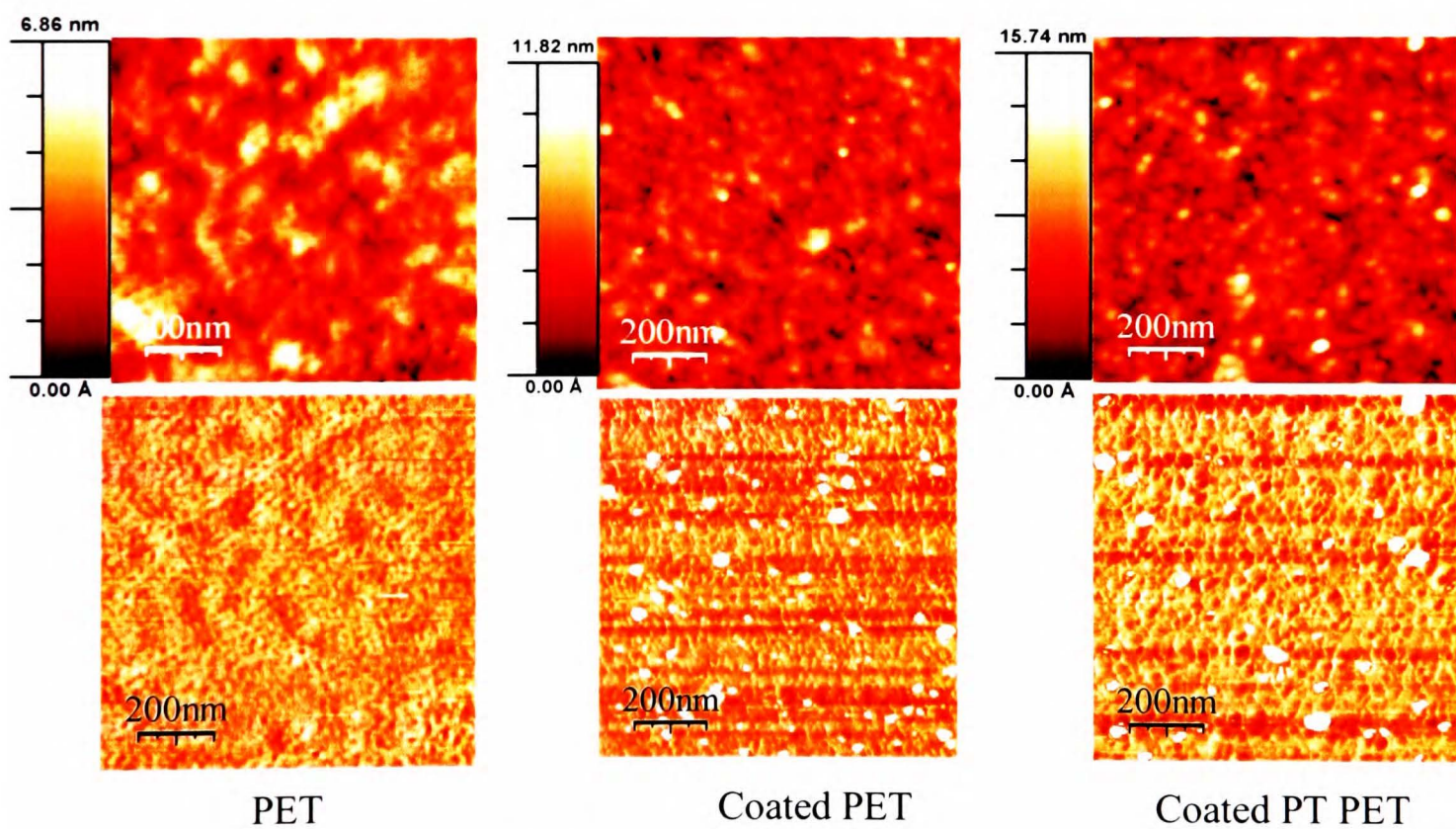


Figure 5.18 1 x 1 μm Tapping mode AFM images with accompanying phase image below, a) PET, b) 2-5 nm thick SiO_x on PET, c) 2-5 nm thick SiO_x on O₂ PT PET.

5.3.3 Interfacial bonding

In a similar method to that for the Al-coated PET, the interfacial chemistry of the PET-SiO_x composites was examined by XPS on thin samples. Once again the C 1s spectrum was analysed and Figure 5.19 shows spectra corresponding to PET, PET_SiO_x and O₂ plasma treated PET_SiO_x.

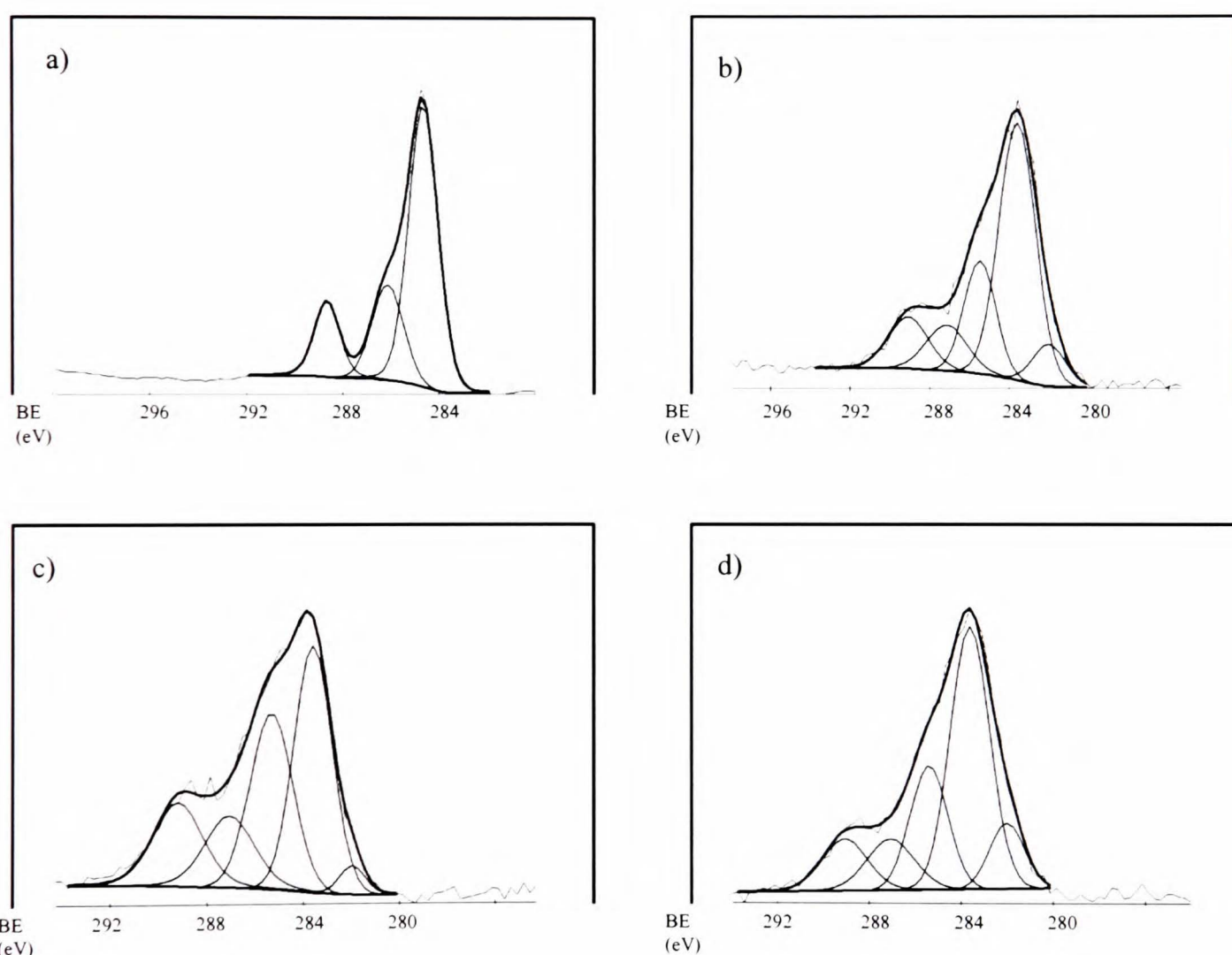


Figure 5.19 XPS C 1s spectra for a) PET, b) – d) 2-5 nm thick SiO_x on b) PET, c) O₂ PT PET, d) O₂ PT PET (glancing angle (60°) incidence of X-rays).

In a similar fashion to the Al-PET bonding, a new peak arises at a binding energy of 287.5 eV for the SiO_x coated samples, corresponding this time to O-C-O-Si covalent bonding between the silica and the ester groups of the polymer. The intensity of the ester

carbon shows a corresponding reduction confirming this observation. Another bonding peak is observed at 283.5 eV and is a result of C-Si carbide bonds [203, 254] although this peak is relatively small and such bonding is in the minority (most likely between phenyl groups and Si).

Determining the effect of the plasma treatment on the interface is much harder for SiO_x than for Al layers as the bonding peaks are in the same positions as the peaks (or peaks which increase in intensity) due to plasma treatment. Any observed increases in the peak height and width may be due to either case and so the increase in bonding (if any) can not be quantified by XPS. In any case the C-Si bonding remains fairly low in relative terms and the increase in intensity of the peaks at 286.3 eV and 287.5 eV can be put down to an increase in i) functional groups at the surface of the polymer, ii) C-O-Si and O-C-O-Si bonding between the two layers. Rotger *et al.* [254], on the other hand, find that O₂ plasma has little effect on improving the interface between polyethylene and SiO_x by XPS measurements and suggest that an N₂ plasma is more effective at increasing interfacial bonding for a completely hydrocarbon polymer.

Spectrum D in Figure 5.19 shows glancing angle (the 60° incidence angle allows the interface to be sampled more selectively) measurements on the plasma treated interface that confirm the importance of the ester group (decrease in peak area) for bonding and the presence of C-Si bonds (increase in peak area).

5.3.4 Adhesion

The adhesion of the SiO_x layer to the polyester is expected to increase after a plasma treatment. Using the Kelly-Tyson model of interfacial shear stress, τ , and expressing the coating strength as the product of coating Young's modulus (80 GPa [161]) and crack onset strain the adhesion between the coating and PET, and Ar and O₂ plasma treated PET was calculated.

Table 5.7 Mechanical properties of 110 nm thick SiO_x coatings on PET.

Substrate	COS (%)	CD _{sat} (mm ⁻¹)	σ_{max} (GPa)	τ (MPa)
PET	0.76	382	0.61	34
PT PET O ₂	1.03	450	0.82	54
PT PET Ar	1.07	413	0.85	52

The coating on the untreated PET cracks at the lowest strain and has inferior adhesion. The two plasma treated substrates increase the COS by 0.3 and the adhesion improves by 50%. The latter is due to improved interfacial bonding between the coating and the polymer with a high amount of C-Si and C-O-Si bonding. The improved strain to failure can be explained by the cleaning nature of the pre-treatment meaning that there is less debris on the polyester substrate that creates large defects in the coating, which are the sites for brittle failure. There is negligible difference in the values for the two plasma treated substrates suggesting that the Ar plasma is just as effective as the oxygen one in creating bonding groups, despite not introducing extra oxygen to the surface.

An interesting observation made during fragmentation was the preferential transverse cracking of the coating directly above scratches on the PET surface, a phenomenon that has been observed elsewhere [169]. Such cracks are caused by compressive stresses introduced by the contraction of the film due to Poisson's ratio effects and it appears that

the scratches cause weakening of the coating in compression. A micrograph of this phenomenon and a schematic of the coating above the scratch are shown in Figure 5.20. The schematic is only a suggestion of what may be happening above a surface scratch – from AFM imaging it is clear that the coating does not simply bridge or fill the gap, but conforms to it in some way. Such a coating element will then be prone to failure such as buckling, due to additional bending stresses, and this is observed in preferential transverse cracking over these sites.

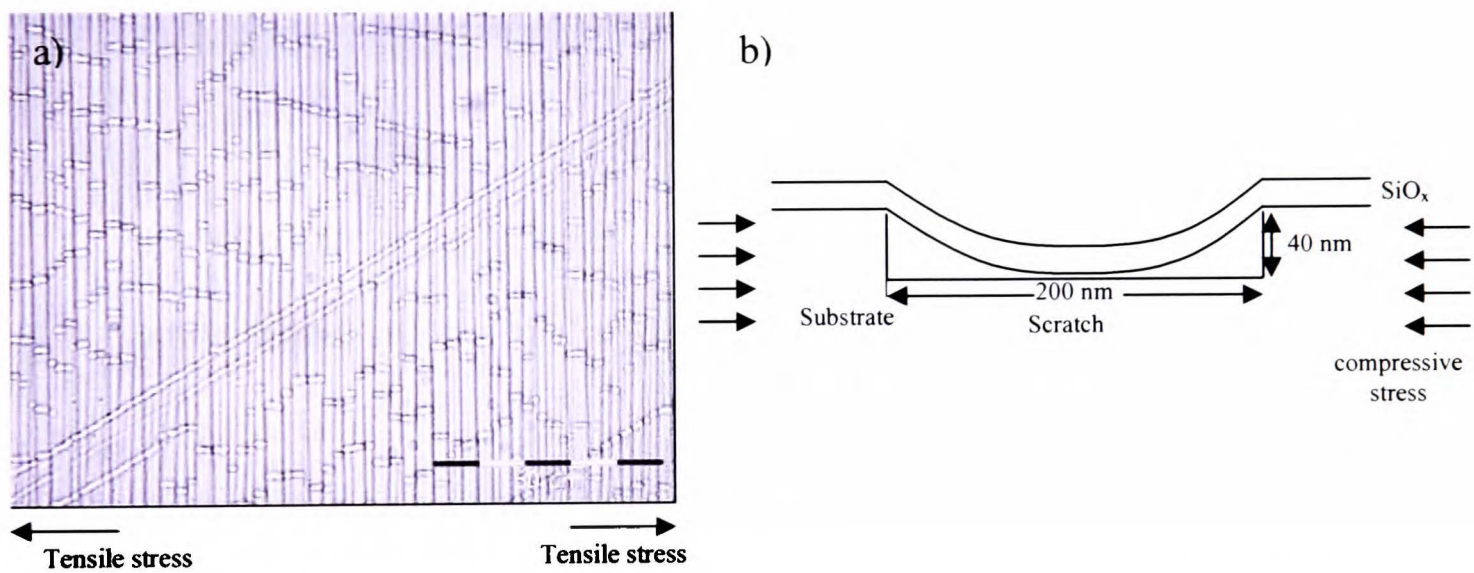


Figure 5.20 a) Reflection optical microscopy image of transverse cracking along scratches on substrate surface, b) simplified schematic of the coating above a scratch in the substrate surface (with typical dimensions as observed by AFM).

5.4 Summary

Plasma treatments are an efficient, effective and environmentally friendly method to modify the surface of polymer films to prepare them to act as good substrates for vacuum deposited films. Oxygen and argon plasma treatments of PET have been examined, with the following conclusions:

- An O₂ plasma introduces an appreciable amount of oxygen to the surface at any plasma power and time of treatment. Even after 10 seconds a significant reduction in the contact angle of water is observed and an increase in oxygen content (due to carbonyl and hydroxyl group formation) is apparent. Over longer periods of time a small increase in functionality is recorded and the surface roughens considerably due to the preferential etching of amorphous regions.
- The effects of the treatment deteriorate with time, due to surface rearrangements and chain motion, so that deposition should immediately follow the pretreatment for maximum benefit.
- An increased plasma power results in an increase in oxygen at the surface and a lower contact angle of water. However, washing experiments indicate that high power treatments create a weakly bonded surface layer that may be detrimental for adhesion.
- Argon plasma increases the hydrophilicity of the surface, but not to the same degree as the O₂ plasma. This is because it does not introduce additional oxygen to the surface but instead causes scission of the ester group and rearrangement of the bonds in the PET chains which is strongly suggested by XPS C 1s spectra of the treated films.
- Similar to the O₂ pretreatment, the majority of the improvement in surface chemistry occurs in the first ten seconds of treatment. The surface is only slightly roughened by the Ar plasma however, with no noticeable increase with treatment time.

- Oxygen/argon gas mixtures, of varying composition, all show very similar attributes to a pure oxygen plasma treatment, suggesting that the addition of Ar does not improve the performance of O₂ plasma in the way that helium has been shown to.

Thin aluminium coatings were deposited on O₂-plasma treated PET to assess any improvement over those on an untreated film. The treatment conditions were chosen to be mild enough so as to not risk damage to the polymer. Significant improvement in the Al film properties was observed for the treated substrate:

- An order of magnitude reduction in pinhole density, due to the etching away of debris/contaminants from the substrate surface.
- Significant increase in covalent interfacial bonding as determined by XPS, primarily at ester groups.
- 50% increase in adhesion between the polymer and aluminium due to the extra interfacial bonding observed (greater number of cracks at saturation in the fragmentation test). However, the adhesion is still relatively poor compared to SiO_x coatings.
- No difference in microstructure of the coatings was observed on the treated PET and no significant improvement of the barrier to water vapour permeation was apparent. It appears that the aluminium layer was too poor for the substrate to have much influence on its properties.

In a similar fashion PECVD SiO_x films 110 nm thick were deposited on untreated and both O₂ and Ar treated films.

- Neither treatment affects the microstructure of the SiO_x layer, either in the nucleation stage or at a thickness of 110 nm. The increase in the number of functional groups has no effect on the “grain” size of the coating suggesting that this property is determined by the deposition process.
- The interfacial bonding between substrate and coating is characterised predominantly by Si-O-C bonds, with a significant contribution from Si-C bonding also apparent. The degree of bonding at the interface is enhanced by the plasma treatment.
- The increased bonding manifests itself in an interfacial shear strength value 50% higher for the treated films compared to the untreated film. The crack-onset strain for the coatings on the treated films is also much higher and can be attributed to the cleaning of the surface, which reduces the amount of debris and consequently defects in the silica film. Failure of the coating takes place first at large defects, so a higher crack onset strain suggests that the largest defects in the film have been eliminated.

The evidence from this chapter suggests that to maximise the adhesion of a coating to the polymer film, a plasma treatment is required and that either O₂ or Ar plasma is suitable. The number of pinhole defects in the film may also be greatly reduced which would have positive implications in the field of gas barriers. In the following chapter, substrates for

gas barrier coatings undergo plasma treatment *in-situ* immediately prior to deposition to improve the performance of the composite material.

Chapter 6. Silicon Oxide Gas Barrier Coatings on Polyester Films: Effect of the Substrate

Thin silicon oxide coatings have become the main rival to metallised polymer for food packaging and have several advantages, such as transparency and microwave compatibility, compared to thin metal coatings such as aluminium. Bulk silicon oxide (glass) is commonly used for packaging products but of course is relatively heavy and fragile, albeit a very effective barrier to gas and water vapour permeation. By coating polymer film with thin silicon oxide layers it is hoped that the barrier properties of the glass and the flexibility and light weight of the polymer film can be married to form a composite that would act like “flexible glass” and would be cheaper, in terms of manufacturing and transport costs, and safer than bulk glass.

Thin SiO_x coatings have been deposited by a number of methods [113], including sputtering [255], electron-beam evaporation [151, 154] and PECVD [80, 115, 117, 123]. The latter technique is most popular due to low temperature deposition, process tunability and films that are flexible, that have a greater strain to failure and superior adhesion to the polymer substrate when compared to equivalent PVD coatings. PECVD SiO_x coatings have been shown to exhibit good gas barrier properties to oxygen and water vapour but are difficult to deposit on a large scale with good uniformity and acceptable deposition rates. In this chapter the properties of silicon oxide films, deposited using a novel roll-to-roll (R2R) process, are reported with a focus on the barrier to water vapour permeation,

which isn't particularly well studied as the majority of the published work on these type of films concentrates on O₂ gas transport [8, 113].

Likewise, the effect of the substrate on the coating properties is often overlooked in the literature. An important factor is the surface chemistry and it is known that functional groups must be present on the substrate surface to allow dense nucleation and good interfacial bonding. Chapter 5 has shown us that plasma treatment of polymer film is an effective way of improving the interface between coating and polymer and is a step routinely used before the vacuum deposition process. High roughness on a scale of 10's and 100's of μm , caused by surface contamination (dust, additives) and filler particles, has been shown to create pinhole defects in vacuum deposited films with a resultant loss of barrier [119], yet little is known about how the nano-scale roughness of the substrate causes a coating to behave, despite the knowledge that coating structure on this scale influences the rate of gas permeation. Smoothing polymer interlayers have been shown to negate extreme roughness and improve barrier quality [142] and other factors such as substrate crystallinity [169] and defects such as scratches have also been considered [129].

In this chapter the six substrates described in Chapter 4 have been coated with SiO_x films much thicker than most reported in the literature. The relationship between the substrate morphological, mechanical and thermal properties and the coating microstructure and barrier properties will be closely examined. Additionally, the mechanical properties of

the coatings are carefully scrutinised as a barrier coating must be flexible, resilient and adhere well to the substrate if it is to maintain high performance throughout its lifecycle.

6.1 Deposition Method

The SiO_x coatings were deposited on a range of films by General Plasma, Inc, a company based in Tuscon in the USA who had developed a new roll-to-roll (R2R) PECVD process that enabled high deposition rates and large area deposition [87]. The main feature of the technique is the Penning Discharge Plasma Source (PDPS), a magnetically confined plasma source optimized for PECVD and a schematic of the apparatus is shown in Figure 6.1.

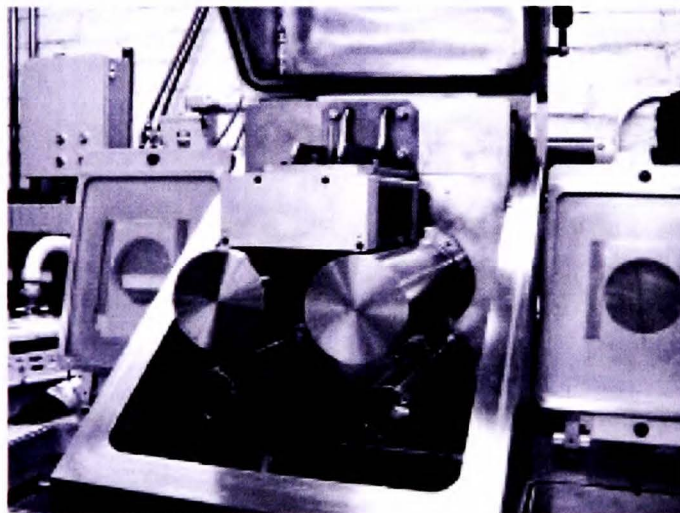
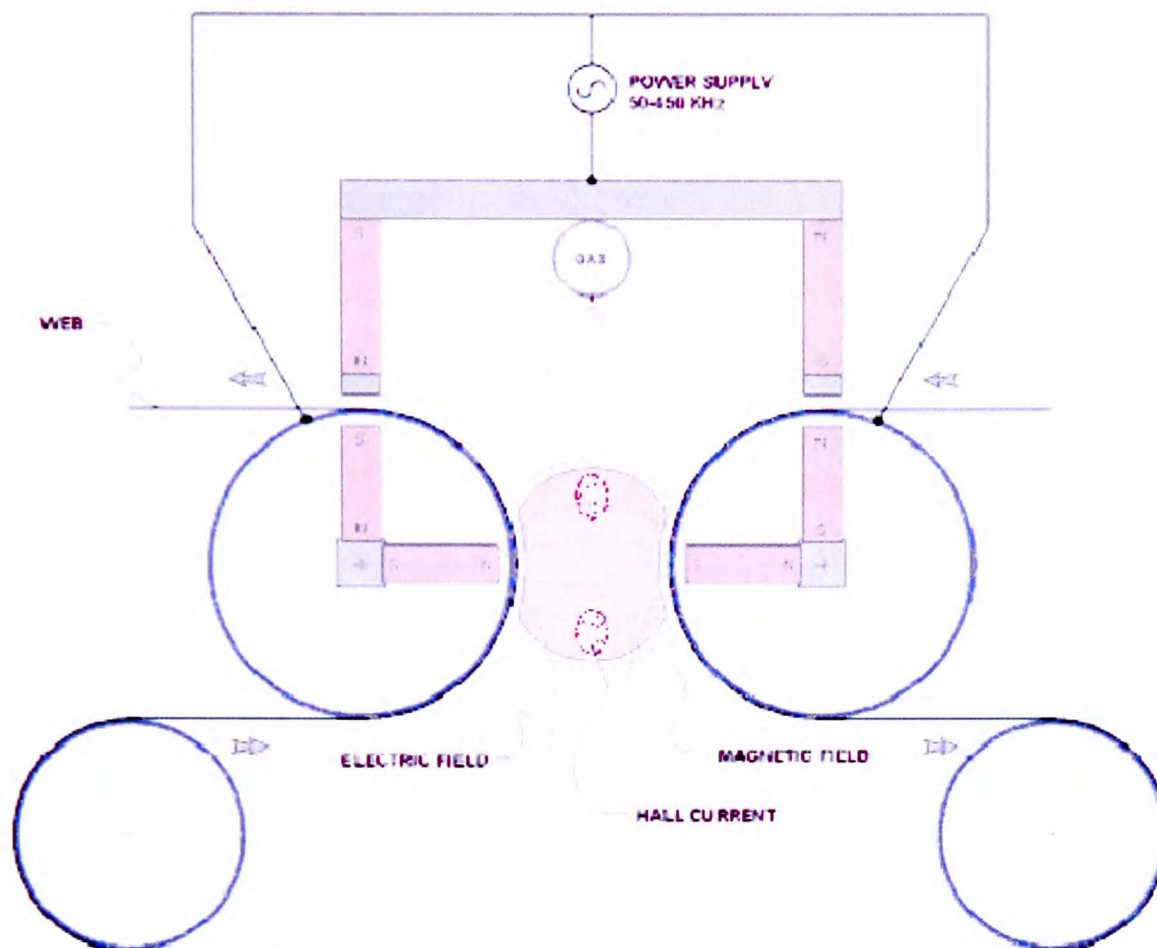


Figure 6.1 A schematic of the PECVD deposition process, with a photograph of the apparatus.

In this setup two rotating, water cooled rollers with non-rotating magnet assemblies face each other across a gap of 4-5 cm and are connected to a mid frequency (50-450 kHz) power supply. A magnetic field is present in the gap between the rolls which is returned by a magnetic shunt positioned over the rolls, the base of which is grounded and hosts the gas distribution manifold. When the power is switched on and the gas is admitted a

plasma is produced and the web/roller acts as a cathode. Electrons try to leave the gap area (towards the chamber ground anode), following the electric field labelled in Figure 6.1, but are blocked by the magnetic field (which the electrons cannot cross) and are confined to the centre of the gap and drift into the Hall current ring.

The practical benefits of the PDPS technology are summarised below [256]:

- The facing cathodes and dipole magnetic fields confine the electron Hall current in the centre of the plasma, producing a uniform, dense plasma ($\sim 10^{12}$ charged particles per cm^3) that enables uniform coating of wide substrates.
- The plasma is of low impedance and operates at low pressures (~ 10 mTorr). This results in high temperature electrons in the plasma, which efficiently produce ions and radicals for deposition. The pressure is low enough for a high mean free path of reactants so that gas phase chemistry and powder formation is avoided and allows high power and monomer flow rates to be used to enhance the deposition rate. The facing cathode configuration of the system minimizes hot secondary electron bombardment on the substrate, so that low temperature deposition is possible.
- The plasma is formed between the web covered rollers (also the electrodes), which means that the majority of condensable species coat the substrate rather than the electrodes or chamber walls. Therefore full rolls of film can be coated consistently without time consuming cleaning and other maintenance operations.

For the deposition of SiO_x on the polyester films, precursor gases hexamethyldisiloxane (HMDSO, Figure 6.2) and oxygen were used. The web width was 150 mm and prior to deposition it underwent plasma treatment using nitrogen gas, with a N₂ flow rate of 50 sccm at a power of 200 W and web speed 0.6 m min⁻¹. The web speed and number of passes of the web through the coater were varied to obtain different thicknesses and this is summarised in Table 6.1. The operating pressure was 20 mTorr.

Table 6.1 Deposition parameters for PECVD SiO_x films.

Batch	Thickness (nm)	HMDSO Flow rate (sccm)	O ₂ flow rate (sccm)	Power (W)	Speed (m min ⁻¹)	Passes
1	1000	50	30	300	0.20	6
2	200	75	30	300	0.33	2
2	400	75	30	300	0.33	4
2	1000	75	30	300	0.20	6

The received samples were fabricated in two separate batches, each with different processing parameters. The production of samples in Batch 2 differed from those in Batch 1 in that:

- 1) The flow rate of HMDSO was increased to 75 sccm from 50 sccm.
- 2) The configuration of the PDPS was altered slightly to prevent coating the idler rollers. The alterations made are thought to have altered the characteristics of the plasma and made it more intense.

For the Batch 1 coatings only four substrates were coated, PET, HS PET, HS PET_P and PEN, and the only thickness of coating examined was 1 μm. For Batch 2, six substrates

were used and in addition to the films used for Batch 1, the aPET and F-PET films were coated. However, the aPET film was visibly damaged by the deposition process, due to thermal shrinkage, and silica films on this substrate were not examined thereafter. Three thicknesses of silica – 200, 400 and 1000 nm were deposited on each substrate and also on silicon wafers. The thickness of the deposited layers was determined by workers at General Plasma with a combination of profilometry and UV-vis spectrophotometry and verified by myself using profilometry on silicon wafers coated simultaneously with the polymer (Batch 2 only, see section 6.2.2).

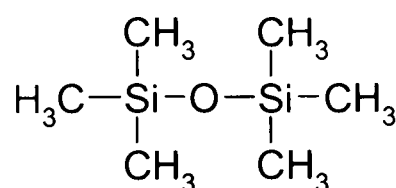


Figure 6.2 Chemical Structure of HMDSO.

6.2 Physical Properties of the Coating

6.2.1 Batch 1

By using X-ray Diffraction analysis the SiO_x coatings were found to be amorphous. The coating composition was examined by XPS and it was found that it was slightly sub-stoichiometric at $\text{SiO}_{1.9}$ with an appreciable amount of carbon detected, which gave the transparent films a yellow/brown tint. To estimate the amount of carbon present in the coating it was first necessary to eliminate the effect of surface contamination and any carbon signal from the substrate. To do this an XPS scan was performed on the SiO_x coatings described in Chapter 5.3 (fabricated with SiH_4 and N_2O precursors and hence

containing no C) so that any carbon detected would be from “background”, not the coating structure, and it was found that the background level was 13%. Once this was accounted for, the atomic composition of carbon contained in the coating, deposited on PET or Si wafer, was found to be 18-21% (mean value 20%), with some variation between areas on the same film. Such a high level of C is thought to be a legacy of using HMDSO as a precursor and that some (partially or totally) unreacted quantity of this is incorporated into the film. Also it is possible that methyl (CH₃) radicals produced in the plasma will be incorporated. A UV-visible absorption spectrum (Figure 6.3) of the coating reveals a small peak between 320 and 500 nm. It can be seen that in some ways calling this material “silicon oxide” is a misnomer – a more accurate representation would be SiO_x.C_yH_z or SiO_x.(CH₃)_y but it is difficult to determine what form the hydrocarbon takes in the film – whether it is covalently bonded to Si or adsorbed - and generally in the literature it is assumed that the coating behaves like SiO_x.

6.2.2 Batch 2

Similar to the SiO_x deposited in Batch 1, the coatings had no detectable crystal structure and the coatings contained an appreciable amount of carbon. The composition was found to be SiO_{1.8} and the atomic composition of carbon estimated to be between 18-25% (mean value 23%), with variation observed for areas on the same film and between samples also. Despite containing at least as much (if not more) C as the coatings in Batch 1, less absorption in the UV-visible region is apparent for these coatings and they are noticeably less coloured, with only a slight yellow tint. For the 200 nm thick silica, practically no absorption is apparent and these films are almost totally transparent as

shown in Figure 6.3. One would expect that a higher flow rate of HMDSO and a generally increased level of carbon would lead to greater absorption by the silica film but this is not the case and may be down to the more intense plasma that was used to produce the coatings. A possible explanation could be that more carbon is introduced as CH_3 radicals into the film rather than unreacted HMDSO because the more intense plasma causes a greater proportion of HMDSO to completely dissociate. However, the chemistry of these films is complicated and not well understood - Si-C, C-O, Si-OH and Si-H bonds have all been previously detected in HMDSO-produced films [257, 258] and it is difficult to deduce the chemical groups responsible for the UV-visible absorption for the SiO_x films examined here, as there are no obvious π -bonding systems. The refractive index of the SiO_x was found to be 1.6 by ellipsometry, a value higher than the standard of 1.46 for SiO_2 which may be a consequence of the sub-stoichiometry and the carbon content in the film [259].

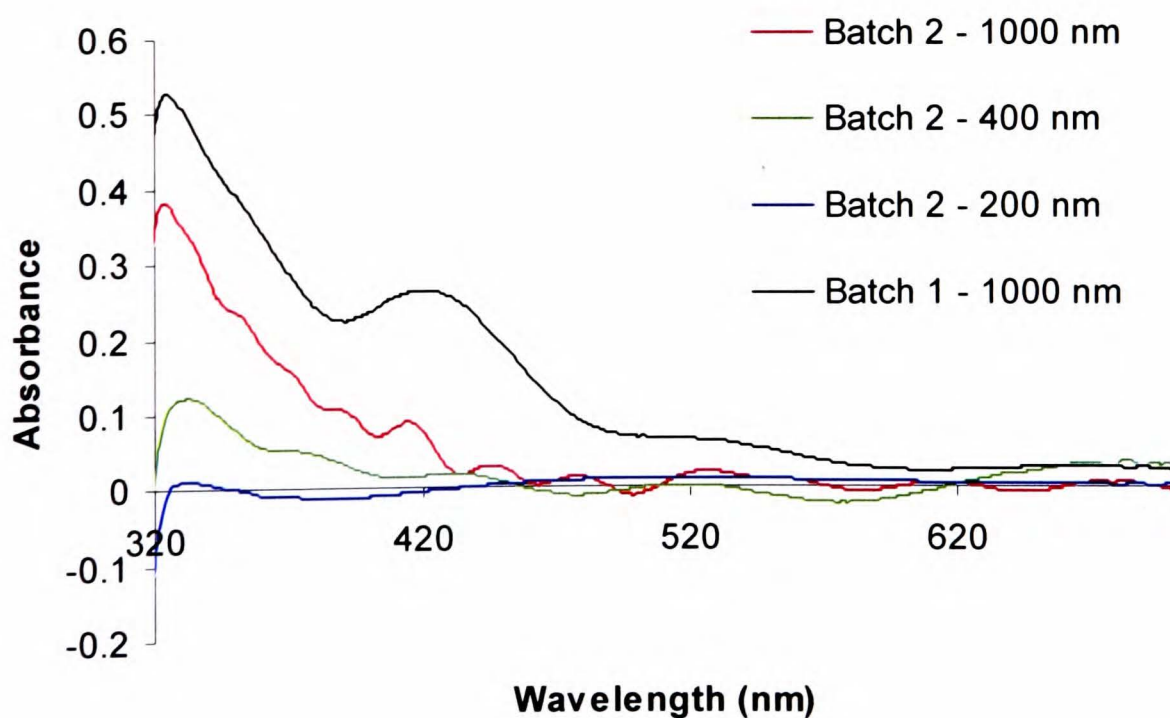


Figure 6.3 UV-visible absorption spectrum for SiO_x coatings.

The thickness of the coatings from Batch 2 was verified by measuring the step height of the silica deposit on a silicon wafer using a Dektak profilometer. The step was produced by placing Kapton tape on part of the wafer, which was coated simultaneously with a polymer web, and peeled off after deposition. Twenty measurements were taken for each thickness and for each case the mean value of the measurements was close enough to the “expected” thickness (within the SD) to assume the reported thicknesses of 200, 400 and 1000 nm are valid. It is hoped that this is representative of the thicknesses of the silica on each substrate – it is difficult to measure this quantity when the coating is on the polymer and X-ray Fluorescence (which I did not have access to) is the best technique for such measurements.

Table 6.2 Thickness measurements for SiO_x films deposited on silicon wafers.

“Expected” h_c (nm)	Measured h_c (nm)	SD (n = 20)
200	217	18
400	417	29
1000	1025	57

6.3 Water Permeation Through the Coated Films

6.3.1 Batch 1

WVTR data taken at 40°C for 1 μm coatings on each substrate are reported in Table 6.3. For three of the coated substrates the permeation is lower than the detectable range of the Permatran instrument ($\sim 0.01 \text{ g m}^{-2} \text{ day}^{-1}$). Extended conditioning times of 10 days were used to check that the observed low permeation rate wasn’t down to a long lag time and still the WVTR’s were unmeasurable. It is believed that the SiO_x films are genuinely

good barriers to water vapour, offering an improvement of at least 150-400 times over the bare substrate.

For the coated PET substrate the WVTR is significantly higher than for the other composites with a barrier improvement factor (BIF) of only 29. That the barrier on this film is at least an order of magnitude inferior to the other composites is surprising and could possibly be explained by the microstructure of the SiO_x.

Table 6.3 Permeation data for PECVD SiO_x films on polyester (40°C).

Substrate	Substrate WVTR (g m ⁻² day ⁻¹)	Composite WVTR (g m ⁻² day ⁻¹)
PET	5.48	0.19
HS PET	4.28	< 0.01
HS PET P	4.28	< 0.01
PEN	1.58	< 0.01

6.3.1.1 Microstructure

SEM was used to examine the coating for pinhole and large scale defects and very few were detected in the films. For all four coated films there were less than 150 defects mm⁻² with about half of these being pinholes of the order of 1 μm and the rest being larger defects such as scratches. The relatively low number of defects on this scale is one reason why the barrier of the coatings is so good, yet gives no clue as to why the PET composite is inferior.

AFM investigations of the sub-micron scale microstructure may help to explain the WVTR observations. 1 x 1 μm contact AFM images of the silica on the 4 substrates are

shown in Figure 6.4 and it is clear that there are differences in the morphology between some of the substrates. The average size of the grains is much larger for the coating on the HS PET_P than the other substrates and lowest on the plain grade of PET. Likewise the roughest coating is observed on the roughest substrate (the one with the primer) and the smoothest on the plain PET which is the smoothest substrate. Plotting substrate roughness against that of the coating shows that a positive correlation between the two quantities could exist, although more data points (substrates) would be required to confirm this.

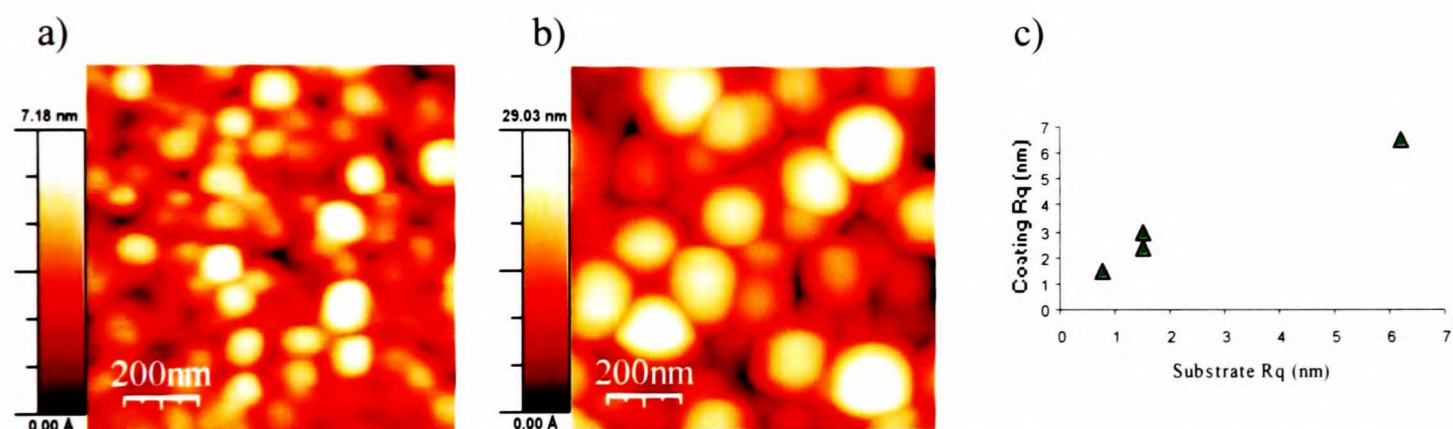


Figure 6.4 Morphology of 1000 nm SiO_x coatings (a) AFM image of SiO_x on PET, (b) on HS PET_P, (c) Plot of substrate roughness against coating roughness.

An attempt was made to quantify the number of nanometre-scale defects in the coatings by counting dark areas of contrast between the silica grains in the AFM images, using the AFM image processing software. Such areas are thought to be possible starting points for tortuous permeation pathways through the coating material, responsible for the transport of water vapour through the film. To count these defects a simple routine was used, known as “flooding”, on 1 x 1 μm images. A plane was specified at a certain value of z so that any areas in the AFM image below it were displayed in an image and the number and coverage (percentage area occupied by such regions) was given. The level was chosen

subjectively, so that by eye all the possible defects had been included, and was kept constant for a given substrate. Although there are several obvious drawbacks to this method (the size of defect detectable is limited by the tip dimensions, unknown likelihood of a dark area being a pore and the element of subjectivity) it at least gives an indication of the number of possible defects in the 20-100 nm range.

Table 6.4 Microstructure of PECVD SiO_x coatings.

Substrate	Substrate R_q (nm)	Coating R_q (nm)	SiO _x average particle size (nm)	Defect density (μm^{-1})	Defect surface coverage (%)
PET	0.8	1.5	143 ± 25	16 ± 13	1.95 ± 1.52
HS PET	1.5	2.4	120 ± 24	13 ± 5	0.73 ± 0.31
HS PET_P	6.2	6.4	230 ± 68	6 ± 3	0.76 ± 0.28
PEN	1.6	3.0	172 ± 46	9 ± 4	1.01 ± 0.57

The coating on the plain grade of PET is found to possess the most defects and has a much higher spread of values. However, the values of error are so large that the difference between the samples may not be significant (8 scans were taken and the error is ± the maximum deviation from the mean - maybe a much larger area/number of scans is required to give a representative figure). In some scans barely any defects were counted while for others up to 30 were detected, indicating a large variability with the possibility that the high defect regions may be caused by debris on the substrate surface or damage caused during or post-deposition. It is difficult to conclude whether the intrinsic properties of the polymer film are causing the defect riddled microstructure, or that we simply have a “bad” sample where regions of the substrate were covered in debris/scratches/defects which cause the localised concentrations of defects. A greater number of scans on a wider scale would be useful to confirm how widespread and uniform the distribution of high defect areas was. The apparently porous microstructure

seems to be consistent with the higher WVTR value for this sample, suggesting that defects on this scale can contribute significantly to the water vapour permeation.

6.3.2 Gas barrier properties of Batch 2 coatings

A more detailed study of the gas barrier performance was possible for the second batch of coatings due to the fact that more samples had WVTRs within the range of measurement. The effective permeability of the coatings were calculated using ILT theory (Chapter 2.4), which assumes that the glass layer is homogenous and defect free [129]. No coating completely satisfies these criteria, due to the inevitable presence of pinholes and nanoscale defects, but in the next section it will be seen that very few pinhole defects exist in these films, so that using ILT may be considered valid, after Erlat *et al* [129]. From viewing the results in Table 6.5 we see that the 200 nm thick coatings only have a barrier improvement factor of 4-21, depending on the substrate, with the WVTR values for the coatings on PET and HS PET in particular comparing poorly to similar SiO_x coatings reported in the literature [80, 113]. By considering the effective permeability it can be seen that although the 200 nm SiO_x/PEN composite outperforms the equivalent filled PET material, the actual coating is inferior and the underlying substrate improves the observed WVTR for that composite. The effective permeability generally decreases with increasing thickness, suggesting that at 1000 nm the critical thickness is not yet reached and the quality of the barrier is superior for the layers deposited after the initial ones.

Table 6.5 Barrier performance of Batch 2 coatings (measurements taken at 50°C).

Substrate	h_c (nm)	Substrate WVTR (g m ⁻² day)	Composite WVTR (g m ⁻² day ⁻¹)	BIF	Effective permeability (μm g m ⁻² day ⁻¹)
PET	200	9.8	1.37	7	0.32
F-PET	200	15.0	0.73	21	0.15
HS PET	200	7.47	1.00	7	0.23
HS PET_P	200	7.47	0.48	16	0.10
PEN	200	3.02	0.71	4	0.19
PET	400	9.80	0.20	49	0.08
F-PET	400	15.0	0.16	94	0.06
F-PET	1000	15.0	0.09	167	0.09
HS PET	1000	7.47	<0.01	>750	<0.01
HS PET_P	1000	7.47	<0.01	>750	<0.01
PEN	1000	3.02	<0.01	>300	<0.01

In the case of F-PET a 200 nm thick coating causes the barrier to increase by a factor of 20, a 400 nm thick coating by a factor of almost a hundred and a 1000 nm one by a factor of 167 to 0.09 g m⁻² day⁻¹ at 50°C. It appears that even at 1000 nm we may not have reached the critical thickness (T_c) where minimum barrier is observed. Such high T_c 's have been observed by other authors for SiO_x [114, 115], interestingly using HMDSO as a precursor in both cases (in batch reactors), although the best WVTR values they report (~0.1 g m⁻² day in each instance) are not quite as low as the ones reported in this thesis. It is also worth noting that the F-PET composite outperforms that of the basic PET despite the extra roughness of the F-PET substrate and its lower thickness. In this case the filler particles certainly don't seem to reduce the barrier of the coating, as was suggested in Chapter 4.6 for sputtered TiO_x, which may be due to the deposition process itself as the

substrate is constantly moving for the PECVD deposition (which is also less “line of sight”) so that atomic shadowing is less of a concern than for the batch sputtered titania.

The increased thickness of the PECVD coating over the TiO_x one may also be relevant.

For the samples in Table 6.5 the water vapour permeation through the films was measured at a range of temperatures, with the aim of calculating the activation energy of permeation of water through the coated and uncoated films, so that insights could be gained into the mechanism of the permeation [10]. The Arrhenius type equation, that expresses the temperature dependence of the transport of gas and vapour through most glasses and polymers below glass transition temperature, T_g , was used:

$$\Pi = \Pi_0 e^{(-E_A/RT)} \quad (6.1)$$

where E_A is the apparent activation energy for gas transmission, Π is the transmission rate, R is the universal gas constant, T is absolute temperature and Π_0 is a constant unique to the system. The data obtained in the temperature range 30-50°C are shown in Figure 6.5 for coatings on the filled PET substrate and are used to calculate the E_A values discussed below. The scarcity of data points is a reflection of the limited range of measurement allowed by the Permatran equipment and the time constraints in obtaining sufficient reliable data.

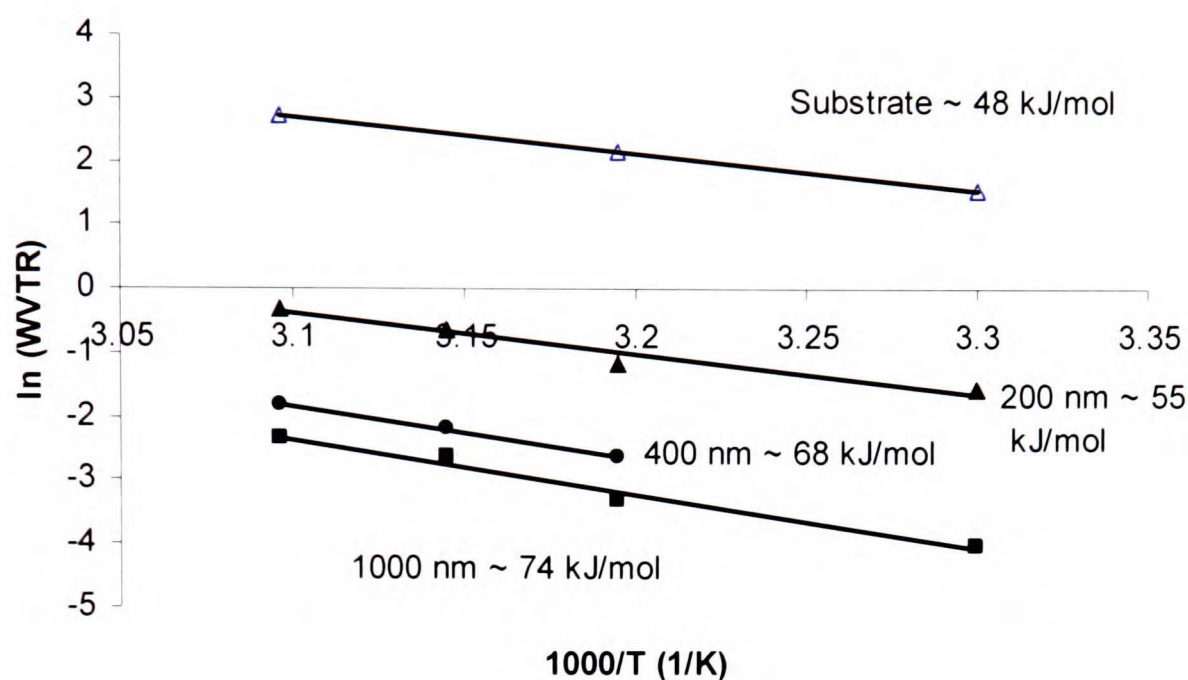


Figure 6.5 WVTR data for uncoated and SiO_x coated F-PET film.

For all substrates the activation energy of permeation for the 200 nm thick coated polyester is 4-7 kJ mol⁻¹ larger than the values of the plain substrates (see Table 6.6), indicating that more energy is required to transport the water through the composite than the polymer itself and that not all the permeation occurs freely through defects in the SiO_x. It is possible that the water permeation follows size-hindered pathways or chemically interacts with the silicon oxide, although the increase in E_A is small so either or both would only happen to a small degree. As coating thickness and gas barrier increase, particularly for the filled PET, the activation energy also increases up to a value of 74.4 kJ mol⁻¹ for the 1000 nm thick SiO_x layer. An explanation for this could be associated with the fact that for the 400 and 1000 nm thick coatings, the extra thickness is achieved by increasing the number of passes of the web through the deposition region. It is probable that these extra passes block off many of the defects that exist after the previous passes, in effect decoupling nanoscale defects and increasing the tortuosity of

the pathways extending through the coating, such that size-hindrance is a factor. This effect would also increase the probability of the water vapour chemically interacting with the SiO_x as it travelled through the film. However, it is unlikely that the water is interacting chemically with the SiO_x to a great extent as this would be more apparent in the 200 nm thick coatings - Tropsha and Harvey [80] notice significant interaction of water with SiO_x coatings of only 100 nm thickness leading to increased activation energy of 18-28 kJ mol^{-1} on a variety of substrates. Perhaps the high proportion of carbon reduces the number of polar interactions between water and the silica for the films reported here – Tropsha and Harvey detect no carbon in the bulk of their SiO_x layers (~10% on surface) and report a higher proportion of oxygen (stoichiometry of SiO_x ; $x = 1.9-2.2$).

Table 6.6 Activation energies of permeation for SiO_x films on polyester substrates.

Substrate	h_c (nm)	Substrate E_A (kJ mol^{-1})	Coated E_A (kJ mol^{-1})
PET	200	50	54
F-PET	200	48	55
HS PET	200	48	52
HS PET_P	200	48	55
PEN	200	55	59
PET	400	50	61
F-PET	400	48	68
F-PET	1000	48	74

WVTR values for the 1000 nm thick SiO_x on HS PET, HS PET_P and PEN are all below the limit of $0.01 \text{ g m}^{-2} \text{ day}^{-1}$ that our system can reliably measure, even at 50°C and with a conditioning time of 10 days to give the system full chance of reaching equilibrium, and show comparable performance to the Batch 1 coatings of this thickness. This signifies a barrier improvement of at least 300-750 times, depending on the substrate, and these

coatings outperform the equivalent layer on the F-PET which has a WVTR of $0.09 \text{ g m}^{-2} \text{ day}^{-1}$, despite this film comparing favourably with the others at 200 nm thickness (admittedly mainly due to substrate WVTR values which become less significant as coating thickness increases).

Measuring WVTR's of ultrahigh barriers presents a considerable challenge and the most widely used high sensitivity technique known at the moment is the calcium degradation test, reported by several authors for characterising gas barriers for OLED's [134, 145], and that has a limit of 10^{-5} - $10^{-6} \text{ g m}^{-2} \text{ day}^{-1}$. Mass spectrometry has also been used to measure low levels of water permeation [260] and was a technique used to characterise the WVTR of 1000 nm SiO_x on PEN, with the experiment carried out by Dr Holger Norenberg of Technolox Ltd. Unfortunately, time constraints meant that it was only possible to measure one sample, as the time to reach steady state for this system is particularly long. The principle of the method is conceptually simple (Figure 6.6) – a gas cell, containing a droplet of water and sealed with the sample to be tested, is positioned opposite a mass spectrometer inside a UHV chamber. Water vapour permeates through the sample and is detected by the mass spectrometer, which measures the partial pressure of the water. This is proportional to the WVTR and can be given in units of $\text{g m}^{-2} \text{ day}^{-1}$ after calibration against samples of known permeability. To improve the sensitivity of the technique, $^{20}\text{H}_2\text{O}$ is used as the permeant species to distinguish the permeating water from that which is present in the chamber, thus eliminating background “noise”.

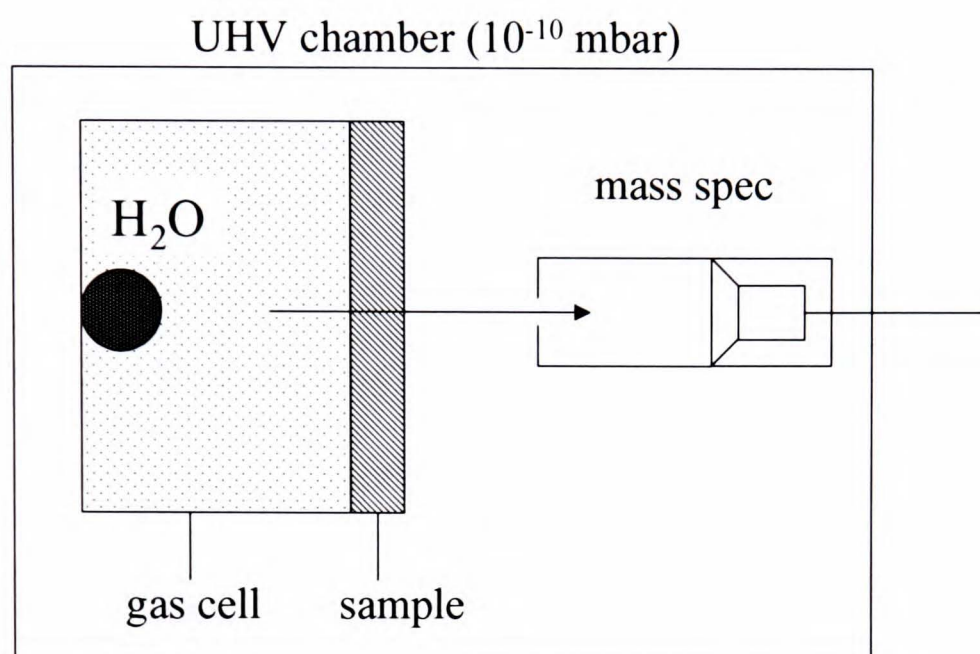


Figure 6.6 Schematic of mass spectrometric measurement of water vapour permeation through a thin film.

The value of WVTR for the 1000 nm film on PEN was found to be $2 \times 10^{-4} \text{ g m}^{-2} \text{ day}^{-1}$ at 25°C. This represents an improvement of ~5000 times over the bare substrate and is lower than WVTR's reported in the literature for single layer SiO_x. What makes the performance more impressive is that the silica is deposited using a roll-to-roll process that is traditionally hard to perform for PECVD.

With the knowledge that the coating is deposited in layers by passing it through the deposition zone multiple times, it is possible to suggest a schematic structure for the coating as it grows, which can explain the increased activation energy and barrier ability as the thickness increases. The initial layer is most prone to defects as it is in contact with the substrate, where debris and substrate thermal effects can cause imperfections in the silica, and is a poor barrier. Subsequent layers “block off” existing defects in the layer immediately below, so that no defects propagate through the whole film after a number of

layers are deposited and a degree of chemical interaction of water with the SiO_x is expected to take place. As suggested by the effective permeability data in Table 6.5 it is possible that the layers deposited directly upon silica, rather than the polymer substrate, nucleate more densely and are intrinsically better barriers, due to the favourable surface chemistry and surface thermal properties of SiO_x over the polyester. Other factors, such as substrate cooling and reheating in between passes, application of reverse tension and passing through the plasma in the “opposite direction” (if the plasma is in any way unsymmetrical) may all affect the nucleation and growth of subsequent layers.

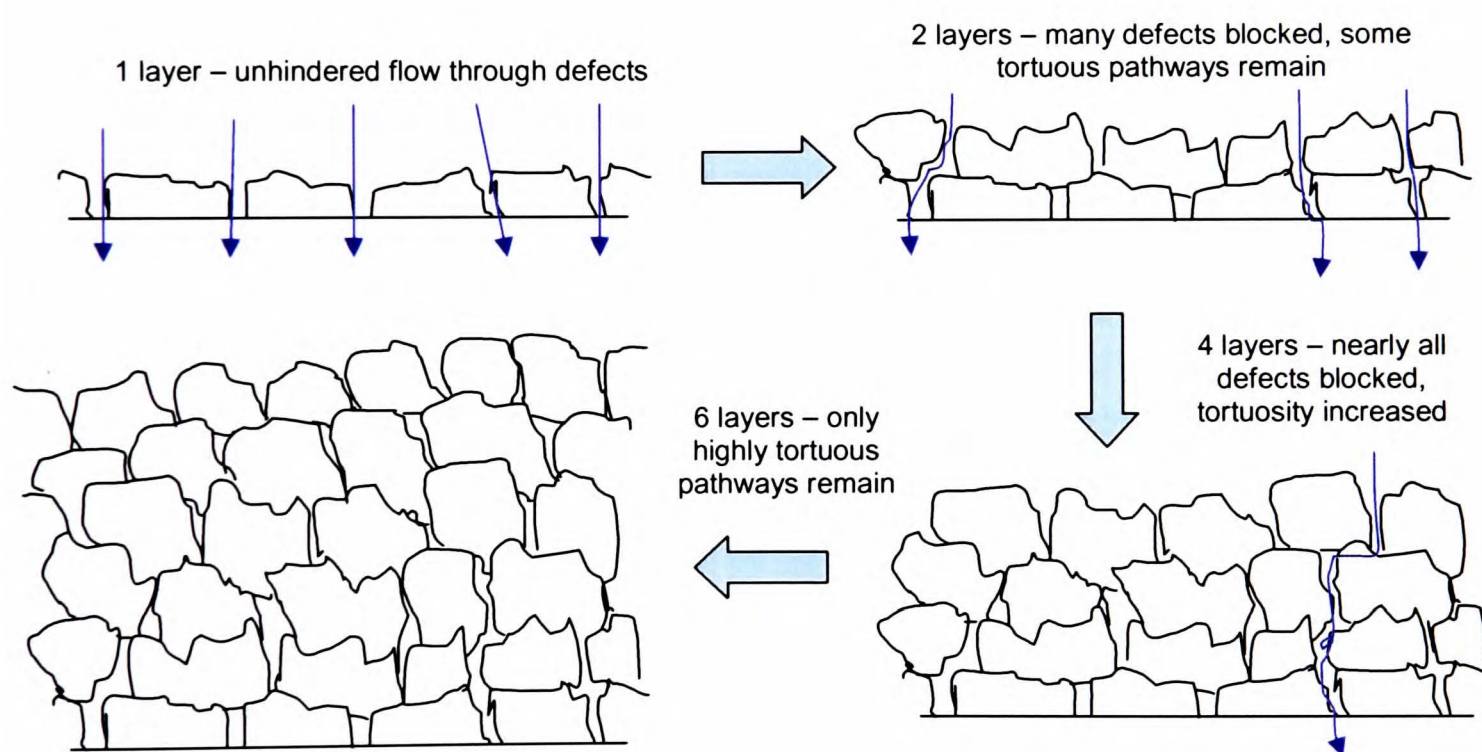


Figure 6.7 Schematic of SiO_x coating structural development as it is deposited in multiple passes.

The principle of this structure is similar to the multilayer stacks of inorganic/organic material but it has the advantage of not needing to deposit polyacrylate layers in between the oxide, which presents several technical difficulties. However, the multilayer stacks have lower reported values of WVTR than the best SiO_x film reported here. The proposed

“multilayer” structure will be useful when we consider the mechanical properties of the coatings.

6.3.2.1 Microstructure of Batch 2 coatings

The deposited SiO_x is found to coat the substrate conformally, and fully covers protruding filler particles as shown in Figure 6.8. Such good coverage reduces the chances of pinhole creation both from filler particles and also any other debris that may be present on the surface, such as dust. By examining a series of SEM images at 3000x magnification, a minimum of pinhole and other large-scale defects ($>0.5 \mu\text{m}$ in diameter) are detected, the defect density being less than 100 mm^{-2} . For the filled PET film this is a much lower density than for the china clay particles (4000 mm^{-2}) indicating that they do not create many defects in the deposited film. The coatings on the plain PET film display more pinholes, approximately 300 mm^{-2} , which could be due to the fact that it is the cheapest grade of film examined here and less effort is made by the manufacturers to ensure the surface is clear of large protrusions such as dust.

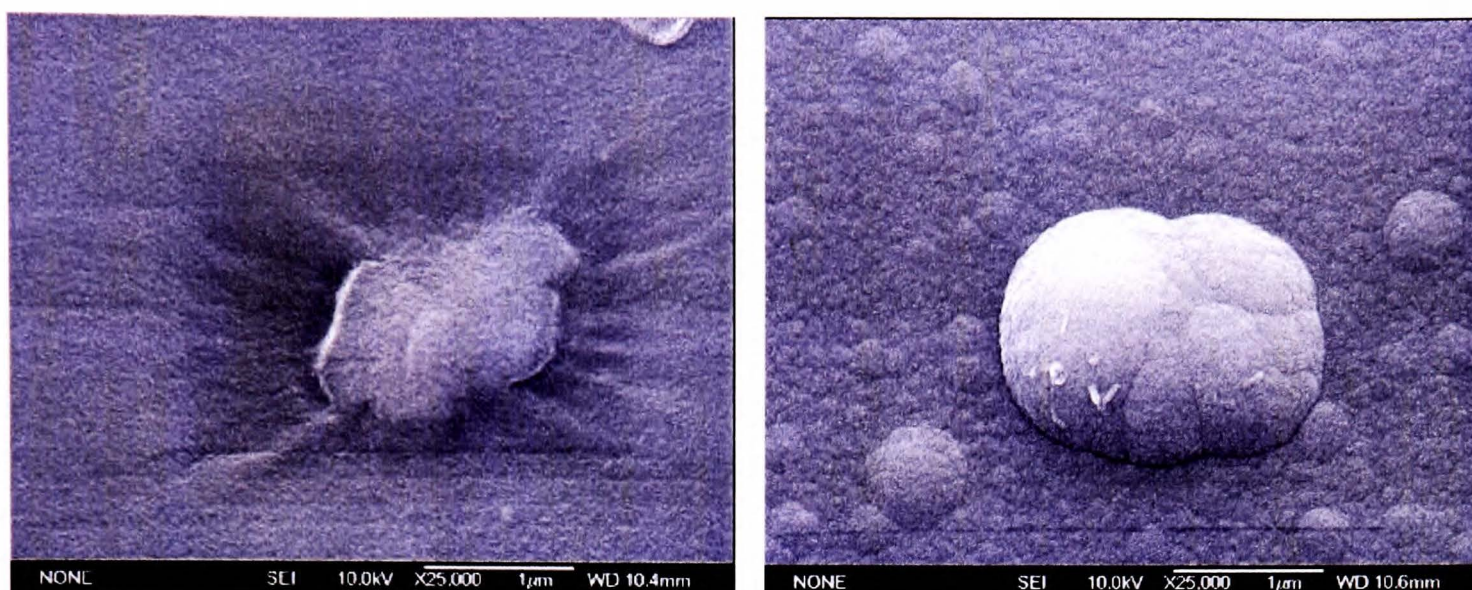


Figure 6.8 SEM micrograph of a) a china clay particle in the F-PET film, b) good coverage of a filler particle by the SiO_x coating.

The morphology of the SiO_x coatings examined by AFM is characterised by closely packed grains varying in diameter from 80 nm to 300 nm. Much more variation in size is noticed for the coatings on the filled PET and the primer layer, whereas the coatings on the HS PET and PEN have grains consistently of a size of 150-200 nm. The roughest substrate, the HS PET_P, produces the roughest coating and despite this it is one of the most effective barriers and it seems that coating roughness has little influence as to what is the best barrier in this instance. The general trend is for the smoother substrate, the smoother the coating, the one exception being for the filled PET where, even in the regions with no filler particles there is an increased roughening and a large variation in particle size as shown in Figure 6.9. Why this should be is difficult to explain as large grains of SiO_x are located randomly over the surface and not concentrated around the filler particles, suggesting that atomic shadowing is not a factor.

The quantity of nanometre-scale defects was also estimated for the thickest coatings using the flooding method. An example is shown in Figure 6.9.

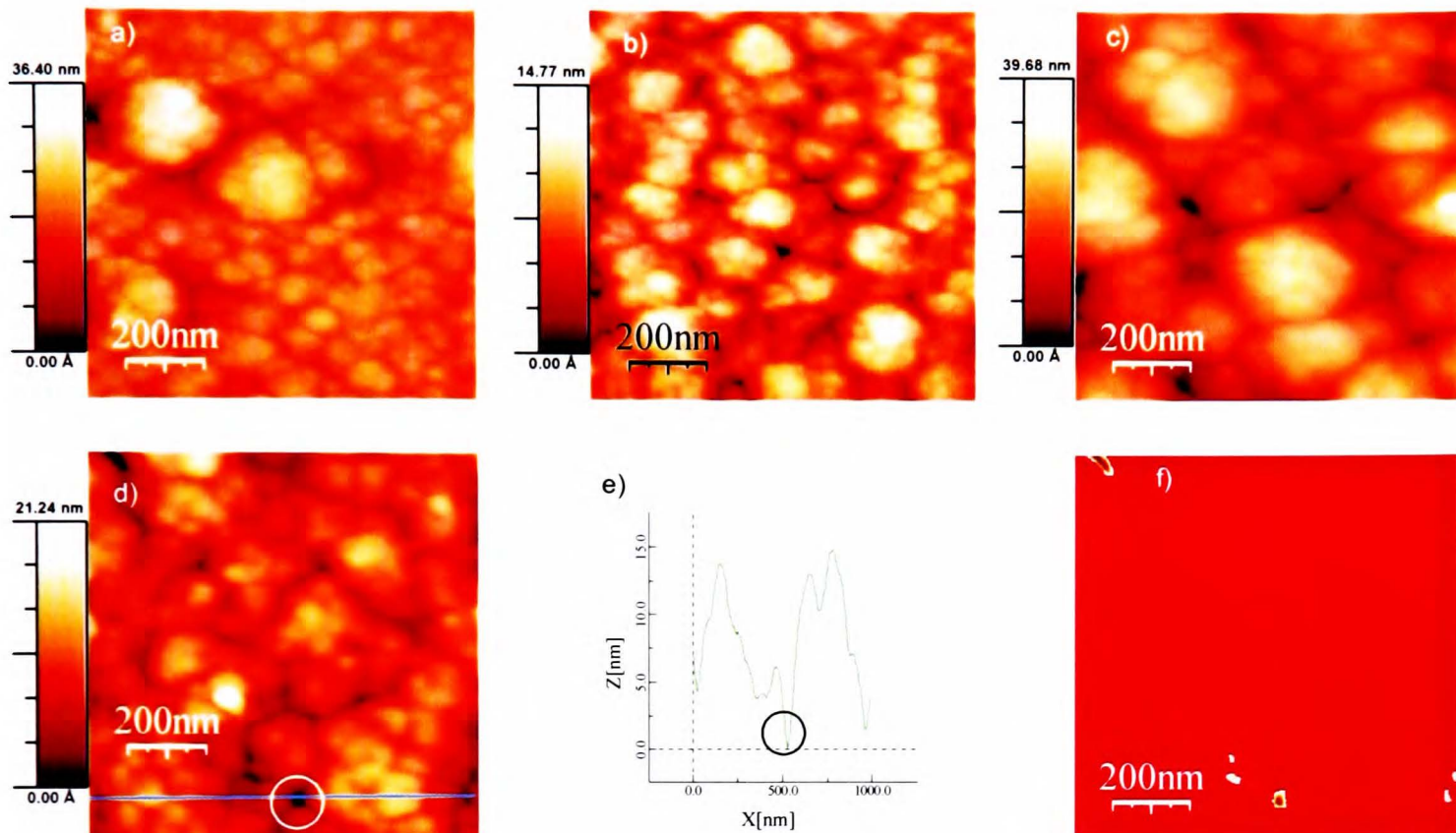


Figure 6.9 1 x 1 μm AFM images of the morphology of 1 μm thick SiO_x coatings on a) F-PET, taken from a region between filler particles, b) HS PET, c) HS PET_P, d) PEN with a possible defect ringed, e) a line profile from image (d) showing possible defect and f) flooding analysis of image (d).

For 1 μm thick SiO_x on each substrate the coverage of defects detected in the films is less than 1% and the average number of defects less than $10 \mu\text{m}^{-1}$ (averaged from 10 scans). There is a large spread (standard deviation) in these figures, showing an uneven distribution of defects and possibly flaws in this quantitative method. For the thinner coatings, the particle size is slightly smaller but the coverage of defects is similar for all thicknesses, within error, although fewer scans (typically 3-4) have been carried out for the thinner films. Currently, there are few ways of quantifying these defects accurately although there are examples in the literature where TEM has been used to detect pores in the 0.5-5 nm range [123].

Table 6.7 Microstructure of 1 μm thick SiO_x coatings on polyester substrates.

Substrate	Coating thickness (nm)	Substrate R_q (nm)	Coating R_q (nm)	SiO_x average particle size (nm)	Defect density (μm^{-2})	Defect surface coverage (%)
HS PET	1000	1.5	2.7	194 ± 63	9 ± 3	0.66 ± 0.51
HS PET_P	1000	6.2	6.4	273 ± 63	4 ± 3	0.68 ± 0.52
F-PET	1000	1.0*	4.6*	142 ± 116	4 ± 2	0.51 ± 0.27
PEN	1000	1.6	3.9	145 ± 34	7 ± 3	0.65 ± 0.18

*in areas where no filler particles are present

6.4 Internal Stresses

6.4.1 Batch 1

The values for the internal stress, σ_i , in the coatings are negative and all less than -200 MPa (Table 6.8) indicating a small amount of compressive stress present in these films, similar to values for much thinner (7-100 nm) PECVD SiO_x films reported in the literature [155, 167]. Considering how thick these films are, such low values of stress are surprising as stress in brittle coatings is expected to either increase with thickness or relax due to cracking. The latter does not appear to be happening as the barrier properties are very good, and nothing of this nature was detected by microscopy. The large amount of carbon in the film is thought to give it a more flexible, organic character with a lower degree of brittleness.

Before considering the origins of the stress it is worth recapping that it can comprise of intrinsic, growth related stress or thermal stress – a result of the different thermomechanical properties of the polymer and SiO_x . The thermally induced stress is

down to two factors – the first is the difference in the natural expansion/contraction (LCTE value) between the two materials upon a change in temperature, which results in the substrate shrinking to a greater degree than the silica upon cooling after deposition, no matter what temperature is experienced. The second is down to thermal shrinkage of the polymer film as a result of chain reorientation/crystallisation – only above the T_g . Generally, intrinsic stress and any post-deposition ageing stress will be similar for coatings on all substrates where the deposition process and storage conditions are the same – major differences arise because of the thermal factors described above.

It is possible to estimate the maximum substrate temperature during deposition by assuming that all the stress is thermal in origin (due to natural thermal expansion), following Leterrier for PECVD coatings [8], and using Equation 6.2 for thermal stress, σ_T :

$$\sigma_T = (E_c / (1 - \nu_c)) \cdot (\alpha_s - \alpha_c) \cdot (T_2 - T_1) \quad (6.2)$$

where E_c = coating Young's modulus (80 GPa), ν_c is the coating Poisson's ratio (0.2), α_s and α_c are the coefficients of thermal expansion (CTE) of the substrate (values in Table 6.4) and coating ($2.7 \times 10^{-6} \text{ K}^{-1}$) respectively. T_2 is the temperature before and after deposition (i.e. ambient room temperature, 20°C) and T_1 is the deposition temperature. The maximum temperature of deposition is found to be over 110°C – way above the PET T_g and close to that of PEN, which would cause thermal shrinkage of the PET film. However, the contribution due to thermal shrinkage of the substrate is assumed to be

close to zero as the PET is most prone to shrinkage, yet has the lowest stress. It therefore appears that there is a significant contribution to the internal stress associated with the growth of the coating and as such our values of T_D are a large overestimate. It is likely that the deposition temperature is close to, or below the glass transition temperature of PET (80°C) if thermal shrinkage is not a factor.

Table 6.8 Internal stresses and strain values of PECVD SiO_x coatings.

Substrate	Internal Stress (MPa)	Internal Strain (%)	CTE (10^{-5} K^{-1}) [6]	T_D (°C; range in brackets)
PET	-142 ± 28	-0.12 ± 0.03	16	113 (95-131)
HS PET	-170 ± 23	-0.15 ± 0.02	19	111 (99-124)
HS PET_P	-148 ± 40	-0.13 ± 0.04	19	99 (77-120)
PEN	-188 ± 6	-0.16 ± 0.01	20	115 (112-118)

Finally, a note concerning the error limits quoted for the internal stress and strain. The average value is simply the mean value of four calculated values, each obtained from a different curvature measurement, and the reported error is the difference between the mean and the data point furthest away from it. This is likely to be an overestimate but the small data sets render any more sophisticated statistical methods unsuitable.

6.4.2 Batch 2

The internal stresses for each thickness of SiO_x on the polyester substrates were measured and the results are shown in Table 6.9.

Table 6.9 Internal stress values for PECVD SiO_x coatings of different thickness – Batch 2.

Substrate	Internal Stress (MPa) 200 nm SiO _x	Internal Stress (MPa) 400 nm SiO _x	Internal Stress (MPa) 1000 nm SiO _x
PET	-852 ± 82	-648 ± 23	N/A
F-PET	-60 ± 9	-68 ± 12	-78 ± 14
HS PET	-452 ± 41	-426 ± 21	-483 ± 20
HS PET_P	-352 ± 12	-335 ± 36	-517 ± 16
PEN	-333 ± 54	-287 ± 40	-195 ± 18

The stress values for the filled PET are negligible and much lower than for the other films. Initially it was thought that the filler particles may have been responsible for stress concentrations in the silica that resulted in cracking and therefore stress relaxation. However, no cracks were observed in these samples by AFM/SEM and no obvious degradation in barrier is noticed for these samples. It was noted however that the coated film has a much larger radius of curvature in the machine direction of the roll, with a related stress level of 400-600 MPa for each thickness. This phenomenon is shown in Figure 6.10 and is not observed to be significant for the other composites. The F-PET film is anisotropic in that it has poorer mechanical properties and is much more prone to shrinkage in the machine direction (Table 4.5), whereas the other films are fairly isotropic, especially in terms of thermal shrinkage. Perhaps preferential curvature in the machine direction, due to the anisotropy of the substrate (as it shrinks preferentially in the MD), results in little curvature in the transverse direction and the resultant low stress. The curvature in the MD also makes it hard to measure that in the TD and it is possible that the curvature was underestimated in the TD.

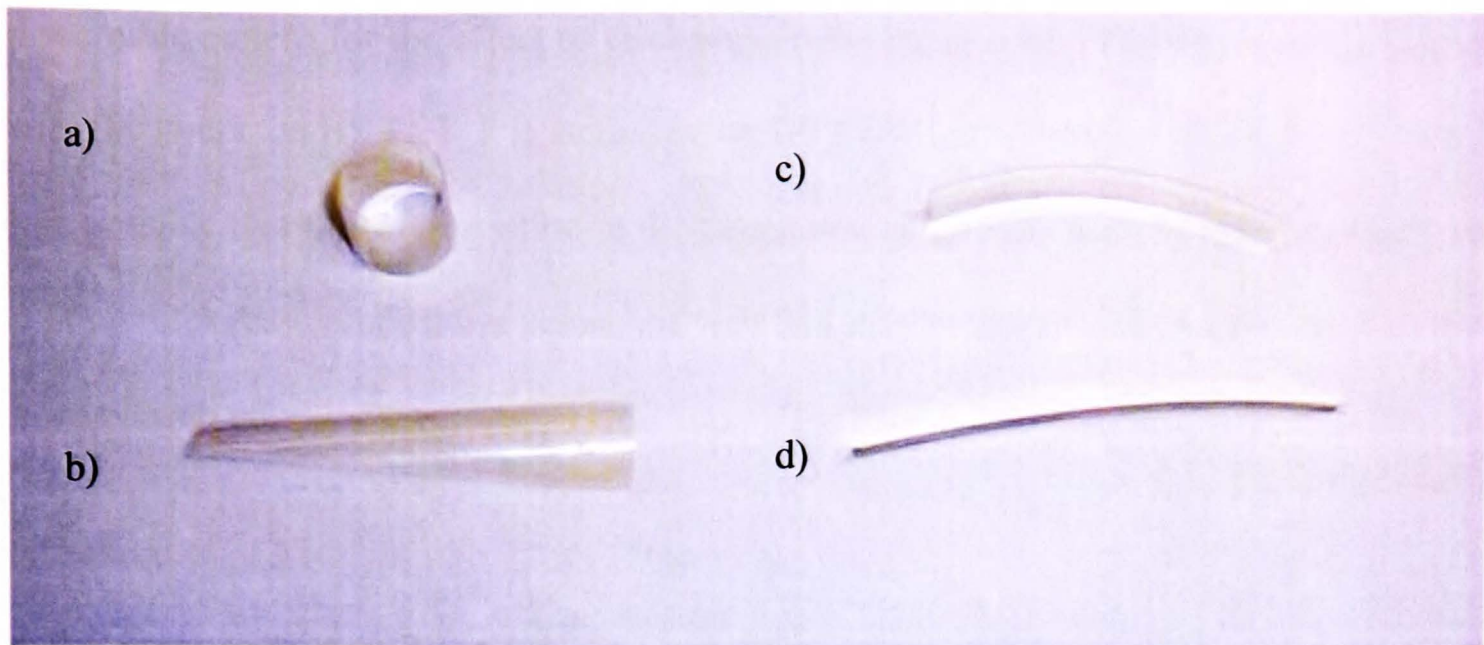


Figure 6.10 Curvature of polyester-SiO_x composites for 1 μm thick coatings showing anisotropy in MD and TD; a) F-PET MD, b) F-PET TD, c) PEN MD, d) PEN TD.

For the remaining samples the stress is higher than for the Batch 1 coatings, suggesting that a higher deposition temperature or denser coatings result from this process, as a result of the more intense plasma used in the deposition. The stress is much higher in the SiO_x on PET films and this could be a result of substrate thermal shrinkage as the plain PET is much more susceptible to this than the other films. The fact that the amorphous PET film visibly suffered from a larger amount of thermal shrinkage supports this assertion. Generally, the coatings on PEN are under less stress than those on HS PET films which is surprising - even though the T_g of PEN is higher, the heat stabilisation process should mean that negligible shrinkage is observed for the HS PET films and similar values of stress should be apparent (in fact the PEN film would be more prone to shrinkage above 120°C, so higher stress for the PEN/SiO_x might be expected). The suggestion is that the internal stresses for the silica on the PEN and heat stabilised substrates are completely due to the growth related stress or differences in LCTE values and there is some natural variation in the deposition conditions. Finally, there is no

discernible pattern for the effect of thickness on the stress – on PEN the stress decreases with thickness, on HS PET_P it increases, on HS PET it is constant – which is confusing. It is possible that there is variation in the deposition conditions from sample to sample or coating thickness/composition across the web that may be responsible for the inconsistent trends observed.

6.5 Fragmentation Testing

6.5.1 Batch 1

The key stages of the fragmentation process for a 1 μm thick coating on PET are shown in Figure 6.11. Micrograph (a) shows a crack originating from a defect at the crack onset strain of 0.6%, (b) is taken at 5% strain with many more vertical cracks apparent and, in addition, transverse (horizontal) cracking, a result of compressive stress caused by the contraction of the substrate and (c) shows the saturation stage of the process when no more cracking is apparent and delamination is observed. The whitish patterns at the ends of some fragments are fringes resulting from multiple reflections of light at zones debonded under strain. The graph of crack density against applied strain, shown in (d), displays differences in the cracking behaviour for the silica layers on PET, PEN and the HS PET_P substrates. First, the COS observed for the PET composite is lower than that of the PEN sample by more than 0.2% while the coating on the HS PET_P almost matches that on PEN. Secondly, a much higher density of cracks is observed for the SiO_x on the primer coated film (~50% higher than the other films) which is a qualitative indicator of superior adhesion.

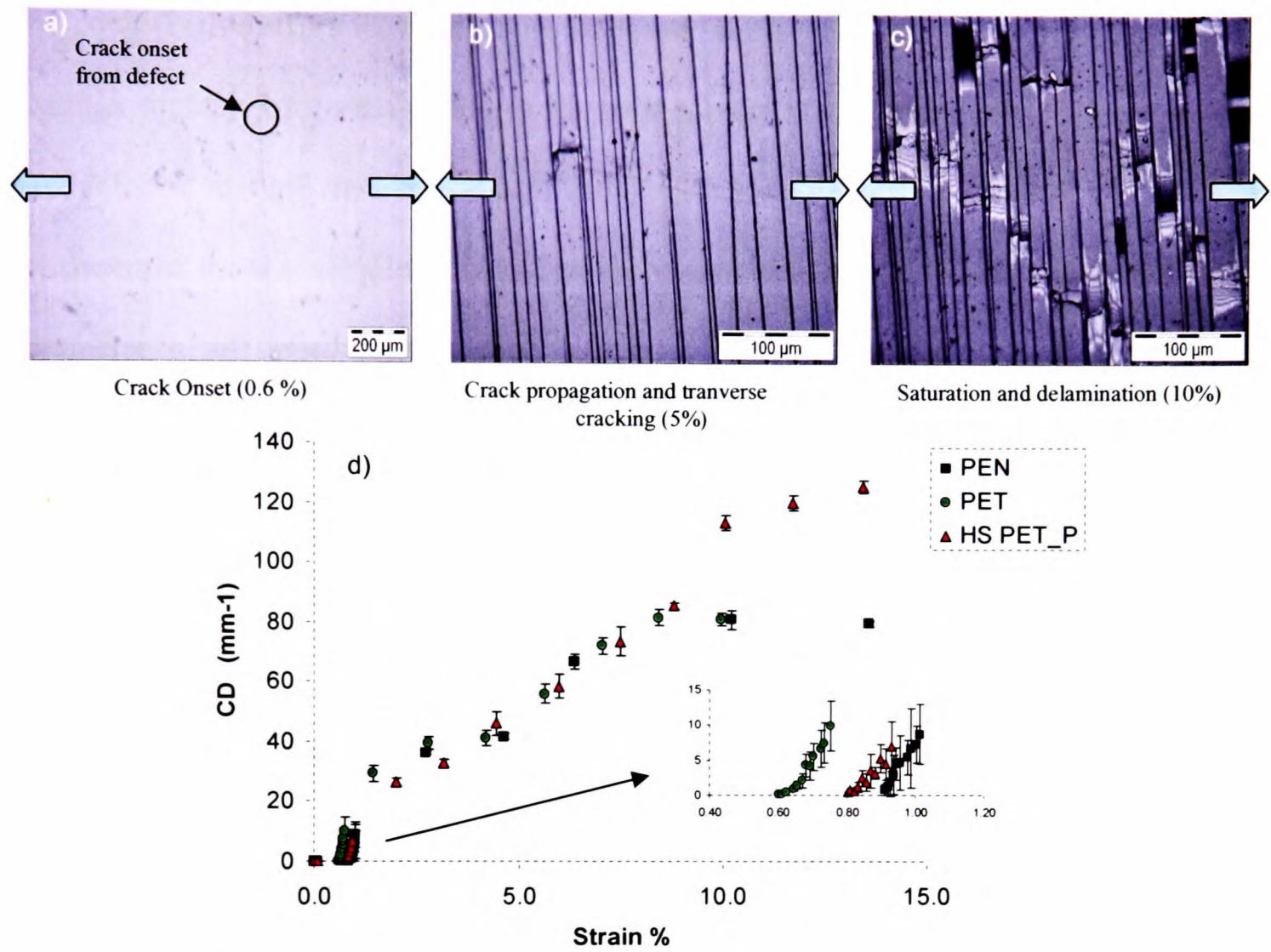


Figure 6.11 (a), (b) and (c) show fragmentation of the SiO_x coatings at various, labelled degrees of strain, using reflection optical microscopy, with the arrows indicating the direction of tensile load, (d) is a plot of crack density as a function of applied tensile strain, inset is a close-up of the initial cracking region below 1% strain.

Table 6.10 summarises the data obtained from fragmentation testing of the four coated polymer films, including crack onset strains and the coating cohesive strength and Weibull parameters.

Table 6.10 Weibull Parameters and Cohesive Strength for PECVD SiO_x coatings.

Substrate	COS (%)	COS* (%)	α	β (GPa)	$\sigma_{max}(l_c)$ (GPa)	$\sigma_{max}^*(l_c)$ (GPa)
PET	0.68 ± 0.07	0.56 ± 0.07	19 ± 7	0.82 ± 0.19	0.63 ± 0.10	0.53 ± 0.10
HS PET	0.83 ± 0.03	0.67 ± 0.03	13 ± 1	1.08 ± 0.01	0.82 ± 0.01	0.72 ± 0.01
HS PET P	0.82 ± 0.02	0.68 ± 0.02	17 ± 2	1.00 ± 0.04	0.81 ± 0.03	0.71 ± 0.03
PEN	0.92 ± 0.06	0.76 ± 0.06	22 ± 9	1.05 ± 0.04	0.86 ± 0.03	0.73 ± 0.03

The compressive stress in the films is shown to improve the observed properties of the coatings slightly, by a similar degree for each substrate. The coating on PET is found to have inferior strength than the other films and the lowest crack onset strain and β values are observed for this sample. It is interesting to note that the values of the Weibull shape parameter, α , are approximately equal within error (which for some samples is large due to the difficulty of obtaining sufficient data in the early fragmentation stage) and are all above ten. This shows that the coatings are good quality ceramic materials with a relatively narrow distribution of failure stresses and therefore a narrow range of defect size. The values of α reported in the literature for SiO_x coatings tend to be much lower (<10) [168, 170, 171]. Figure 6.12 shows how the values of alpha and beta affect a cumulative distribution function (cdf) for probability of failure $P(f)$ of coating fragments, as a function of stress. An increase in alpha shifts the cdf to the right and results in a lower range of failure stresses, an increase in beta expands the cdf to the right and results in a higher range of failure stresses but only towards the high stress region (effectively increasing the average fragment strength).

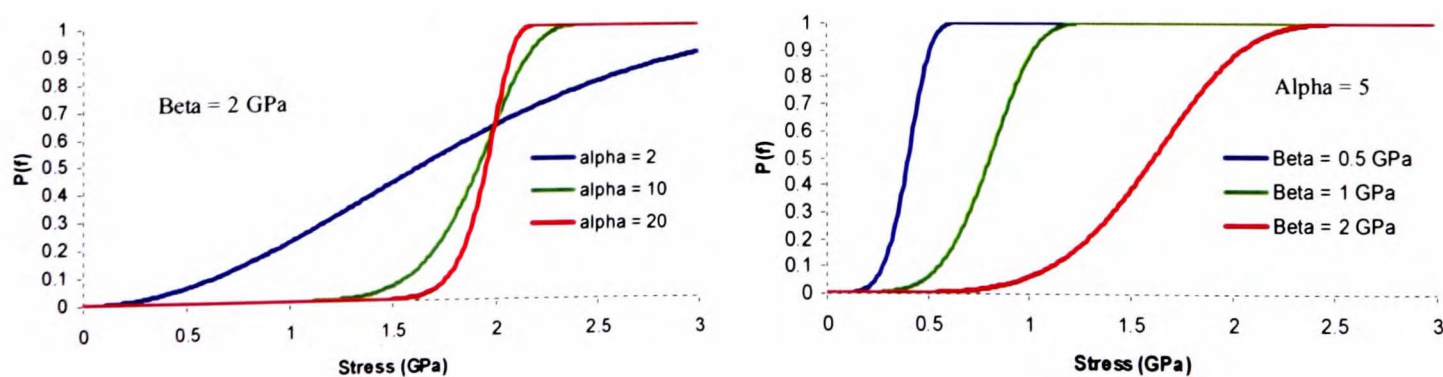


Figure 6.12 The effect of alpha and beta on the cumulative distribution function for the probability of coating failure as a function of stress. (For fragment length = 1 μm).

6.5.1.1 A note concerning the error bounds for fragmentation test data

Only 3 fragmentation tests were performed for each sample, due to severe time constraints on equipment access in Lausanne, making it difficult to obtain results that were statistically significant. The values of COS, α , and β in Tables 6.10-6.12 are simply the mean of three experimentally determined values with the maximum deviation of the raw data from this value giving the precision. For the quoted values of $\sigma_{max}(l_c)$, the value for each of three samples was calculated from each sample's respective values of α , β and l_c , and then the mean and precision was determined as before. For the intrinsic values of COS and strength, the error limits were taken to be the same and the mean value of internal stress for each sample was used in the calculations. The variation in the value of internal stress has little impact on the calculated values of COS* and $\sigma_{max}^*(l_c)$ and was ignored. In Tables 6.13 and 6.14 the value of CD_{sat} is simply the mean of 3 individual measurements and the error limits are the maximum deviation from the mean. The IFSS has been calculated for each sample from its respective measured variables and the average and error value determined as mean and maximum deviation of the resulting values. Error in the coating thickness was not accounted for but the thickness should be the same on each substrate (for identical processing conditions) – we are more concerned with comparing substrate effects, not necessarily the absolute values. For silicon wafers coated simultaneously with the film, the measured thickness was found to be very close to the quoted values and the range of error sufficiently small not to include it in the calculation of interfacial shear strength.

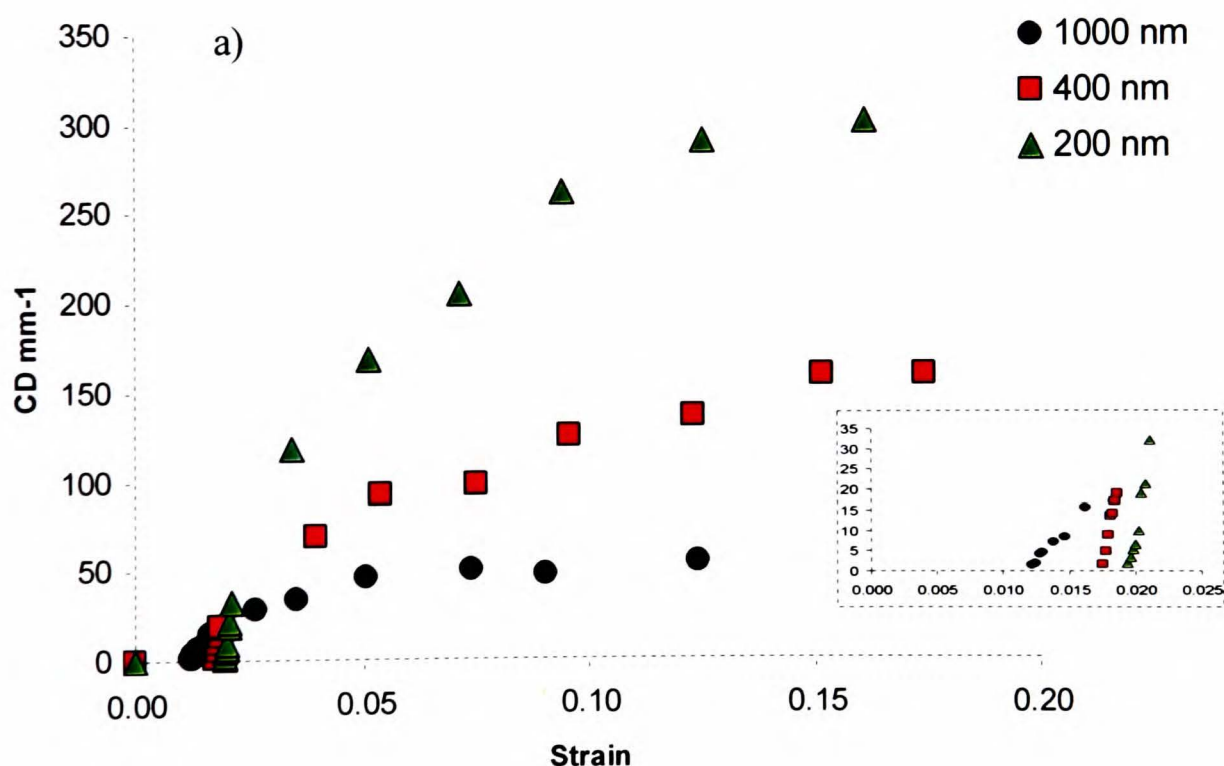
6.5.2 Fragmentation testing of Batch 2 samples

Fragmentation testing was performed for each of the three different thicknesses of silica on each substrate and we concentrate in this section on the thickest and thinnest samples (1000 and 200 nm respectively). The properties of the 400 nm SiO_x are practically identical to the 200 nm layers and are not reported in detail to avoid repetition. As we saw in Section 6.5 there are large differences in the internal stresses for each substrate and thickness so that the intrinsic material properties, COS^* and $\sigma_{\text{max}}^*(l_c)$, will give more useful comparison between the substrates than the observed properties. For the 200 nm thick SiO_x coatings it is seen that the deposit on PET has the largest crack onset strain and the highest strength of all the samples. However, this is due to the large amount of internal stress in this coating so that the intrinsic properties are actually the worst out of this sample set. This could be a result of the formation of defects caused by thermal motion of the polymer at the substrate surface during the initial deposition pass. The filled PET has the worst observed properties but because of the negligible stress measured in the TD for these films, the intrinsic strength and crack onset strain turn out to be the best. This is a clear indication that for these materials the filler particles do not promote defects in the SiO_x and that the F-PET film actually enhances the structure of the coating in some way, although the difficulties in measuring the stress for this film make this conclusion far from secure. Another important note to make about these films is the high values of alpha observed for the coatings – indicative of a high quality of ceramic with a very narrow range of failure stresses.

Table 6.11 Mechanical properties of 200 nm thick SiO_x films on polyester substrates.

Substrate	COS (%)	COS* (%)	α	β (GPa)	$\sigma_{max}(l_c)$ (GPa)	$\sigma_{max}^*(l_c)$ (GPa)
PET	1.84 ± 0.12	1.11 ± 0.19	29 ± 7	1.90 ± 0.14	1.68 ± 0.09	1.12 ± 0.14
F-PET	1.49 ± 0.11	1.43 ± 0.11	25 ± 5	1.56 ± 0.16	1.39 ± 0.16	1.34 ± 0.18
HS PET	1.67 ± 0.27	1.27 ± 0.29	31 ± 6	1.64 ± 0.22	1.48 ± 0.2	1.17 ± 0.22
HS PET_P	1.58 ± 0.08	1.27 ± 0.08	21 ± 1	1.63 ± 0.02	1.46 ± 0.01	1.22 ± 0.01
PEN	1.74 ± 0.2	1.45 ± 0.21	27 ± 9	1.71 ± 0.15	1.52 ± 0.17	1.30 ± 0.2

The plot in figure 6.13(a) shows how in general thicker films fragment earlier and more slowly than thinner ones, which is due to the wider size distribution of the defects in the thicker coatings (data taken for SiO_x coatings on F-PET). Thinner films also exhibit a much higher crack density at saturation.



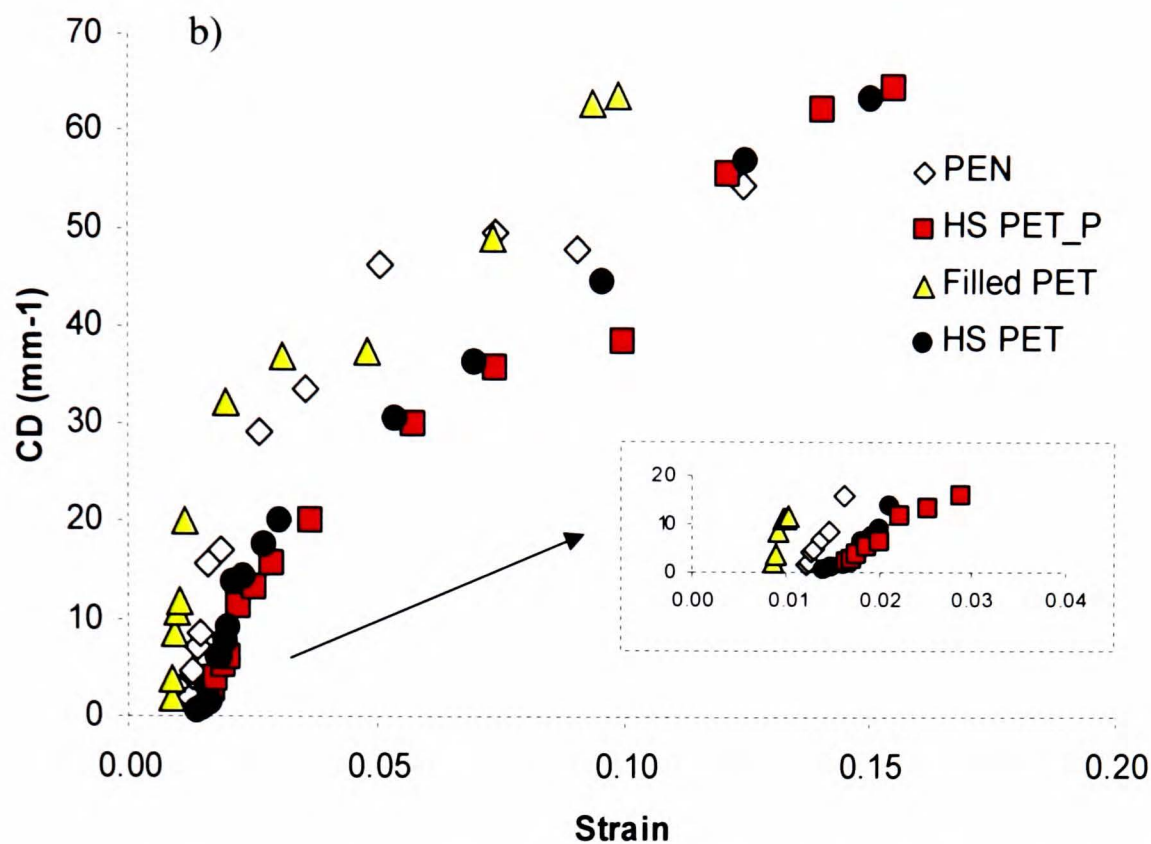


Figure 6.13 (a) Plot of CD against applied strain for 3 thicknesses of SiO_x coating on F-PET, (b) Plot of CD against applied strain for 1 μm thick SiO_x coatings on different substrates.

Plot 6.13(b) shows the different fragmentation characteristics for 1 μm-thick coatings on four substrates with the superior properties of the HS PET_P composite being noticeable. The coating on the F-PET substrate is seen to behave particularly poorly and even after stresses are accounted for is the weakest coating at that thickness (Table 6.12). The properties of the films are inferior at 1 μm thickness than 200 nm, with a lower observed value of alpha that results in lower crack onset strains and cohesive strength of the fragments at critical length (due to their size). The exception to this is the coating on the HS PET_P substrate that actually displays comparable properties at each thickness of SiO_x, despite the lower alpha value.

Table 6.12 Mechanical properties of 1 micron thick SiO_x films on polyester substrates.

Substrate	COS (%)	COS* (%)	α	β (GPa)	$\sigma_{max}(l_c)$ (GPa)	$\sigma_{max}^*(l_c)$ (GPa)
F-PET	0.92 ± 0.05	0.85 ± 0.05	8 ± 3	1.65 ± 0.24	1.00 ± 0.03	0.95 ± 0.02
HS PET	1.26 ± 0.16	0.84 ± 0.15	10 ± 1	2.04 ± 0.57	1.39 ± 0.26	1.07 ± 0.27
HS PET_P	1.61 ± 0.11	1.16 ± 0.12	9 ± 2	2.44 ± 0.31	1.66 ± 0.11	1.31 ± 0.12
PEN	1.16 ± 0.06	0.99 ± 0.06	8 ± 2	2.14 ± 0.47	1.3 ± 0.1	1.17 ± 0.1

The mechanism of the coating process may help to explain the poorer performance of the thicker coatings, and the more noticeable substrate effects observed. The 200 nm coatings can be thought of as being formed of two 100 nm thick layers, as this is the thickness of SiO_x deposited in each pass. The 1000 nm coating on the other hand would in effect consist of 6 x 167 nm thick layers. It may well be that for these coatings the web speed and number of passes is an important factor in determining coating properties, particularly the speed of the initial pass where the coating is deposited upon the virgin polyester. A pertinent factor may be the heating effect caused by deposition, which increases the temperature at the polymer surface to or above the region of T_g . Such heating may cause relaxation of constrained amorphous chains and in addition could induce crystallisation at the surface. The molecular motion of polymer chains at the surface may be responsible for creating defects in the interfacial region. For the thinner coatings (200 and 400 nm where the substrate passes through the deposition zone more quickly) this heating will be less severe and the volume of the coating deposited in the initial pass that experiences any adverse effects due to polymer motion or crystallisation will also be less than that for the 1000 nm coating. The deposition of the latter will cause more substrate heating due to the slower web speed and there will be a larger volume of coating deposited on the initial pass that would be affected by such substrate effects. Therefore the heat stabilised PET and PEN composites see less deterioration in quality

than the filled PET as they are more resistant to heat. Both 200 nm and 1000 nm coatings on the primer-coated HS substrate exhibit almost identical mechanical behaviour, indicating that the primer surface is not adversely affected by the heating experienced during deposition. Maybe, because the temperature of deposition is greater than the T_g of the acrylate, the surface of this film will be soft and allow the oxide to stick easily and form a dense layer without the acrylate molecules contracting and moving the initial SiO_x deposits around. It is assumed that the acrylate chains are unoriented, due to the heat stabilisation step after the drawing process. Consequently, they are not expected to relax during deposition, despite the temperature being above the T_g of the primer (the underlying PET doesn't shrink either as it is also heat stabilised).

Bearing in mind the multilayer-like structure proposed in section 6.3.2 and the permeation data supporting it, it is likely that defects don't propagate through the film so that the thickness produced by an individual pass controls the mechanical properties and the defect size. Therefore the 200 and 400 nm thick coatings would be characterised by the mechanical properties of the initial 100 nm thick layer and the 1000 nm thick coating by the initial 167 nm thick layer (because the initial layer is likely to have most defects due to the substrate roughness and polymer chain motion). This is supported by the very similar properties of the 200 nm and 400 nm thick coatings and the fact that the 167 (1000) nm thick layer still behaves worse than the 100 (200 and 400) nm thick ones.

The crack onset strains and strength of the PECVD coatings compare particularly well with thinner silica coatings reported in the literature. As an example the 200 nm and 400

nm thick coatings (and even a 1000 nm thick coating on HS PET_P) described here display very similar COS and $\sigma_{max}(l_c)$ values to 100 nm thick SiO_x coatings reported by Leterrier *et al.* [161, 168], accounted for by the fact that their behaviour is characterised by the initial deposit of 100 nm. More recently, coatings as thin as 7 nm have been fabricated that display COS values up to 6% and cohesive strength of 9 GPa but at present a relatively poor barrier is a consequence of their thinness [155].

6.5.3 Adhesive strength of the composites

To illustrate a number of important points the results from Batch 1 and Batch 2 will be reported together and a few general points about the theory and observed values of IFSS will be outlined. One of the assumptions of the Kelly-Tyson model of interfacial shear stress is that the stress experienced by the coating is from shear forces, caused by bonds at the interface as the polymer yields beneath it, and is limited by the strength of the interface or the polymer under shear, whichever is the weakest (plastifies first). If the polymer substrate becomes completely plastic then no more stress can be transferred across the interface to cause further cracks and saturation will be observed (Figure 6.13).

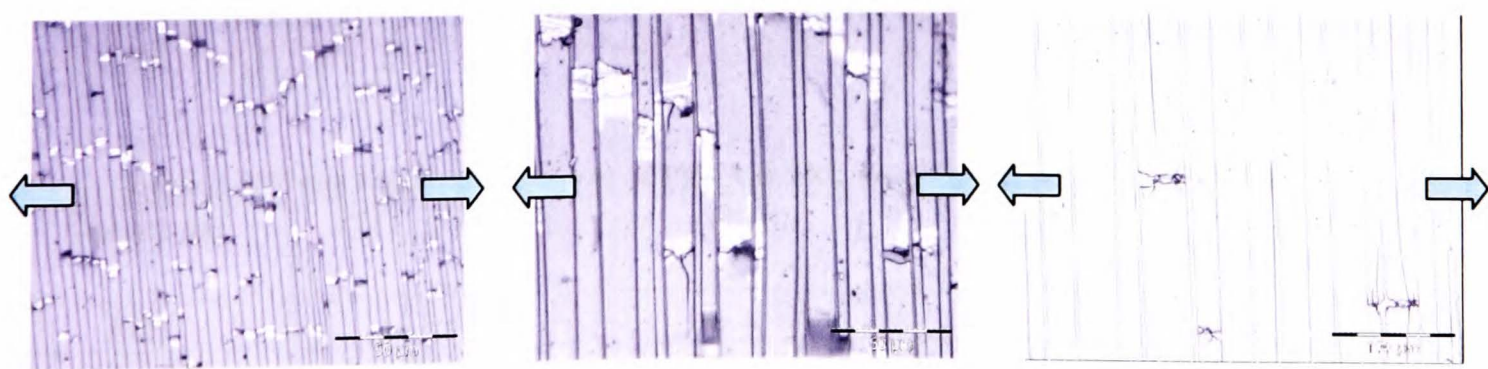


Figure 6.13 Reflection optical microscopy images of the saturation stage of cracking for (l-r) 200, 400 and 1000 nm thick SiO_x on PEN substrate. The tensile load was applied in the horizontal direction.

It is therefore interesting to note that once internal stresses are accounted for, the intrinsic interfacial shear strength τ^* is found to be equal to, or greater than, the substrate shear yield stress for each composite at any coating thickness and from either batch (Tables 6.13 and 6.14). The shear yield stress, τ_y , of the polymer is calculated using the Von Mises relationship ($\tau_y = \sigma_y/\sqrt{3}$ [161] where σ_y is the tensile yield stress of the polymer film, reported in Chapter 4). For coated polymers if the IFSS* is similar to the substrate shear yield stress then it is likely that the substrate is plastically yielding, causing the interface to plastify, meaning that for SiO_x coatings there is a large density of Si-O-C and Si-C covalent bonds at the interface between polymer and silica, causing a strong bond. Therefore, as all the values of IFSS are above the substrate shear yield stresses the adhesion, i.e. covalent bonding between the two layers, is excellent and any observed differences are due to the mechanical properties of the polymer. This is demonstrated for the PET and PEN samples where in each case the IFSS is comparable to the respective τ_y values and is consequently higher for the PEN composite although the extent of interfacial covalent bonding for each composite is probably similar. As the values of IFSS are similar for each batch and each thickness of coating for a given substrate, the IFSS data will be explained in terms of the substrate properties. The effects of the substrate surface mechanical properties on the IFSS are summarised in Figure 6.14.

Table 6.13 Interfacial shear stress of PECVD SiO_x coatings on polyester films-Batch 1.

Substrate	CD_{sat} (mm ⁻¹)	τ (MPa)	τ^* (MPa)	τ_y substrate (MPa)
PET	81 ± 7	68 ± 17	58 ± 16	~ 58
HS PET	88 ± 8	97 ± 6	84 ± 5	~ 52
HS PET P	116 ± 4	125 ± 6	110 ± 6	~ 52
PEN	77 ± 6	89 ± 8	76 ± 7	~ 80

Table 6.14 Interfacial shear stress values for SiO_x films on polyester substrates - Batch 2.

Substrate	Thickness (nm)	CD_{sat} (nm ⁻¹)	τ (MPa)	τ^* (MPa)	τ_y polymer (MPa)
PET	200	217 ± 15	93 ± 13	60 ± 13	~ 58
Filled PET	200	307 ± 46	114 ± 19	103 ± 18	~ 58
HS PET	200	342 ± 20	135 ± 15	107 ± 15	~ 52
HS PET_P	200	423 ± 7	163 ± 2	138 ± 2	~ 52
PEN	200	294 ± 6	120 ± 14	102 ± 14	~ 80
Filled PET	1000	63 ± 2	84 ± 4	79 ± 4	~ 58
HS PET	1000	62 ± 7	116 ± 33	89 ± 33	~ 52
HS PET_P	1000	69 ± 15	152 ± 24	120 ± 17	~ 52
PEN	1000	55 ± 8	94 ± 10	85 ± 9	~ 80

The IFSS is much greater than the estimated shear yield stress of the substrate for the heat-stabilised PET film. This is most likely a result of the increased degree of crystallisation detected at the surface by AFM phase and force-distance measurements, but which may not be present throughout the bulk. A high degree of crystallisation is known to increase the tensile yield stress (hence shear yield stress) of PET [34] and may also encourage strain hardening of the polymer. No elevated yield stress or strain hardening in the saturation regime (10-15% tensile strain) is observed for the HS PET film during tensile testing but this is probably due to the relaxed bulk amorphous phase and the localisation of the increased crystallinity at the surface of the film, as also reported in the literature [240, 241]. It appears that the crystalline surface morphology caused by heat treatment strengthens the polymer in the interfacial region allowing a superior IFSS to be observed that matches that of PEN. Similarly, the IFSS for filled PET is greater than that of the plain PET and the shear yield stress of the F-PET substrate – this may again be explained by the increased crystallinity at the surface of the film witnessed by AFM both in this thesis and also by other authors on similar films [175].

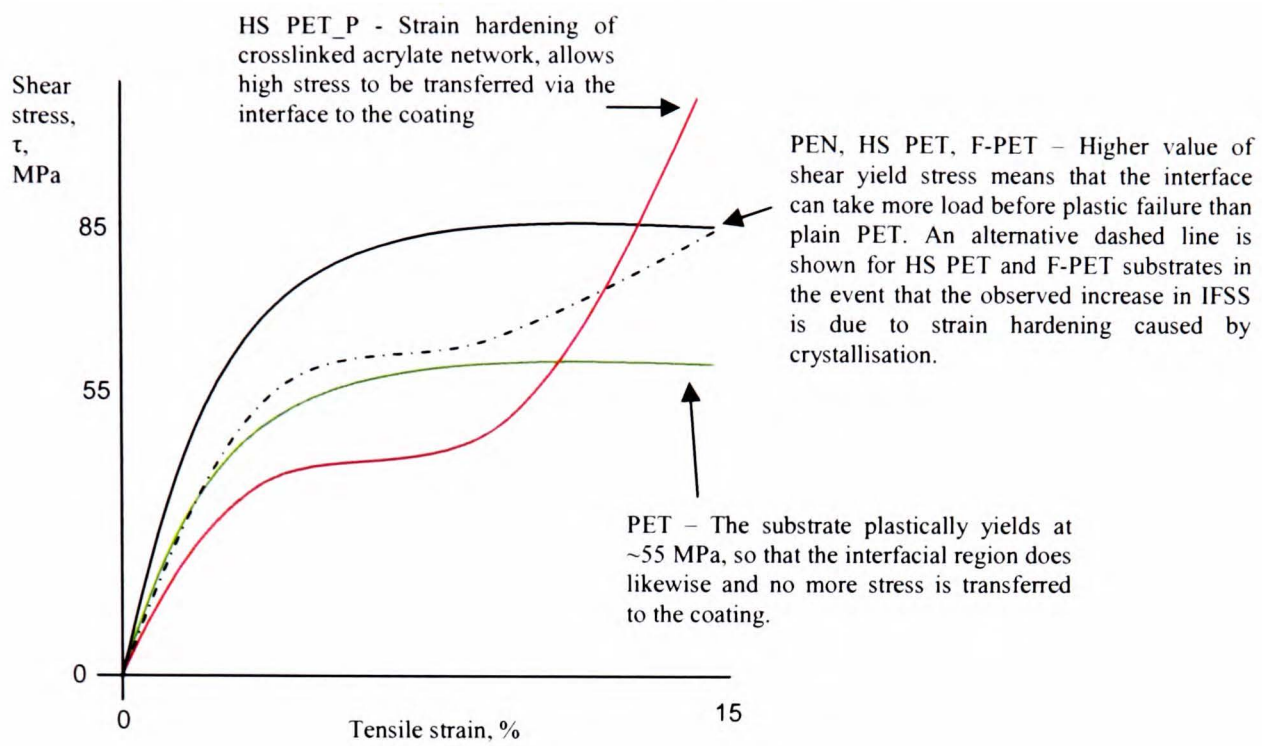


Figure 6.14 Proposed mechanical behaviour of the polyester substrates in the strain regime of the fragmentation test. The curves represent the characteristics of the near surface regions of the polymers.

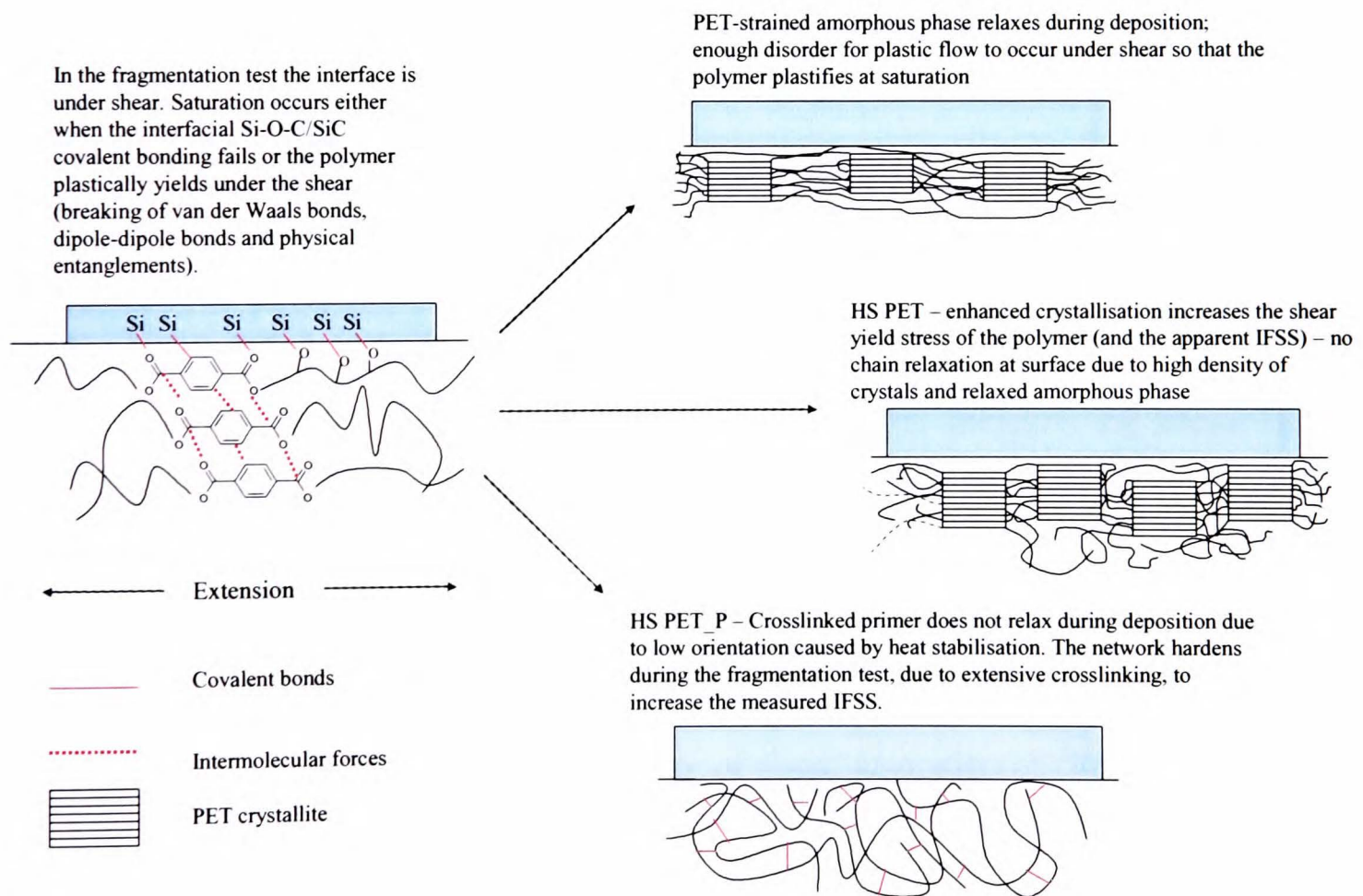


Figure 6.15 Simplified schematic of the structure of polymer substrates at the interface to explain mechanical properties in Figure 6.14.

6.5.3.1 The case of the acrylate primer layer

The addition of the primer layer to the HS PET causes the IFSS to increase to above 110 MPa and a much higher CD_{sat} is observed for this composite. Such a high IFSS value could be due to the increased functionality of the primer surface (shown by XPS and water contact angle measurements) resulting in substantially increased covalent bonding at the interface, but the acrylate itself must also have superior mechanical properties.

The properties of acrylate “latex” films are not well understood although recently more literature has been devoted to aspects of their formation and structure [261, 262], if not their mechanical properties. In this case the acrylate is a terpolymer which contains mainly MMA (PMMA is a glassy polymer [263]) and ethyl acrylate (polyethylacrylate is an elastomer [262, 264]) with an appreciable amount of methacrylamide to facilitate crosslinking. There are also significant quantities of crosslinking agent and surfactant in the film and overall it is difficult to predict the structure and mechanical properties of this layer. There are a number of morphologies of acrylate latex films reported in the literature [262, 265], depending on the synthesis of the polymer and recipe of the emulsion, with random “blocky” morphology, core/shell particles and dispersion of particles in a matrix all reported (Figure 6.16). It is likely that in our case the acrylate is a random copolymer as the measured T_g is intermediate between the values of the two monomers. However, there could be a degree of phase separation of (P)EA and (P)MMA, suggested by the large variation in snap-off displacements reported in the AFM force distance measurements (Chapter 4) and elements of structures 6.16(b) and (c) may also be present.

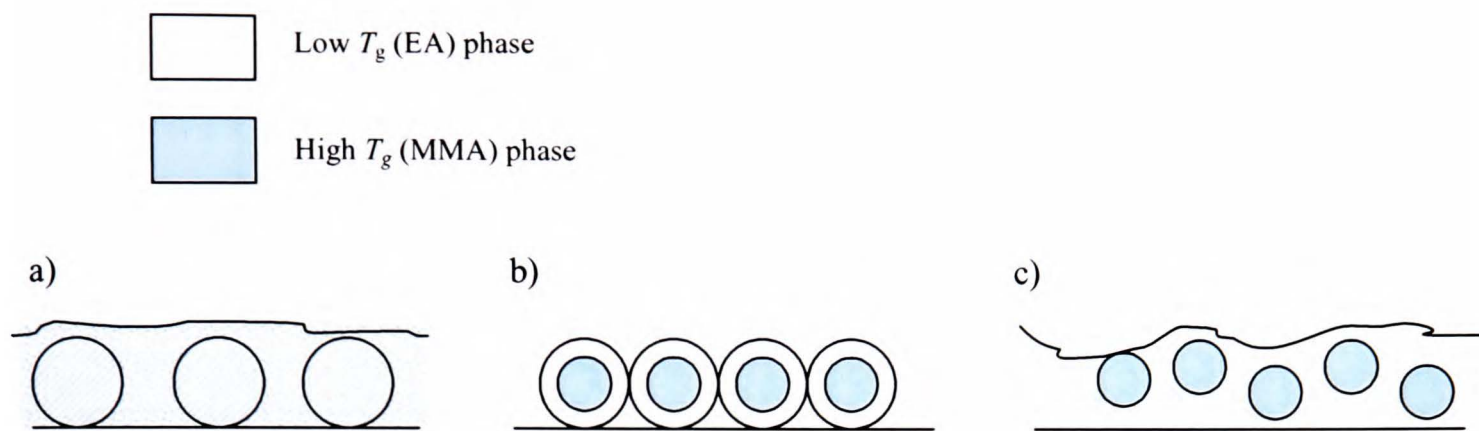


Figure 6.16 Possible morphology of acrylate coating: (a) random block copolymer particles in a copolymer matrix, (b) core/shell particles, (c) PMMA particles in a PEA matrix.

The acrylate is thought to exhibit elastomeric behaviour, as it is likely to be highly crosslinked and contains EA, which would explain why the IFSS value is so large (although the temperature the fragmentation test takes place at is below the T_g (50°C) of the acrylate, and hence one would expect it to be glassy, the same could be said for PET and PEN which yield plastically despite T_g 's higher than the acrylate). By considering the stress-strain behaviour of a highly crosslinked rubber (Figure 6.14) it can be seen that the hardening observed for such a material at a higher strain would lead to a high value of IFSS.

Much more work is required to confirm that elastomeric behaviour is exhibited for such thin acrylate films and that this is responsible for the high IFSS observed but it seems to be the most reasonable explanation given the available data. Unfortunately, no work has been published on the mechanical properties of crosslinked acrylates containing EA and MMA so it is difficult to verify this suggestion. It has been suggested that (uncrosslinked) P(MMA/EA) films may exhibit elastic behaviour [266, 267] and it has been shown [268] that copolymerising EA with polystyrene (a glassy polymer like PMMA) leads to a softer

polymer than the PS by itself, but no elastomeric behaviour was observed for the copolymer which may be due to a lack of physical or chemical crosslinking.

Finally, an interesting observation made for 1 μm thick SiO_x layers on primer coated PET that hadn't undergone heat stabilisation was that delamination occurred after a few weeks of storage and the coating just flaked off the substrate. It appears that a heat treatment is necessary to make the primer a useful adhesion promoter for these silicon oxide films. AFM images of the acrylate coating with and without heat stabilisation are shown in Figure 6.17.

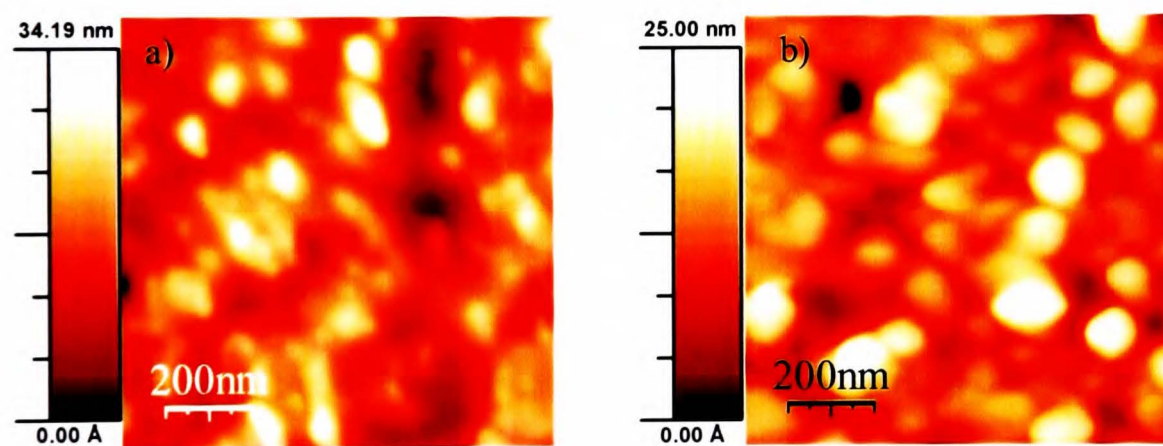


Figure 6.17 AFM image of primer coating – a) with a heat stabilisation stage; b) without a heat stabilisation stage.

The primer that is not heat stabilised appears to have retained a latex particle morphology, with a layer of roughly spherical particles apparent, whereas the heat stabilised film displays a more continuous structure with less uniformly shaped and organised particle features. It is a possibility that the extra heating stage (incidentally above the T_g of any “hard” PMMA phase) allows diffusion of polymer (including crosslinked regions) from the particles [262, 269] causing them to coalesce with the matrix to form a continuous elastic phase, that also undergoes further thermal

crosslinking, and is able to harden in the relevant strain regime. Much more work is required to investigate the properties of these acrylate films as substrates for vacuum deposition, particularly if such a simple heating stage can induce such a large change in properties.

6.6 Summary

In this Chapter highly effective silicon oxide gas barrier coatings have been reported that can reduce the rate of water vapour permeation through a polyester film by up to 5000 times. The coatings are so effective because they are relatively thick and deposited in a series of layers, which results in the decoupling of defects throughout the structure. For the thickest coatings the water molecules must diffuse through highly tortuous pathways, while chemically interacting with the oxide, thereby increasing dramatically the diffusion path length required in traversing the coating. There are very few large-scale defects evident and the SiO_x is conformal to the substrate surface with excellent coverage of features such as filler particles. In addition, the high level of carbon present in the coating structure lends it a flexible, organic character that means that stress-induced cracking and defects are not a concern. Barrier to water vapour increases as the thickness increases and it is possible that the critical thickness could be beyond 1000 nm. The mechanical properties of these coatings are impressive when the thickness is taken into account, with equivalent crack onset strains and cohesive strength to much thinner SiO_x coatings reported in the literature. The adhesion of the coatings to the substrate is good in all cases and is not an area requiring improvement. In the case of the 2nd Batch of coatings, which are superior to the Batch 1 films in all respects as a result of a more intense plasma source, the coatings show good transmission of light which means that they show

promise for applications where transparency is important. Equally promising is the ability to deposit excellent silica films by the PEVCD method on a roll-to-roll system (albeit over a relatively thin web and rather slowly) – something that has been difficult to achieve in the past.

It has also been observed that the choice of substrate can seriously impact the properties of the composite structure and it seems that the surface properties in particular dictate how well the coating behaves mechanically and as a permeation barrier. In summary:

- Deposition temperatures are estimated to be 80-100°C (above the T_g of PET) which is thought to lead to relaxation and/or crystallisation of oriented molecules at the surface of a standard PET film as the coating nucleates and grows. This nanoscale movement is thought to cause a silica structure riddled with defects that consequently displays inferior barrier and mechanical properties.
- A more crystalline substrate surface structure, as observed for heat stabilised and filled PET films, results in a coating with superior properties to one on a plain PET film as there are fewer oriented amorphous chains that relax during deposition in these substrates. The benefit of increased crystallinity is also manifested by a superior IFSS in these films.
- Filler particles are not found to be detrimental to the composite's performance, indeed coatings on this substrate match or outperform those on plain PET. Atomic shadowing is thought not to be a problem on these films because the substrate is

mobile during deposition and high energy PECVD species are able to move laterally across the surface.

- The addition of an acrylate primer layer to HS PET leads to a composite structure that has excellent barrier and mechanical properties. The acrylate has a low T_g and is thought to be elastomeric so that during deposition it presents a soft, “sticky” surface that the silica nucleates on to form a dense layer. Due to the fact that it is not highly oriented, the acrylate chains do not contract and move the nucleating SiO_x around. The relatively polar surface and mechanical properties of the primer layer lead to a much increased interfacial shear strength for silica films on this composite. The heat stabilisation stage may be necessary for these effects to be observed.
- Coating a PEN film is found to result in a superior composite than for PET due to its impressive thermal and mechanical properties. Coatings on this film rival those on the HS PET_P film as the best studied here. Interestingly, these two films are the roughest on the nanoscale (as are the SiO_x layers deposited on them) indicating that roughness on this scale is not detrimental to the performance of the coating.

Finally, it has been shown in this chapter that to obtain the best flexible gas barrier material possible it is not sufficient just to concentrate on the deposition method and processing parameters to get a superior thin film. The polymer substrate must also be chosen wisely, particularly with regard to thermal, mechanical and, to some degree,

Chapter 6. Silicon Oxide Gas Barrier Coatings on Polyester Films: Effect of the Substrate

barrier properties as it can influence the gas barrier performance of the composite a factor of 100 times or more.

Chapter 7. Conclusions and Suggestions for Further Work

The aims of this thesis were to investigate novel gas barrier coatings on polyester film and the effects of modifying the substrate on the properties of the deposited coating. The main conclusions of this work are detailed, followed by suggestions for future development.

7.1 Conclusions

1) Plasma pretreatment increases the adhesion of the coatings to the substrate and reduces the pinhole density.

Chapter 5 presented an investigation into plasma pretreatment of the polymer surface, showing that the surface became more hydrophilic with an increased density of functional groups that led to increased interfacial bonding and adhesion between the polymer and both sputtered aluminium and PECVD-SiO_x layers. No obvious difference in coating microstructure was observed for either the Al or SiO_x coatings on treated or untreated PET film, suggesting that this factor is controlled by the deposition process or that there are already sufficient nucleation sites prior to plasma treatment and adding more is unnecessary (the spacing of functional groups is very much smaller than coating grain size). Instead, plasma treatment is useful for reducing pinhole density in aluminium layers by etching away debris. Although oxygen plasma is more effective than argon in adding more functionality and increasing the hydrophilicity of the surface, the

improvement in adhesion and mechanical properties for the PET/SiO_x composites was the same for both plasma species.

2) Depositing SiO_x in multiple layers leads to excellent gas barrier properties.

In Chapter 6 a novel R2R PECVD process was reported that deposited SiO_x films with excellent barrier to water vapour permeation – in fact a transmission rate of $2 \times 10^{-4} \text{ g m}^{-2} \text{ day}^{-1}$ is reported for a 1 μm thick film, lower than literature values for equivalent coatings (of uniform composition throughout its thickness). The high thickness of these films is a crucial factor as the coating is deposited in multiple passes that ultimately leads to a “multilayer” like structure that decouples defects and results in highly tortuous permeation pathways. The water molecules may also chemically interact with the silica, but not extensively. The high level of carbon in these films causes them to have low levels of internal stress and impressive mechanical properties. Again, the multilayer structure is beneficial as the mechanical properties are controlled by the thickness of individual layers rather than the whole thickness meaning that 200 nm, 400 nm and 1 μm thick layers show comparable properties to 100-150 nm thick coatings reported in the literature. The adhesion of these coatings to the polyester is high, indicating a high density of Si-C and Si-O-C covalent bonds. As such, the PECVD process shows high promise in the production of transparent, flexible ultra high barrier materials.

3) Substrate surface roughness affects the morphology of the coating but not necessarily the barrier properties.

The topographies of a range of polyester films were studied by AFM and it was found that filler particles significantly roughened the surface, as did an acrylate primer coating. A heat stabilisation step increased the roughness over that of a plain PET film due to crystallisation. Conversely a coextruded amorphous PET layer was found to be the smoothest. The surface roughness was found to often affect the microstructure of the coating. For sputtered 50 nm thick TiO_x films, filler particles in the substrate caused defects to form adjacent to them, due to atomic shadowing. The same coating on the amorphous PET caused significant thermal shrinkage of the substrate as the oriented chains relaxed. However, a 10 nm coating on the same substrate resulted in no shrinkage and a smoother and finer microstructure than that on BD PET was observed. Thermal shrinkage of the aPET substrate was also observed for PECVD coatings and it is concluded such a film is unsuitable for vacuum deposition, unless the coating is extremely thin and heating is minimal. Even though surface roughness affected the microstructure of PECVD SiO_x coatings – rougher substrates resulted in rougher coatings with larger grain sizes – no adverse effect was observed in terms of gas barrier or mechanical properties. In fact the best coatings were observed for the two roughest polymers on the nanoscale. SiO_x layers conformed well to the substrate and no discernible defects were caused by filler particles.

4) The surface thermal and mechanical properties are found to be the most important substrate factor in determining how well a barrier coating performs.

For PECVD SiO_x coatings in Chapter 6 the films deposited on BD PET, and to a lesser extent filled PET, were inferior to those on heat stabilised PET with or without a primer

layer and PEN. An explanation for this is that the temperature the polyester film experiences during deposition is close to, or above, the T_g (80°C) which causes the oriented chains in a drawn PET film to relax (or crystallise), particularly at the surface. The movement of these molecules during deposition causes the initial deposits to move laterally across the surface resulting in a structure that possesses many defects. This process is responsible for the high levels of stress and the poor barrier and mechanical properties of coatings on the PET. The low thermal shrinkage of the heat stabilised PET (due to relaxed amorphous regions and high crystallinity) and high T_g of the PEN films result in superior coatings on these substrates. Superior mechanical and adhesive properties are observed when the coating is deposited on the HS PET with an additional acrylate layer. The acrylate primer layer is a highly crosslinked terpolymer that, despite a low T_g , does not relax upon heating as it is likely to be relatively unoriented. A heat stabilisation step may be necessary for the acrylate layer to be beneficial.

5) To achieve optimum barrier performance, correct substrate selection is just as important as the deposition technique.

It was demonstrated in Chapter 6 that a significant improvement in gas barrier (>100) and mechanical durability could be achieved for silicon oxide coatings by simply replacing a biaxially drawn PET film with a heat stabilised film (with or without a primer layer) or with PEN. Such an improvement in barrier due to substrate influence is comparable to that caused by deposition of a coating onto a bare polymer surface in the first place.

7.2 Suggestions for Further Work

1) Barrier Coatings – In the case of the PECVD SiO_x coatings reported in Chapter 6 there are several avenues that are worth following up. For the fabrication of these films it would be useful to increase the web speed and width that are currently used if the process is to be commercially viable. It would also be useful to see if much thinner layers could be deposited as good barriers by depositing several layers of 10~20 nm thickness to get the multilayer effect at a minimum thickness. To check that the multilayer structure is a good explanation of the high barrier observed for the thicker coatings it would be instructive to compare them to a similar thickness of silica deposited in one pass by the same method. On a similar theme, by conducting a series of runs at different pass speeds it should be possible to determine whether the poorer mechanical performance of the 1000 nm thick layers, compared to 200 and 400 nm ones, is due to the slower web speed and increased substrate heating. A thorough understanding of what form the carbon takes in these films would also be useful and could possibly be achieved by IR or solid state NMR to characterise the chemical bonding in the ceramic.

2) Polyester Substrates - For the polyester substrates two points stand out. First, does the heat stabilisation process affect the bulk and surface crystallinity to different extents? This could possibly be solved by x-ray diffraction studies or ATR-IR depth profiling techniques and include an investigation over a range of temperatures. Secondly, much more needs to be known about the acrylate layer – particularly the mechanical properties, composition and morphology – if we are to fully explain why it improves the coating properties. The effect of changing the composition of the acrylate layer (proportion of EA

to MMA, use of different monomers, various heat treatments) on the properties of the acrylate would also be worth investigating.

3) Substrate Effect - Another useful experiment would be to monitor the orientation of the amorphous phase before and after deposition to see if it decreased due to chain relaxation, possibly using fluorescent probes or a combination of infra red spectroscopy and X-ray diffraction. Such work would substantiate some of the claims made in this thesis but it would be difficult to differentiate what was happening at the surface with that in the bulk. The influence of the acrylate coating that has not undergone an additional heat stabilisation step also requires further scrutiny to confirm that it promotes delamination of the coating from the polymer and to explain why it may do so. Further clarification as to whether filler particles are detrimental to coating performance, particularly with respect to thinner PVD coatings, is also required.

Chapter 8. Bibliography

1. Ackermann, P., Jagerstad, M., and Ohlsson, T., eds. *Foods and packaging materials: chemical interactions*. Royal Society of Chemistry: Cambridge. 1995.
2. Coles, R., McDowell, D., and Kirwan, M.J., eds. *Food Packaging Technology*. Blackwell: Oxford. 2003.
3. Piringer, O.G. and Baner, A.L., eds. *Plastic packaging materials for food: barrier function, mass transport, quality assurance and legislation*. Wiley-VCH: Chichester. 2000.
4. Dean, D.A., *Plastics in Pharmaceutical Packaging: A literature review*: Pira. Leatherhead. 1990.
5. Hall, R., *Medical Device Technology* 1993, **4**(1), p. 23.
6. MacDonald, W.A., *J. Mater. Chem.* 2004, **14**, p. 4.
7. Burrows, P.E., Graff, G.L., Gross, M.E., Martin, P.M., Shi, M.K., Hall, M., Mast, E., Bonham, C., Bennett, W., and Sullivan, M.B., *Displays* 2001, **22**, p. 65.
8. Leterrier, Y., *Prog. Mater. Sci.* 2003, **48**, p. 1.
9. Melinex, *DuPont-Teijin Films Technical Notes on Polyester Films*.
10. Brooks, D. and Giles, G., in *PET Packaging and Technology*, G. Giles, Editor. 2002, Sheffield Academic Press: Sheffield. p. 1.
11. Fakirov, S., in *Handbook of Thermoplastics*, O. Olabisi, Editor. 1997, Marcel Dekker: New York. p. 449.
12. Hergenrother, W.L., *J. Polym. Sci., Polym. Phys. Ed.* 1974, **12**, p. 875.
13. Dixon, E.R. and Jackson, J.B., *J. Mater. Sci.* 1968, **3**, p. 464.
14. Daubeny, R.D., Bunn, C.W., and Brown, C.J., *Proc. R. Soc. London. Ser. A.* 1954, **226**, p. 531.
15. Fakirov, S., Seganov, I., and Kurdova, E., *Macromol. Chem.* 1985, **182**, p. 185.
16. Werner, E., Janocha, S., Hopper, M.J., and MacKenzie, K.J., in *Encyclopaedia of Polymer Science and Engineering*, g. Mengues, Editor. 1988, John Wiley and Sons: New York.
17. Painter, P.C. and Coleman, M.M., *Fundamentals of Polymer Science*: Technomic Publishing AG. Basel. 1994.
18. Flory, P.J., *J. Am. Chem. Soc.* 1962, **34**, p. 2857.
19. Bassett, D.C., *Principles of Polymer Morphology*: Cambridge University Press. Cambridge. 1981.
20. Ajji, A., Guevremont, J., Cole, K.C., and Dumoulin, M.M., *Polymer* 1996, **37**, p. 3707.
21. Chang, H., Schultz, J.M., and Gohil, R.M., *J. Macromol. Sci., Phys* 1993, **B32**, p. 99.

Chapter 8. Bibliography

22. Ward, I.M., *Adv. Polym. Sci.* 1985, **66**, p. 81.
23. Qian, R., Shen, D., Sun, F., and Wu, L., *Macromol. Chem. Phys.* 1996, **197**, p. 1485.
24. Duschene, C., Kong, X., Brisson, J., Pezolet, M., and Prud'homme, R.E., *Macromolecules* 2002, **35**, p. 8768.
25. MacDonald, W.A., Mace, J.M., and Polack, N.P. *45th Annual Technical Conference Proceedings of the Society of Vacuum Coaters.* 2002, p. 482
26. Cakmak, M., Wang, Y.D., and Simhambhatla, M., *Polym. Eng. Sci.* 1990, **30**(12), p. 721.
27. Jakeways, R., Klein, J.L., and Ward, I.M., *Polymer* 1996, **37**(16), p. 3761.
28. MacDonald, W.A., MacKerron, D.H., and Brooks, D.W., in *PET Packaging and Technology*, G. Giles, Editor. 2002, Sheffield Academic Press: Sheffield. p. 116.
29. Gohil, R.M., *J. Appl. Polym. Sci.* 1994, **52**, p. 925.
30. Matthews, R.G., Ajji, A., Dumoulin, M.M., and Prud'homme, R.E., *Polymer* 2000, **41**, p. 7139.
31. Pearce, R., Cole, K.C., Ajji, A., and Dumoulin, M.M., *Polym. Eng. Sci.* 1997, **37**(11), p. 1795.
32. Gupta, V.B., Radhakrishnan, J., and Sett, S.K., *Polymer* 1993, **34**(18), p. 3814.
33. Le Bourvellec, G. and Monnerie, L., *Polymer* 1986, **27**, p. 856.
34. Jabarin, S.A., *Polym. Eng. Sci.* 1991, **31**(14), p. 1071.
35. Padibjo, S.R. and Ward, I.M., *Polymer* 1983, **24**, p. 1103.
36. Cunningham, A., Ward, I.M., Willis, H.A., and Zichy, V., *Polymer* 1974, **15**, p. 749.
37. Smith, F.S. and Steward, R.D., *Polymer* 1974, **15**, p. 283.
38. Alfonso, G.C. and Verdone, M.R., *Polymer* 1978, **19**, p. 711.
39. Gorlier, E., Haudin, J.M., and Billon, N., *Polymer* 2001, **42**, p. 9541.
40. Kawakami, D., Hsiao, B.S., Ran, S., Burger, C., Fu, B., Sics, I., Chu, B., and Kikutani, T., *Polymer* 2004, **45**, p. 905.
41. Mahendrasingham, A., Blundell, D.J., Martin, C., Fuller, W., MacKerron, D.H., Harvie, J.L., Oldman, J.L., and Riekkel, C., *Polymer* 2000, **41**, p. 7803.
42. Salem, D.R., *Polymer* 1992, **33**, p. 3189.
43. Buckley, C.P., Jones, D.C., and Jones, D.P., *Polymer* 1996, **37**(12), p. 2403.
44. Gordon, D.H., Duckett, R.A., and Ward, I.M., *Polymer* 1994, **35**(12), p. 2554.
45. Faisant de Champchesnel, J.B., Tassin, J.F., Bower, D.I., Ward, I.M., and Lorentz, G., *Polymer* 1994, **35**, p. 19.
46. Lee, K.G. and Schultz, J.M., *Polymer* 1993, **34**, p. 4455.

47. Goschel, U. and Urban, G., *Polymer* 1995, **36**(19), p. 3633.
48. Welsh, G.E., Blundell, D.J., and Windle, A.H., *Macromolecules* 1998, **31**, p. 7562.
49. Blundell, D.J., Mahendrasingham, A., Martin, C., Fuller, W., MacKerron, D.H., Harvie, J.L., Oldman, J.L., and Riekell, C., *Polymer* 2000, **41**, p. 7793.
50. Cakmak, M. and Lee, S.W., *Polymer* 1995, **36**, p. 4039.
51. Murakami, S., Yamakawa, M., Tsuji, M., and Kohjiya, S., *Polymer* 1996, **37**(17), p. 3945.
52. Faisant de Champchesnel, J.B., Bower, D.I., Ward, I.M., Tassin, J.F., and Lorentz, G., *Polymer* 1993, **34**(18), p. 3763.
53. Faisant de Champchesnel, J.B., Tassin, J.F., Monnerie, L., Sergot, P., and Lorentz, G., *Polymer* 1997, **38**(16), p. 4165.
54. Tassin, J.F., Vigny, M., and Vegrat, D., *Macromol. Symp.* 1999, **147**, p. 209.
55. Gohil, R.M. and Salem, D.R., *J. Appl. Polym. Sci.* 1993, **47**, p. 1989.
56. Adams, A.M., Buckley, C.P., and Jones, D.P., *Polymer* 1998, **39**(23), p. 5761.
57. Adams, A.M., Buckley, C.P., and Jones, D.P., *Polymer* 2000, **41**, p. 771.
58. Long, S.D. and Ward, I.M., *J. Appl. Polym. Sci.* 1991, **42**, p. 1921.
59. Varma, P., Lofgren, E.A., and Jabarin, S.A., *Polym. Eng. Sci.* 1998, **38**, p. 245.
60. Greener, J., Tsou, A.H., and Blanton, T.N., *Polym. Eng. Sci.* 1999, **39**(12), p. 2403.
61. Schoukens, G. and Verschuere, M., *Polymer* 1999, **40**, p. 3753.
62. Douillard, A., Hardy, L., Stevenson, I., Boiteux, G., Seytre, G., Kazmiercak, T., and Galeski, A., *J. Appl. Polym. Sci.* 2003, **89**, p. 2224.
63. Hardy, L., Stevenson, I., Voice, A.M., and Ward, I.M., *Polymer* 2002, **43**, p. 6013.
64. Mascia, L., *Thermoplastics: Materials Engineering*. 2nd ed: Elsevier Applied Science. London. 1989.
65. Briggs, D. and Seah, M.P., eds. *Practical Surface Analysis - Volume 1: Auger and X-ray Photoelectron Spectroscopy*. 2nd ed., John Wiley and Sons: New York. 1990.
66. Davis, R. and Peiffer, H. in *42nd Annual Technical Conference Proceedings of the Society of Vacuum Coaters*. 1999, p. 511
67. Decker, W. and Henry, B.M. in *45th Annual Technical Conference Proceedings of the Society of Vacuum Coaters*. 2002, p. 492
68. Crank, J. and Park, G.S., eds. *Diffusion in Polymers*. Academic Press: New York. 1968.
69. Rogers, C.E., in *Polymer Permeability*, J. Comyn, Editor. 1985, Elsevier Applied Science Publishing LTD: London. p. 11.

Chapter 8. Bibliography

70. Michaels, A.S., Vieth, W.R., and Barrie, J.A., *J. Appl. Phys.* 1963, **34**(1), p. 13.
71. Ghosal, K. and Freeman, B.D., *Polym. Adv. Tech.* 1994, **5**, p. 673.
72. Slee, J.A., Orchard, G.A.J., Bower, D.I., and Ward, I.M., *J. Polym. Sci. B* 1989, **27**, p. 71.
73. Orchard, G.A.J., Spiby, P., and Ward, I.M., *J. Polym. Sci. B* 1990, **28**, p. 603.
74. McGonigle, E.-A., Liggat, J.J., Pethrick, R.A., Jenkins, S.D., Daly, J.H., and Hayward, D., *Polymer* 2001, **42**, p. 2413.
75. Hodge, R.M., BAstow, T.J., Edward, G.H., Simon, G.P., and Hill, A.J., *Macromolecules* 1996, **29**, p. 8137.
76. Yasuda, H. and Stannett, V., *J. Polym. Sci.* 1962, **57**, p. 907.
77. Shigetomi, T., Tsuzumi, H., Toi, K., and Ito, T., *J. Appl. Polym. Sci.* 2000, **76**, p. 67.
78. Fukuda, M., Kawai, H., Yugi, N., and Kimura, O., *Polymer* 1990, **31**, p. 295.
79. Lasoki, S.W. and Hobbs, W.H., *J. Polym. Sci.* 1959, **36**, p. 21.
80. Tropsha, Y.G. and Harvey, N.G., *J. Phys. Chem. B.* 1997, **101**, p. 2259.
81. Schrenk, P. and Alfrey, T., *J. Polym. Eng. Sci.* 1969, **3**, p. 393.
82. Moulson, J. and Roberts, J.P., *Trans. Faraday Soc.* 1961, **57**, p. 1208.
83. Norton, F.J., *Nature* 1961, **191**, p. 101.
84. Hitchman, M.L. and Jensen, K.F., eds. *Chemical Vapour Deposition: Principles and Applications*. Academic Press: London. 1993.
85. Cote, D.R., Nguyen, S.V., Stamper, A.K., Armbrust, D.S., Tobben, D., Conti, R.A., and Lee, G.Y., *IBM Journal of Research and Development* 1999, **43**, p. 5.
86. Inoue, Y., Sugimura, H., and Takai, O., *Thin Solid Films* 1999, **345**, p. 90.
87. Madocks, J., Rewhinkle, J., and Barton, L., *Mat. Sci. Eng. B.* 2005, **119**(3), p. 268.
88. Felts, J. and Grub, A., *J. Vac. Sci. Technol. A* 1992, **10**, p. 1675.
89. Teshima, K., Inoue, Y., Sugimura, H., and Takai, O., *Surf. Coat. Technol.* 2001, **146-147**, p. 451.
90. Teshima, K., Inoue, Y., Sugimura, H., and Takai, O., *Surf. Coat. Technol.* 2003, **169-170**, p. 583.
91. Howells, D.G., Henry, B.M., Medico, L., Leterrier, Y., Manson, J.-A.E., and Assender, H.E. in *48th Annual Technical Conference Proceedings of the Society of Vacuum Coaters*. 2005, p. 638
92. Komada, M., Oboshi, T., and Ichimura, K. in *43rd Annual Technical Conference Proceedings of the Society of Vacuum Coaters*. 2000, p. 352
93. Mattox, D.M., *Handbook of Physical Vapor Deposition (PVD) Processing*: Noyes Publications. New York. 1998.

Chapter 8. Bibliography

94. Mahan, J.E., *Physical Vapor Deposition of Thin Films*: John Wiley & Sons. New York. 2000.
95. Mattox, D.M. in *40th Annual Technical Conference Proceedings of the Society of Vacuum Coaters*. 1997, p. 109
96. Maissel, L.I. and Schaible, P.M., *J. Appl. Phys.* 1965, **36**, p. 237.
97. Kharazzi Olsson, M., Macak, K., Helmersson, U., and Hjorvarsson, B., *J. Vac. Sci. Technol. A*. 1998, **16**(2), p. 639.
98. Safi, I., *Surf. Coat. Technol.* 2000, **127**, p. 203.
99. Thornton, J.A., *J. Vac. Sci. Technol.* 1974, **11**, p. 666.
100. Thornton, J.A., *Annu. Rev. Mater. Sci.* 1977, **7**, p. 239.
101. Thornton, J.A., *J. Vac. Sci. Technol. A*. 1986, **4**(6), p. 3059.
102. Ben Amor, S., Baud, G., Besse, J.P., and Jacquet, M., *Thin Solid Films* 1997, **293**, p. 163.
103. Ben Amor, S., Baud, G., Jacquet, M., and Pichon, N., *Surf. Coat. Technol.* 1998, **102**, p. 63.
104. Cueff, R., Baud, G., Besse, J.P., and Jacquet, M., *Thin Solid Films* 1995, **266**, p. 198.
105. Cueff, R., Baud, G., Benmalek, M., Besse, J.P., Butruille, J.R., and Jacquet, M., *Surf. Coat. Technol.* 1996, **80**, p. 96.
106. Cueff, R., Baud, G., Benmalek, M., Besse, J.P., Butruille, J.R., Dunlop, H.M., and Jacquet, M., *Thin Solid Films* 1995, **270**, p. 230.
107. Ben Amor, S., Baud, G., Besse, J.P., and Jacquet, M., *Mat. Sci. Eng. B*. 1997, **47**, p. 110.
108. Reichelt, K. and Jiang, X., *Thin Solid Films* 1991, **191**, p. 91.
109. Deng, C.-S., Assender, H.E., Dinelli, F., Kolosov, O.V., Briggs, G.A.D., Miyamoto, T., and Tsukahara, Y., *J. Polym. Sci. B*. 2000, **38**, p. 3151.
110. Henry, B.M., Dinelli, F., Zhao, K.Y., Grovenor, C.R.M., Kolosov, O.V., Briggs, G.A.D., Roberts, A.P., Kumar, R.S., and Howson, R.P., *Thin Solid Films* 1999, **355-356**, p. 500.
111. Dennler, G., Houdayer, A., Segui, Y., and Wertheimer, M.R., *J. Vac. Sci. Technol. A* 2001, **19**(5), p. 2320.
112. Felts, J. in *34th Annual Technical Conference Proceedings of the Society of Vacuum Coaters*,. 1991, p. 184
113. Chatham, H., *Surf. Coat. Tech.* 1996, **78**, p. 1.
114. Klemberg-Sapieha, J.E., Martinu, L., Kuttel, O.M., and Wertheimer, M. in *36th Annual Technical Conference Proceedings of the Society of Vacuum Coaters*. 1993, p. 445
115. Bieder, A., Gruniger, A., and Rudolf von Rohr, P., *Surf. Coat. Tech.* 2005, **200**, p. 928.
116. Yanaka, M., Henry, B.M., Roberts, A.P., Grovenor, C.R.M., Briggs, G.A.D., Sutton, A.P., Miyamoto, T., Tsukahara, Y., Takeda, N., and Chater, R.J., *Thin Solid Films* 2001, **397**, p. 176.

Chapter 8. Bibliography

117. da Silva Sobrinho, A.S., Czeremuszkina, G., Latreche, M., and Wertheimer, M.R., *J. Vac. Sci. Technol. A* 2000, **18**(1), p. 149.
118. Prins, W. and Hermans, J.J., *J. Phys. Chem.* 1959, **63**, p. 716.
119. Jamieson, E.H.H. and Windle, A.H., *J. Mat. Sci.* 1983, **18**, p. 64.
120. Rossi, G. and Nulman, M., *J. Appl. Phys.* 1993, **74**(9), p. 5471.
121. Hanika, M., Langowski, H.C., Moosheimer, U., and Peukert, W., *Chem. Eng. Tech.* 2003, **26**, p. 5.
122. da Silva Sobrinho, A.S., Czeremuszkina, G., Latreche, M., and Wertheimer, M.R., *Appl. Phys. A* 1999, **68**, p. 103.
123. Erlat, A.G., Spontak, R.J., Clarke, R.P., Robinson, T.C., Haaland, P.D., Tropsha, Y.G., Harvey, N.G., and Vogler, E.A., *J. Phys. Chem. B.* 1999, **103**, p. 6047.
124. Roberts, A.P., Henry, B.M., Sutton, A.P., Briggs, G.A.D., Grovenor, C.R.M., Miyamoto, T., and Yanaka, M., *J. Membrane Sci.* 2002, **208**((1-2)), p. 75.
125. Garcia-Ayuso, G., Vazquez, L., and Martinez-Duart, J.M., *Surf. Coat. Technol.* 1996, **80**, p. 203.
126. Henry, B.M., Erlat, A.G., McGuigan, A., Grovenor, C.R.M., Briggs, G.A.D., and Tsukahara, Y., *Thin Solid Films* 2001, **382**, p. 194.
127. Erlat, A.G., Henry, B.M., Grovenor, C.R.M., Briggs, G.A.D., Chater, R.J., and Tsukahara, Y., *J. Phys. Chem. B.* 2004, **108**, p. 883.
128. Garcia-Ayuso, G., Salvarezza, R., Martinez-Duart, J.M., Sanchez, O., and Vazquez, L., *Surf. Coat. Technol.* 1996, **100-101**, p. 459.
129. Erlat, A.G., Henry, B.M., Ingram, J.J., Mountain, D.B., McGuigan, A., Howson, R.P., Grovenor, C.R.M., Briggs, G.A.D., and Tsukahara, Y., *Thin Solid Films* 2001, **388**, p. 78.
130. Koo, W.H., Jeong, S.M., Choi, S.H., Kim, W.J., H.K., B., Lee, S.M., and Lee, S.J., *J. Phys. Chem. B* 2005, **109**, p. 11354.
131. Wu, D.S., Lo, W.C., Chang, L.S., and Horng, R.H., *Thin Solid Films* 2004, **468**, p. 105.
132. Barker, C.P., Kochem, K.H., Revell, K.M., Kelly, R.S.A., and Badyal, J.P.S., *Thin Solid Films* 1995, **257**, p. 77.
133. Benmalek, M. and Dunlop, H.M., *Surf. Coat. Technol.* 1995, **76-77**, p. 821.
134. Lewis, J.S. and Weaver, M.S., *IEEE Journal of Selected Topics in Quantum Electronics* 2004, **10**(1), p. 45.
135. Stevens, M., Tuomela, S., and Mayer, D. in *48th Annual Technical Conference Proceedings of the Society of Vacuum Coaters.* 2005, p. 189
136. MOCON, *Permatran W 3/31 Manual*: MOCON, Inc. Minnesota, MN.
137. Kumar, R.S., Auch, M., Ou, E., Ewald, G., and Jin, C.S., *Thin Solid Films* 2002, **417**, p. 120.

Chapter 8. Bibliography

138. Kim, T.W., Yan, M., Erlat, A.G., McConnelee, P.A., Pellow, M., Deluca, J., Feist, T.P., and Duggal, A.R., *J. Vac. Sci. Technol. A* 2005, **23**(4), p. 971.
139. Paetzold, R., Winnacker, A., Henseler, D., Cesari, V., and Heuser, K., *Rev. Sci. Instr.* 2003, **74**(12), p. 5147.
140. Roehrig, M., Shaw, D.G., Langlois, M., and Sheehan, C., *J. Plast. Film Sheet.* 1997, **13**(3), p. 235.
141. Shaw, D.G. in *34th Annual Technical Conference Proceedings of the Society of Vacuum Coaters.* 1991, p. 180
142. Affinito, J.D., Eufinger, S., Gross, M.E., Graff, G.L., and Martin, P.M., *Thin Solid Films* 1997, **308-309**, p. 19.
143. Affinito, J.D., Gross, M.E., Coronado, C.A., Graff, G.L., Greenwell, E.N., and Martin, P.M. in *39th Annual Technical Conference Proceedings of the Society of Vacuum Coaters.* 1996, p. 392
144. Weaver, M.S., Michalski, L.A., Rajan, K., Rothman, M.A., Silvernail, J.A., Brown, J.J., Burrows, P.E., Graff, G.L., Gross, M.E., Martin, P.M., Hall, M., Mast, E., Bonham, C., Bennett, W., and Zumhoff, M., *Appl. Phys. Lett.* 2002, **81**(16), p. 2929.
145. Yan, M., Kim, T.W., Erlat, A.G., Pellow, M., Foust, D.F., Liu, J., Schaepkens, M., Heller, C.M., McConnelee, P.A., Feist, T.P., and Duggal, A.R., *Proceedings of the IEEE* 2005, **93**(8), p. 1468.
146. Graff, G.L., Williford, R.E., and Burrows, P.E., *J. Appl. Phys.* 2004, **96**(4), p. 1840.
147. Lin, C.H., Wang, H.L., and Hon, M.H., *Thin Solid Films* 1996, **283**, p. 171.
148. Stoney, G.G., *Proc. Roy. Soc. London* 1909, **a82**, p. 172.
149. Klein, C.A., *J. Appl. Phys.* 2000, **88**, p. 5487.
150. Leplan, H., Geenen, B., Robic, J.Y., and Pauleau, Y., *J. Appl. Phys.* 1995, **78**(2), p. 962.
151. Leplan, H., Robic, J.Y., and Pauleau, Y., *J. Appl. Phys.* 1996, **79**(9), p. 6926.
152. Ohring, M., *The materials science of thin films: deposition and structure.* 2nd ed: Academic Press. London. 2002.
153. Yanaka, M., Tsukahara, Y., Nakaso, N., and Takeda, N., *J. Mat. Sci.* 1998, **33**, p. 2111.
154. Henry, B.M., Roberts, A.P., Grovenor, C.R.M., Sutton, A.P., and Briggs, G.A.D. in *41st Annual Technical Conference Proceedings of the Society of Vacuum Coaters.* 1998, p. 434
155. Rochat, G., Leterrier, Y., Fayet, P., and Manson, J.-A.E., *Thin Solid Films* 2005, **484**, p. 94.
156. Mittal, K.L., *J. Vac. Sci. Technol.* 1976, **13**(1), p. 19.
157. Silvain, J.F. and Ehrhardt, J.J., *Thin Solid Films* 1993, **236**, p. 230.
158. Bichler, C., Kerbstadt, T., Langowski, H.C., and Moosheimer, U., *Surf. Coat. Technol.* 1997, **97**, p. 229.
159. Bichler, C., Kerbstadt, T., Langowski, H.C., and Moosheimer, U., *Surf. Coat. Technol.* 1999, **112**, p. 373.

160. Steinmann, P.A. and Hintermann, H.E., *J. Vac. Sci. Technol. A*. 1989, **7**, p. 2267.
161. Leterrier, Y., Boogh, L., Andersons, J., and Manson, J.-A.E., *J. Polym. Sci B. Polym. Phys.* 1997, **35**, p. 1449.
162. Kelly, A. and Tyson, W.R., *J. Mech. Phys. Sol.* 1965, **13**, p. 329.
163. Davidge, R.W., *Mechanical Behaviour of Ceramics*: Cambridge University Press. Cambridge. 1979.
164. Wachtman, J.B., *Mechanical Properties of Ceramics*: Wiley. New York. 1996.
165. Weibull, W., *J. Appl. Mech.* 1951, **18**, p. 293.
166. Leterrier, Y., Medico, L., Demarco, F., Manson, J.-A.E., Betz, U., Escola, M.F., Kharazzi Olsosn, M., and Atamny, F., *Thin Solid Films* 2004, **460**, p. 156.
167. Leterrier, Y., Wyser, Y., and Manson, J.A.E., *J. Adhesion. Sci. Technol.* 2001, **15(7)**, p. 841.
168. Leterrier, Y., Andersons, J., Pitton, Y., and Manson, J.-A.E., *J. Polym. Sci B. Polym. Phys.* 1997, **35**, p. 1463.
169. Rochat, G., Leterrier, Y., Plummer, C.J.G., Manson, J.-A.E., Szoszkiewick, R., Kulik, A.J., and Fayet, P., *J. Appl. Phys.* 2004, **95(10)**, p. 5429.
170. Rochat, G., Leterrier, Y., Fayet, P., and Manson, J.-A.E., *Thin Solid Films* 2003, **437**, p. 204.
171. Rochat, G., Leterrier, Y., Garamszegi, L., Manson, J.-A.E., and Fayet, P., *Surf. Coat. Technol.* 2003, **174-175**, p. 1029.
172. McGuigan, A.P., Briggs, G.A.D., Burlakov, V.M., Yanaka, M., and Tsukahara, Y., *Thin Solid Films* 2003, **424**, p. 219.
173. Yanaka, M., Kato, Y., Tsukahara, Y., and Takeda, N., *Thin Solid Films* 1999, **356**, p. 337.
174. Dinelli, F., Assender, H.E., Kirov, K., and Kolosov, O., *Polymer* 2000, **41**, p. 4285.
175. Beake, B.D., Leggett, G.J., and Shipway, P.H., *Surf. Interface Anal.* 2001, **31**, p. 39.
176. Ling, J.S.G. and Leggett, G.J., *Polymer* 1997, **38(11)**, p. 2617.
177. Rochat, G., Delachaux, A., Leterrier, Y., Manson, J.-A.E., and Fayet, P., *Surf. Interface Anal.* 2003, **35**, p. 948.
178. Collaud Coen, M., Lehmann, R., Groening, P., and Schlapbach, L., *Appl. Surf. Sci.* 2003, **9729**, p. 1.
179. Beake, B.D., Leggett, G.J., and Ling, J.S.G., *J. Mater. Chem.* 1998, **8**, p. 2845.
180. Beake, B.D., Ling, J.S.G., and Leggett, G.J., *J. Mater. Chem.* 1998, **8(8)**, p. 1735.
181. Gupta, B., Hilborn, J., Hollenstein, C., Plummer, C.J.G., Houriet, R., and Xanthopoulos, N., *J. Appl. Polym. Sci.* 2000, **78**, p. 1083.
182. Inagaki, N., Tasaka, S., and Shimada, S., *J. Appl. Polym. Sci.* 2001, **79**, p. 808.

Chapter 8. Bibliography

183. Inagaki, N., Narushima, K., and Lim, S.K., *J. Appl. Polym. Sci.* 2003, **89**, p. 96.
184. Inagaki, N., Narushima, K., Tuchida, N., and Miyazaki, K., *J. Polym. Sci. Part B.* 2004, **42**(20), p. 2727.
185. O'Hare, L.A., Smith, J.A., Leadley, S.R., Parbhoo, B., Goodwin, A.J., and Watts, J.F., *Surf. Interface. Anal* 2002, **33**, p. 617.
186. Paynter, R.W., *Surf. Interface Anal.* 1998, **26**, p. 674.
187. Inagaki, N., *Plasma Surface Modification and Plasma Polymerisation*: Technomic Publishing Ag. Basel. 1996.
188. Grace, J.M., Zhuang, H.K., Gerenser, L.J., and Freeman, D.R., *J. Vac. Sci. Technol. A.* 2002, **21**(1), p. 37.
189. Shenton, M.J., Lovell-Hoare, M.C., and Stevens, G.C., *J. Phys. D: Appl. Phys.* 2001, **34**, p. 2754.
190. Prat, R., Clouet, F., and Shi, M.K., *J. Macromol. Sci. A: Pure Appl. Chem.* 1997, **34**, p. 471.
191. Inagaki, N., Narushima, K., Tasaka, S., and Kobayashi, H., *J. Appl. Polym. Sci.* 2002, **85**, p. 2845.
192. van Oss, C.J., Chaudhury, M.K., and Good, R.J., *Chem. Rev.* 1988, **88**, p. 927.
193. Cueff, R., Baud, G., Besse, J.P., Jacquet, M., and Benmalek, M., *J. Adhes.* 1993, **42**, p. 249.
194. Behnisch, J., Hollander, A., and Zimmerman, H., *J. Appl. Polym. Sci.* 1993, **49**, p. 117.
195. Gerenser, L.J., *J. Vac. Sci. Technol. A.* 1990, **8**(5), p. 3682.
196. Paynter, R.W., *Surf. Interface Anal.* 2000, **29**, p. 56.
197. Placinta, G., Arefi-Khonsari, F., Gheorghiu, M., Amouroux, J., and Popa, G., *J. Appl. Polym. Sci.* 1997, **66**, p. 1367.
198. d'Agostino, R., Lamendola, R., Tenuto, G., and Creatore, M. in *Society of Vacuum Coaters 41st Technical Conference Proceedings.* 1998, p. 358
199. Moosheimer, U., *Surf. Coat. Tech.* 1999, **116-119**, p. 812.
200. Porta, G.M., Rancourt, J.D., and Taylor, L.T., *Chem. Mater.* 1991, **3**, p. 423.
201. Silvain, J.F., Veyrat, A., and Ehrhardt, J.J., *Thin Solid Films* 1992, **221**, p. 114.
202. Rotger, J.C., Pireaux, J.J., Caudano, R., Thorne, N.A., Dunlop, H.M., and Benmalek, M., *J. Vac. Sci. Technol. A.* 1995, **13**(2), p. 260.
203. da Silva Sobrinho, A.S., Schuhler, N., Klemberg-Sapieha, J.E., Wertheimer, M.R., Andrews, M., and S.C., G., *J. Vac. Sci. Technol. A.* 1998, **16**(4), p. 2021.
204. Binnig, G., Quate, C.F., and Gerber, C., *Phys. Rev. Lett.* 1986, **56**(9), p. 930.
205. Magonov, S.N. and Whangbo, M.-H., *Surface Analysis with STM and AFM.*: VCH (UK). Cambridge. 1996.

Chapter 8. Bibliography

206. Overney, R. and Meyer, E., *MRS Bull.* 1993, p. 26.
207. Overney, R., Meyer, E., Frommer, J., Brodbeck, D., Luthi, R., Howald, L., Guntherodt, H.-J., Fujihara, M., Takano, H., and Gotoh, Y., *Nature* 1992, **359**, p. 133.
208. Frisbie, C.D., Rozsnyai, L.F., Noy, A., Wrighton, M.S., and Lieber, C.M., *Science* 1994, **265**, p. 2071.
209. Schonherr, H., Hruska, Z., and Julius Vansco, G., *Macromolecules* 1998, **31**, p. 3679.
210. Magonov, S.N. and Reneker, D.H., *Annu. Rev. Mater. Sci.* 1997, **27**, p. 175.
211. Sauer, B., McLean, R.S., and Thomas, R.R., *Langmuir* 1998, **14**, p. 3045.
212. Bliznyuk, V., Assender, H.E., and Briggs, G.A.D., *Macromolecules* 2002, **35**(17), p. 6613.
213. Feldman, L.C. and Mayer, J.W., *Fundamentals of Surface and Thin Film Analysis*: North-Holland. New York. 1986.
214. ICI, *Database of XPS spectra of polymer films*.
215. Yasuda, T. and Okuno, T., *Langmuir* 1994, **10**, p. 2435.
216. Good, R.J., *Contact Angle, Wettability and Adhesion*, ed. K.L. Mittal: VSP. Utrecht. 1993. 3.
217. Yildirim Erbil, H., McHale, G., Rowan, S.M., and Newton, M.I., *Langmuir* 1999, **15**, p. 7378.
218. Roll, K., *J. Appl. Phys.* 1976, **47**, p. 3224.
219. *DuPont-Teijin Films Technical Notes on Polyester Films*.
220. Assender, H.E., Bliznyuk, V., and Porfyrakis, K., *Science* 2002, **297**, p. 973.
221. Whitehouse, D.J., *Handbook of Surface Metrology*: Institute of Physics. Bristol. 1994.
222. Meakin, P., *Fractals, Scaling and Growth Far From Equilibrium*: Cambridge University Press. Cambridge. 1998.
223. Russ, J.C., *Fractal Surfaces*: Plenum Press. New York. 1994.
224. Bliznyuk, V., Burlakov, V.M., Assender, H.E., Briggs, G.A.D., and Tsukahara, Y., *Macromol. Symp.* 2001, **167**, p. 89.
225. Krim, J. and Indekeu, J.O., *Phys. Rev. A.* 1993, **48**(2), p. 1576.
226. Lapique, F., Meakin, P., Feder, J., and Jossang, T., *J. Appl. Polym. Sci.* 2002, **86**, p. 973.
227. Goldbeck-Wood, G., Bliznyuk, V., Burlakov, V.M., Assender, H.E., Briggs, G.A.D., Tsukahara, Y., Anderson, K.L., and Windle, A.H., *Macromolecules* 2002, **35**, p. 5283.
228. Wang, L., Huang, T., Kamal, M.R., Rey, A.D., and Teh, J., *Polym. Eng. Sci.* 2000, **40**(3), p. 747.
229. Porfyrakis, K., Marston, N., and Assender, H.E., *Awaiting Publication*.
230. Gerenser, L.J., Grace, J.M., Apai, G., and Thompson, P.M., *Surf. Interface. Anal* 2000, **29**, p. 12.

Chapter 8. Bibliography

231. Lang, F.-R., Pitton, Y., Mathieu, H.J., Landolt, D., and Moser, E.M., *Fresenius J. Anal. Chem.* 1997, **358**, p. 251.
232. Olabisi, O., ed. *Handbook of Thermoplastics*. Marcel Dekker: New York. 1997.
233. Roehrig, M., Bright, C., and Evans, D. in *43rd Annual Technical Conference Proceedings of the Society of Vacuum Coaters*. 2000, p. 335
234. Thornton, J.A. and Lamb, J.L., *Thin Solid Films* 1984, **119**, p. 87.
235. Bishop, C.A. and McCann, M.J. in *48th Annual Technical Conference Proceedings of the Society of Vacuum Coaters*. 2005, p. 626
236. Zhang, Y., Zhang, J., Lu, Y., Duan, Y., Yan, S., and Shen, D., *Macromolecules* 2004, **37**, p. 2532.
237. Forrest, J.A., Dalnoki-Veress, K., Stevens, J.R., and Dutcher, J.R., *Phys. Rev. Lett.* 1996, **77**(10), p. 2002.
238. Aharoni, S.M., *Polym. Adv. Tech.* 1999, **9**, p. 169.
239. Alves, N.M., Mano, J.F., Balaguer, E., Meseguer Duenas, J.M., and Gomez Ribelles, J.L., *Polymer* 2002, **43**, p. 4111.
240. Jukes, P.C., Das, A., Durell, M., Trolley, D., Higgins, A.M., Geoghegan, M., MacDonald, J.E., Jones, R.A.L., Brown, S., and Thompson, P., *Macromolecules* 2005, **38**, p. 2315.
241. Hayes, N.W., Beamson, G., Clark, D.T., Law, D.S.-L., and Raval, R., *Surf. Interface Anal.* 1996, **24**(10), p. 723.
242. Petit, S., Laurens, P., Amouroux, J., and Arefi-Khonsari, F., *Appl. Surf. Sci.* 2000, **168**, p. 300.
243. Ektebassi, A.M. and Yamaguchi, K., *Thin Solid Films* 2000, **377-378**, p. 793.
244. Yang, S. and Gupta, M.C., *Surf. Coat. Tech.* 2004, **187**, p. 172.
245. France, R.M. and Short, R.D., *J. Chem. Soc., Faraday Trans.*, 1997, **93**(17), p. 3173.
246. Milde, F., Goedicke, K., and Fahland, M., *Thin Solid Films* 1996, **279**, p. 169.
247. Owens, D.K. and Wendt, R.C., *J. Appl. Polym. Sci.* 1969, **13**, p. 1741.
248. Shalel-Levanon, S. and Marmur, A., *J. Colloid Interface Sci.* 2003, **262**, p. 489.
249. Bou, M., Martin, J.M., and Le Mogne, T., *Appl. Surf. Sci.* 1991, **47**, p. 149.
250. Sandrin, L. and Sacher, E., *Appl. Surf. Sci.* 1998, **135**, p. 339.
251. Ardelean, H., Petit, S., Laurens, P., Marcus, P., and Arefi-Khonsari, F., *Appl. Surf. Sci.* 2005, **243**, p. 304.
252. Pliskin, W.A., *Thin Solid Films* 1969, **2**, p. 1.
253. Robic, J.Y., Leplan, H., Pauleau, Y., and Rafin, B., *Thin Solid Films* 1996, **290-291**, p. 34.

Chapter 8. Bibliography

254. Rotger, J.C., Pireaux, J.J., Caudano, R., Thorne, N.A., Dunlop, H.M., and Benmalek, M., *J. Vac. Sci. Technol. A* 1994, **13**(2), p. 260.
255. Felts, J.T. in *33rd Annual Technical Conference Proceedings of the Society of Vacuum Coaters*. 1990, p. 184
256. Madocks, J. in *46th Annual Technical Conference Proceedings of the Society of Vacuum Coaters*. 2003, p. 137
257. Theil, J.A., Brace, J.G., and Knoll, R.W., *J. Vac. Sci. Technol. A* 1994, **12**(4), p. 1365.
258. Poll, H.-U., Meischner, J., Arzt, M., Friedrich, M., Rochotzki, R., and Kreyßig, E., *Surf. Coat. Tech.* 1993, **59**, p. 365.
259. Sakakura, O., Nakajima, T., and Oboshi, T. in *47th Annual Technical Conference Proceedings of the Society of Vacuum Coaters*. 2004, p. 194
260. Norenberg, H., Smith, G.D.W., Briggs, G.A.D., Miyamoto, T., and Tsukahara, Y. in *45th Annual Technical Conference Proceedings of the Society of Vacuum Coaters*. 2002, p. 546
261. Steward, P.A., Hearn, J., and Wilkinson, M.C., *Adv. Coll. Interface. Sci*, 2000, **86**, p. 195.
262. Keddie, J.L., *Mat. Sci. Eng. R*. 1997, **21**, p. 101.
263. Davis, T.P., in *Handbook of Thermoplastics*, O. Olabisi, Editor. 1997, Marcel Dekker: New York.
264. Paul, S., *Surface Coatings Science and Technology*: Wiley Inter Science. New York. 1986.
265. Chevalier, Y., Hidalgo, M., Cavaille, J.-Y., and Cabane, B., *Macromolecules* 1999, **32**, p. 7887.
266. Seda Tigh, R. and Evren, V., *Prog. Org. Coat.* 2005, **52**, p. 144.
267. Charneau, J.Y., Berthet, R., Gringreau, C., and Holl, Y., *Int. J. Adhesion and Adhesives* 1997, **17**, p. 169.
268. Okubo, M., Seike, M., and Matsumoto, T., *J. Appl. Polym. Sci.* 1983, **28**, p. 383.
269. Colombini, D., Hassander, H., Karlsson, O.J., and Maurer, F.H.J., *J. Polym. Sci. B* 2005, **43**, p. 2289.